

---

# **Nichtlineare Optik mit ultrakurzen Laserpulsen:**

**Suszeptibilität dritter Ordnung und kleine Polaronen  
sowie Interferenz und Holographie verschiedenfarbiger  
Laserpulse**

---

Kumulative Dissertation  
zur Erlangung des Grades  
eines Doktors der Naturwissenschaften

von

Holger Badorreck

genehmigt vom Fachbereich Physik der



Osnabrück, im Oktober 2015



# Inhaltsverzeichnis

<b>1</b>	<b>Einleitung</b>	<b>1</b>
<b>2</b>	<b>Grundlagen</b>	<b>5</b>
2.1	Erzeugung von Femtosekunden-Pulsen . . . . .	5
2.2	Beschreibung von fs-Pulsen . . . . .	6
2.2.1	Fokussierung von Gaußstrahlen . . . . .	7
2.2.2	Intensitätsberechnung . . . . .	7
2.3	Nichtlineare Optik . . . . .	8
2.3.1	Elektrooptischer Kerr-Effekt . . . . .	8
2.3.2	Zwei-Photonen-Absorption (TPA) . . . . .	9
2.3.3	Theorie des Z-Scan-Experiments . . . . .	10
2.3.4	Holographische Gitter . . . . .	12
<b>3</b>	<b>Optische Nichtlinearitäten in photonischen Materialien</b>	<b>15</b>
3.1	Optische Nichtlinearitäten in Lithiumniobat . . . . .	15
3.1.1	Publikationen . . . . .	15
3.1.2	Nichtlinearer Brechungsindex in Lithiumniobat . . . . .	17
3.2	Optische Nichtlinearitäten in Di-Zinn-Hexathiohypodiphosphat . . . . .	22
<b>4</b>	<b>Interferenz verschiedenfarbiger ultrakurzer Lichtpulse</b>	<b>25</b>
4.1	Publikationen . . . . .	25
<b>5</b>	<b>Zusammenfassung</b>	<b>27</b>
	<b>Literaturverzeichnis</b>	<b>29</b>
<b>A</b>	<b>Publikationen</b>	<b>33</b>
A.1	Scanning nonlinear absorption in lithium niobate over the time regime of small polaron formation . . . . .	35
A.2	Optical nonlinearities of small polarons in lithium niobate . . . . .	51
A.3	Tin hypthiodiphosphate: nonlinear response in the sub-100fs time domain . . . . .	103
A.4	Self-diffraction from two-photon absorption gratings in Sn2P2S6 . . . . .	113
A.5	Interference and holography with femtosecond laser pulses of different colours . . . . .	119
A.6	Doppler-shifted Raman-Nath diffraction from gratings recorded in LiNbO3 with ultra-short laser pulses of different color . . . . .	135



# Kapitel 1

## Einleitung

Mit der Vereinheitlichung der Theorie von Elektrizität und Magnetismus zum Elektromagnetismus legte James C. Maxwell [1] 1865 den Grundstein für das Verständnis elektromagnetischer Wellen und ihrer Wechselwirkung mit Materie. Dabei erkannte er, dass Licht nichts anderes als eben eine elektromagnetische Welle darstellt. Albert Einstein [2] fügte diesem Verständnis 1905 den wichtigen quantentheoretischen Aspekt hinzu, dass Licht in Photonen energetisch quantisiert ist. In einer weiteren Arbeit sagte Einstein 1916 die stimulierte Emission von Licht voraus [3]. Während Nikolai Bassov, Alexander Prokhorov und Charles Towns in den 50er Jahren dies experimentell im Mikrowellenbereich durch die Entwicklung eines Masers bereits nachweisen konnten, gelang Theodore H. Maiman dies zuerst im sichtbaren Spektralbereich 1960 mit der Entwicklung des ersten Lasers [4].

Der Laser ist heutzutage in unterschiedlichsten Bereichen des Alltags im Einsatz. Von der räumlichen Vermessung per 3D-Laserscanner und Geschwindigkeitsmessungen per Laserpistole über die optische Speicherung auf Datenträgern (CD, DVD, Bluray) und Datenübertragung per Glasfaser bis hin zu Anwendungen in der Medizin, bspw. in der Augenheilkunde oder Dermatologie. Auch in der Wissenschaft ist der Laser von größter Bedeutung, neben dem Thema dieser Arbeit ist dies zum Beispiel die Trägheitsfusion, bei der extrem hohe Energiedichten von Bedeutung sind, oder die Observation von Gravitationswellen, bei denen kleinste Abstandsänderungen in der Größenordnung des Durchmessers eines Atomkerns gemessen werden müssen.

Mit dem Laser stand erstmals eine Lichtquelle mit gleichzeitig hoher Intensität und hoher Kohärenz zur Verfügung, die zum neuen Forschungsgebiet der nichtlinearen Optik führte. Beginnend mit der Beobachtung der Frequenzverdopplung [5] wurden zahlreiche weitere nichtlineare optische Effekte beobachtet, darunter z.B. die bereits 1931 theoretisch beschriebene Zwei-Photonen-Absorption [6, 7]. Auch für die von Dennis Gabor entwickelte Holographie [8], die eine kohärente Lichtquelle voraussetzt, bedeutete der Lasers eine enorme Entwicklung in diesem Forschungsgebiet. Emmett Leith und Juris Upatnieks zeichneten das erste Bildhologramm eines 3D-Objekts auf [9] und Yuri N. Denisyuk erzeugte das erste Weißlichthologramm, welches auch bei inkohärenter Beleuchtung betrachtet werden konnte [10].

Die höhere Effizienz nichtlinearer optischer Prozesse bei hohen Intensitäten sowie der Drang immer kürzere Prozesse zeitlich auflösen zu können, führte zur Entwicklung von Pulslasern mit immer kürzeren Pulslängen, von Pikosekunden [11] über Femtosekunden [12] bis hin zu Attosekunden [13]. Dadurch können Prozesse untersucht werden, die durch die Begrenzung der Geschwindigkeit elektronischer Messverfahren

im Bereich von Nanosekunden nicht zugänglich sind. Auf der Femtosekunden Zeitskala können mit diesen Pulslasern die Dynamik molekularer Strukturen [14] und im Bereich von Attosekunden elektronische Prozesse [13] untersucht werden.

Doch auch wenn das theoretische Verständnis von Licht und seiner Wechselwirkung mit Materie weit fortgeschritten ist, sind noch viele Aspekte zu erforschen. Entscheidend für zukünftige Entwicklungen ist die Kontrolle von Licht um beispielsweise Computer zu entwickeln, die durch die komplette Umstellung von einer elektronischen zu einer optischen Funktionsweise (Schlagwort: all-optical-computing) wesentlich beschleunigt werden könnten [15], oder auch die Darstellung bewegter 3D Hologramme [16, 17]. Für die Kontrolle von Licht sind passende Materialien wichtig, die eine effiziente Licht-Materie-Wechselwirkung aufweisen.

Von großer Wichtigkeit für die nichtlineare Optik ist dabei das Material Lithiumniobat ( $\text{LiNbO}_3$ ), welches aufgrund seiner vielfältigen Eigenschaften zahlreiche Effekte aufweist [18, 19], z.B. die Frequenzverdopplung durch Quasi-Phasenanpassung [20] oder die holographische Datenspeicherung durch den photorefraktiven Effekt in dotiertem Lithiumniobat [21, 22]. Einen zudem interessanten Aspekt stellen in Lithiumniobat durch eine Gitterverzerrung lokalisierte Ladungsträger (sogenannte kleine Polaronen [23]) dar. Deren Entstehung wird in undotiertem Lithiumniobat durch die intrinsische Defektstruktur ermöglicht. Die Erzeugung von Polaronen kann dabei über hohe Intensitäten durch Zwei-Photonen-Absorption temporär oder auch durch thermische Reduktion dauerhaft vorgenommen werden [24, 25]. Die Anregung polaronischer Zustände erfolgt sehr schnell, bisher konnten Zeiten im Bereich von etwa 100 fs gemessen werden [26–28]. Die Lebensdauer reicht dabei von Mikro- bis Millisekunden [29, 30]. Durch den Einfluss auf die Absorption und den Brechungsindex ermöglichen Polaronen auch holographische Anwendungen [31]. Neben Lithiumniobat weisen auch zahlreiche andere Materialien polaronische Zustände auf, darunter Saphir [32], Kaliumniobat [33] und Di-Zinn-Hexathiohypodiphosphat [34]. Zudem sind Polaronen bei der Erforschung von Solarzellen durch den volumenphotovoltaischen Effekt von Bedeutung [35].

Diese Arbeit beschäftigt sich mit der Messung der nichtlinearen Suszeptibilität dritter Ordnung mittels Femtosekundenpulsen, also der Zwei-Photonen-Absorption und dem nichtlinearen Brechungsindex von Lithiumniobat und geht der Frage nach, inwiefern nichtlineare Effekte auf kleine Polaronen zurückzuführen sind. Zudem wird die zeitliche Auflösung der Entstehung von Polaronen behandelt. Dazu wird die nichtlineare Absorption und der nichtlineare Brechungsindex von Lithiumniobat mithilfe des Z-Scan-Experiments mit unterschiedlichen Pulslängen in einem Bereich von 70–1000 fs untersucht. Die Weiterentwicklung eines Polaronenanregungsmodells von Qiu et al. [26] führt dabei zu einer geeigneten Interpretation der Generation von Polaronen und erlaubt die Separation der polaronischen Nichtlinearitäten von den Effekten der Suszeptibilität dritter Ordnung.

Als weiteres Material wird Di-Zinn-Hexathiohypodiphosphat ( $\text{Sn}_2\text{P}_2\text{S}_6$ ) untersucht, welches insbesondere für den nahinfraroten Bereich mit der Telekommunikationswellenlänge bei 1550 nm von Bedeutung ist. Es kann ein sehr großer Zwei-Photonen-Absorptionskoeffizient festgestellt werden sowie eine transiente Absorption nach optischer Anregung, die Polaronen zugeordnet werden kann. Die starke Zwei-Photonenabsorption erlaubt die Aufzeichnung von dynamischen holographischen Amplituden-

---

gittern in  $\text{Sn}_2\text{P}_2\text{S}_6$ .

Ein weiteres Thema dieser Arbeit ist die Interferenz und Holographie zwischen verschiedenfarbigen Femtosekundenpulsen. Während die Möglichkeit zur Interferenz zwischen zwei verschiedenen Lasern mit gleicher Frequenz bereits 1963 [36] gezeigt wurde und damit dem Postulat von Paul Dirac widersprach, dass Photonen ausschließlich mit sich selbst interferieren [37], wird in dieser Arbeit die Interferenz zwischen Laserpulsen verschiedener Frequenz gezeigt. Die Bewegung des Interferenzmusters, die bei verschiedenen Frequenzen vorliegt, und deren Geschwindigkeit im Bereich der Lichtgeschwindigkeit liegt, führt bei kontinuierlichem Laserlicht zu einem Verschmieren und macht die Beobachtung unmöglich. Die enorme Kürze der Pulse lässt das Gitter allerdings eingefrieren und erlaubt somit die Aufzeichnung eines Schnappschusses des bewegten Gitters. Das bewegte Gitter erzeugt dabei durch den Dopplereffekt die Frequenzverschiebung weiterer Beugungsordnungen und kann somit auch zur Frequenzkonversion genutzt werden.



# Kapitel 2

## Grundlagen

In diesem Kapitel werden die Grundlagen der Erzeugung von Femtosekunden-Pulsen und die aus den hohen Intensitäten resultierenden nichtlinearen Effekte dargestellt sowie die Holographie erläutert. Dies wurde vom Autor größtenteils aus [38] übernommen.

### 2.1 Erzeugung von Femtosekunden-Pulsen

Hier wird die Erzeugung von Laserpulsen mit einer Pulslänge im Bereich von Femtosekunden behandelt, die Darstellung folgt dabei in großen Teilen der Referenz [39]. Zur Erzeugung von Femtosekunden-Pulsen wird ein Laser im sogenannten *Mode-Locking*-Betrieb verwendet. Damit ist die Phasenkopplung einer großen Anzahl  $M$  von longitudinalen Moden des Laserresonators gemeint. Als transversale Mode wird im Allgemeinen ausschließlich die TEM<sub>00</sub>-Mode verwendet. Die Frequenz der longitudinalen Moden  $\nu_j$  muss die Resonatorbedingung

$$\nu_j = \frac{j c}{2 n(\nu_j) L} \quad (2.1)$$

erfüllen, dabei ist  $c$  die Lichtgeschwindigkeit,  $n(\nu_j)$  der über die verschiedenen optischen Elemente im Resonator gemittelte Brechungsindex bei der Frequenz  $\nu_j$  und  $L$  die geometrische Weglänge des Resonators. Sofern die sogenannte *Group Velocity Dispersion* (GVD) verschwindet, ist der Frequenzabstand  $\delta$  zwischen zwei longitudinalen Moden aufgrund des frequenzunabhängigen Brechungsindex ( $n(\nu_j) = n = \text{const.}$ ) äquidistant:

$$\delta = \nu_{j+1} - \nu_j = \frac{c}{2 n L} \quad (2.2)$$

Das elektrische Feld eines Lasers mit  $M$  nebeneinanderliegenden Moden gleicher Amplitude  $E_0$  lässt sich dann als

$$E(t) = \frac{1}{2} E_0 e^{i \omega_\ell t} \sum_{j=(-M+1)/2}^{(M-1)/2} e^{i(2\pi j \delta t + \phi_j)} \quad (2.3)$$

beschreiben. Die mittlere Frequenz wird durch  $\omega_\ell$  angegeben und die Phase der jeweiligen Mode ist  $\phi_j$ . Es ergibt sich eine Periodizität bis auf einen Phasenfaktor

$$E\left(t + \frac{n}{\delta}\right) = E(t) \exp\left(i \omega_\ell \frac{n}{\delta}\right) \quad (2.4)$$

mit  $n \in \mathbb{Z}$ . Diese Periodizität  $\tau_R = 1/\delta$  entspricht der Umlaufzeit des Resonators. Unter der zusätzlichen Bedingung, dass die Phasen der einzelnen Moden identisch sind ( $\phi_j = \phi = \text{const.}$ ) – das wird als *Mode-Locking* bezeichnet – addieren sich die Amplituden und ein kurzer intensiver Puls entsteht. Das entstehende elektrische Feld lässt sich folgendermaßen beschreiben:

$$E(t) = \frac{1}{2} E_0 e^{i\phi_0} e^{i\omega_\ell t} \frac{\sin(M\pi\delta t)}{\sin(\pi\delta t)} \quad (2.5)$$

Für große  $M$  ergibt sich, dass die Länge der Pulse  $\tau_p$ , entsprechend der Unbestimmtheitsrelation, proportional zur inversen spektralen Bandbreite  $\Delta\nu_p$  des Lasers ist:

$$\tau_p \propto \frac{1}{M\delta} = \frac{1}{\Delta\nu_p} \quad (2.6)$$

Aus der Frequenzbandbreite ergibt sich somit die minimale Länge eines Laserpulses. Für die praktische Realisierung eines fs-Pulslasers benötigt man also ein spektral breitbandig emittierendes Lasermedium. Dabei haben sich Ti:Saphir( $\text{Ti}_2\text{O}_3:\text{Al}_2\text{O}_3$ )-Kristalle als vorteilhaft erwiesen. Diese absorbieren Licht über einen großen Wellenlängenbereich von etwa 400–600 nm mit der größten Absorption bei 500 nm, Fluoreszenz tritt bei Wellenlängen von 600–1000 nm auf. Eine maximale Verstärkung ist bei 795 nm zu erreichen [40]. Dabei ist die GVD nicht zu vernachlässigen, für eine konstante Phasenbeziehung zwischen den einzelnen Moden muss diese also kompensiert werden. Das geschieht dadurch, dass die Resonatorlänge in Abhängigkeit der Frequenz verändert wird: Dies kann durch zwei Prismen geschehen, die in den Resonator eingebracht werden, zur Vermeidung von transmittierenden Optiken werden alternativ Spiegel mit negativer Dispersion verwendet. Damit sind von der Frequenz unabhängige Feldamplituden und Brechungsindices im Resonator möglich und Gleichung (2.5) ist somit gültig.

Eine Möglichkeit zur Realisierung gleicher Phase  $\phi_j = \phi = \text{const.}$  zwischen den longitudinalen Moden ist das Mode-Locking über die *Kerr-Linse*. Durch die hohen Intensitäten bei kurzen Laserpulsen kommt im Lasermedium der elektrooptische Kerr-Effekt zum Tragen, der den Brechungsindex in Abhängigkeit der Intensität verändert (siehe dazu auch Abschnitt 2.3.1). Der Laserstrahl hat ein räumlich moduliertes gaußförmiges Intensitätsprofil, dadurch entsteht ein Brechungsindexprofil im Lasermedium, die sogenannte Kerr-Linse. Durch die Verwendung einer geeigneten Apertur im Strahlengang wird ein durch die Kerr-Linse fokussierter Laserpuls gegenüber einem nicht fokussierten cw-Laserstrahl bevorzugt (Passives Mode-Locking). Um den Mode-Locking-Prozess zu starten, können durch Variation der Resonatorlänge und der damit verbundenen Änderung der Phasenbeziehung der Moden untereinander große Leistungsfluktuationen induziert werden [41].

## 2.2 Beschreibung von fs-Pulsen

Femtosekundenpulse werden hier als gaußförmige Pulse beschrieben. Das heißt, die Pulsform wird sowohl zeitlich als auch räumlich als gaußförmig angenommen. Im

Folgenden werden diese als Gauß-Pulse bezeichnet. Für Gauß-Pulse lautet die Unbestimmtheitsrelation (Gleichung (2.6)) [39]:

$$\tau_p \Delta\nu_p = 0,441 \quad (2.7)$$

Hierbei ist  $\tau_p$  die zeitliche und  $\Delta\nu_p$  die spektrale Halbwertsbreite (FWHM) des Pulses. Die Intensitätsverteilung des Gauß-Pulses ist durch

$$I(r,t) = I_0 \exp\left(-\left(t/t_p\right)^2 - \left(r/r_p\right)^2\right) \quad (2.8)$$

mit der Peak-Intensität  $I_0$ , der Pulslänge  $t_p = \tau_p/(2\sqrt{\ln 2})$  und dem Strahlradius  $r_p$  gegeben.

### 2.2.1 Fokussierung von Gaußstrahlen

Der Strahlradius ( $1/e$ -Wert der elektrischen Feldamplitude,  $1/e^2$ -Wert der Intensität) eines fokussierten Gauß-Strahls kann folgendermaßen berechnet werden [42]

$$w_0 = \frac{\lambda f M^2}{\pi w_L} \quad (2.9)$$

$$w_R(z) = w_0 \sqrt{1 + \left(\frac{z \lambda M^2}{\pi w_0^2}\right)^2} \quad (2.10)$$

Der Strahlradius im Fokus  $w_0$  ist von der Wellenlänge  $\lambda$ , der Brennweite  $f$  (von Linse, Spiegel), der Strahlqualität  $M^2$  und dem Durchmesser vor der Fokussierung  $w_L$  abhängig.  $w_R(z)$  gibt den  $1/e$ -Strahlradius an einer beliebigen Entfernung  $z$  vom Fokuspunkt an. Die Strahlqualität  $M^2$  gibt die Abweichung eines realen Strahls vom Gaußstrahl an und ist im Vakuum durch

$$M^2 = \Theta w_0 \frac{\pi}{\lambda} \geq 1 \quad (2.11)$$

mit  $\Theta$  als Divergenzwinkel des Strahls und  $\lambda$  als Wellenlänge definiert. Für Gauß-Strahlen ist  $M^2 = 1$ , reale Strahlen haben Werte größer als 1 und sind gemäß Gleichung (2.9) weniger stark fokussierbar.

### 2.2.2 Intensitätsberechnung

Intensitäten von fs-Pulsen werden aus einer Messung von Pulsenergie, -länge sowie Strahlradius berechnet. Die Peak-Leistung  $P$  eines gaußförmigen Pulses ergibt sich aus der Pulsenergie  $E_p$  und der Halbwertsbreite  $\tau_p$  zu

$$\begin{aligned} P &= \sqrt{\frac{\ln(16)}{\pi}} \frac{E_p}{\tau_p} \\ &\approx 0,94 \frac{E_p}{\tau_p} \end{aligned} \quad (2.12)$$

Der Strahlradius  $w(z)$  an einer beliebigen Stelle hinter einer Linse ergibt sich nach Gleichung (2.9) und (2.10) zu

$$w(z) = \frac{\lambda f M^2}{\pi w_L} \cdot \sqrt{1 + \frac{\pi^2 w_L^2 z^2}{f^4 M^4 \lambda^2}} \quad (2.13)$$

Dabei ist  $z$  der Abstand vom Fokuspunkt. Die Peak-Intensität  $I_0(z)$  eines Pulses ergibt sich damit zu

$$\begin{aligned} I_0(z) &= \frac{2P}{\pi w^2(z)} \\ &\approx 1,88 \frac{E_p}{\tau_p} \frac{\pi f^2 w_L^2}{\pi^2 w_L^4 z^2 + f^4 M^4 \lambda^2} \end{aligned} \quad (2.14)$$

## 2.3 Nichtlineare Optik

Eine Wechselwirkung zwischen Photonen des sichtbaren Spektralbereich im Vakuum ist sehr unwahrscheinlich, sodass sie bei Intensitäten von heutzutage verfügbaren Lichtquellen nicht auftritt [43]. Wenn von nichtlinearer Optik gesprochen wird, ist stets eine nichtlineare Wechselwirkung zwischen Photonen und Materie gemeint. Eine Abhängigkeit der Brechungsindex- und Absorptionskoeffizienten, welche linear mit der Intensität skaliert, entsteht durch die 3. Ordnung der Suszeptibilität. Dies wird exemplarisch für den elektrooptischen Kerr-Effekt (nichtlinearer Brechungsindex) gezeigt [44, 45].

### 2.3.1 Elektrooptischer Kerr-Effekt

Die elektrische Polarisierung eines Mediums ist im linearen Fall durch

$$\mathbf{P} = \epsilon_0 \chi \mathbf{E} \quad (2.15)$$

gegeben. Die dielektrische Suszeptibilität  $\chi$  wird hier zur Vereinfachung als Skalar angenommen, im Allgemeinen ist dies eine tensorielle Größe. Bei hohen Intensitäten, und dementsprechend hohen elektrischen Feldstärken, muss man beachten, dass die Suszeptibilität abhängig von höheren Ordnungen der elektrischen Feldstärke ist. Obige Gleichung lautet dann

$$\begin{aligned} \mathbf{P} &= \epsilon_0 \sum_n \chi^{(n)} \mathbf{E}^n \\ &= \epsilon_0 (\chi^{(1)} + \chi^{(2)} \mathbf{E} + \chi^{(3)} |\mathbf{E}|^2 + \dots) \mathbf{E} \end{aligned} \quad (2.16)$$

Der erste Term ( $\chi^{(1)}$ ) stellt dabei die lineare Wechselwirkung dar, der zweite ( $\chi^{(2)}$ ) erklärt nichtlineare Effekte von 2. Ordnung wie die Frequenzverdopplung oder den Pockels-Effekt. Sofern kein gerichtetes elektrisches Feld an das Medium angelegt wird, stellt der Term 3. Ordnung ( $\chi^{(3)}$ ) die niedrigste nicht verschwindende Nichtlinearität dar. Die Antwort des nichtlinearen Mediums auf eine Bestrahlung mit der Frequenz  $w$

enthält einen Anteil bei der Grundfrequenz  $w$  sowie auch bei der dreifachen Frequenz  $3w$ .

$$\begin{aligned}
 \frac{\mathbf{P}^{(3)}}{\epsilon_0 \chi^{(3)}} &= \mathbf{E}(w)^3 \\
 &= (\mathbf{E}_0 \cos(wt))^3 \\
 &= \mathbf{E}_0 |\mathbf{E}_0|^2 \left( \frac{3}{4} \cos(wt) + \frac{1}{4} \cos(3wt) \right)
 \end{aligned} \tag{2.17}$$

Die Polarisation des Mediums in Abhängigkeit der Grundfrequenz  $w$  lautet dann

$$\mathbf{P}(w) = \epsilon_0 \left( \chi^{(1)} + \frac{3}{4} \chi^{(3)} |\mathbf{E}_0|^2 \right) \mathbf{E}(w) \tag{2.18}$$

Für Dielektrika ist der Brechungsindex mit dem Realteil der Suszeptibilität  $\chi_{\text{Re}}$  durch  $n = \sqrt{1 + \chi_{\text{Re}}}$  gegeben. Im Fall einer Suszeptibilität von 1. und 3. Ordnung ergibt sich mit  $|\mathbf{E}_0|^2 = 2I/\epsilon_0 c n_0$  für den Brechungsindex:

$$\begin{aligned}
 n &= \sqrt{1 + \chi_{\text{Re}}^{(1)} + \frac{3}{4} \chi_{\text{Re}}^{(3)} \frac{2}{\epsilon_0 c n_0} I} \\
 &= n_0 \sqrt{1 + \frac{6 \chi_{\text{Re}}^{(3)}}{4 \epsilon_0 c n_0^3} I} \\
 &\approx n_0 \left( 1 + \frac{3 \chi_{\text{Re}}^{(3)}}{4 \epsilon_0 c n_0^3} I \right) \quad (\text{Taylor-Entwicklung}) \\
 &= n_0 + \frac{3 \chi_{\text{Re}}^{(3)}}{4 \epsilon_0 c n_0^2} I \\
 &= n_0 + n_2 I
 \end{aligned} \tag{2.19}$$

Der von der Intensität abhängige Brechungsindex wird also durch eine Suszeptibilität von 3. Ordnung erzeugt und kann für  $\chi_{\text{Re}}^{(3)} I \ll n_0^2$  durch Gleichung (2.19) beschrieben werden. Zu beachten ist, dass  $n_2$  wie  $n_0$  ein Dispersionsverhalten aufweist. Dies resultiert aus dem Dispersionsverhalten der Suszeptibilität, also den Materialeigenschaften.

### 2.3.2 Zwei-Photonen-Absorption (TPA)

Die Zwei-Photonen-Absorption (TPA, von *Two Photon Absorption*) bezeichnet die gleichzeitige Absorption zweier Photonen durch ein Medium. Das Medium geht dabei in einen energetisch angeregten Zustand über. Zwischen den Energieniveaus von Grundzustand und angeregtem Zustand existiert kein reales energetisches Zwischen-niveau. Zur Beschreibung nimmt man aber ein virtuelles Zwischen-niveau an, dessen Lebensdauer der Dauer des Absorptionsprozesses entspricht. Der TPA-Koeffizient  $\beta$  wird analog zum nichtlinearen Brechungsindex definiert, sodass die Gesamtabsorption durch

$$\alpha(I) = \alpha + \beta I \tag{2.20}$$

gegeben ist. Für reine nichtlineare Absorption gilt für die Intensität in Abhängigkeit der Propagationlänge  $d$  durch das Medium die Differentialgleichung

$$I'(d) = -\beta I^2(d) \quad (2.21)$$

Für die Intensität hinter einem Medium der Dicke  $d$  ergibt sich also für ein Strahlprofil mit konstanter Intensität (bspw. Rechteckprofil):

$$I(d) = \frac{I(0)}{1 + \beta d I(0)} \quad (2.22)$$

### 2.3.3 Theorie des Z-Scan-Experiments

Bei dem Z-Scan-Experiment fährt man eine zu untersuchende Probe durch den Fokus eines fokussierten Lichtstrahls (s. Abbildung 2.1). Hierdurch lassen sich nichtlinearer Brechungsindex und nichtlineare Absorption aus der Messung der Transmission als Funktion der Intensität bestimmen. Die Theorie des Z-Scan-Experiments wurde von *Sheik-Bahae* [46] entwickelt. Die wichtigsten Ergebnisse dieser Arbeit werden im Folgenden vorgestellt:

Durch die nichtlineare Änderung des Brechungsindex  $\Delta n_{\text{nl}}$  und damit auch der Lichtgeschwindigkeit im Medium erfährt eine Lichtwelle die Phasenverschiebung  $\Delta\phi$ :

$$\Delta\phi = \frac{2\pi}{\lambda} \Delta n_{\text{nl}} d \quad (2.23)$$

Hierbei bezeichnen  $\lambda$  die Vakuumwellenlänge und  $d$  die Probendicke. Eine nicht vernachlässigbare lineare Absorption  $\alpha$  kann durch eine effektive Probendicke berücksichtigt werden, die sich aus dem linearen Absorptionkoeffizienten ergibt:

$$d_{\text{eff}} = \frac{1 - \exp(-\alpha d)}{\alpha} \quad (2.24)$$

Durch eine lichtinduzierte Kerr-Linse wird ein Gaußstrahl je nach Richtung der Brechungsindexänderung fokussiert oder defokussiert. Indem man eine Apertur in den Strahlengang hinter der Probe einbringt, hängt die Transmission mit der Strahldivergenz nach der Probe zusammen. Die Größe der Apertur  $S$  ist mit dem Aperturradius

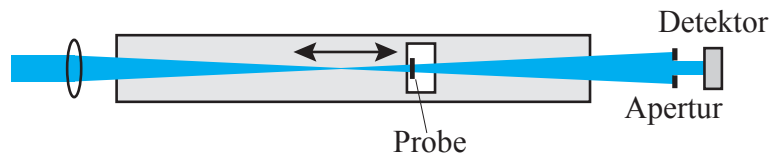


**Abbildung 2.1:** Prinzipieller Aufbau eines Z-Scan-Experiments. Die zu untersuchende Probe wird durch den Fokus eines Strahls gefahren und damit das Transmissionssignal, welches teilweise durch eine Apertur abgeschnitten wird, als Funktion der Intensität gemessen.

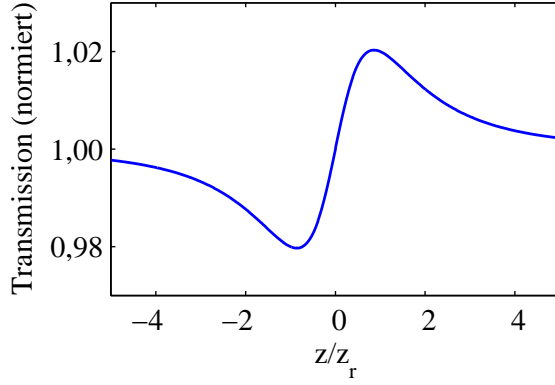


**Abbildung 2.2:** Exemplarischer Verlauf der Transmission des Z-Scan-Experiments gemäß Gleichung (2.26) für  $\Delta\phi = 0,1$ .

$r_a$  und dem Strahlradius  $w_a$  an der Apertur durch

$$S = 1 - \exp\left(-2 \frac{r_a^2}{w_a^2}\right) \quad (2.25)$$

definiert. Die Transmission hinter der Apertur ergibt sich für einen Gauß-Puls unter der Annahme eines nichtlinearen Brechungsindex 3. Ordnung, verschwindender nichtlinearer Absorption, einer Phasenverschiebung von  $|\Delta\phi| \ll 1$  sowie einer kleinen Apertur ( $S = 0,01$ ) im Fernfeld zu:

$$T(z, \Delta\phi) \approx 1 - \frac{4(z/z_r) \Delta\phi}{((z/z_r)^2 + 9)((z/z_r)^2 + 1)} \quad (2.26)$$

Hierbei ist  $z$  die Probenposition;  $z_r$  ist die Rayleighlänge des verwendeten Strahls. In Abbildung 2.2 ist der Verlauf der Funktion (2.26) beispielhaft für eine Phasenverschiebung von  $\Delta\phi = 0,1$  gezeigt. Für größere Phasenverschiebungen ( $1 < |\Delta\phi| < \pi$ ) verschiebt sich die Funktion in  $z$ -Richtung, die folgenden Gleichungen gelten allerdings weitgehend unverändert. Der Abstand von Maximum zu Minimum dieser Funktion auf der Abzisse ist etwa

$$\Delta Z \approx 1,7 z_r \quad (2.27)$$

und die Höhendifferenz ergibt sich unter Beachtung auch von größeren Aperturen zu

$$\Delta T \approx 0,406 (1 - S)^{0,25} \Delta\phi. \quad (2.28)$$

Die nichtlineare Brechungsindexänderung von dritter Ordnung kann also aus den Messdaten mit folgender Beziehung bestimmt werden:

$$\Delta n = \Delta T \frac{\lambda}{2\pi d_{\text{eff}}} \frac{1}{0,406(1 - S)^{0,25}} \quad (2.29)$$

Bei Beachtung einer nichtlinearen Absorption ergibt sich für eine offene Apertur ( $S = 1$ ) die Transmission:

$$T(z) = \frac{1}{q(z)\sqrt{\pi}} \int_{-\infty}^{\infty} \ln(1 + q(z) e^{-s^2}) ds \quad (2.30)$$

Der einzige unbekannt Parameter dieser Funktion ist der Zweiphotonenabsorptionskoeffizient  $\beta$ , der im Absorptionsparameter  $q$  enthalten ist:

$$q(z) = \beta I(z) d_{\text{eff}} \quad (2.31)$$

### 2.3.4 Holographische Gitter

Mithilfe von Zweistrahlinterferometrie lassen sich elementare holographische Gitter erzeugen. Dies ist in Abbildung 2.3 dargestellt. Indem zwei ebene Wellen (P1 und P2) überlagert werden, entsteht ein räumlich moduliertes Intensitätsmuster. Dieses ist durch

$$I(x) = I_0 (1 + m \cos(|\mathbf{K}| x)) \quad (2.32)$$

gegeben,  $m$  ist der Modulationsgrad, der den Kontrast des Gitters angibt:

$$m = \frac{2\sqrt{I_{P1}I_{P2}}}{I_{P1} + I_{P2}} \quad (2.33)$$

Photochrome bzw. photorefraktive Materialien können durch die räumlich modulierte Beleuchtung ein Absorptions- bzw. Phasengitter ausbilden. Die Gitterkonstante  $\Lambda$  des lichtinduzierten Gitters berechnet sich wie folgt: Aus den Wellenvektoren beider ebenen Wellen ergibt sich der Gittervektor:

$$\mathbf{K} = \mathbf{k}_{P1} - \mathbf{k}_{P2} \quad (2.34)$$

Für die Wellenlänge  $\lambda_P$  und die Neigung der beiden ebenen Wellen gegeneinander mit dem Winkel  $2\Theta_P$  ergibt sich die Gitterkonstante zu:

$$\Lambda = \frac{|\mathbf{K}|}{2\pi} = \frac{\lambda_P}{2 \sin(\Theta_P)} \quad (2.35)$$

Das holographische Gitter lässt sich mit einer weiteren ebenen Welle (T) auslesen, dazu muss diese die Braggbedingung des Gitters erfüllen:

$$n\lambda_T = 2 \Lambda \sin(\Theta_T) \quad (2.36)$$

Gemäß *Kogelnik* [47] verschwinden für dicke Gitter alle Beugungsordnungen außer der 0. und der  $\pm 1$ . Beugungsordnung. Es ergibt sich die Bedingung für den Winkel der Beugung von 1. Ordnung:

$$\Theta_T = \arcsin\left(\frac{\lambda_T}{\lambda_P} \sin(\Theta_P)\right) \quad (2.37)$$

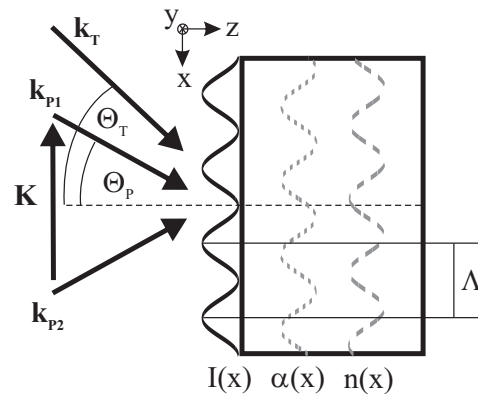


**Abbildung 2.3:** Gezeigt ist die Erzeugung eines holographischen Gitters über Brechungsindex- sowie Absorptionsmodulation durch die Überlagerung zweier ebener Wellen (P1 und P2). Ausgelesen werden kann das Hologramm mit einem Taststrahl (T).

Die Effizienz der Beugungsgitter wird über den Beugungswirkungsgrad beschrieben, der als Quotient der abgebeugten und der eingestrahnten Intensität definiert ist:

$$\eta = \frac{I(d)}{I(0)} \quad (2.38)$$

Gemäß *Kogelnik* [47] ergibt sich der Beugungswirkungsgrad zu

$$\eta = \exp\left(\frac{-2\alpha d}{\cos\Theta_T}\right) \cdot \left[ \sin^2\left(\frac{\pi\Delta n d}{\lambda\cos\Theta_T}\right) + \sinh^2\left(\frac{\Delta\alpha d}{2\cos\Theta_T}\right) \right] \quad (2.39)$$

Dabei wird die Absorption durch den Exponential-Term beschrieben, der  $\sin^2$ -Term stellt die durch Phasengitter verursachte Beugung, der  $\sinh^2$ -Term die durch Absorptionsgitter verursachte Beugung dar. Der Beugungswirkungsgrad für reine Absorptionsgitter ist dabei auf 3,7% beschränkt, reine Phasengitter können bis zu 100% erreichen.



# Kapitel 3

## Optische Nichtlinearitäten in photonischen Materialien

Für das Verständnis der Licht-Materie-Wechselwirkung sind die optischen Parameter von Materialien entscheidend. Von großer Bedeutung sind insbesondere nichtlineare Parameter, die die Stärke der Effekte von der elektrischen Feldstärke, der Intensität oder der Polarisation abhängig machen. Im Folgenden wird dabei auf intensitätsabhängige Effekte eingegangen. Untersucht werden hierbei die Materialien Lithiumniobat und Di-Zinn-Hexathiohypodiphosphat. Lithiumniobat ist aufgrund seiner vielfältigen Eigenschaften [19] von großer Bedeutung für die Photonik, Di-Zinn-Hexathiohypodiphosphat ebenfalls, da es Anwendungen bei der Telekommunikationswellenlänge bei 1550 nm erlaubt [48].

### 3.1 Optische Nichtlinearitäten in Lithiumniobat

In der ersten Veröffentlichung wird der Koeffizient der Zwei-Photonen-Absorption in Lithiumniobat bestimmt und der Einfluss kleiner Polaronen auf die nichtlineare Absorption für verschiedene Pulsdauern mithilfe eines Modells diskutiert. Die zweite Veröffentlichung fasst die bereits bekannten optischen Nichtlinearitäten von kleinen Polaronen in Lithiumniobat zusammen. In Abschnitt 3.1.2 wird auf den nichtlinearen Brechungsindex in Lithiumniobat eingegangen und im Rahmen der Suszeptibilität dritter Ordnung sowie freien Ladungsträgern und Polaronen diskutiert.

#### 3.1.1 Publikationen

Der Autor hat zu den im Folgenden aufgeführten Artikeln im Bereich optischer Nichtlinearitäten in Lithiumniobat beigetragen. Die Zusammenfassungen werden hier mit freundlicher Genehmigung der *The Optical Society (OSA)* und des *American Institute of Physics* angegeben, die vollständigen Publikationen finden sich im Anhang unter A.1 und A.2.

- H. Badorreck, S. Nolte, F. Freytag, P. Bäune, V. Dieckmann, M. Imlau.  
*Scanning nonlinear absorption in lithium niobate over the time regime of small polaron formation*  
Opt. Mater. Exp. **5**, 2729–2741, (2015). doi: 10.1364/OME.5.002729.

**Abstract:** Nonlinear absorption is studied in presence of small polaron formation in lithium niobate using the  $z$ -scan technique and ultrashort laser pulses with pulse durations of 70 – 1.000 fs. A model for the analysis of the transmission loss as a function of pulse duration is introduced that considers (i) the individual contributions of two-photon and small polaron absorption, (ii) the small polaron formation time and (iii) an offset time between the optical excitation of free carriers by two-photon absorption and the appearance of small polarons. It is shown that the model allows for the analysis of the experimentally determined  $z$ -scan data with high precision over the entire range of pulse durations using a two-photon absorption coefficient of  $\beta = (5.6 \pm 0.8) \text{ mm/GW}$ . A significant contribution by small polaron absorption to the nonlinear absorption is uncovered for pulse durations exceeding the characteristic small polaron formation time of  $\approx 100$  fs. It can be concluded that the small polaron formation time is as short as (70 – 110) fs and the appearance of small polaron formation is delayed with respect to two-photon absorption by an offset of about 80 fs.

- M. Imlau, H. Badorreck, C. Merschjann.

*Optical nonlinearities of small polarons in lithium niobate*

Reprinted with permission from Appl. Phys. Rev. **2**, 040606, (2015).

doi: 10.1063/1.4931396. Copyright 2015, AIP Publishing LLC.

**Abstract:** An overview of optical nonlinearities of small bound polarons is given, which can occur in the congruently melting composition of  $\text{LiNbO}_3$ . Such polarons decisively influence the linear and nonlinear optical performance of this material, that is important for the field of optics and photonics. On the basis of an elementary phenomenological approach, the localization of carriers in a periodic lattice with intrinsic defects is introduced. It is applied to describe the binding energies of four electron and hole small polarons in  $\text{LiNbO}_3$ : small free  $\text{Nb}_{\text{Nb}}^{4+}$  polarons, small bound  $\text{Nb}_{\text{Li}}^{4+}$  polarons, small bound  $\text{Nb}_{\text{Li}}^{4+}:\text{Nb}_{\text{Nb}}^{4+}$  bipolarons, and small bound  $\text{O}^-$  hole polarons. For the understanding of their linear interaction with light, an optically induced transfer between nearest-neighboring polaronic sites is assumed. It reveals spectrally well separated optical absorption features in the visible and near-infrared spectral range, their small polaron peak energies and lineshapes. Nonlinear interaction of light is assigned to the optical formation of short-lived small polarons as a result of carrier excitation by means of band-to-band transitions. It is accompanied by the appearance of a transient absorption being spectrally constituted by the individual fingerprints of the small polarons involved. The relaxation dynamics of the transients is thermally activated and characterized phenomenologically by a stretched exponential behavior, according to incoherent 3D small polaron hopping between regular and defect sites of the crystal lattice. It is shown that the analysis of the dynamics is a useful tool for revealing the recombination processes between small polarons of different charge. Nonlinear interaction of small polarons with light furthermore results in changes of the index of refraction. Besides its causal relation to the transients via Kramers-Kronig relation, pronounced index changes may occur due to optically generated electric fields modulating the index of refraction

via the linear electro-optic effect, also. Based on a microscopic picture and by considering the local structural environment of bound polarons, the appearance of photovoltaic currents is explained straightforwardly as a result of the optically induced carrier transfer. Both transient absorption and index changes are spatially confined to the intensity profile of the interacting light allowing for the recording of efficient mixed absorption and phase volume holograms. By means of holographic spectroscopy, these small-polaron based optical nonlinearities are verified either without or with the action of the linear electro-optic effect; their prominent features are highlighted by appropriate experimental studies wherein the ultrafast response on the picosecond time scale is the most recognized one. Based on these findings, the consequences for applications of  $\text{LiNbO}_3$  in the field of nonlinear optics & photonics are presented. Besides visionary examples like real-time, 3D holographic displays, the impact of optical nonlinearities of small polarons for present applications are discussed with frequency conversion and respective limiting effects, such as green-induced infrared absorption and optical damage, as important example.

#### 3.1.2 Nichtlinearer Brechungsindex in Lithiumniobat

In der oben genannten Veröffentlichung *Scanning nonlinear absorption in lithium niobate over the time regime of small polaron formation* konnte gezeigt werden, dass kleine Polaronen die Messung des Zwei-Photonen-Absorptionskoeffizienten in Lithiumniobat mit ultrakurzen Laserpulsen beeinflussen und nur für die kürzeste verwendete Pulsdauer von 70 fs die polaronische Absorption verschwindend gering ist. Inwieweit die Messung des nichtlinearen Brechungsindex ebenfalls durch polaronische Effekte oder freie Ladungsträger beeinflusst wird, wird im Folgenden dargestellt. Der Aufbau des pulslängenabhängigen Z-Scan-Experiments ist in der genannten Publikation beschrieben. Die im Folgenden präsentierten Messungen wurden bei einer Wellenlänge von 488 nm durchgeführt.

Für die Auswertung des nichtlinearen Brechungsindex ist entscheidend, den transmittierten Puls mit räumlicher Auflösung aufzuzeichnen. Eine Brechungsindexänderung in der Probe führt bei einem gaussförmigen Strahlprofil zu einer optisch induzierten Linse, die den Puls fokussiert oder defokussiert. Wie Sheik-Bahae et al. [46] gezeigt haben, lässt sich dies experimentell durch das Einbringen einer Apertur in den Strahlengang bewerkstelligen, sodass nur der mittige Teil des Pulses aufgezeichnet wird. In Abbildung 3 der oben genannten Publikation zeichnet dieses Signal die Diode D3 auf. Um ein von der nichtlinearen Absorption bereinigtes Signal zu erhalten, wird dieses Signal durch das der Diode D2 geteilt. Über die durch Sheik-Bahae et al. [46] dargestellte Näherung (2.29) kann der nichtlineare Brechungsindex  $\Delta n$  über die Differenz von maximaler und minimaler Transmission bestimmt werden.

#### Nichtlinearer Brechungsindex in Abhängigkeit der Pulsdauer

Die Abbildung 3.1 zeigt die Entwicklung der nichtlinearen Brechungsindexänderung  $\Delta n$  für verschiedene Pulslängen. Dabei ist zu beachten, dass die Energie der Pulse nahezu konstant ist, die Intensität folglich kontinuierlich mit größerer Pulslänge ab-

nimmt. Zu beobachten ist, dass bei der kürzesten verwendeten Pulslänge von 70 fs die Messung deutlich von der theoretischen Näherung (2.26) abweicht. Für größere Pulsdauern und kleinere Intensitäten nimmt die Übereinstimmung mit der theoretischen Beschreibung zu. Insgesamt lässt sich allerdings eine nahezu konstante nichtlineare Brechungsindexänderung feststellen, wie in Abbildung 3.2 gezeigt. Dabei stellt lediglich die Messung mit 70 fs eine Ausnahme mit einem knapp 50% höheren Wert dar.

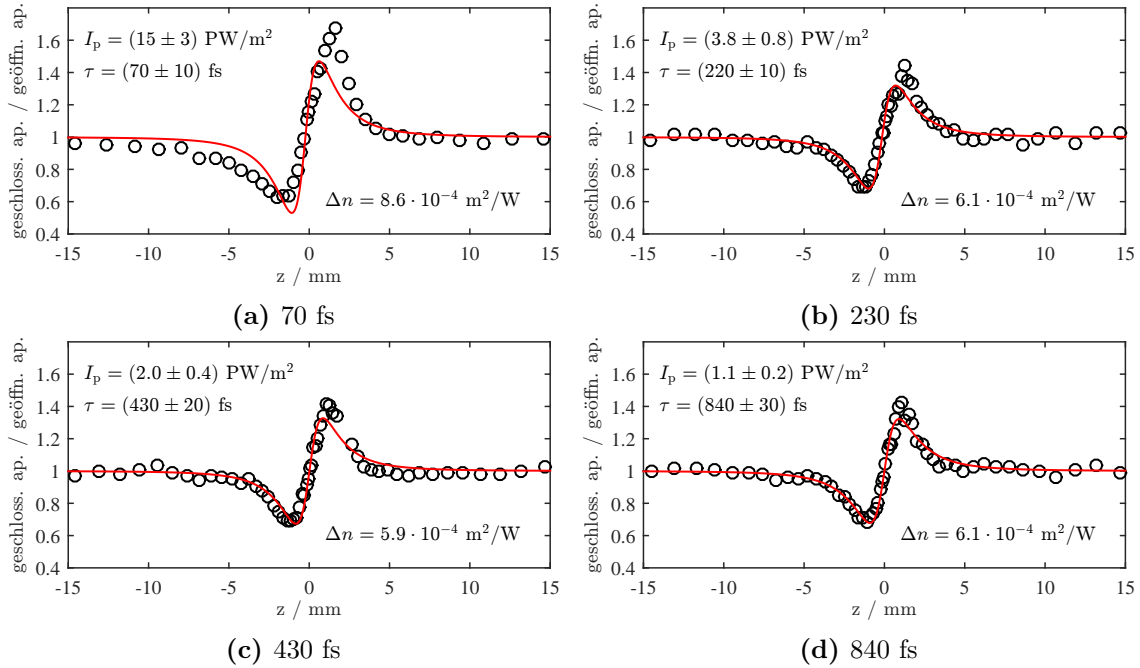


**Abbildung 3.1:** Nichtlineare Brechungsindexänderung  $\Delta n$  in Lithiumniobat für verschiedene Pulslängen bei konstanter Pulsenergie. (3.1(a)) zeigt für eine Pulslänge von 70 fs eine deutliche Abweichung zu (2.26) (durchgezogene Linie), die Übereinstimmung bei größeren Pulsdauern ist dagegen größer. Angegeben sind jeweils die Peakintensität  $I_p$ , Pulslänge  $\tau$  und die nichtlineare Brechungsindexänderung  $\Delta n$ . Der Fehler bei der Bestimmung von  $\Delta n$  liegt bei 20%.

### Nichtlinearer Brechungsindex in Abhängigkeit der Intensität

Die Abbildungen 3.3 und 3.4 zeigen die Abhängigkeit der nichtlinearen Brechungsindexänderung  $\Delta n$  für die zwei verschiedenen Pulslängen 70 fs und 330 fs. Eine große Übereinstimmung des durch die Apertur beschnittenen transmittierten Signals mit der Näherung (2.26) ist dabei für alle Messungen zu erkennen; nur die Messung mit höchster Intensität und kürzester Pulslänge (Abbildung 3.3(a)) stellt eine Ausnahme dar.

Die Abbildung 3.5 zeigt die nichtlineare Brechungsindexänderung  $\Delta n$  in Abhängigkeit der Intensität. Dabei nimmt  $\Delta n$  mit größerer Intensität zu, allerdings wird deutlich, dass zwischen diesen Größen für beide unterschiedliche Pulsdauern jeweils ein nichtlinearer Zusammenhang besteht. Die Entwicklung erfolgt sublinear, für große Intensitäten scheint die nichtlineare Brechungsindexänderung zu konvergieren.

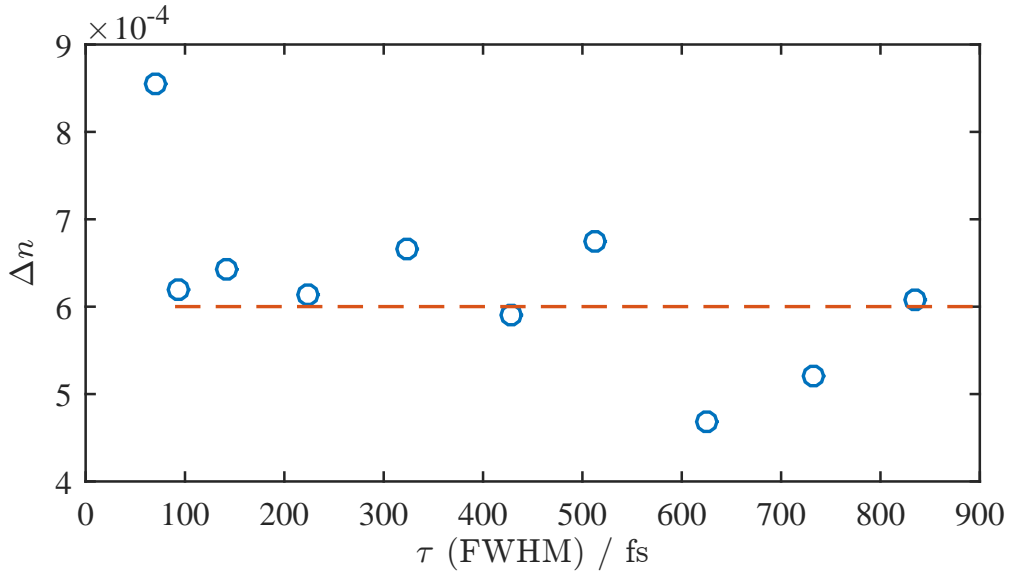


**Abbildung 3.2:** Nichtlineare Brechungsindexänderung  $\Delta n$  in Lithiumniobat in Abhängigkeit der Pulslänge und konstanter Pulsenergie. Angedeutet durch die gestrichelte Linie ist im Rahmen des Fehlers ein nahezu gleichbleibender Wert zu beobachten, nur der Wert für eine Pulslänge von 70 fs zeigt eine größere Abweichung.

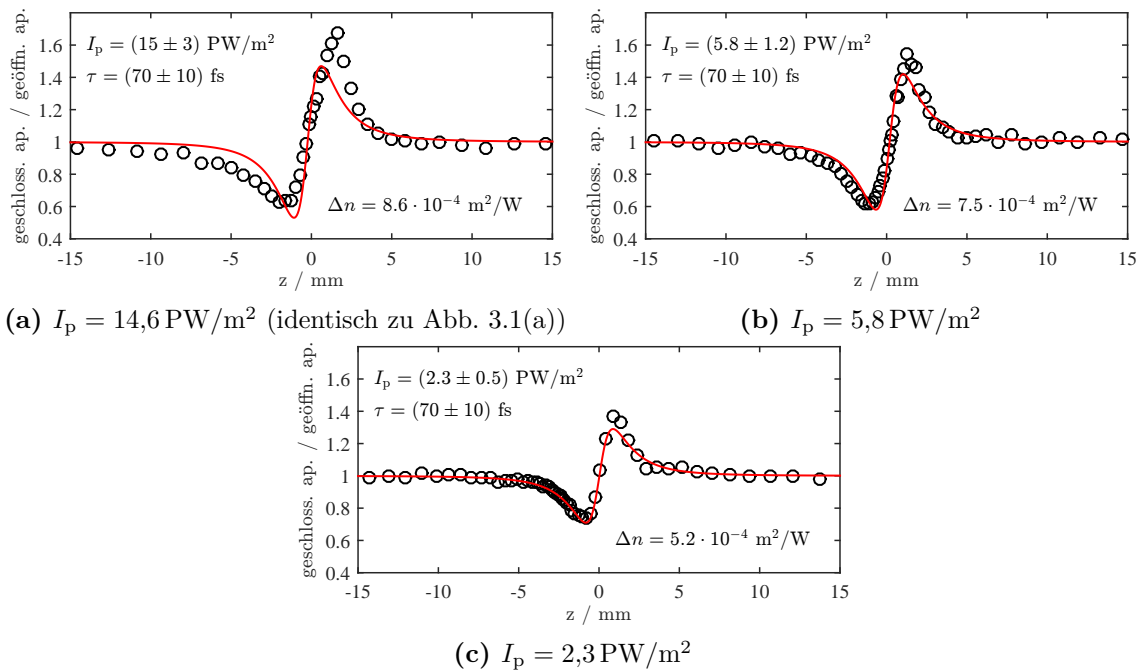


**Abbildung 3.3:** Nichtlineare Brechungsindexänderung  $\Delta n$  in Lithiumniobat für eine Pulslänge von 70 fs. Bei der höchsten Intensität ist eine deutliche Abweichung von der theoretischen Näherung (durchgezogene Linie) erkennbar. Die Übereinstimmung nimmt mit sinkender Intensität zu. Angegeben sind jeweils die Peakintensität  $I_p$ , Pulslänge  $\tau$  und die nichtlineare Brechungsindexänderung  $\Delta n$ . Der Fehler bei der Bestimmung von  $\Delta n$  liegt bei 20%.

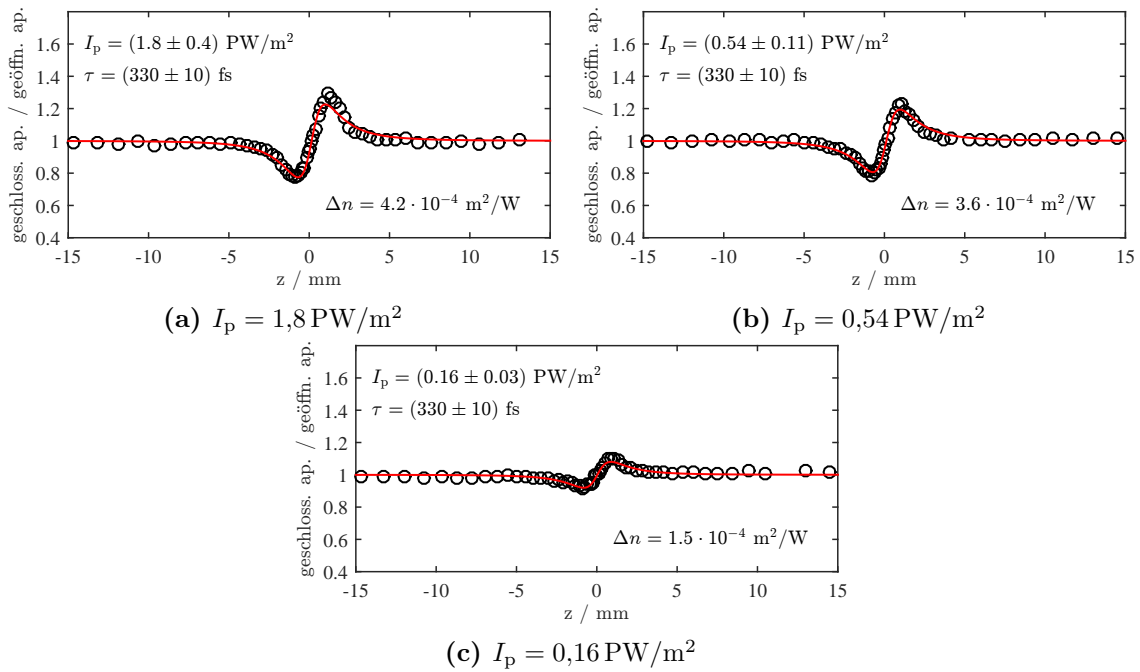


**Abbildung 3.4:** Nichtlineare Brechungsindexänderung  $\Delta n$  in Lithiumniobat für eine Pulslänge von  $330 \text{ fs}$ . Für alle Intensitäten ist eine gute Überstimmung mit (2.26) feststellbar. Angegeben sind jeweils die Peakintensität  $I_p$ , Pulslänge  $\tau$  und die nichtlineare Brechungsindexänderung  $\Delta n$ . Der Fehler bei der Bestimmung von  $\Delta n$  liegt bei 20%.

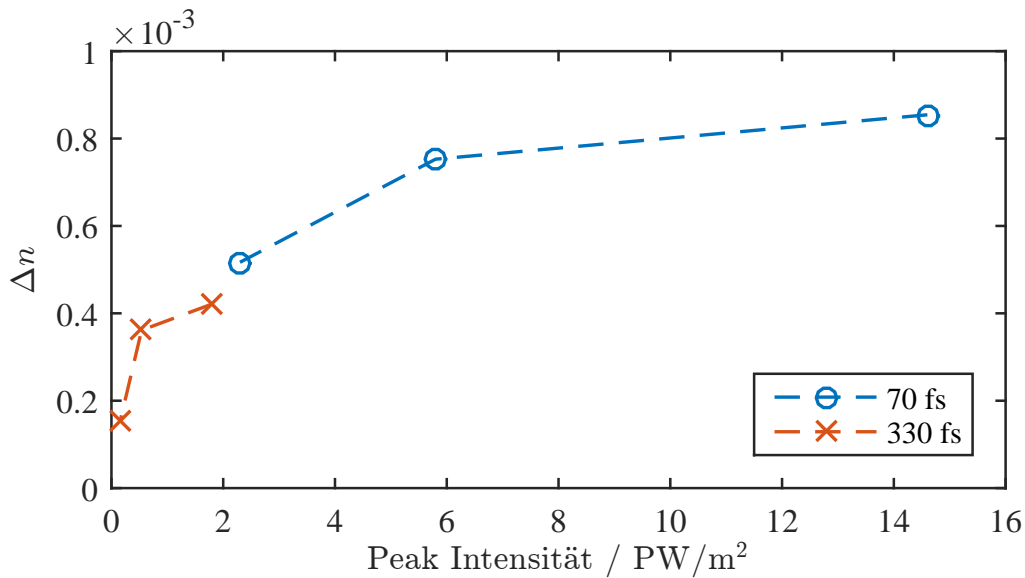


**Abbildung 3.5:** Abhängigkeit des nichtlinearen Brechungsindex in Abhängigkeit der Intensität für zwei verschiedene Pulslängen. Die gestrichelten Linien zeigen den nichtlinearen Zusammenhang zwischen  $\Delta n$  und Peakintensität  $I_p$ .

#### Diskussion

Die oben präsentierten Messdaten zeigen, dass für die Erklärung der nichtlinearen Brechungsindexänderung in Lithiumniobat für Femtosekundenpulse nicht allein die Suszeptibilität dritter Ordnung ausreicht. Es müssen noch weitere Effekte berücksichtigt werden. Bei den Messungen der nichtlinearen Absorption konnte bereits gezeigt werden, dass sowohl Zwei-Photonen-Absorption als auch polaronische Absorption Einfluss ausüben, die polaronische Absorption bei kürzeren Pulsen allerdings abnimmt und bei der kürzesten verwendeten Pulslänge von 70 fs nicht mehr messbar ist. Ein direkter Einfluss freier Ladungsträger auf die Absorption, die nach optischer Anregung zunächst entstehen und dann gegebenenfalls zu polaronischen Zuständen relaxieren, konnte nicht festgestellt werden.

Für den nichtlinearen Brechungsindex stellt sich dies folgendermaßen dar. Ein ausschließlicher Effekt der Suszeptibilität dritter Ordnung ließe aufgrund des Zusammenhangs (2.19) einen linearen Anstieg für  $\Delta n$  in Abhängigkeit der Intensität vermuten. Dies ist weder für die Pulslänge von 70 fs noch für 330 fs gegeben. Somit kann ein Messartefakt ausgeschlossen werden, welches durch die in Abbildung 3.3(a) dargestellte schlechte Übereinstimmung der Messung mit der theoretischen Beschreibung (2.26) entsteht. Zudem ist der nahezu konstante Wert der nichtlinearen Brechungsindexänderung in Abhängigkeit der Pulslänge auffällig, da durch die konstante Pulsenergie die Pulsintensität ebenfalls variiert wird.

Der bisher einzige in der Literatur existierende Wert für den nichtlinearen Brechungsindex dritter Ordnung  $n_2$  in Lithiumniobat liegt bei  $(8,3 \pm 1,4) \cdot 10^{-19} \text{ m}^2/\text{W}$  für die Wellenlänge 532 nm [49]. Mit diesem Wert stimmt am besten der ableitbare Wert für  $n_2$  für die in Abbildung 3.4(c) gezeigte Messung von etwa  $8,2 \cdot 10^{-19} \text{ m}^2/\text{W}$  (bei einer Wellenlänge von 488 nm) überein. Angesichts des festgestellten nichtlinearen Zusammenhangs zwischen Brechungsindexänderung  $\Delta n$  und Peakintensität  $I_p$  ist die alleinige Zuordnung zum nichtlinearen Brechungsindex dritter Ordnung  $n_2$  allerdings unzureichend. Vielmehr ist davon auszugehen, dass hier eine Überlagerung der Effekte durch  $n_2$  und Brechungsindexänderungen durch freie Ladungsträger und kleine Polaronen vorliegt. Wie Bennett et al. [50] zeigen, können freie Ladungsträger zu einer Brechungsindexänderung aufgrund von Bandfüllung (Burstein-Moss-Effekt) führen. Diese Änderung des Brechungsindex skaliert bei durch Zwei-Photonen-Absorption erzeugten Ladungsträgern mit dem Quadrat der Intensität [51]. Die Absorption kleiner Polaronen führt über die Kramers-Kronig-Relation ebenfalls zu einer Brechungsindexänderung [52]. Somit stellt hier eine Überlagerung aus positivem  $\Delta n$  proportional zur Intensität durch  $n_2$  und negativem  $\Delta n$  proportional zum Quadrat der Intensität durch freie Ladungsträger und kleine Polaronen eine mögliche Erklärung der Messdaten dar.

## 3.2 Optische Nichtlinearitäten in Di-Zinn-Hexathiohypodiphosphat

Di-Zinn-Hexathiohypodiphosphat ( $\text{Sn}_2\text{P}_2\text{S}_6$ ) ist ein vielversprechendes Material für die Photonik im spektralen Bereich der Telekommunikationswellenlänge von 1550 nm. In der ersten Veröffentlichung wird gezeigt, dass das Material im roten und nahinfraroten Spektralbereich einen hohen Zwei-Photonen-Absorptions-Koeffizienten aufweist, zudem konnte eine lichtinduzierte transiente Absorption festgestellt werden, die auf die Entstehung von Polaronen hinweist. Die weitere Veröffentlichung beschäftigt sich mit der Frage, inwieweit Gitter in  $\text{Sn}_2\text{P}_2\text{S}_6$  über die Zwei-Photonen-Absorption aufgezeichnet werden können, und welchen Anteil daran Absorptions- und Brechungsindexgitter haben.

Der Autor hat zu den im Folgenden aufgeführten Artikeln im Bereich optischer Nichtlinearitäten in Di-Zinn-Hexathiohypodiphosphat beigetragen. Die Zusammenfassungen werden mit freundlicher Genehmigung der *The Optical Society (OSA)* hier angegeben, die vollständigen Publikationen finden sich im Anhang unter A.3 und A.4.

- M. Imlau, V. Dieckmann, H. Badorreck, A. Shumelyuk.

*Tin hypthiodiphosphate: nonlinear response in the sub-100fs time domain*

Opt. Mater. Exp. **1**, 953–961, (2011). doi: 10.1364/OME.1.000953.

**Abstract:** The interaction of sub-100 fs light pulses ( $\tau_p \lesssim 75$  fs) with single crystals of nominally undoped tin hypthiodiphosphate,  $\text{Sn}_2\text{P}_2\text{S}_6$ , is studied in the near-infrared spectral range (590 – 1630 nm). A predominant contribution of the two-photon absorption (TPA) is verified in the measurements of the sample transmission as a function of pulse intensity and of the time delay between pump and probe pulses. Scans over the photon energy show that the two-photon absorption coefficient  $\beta$  increases in a superlinear way for photon energies  $\hbar\omega$  exceeding  $E_g/2$ ; for any quantum energy it is nearly independent of propagation direction and polarization of the incident beam. Such a behavior is qualitatively similar to that predicted by perturbation theory within models with allowed-forbidden transitions. The TPA coefficient saturates at a maximum value of  $\beta \approx 8 \text{ cm GW}^{-1}$  at  $\hbar\omega = 1.80 \text{ eV}$ . It drops when reaching the bandgap  $E_g$ . Using pump-probe measurements at 626 nm, a transient absorption is verified that persists for probe pulse delays much longer than the pump pulse duration, up to 2.5 ns. We discuss our results in the framework of the microscopic structure of  $\text{Sn}_2\text{P}_2\text{S}_6$  with emphasis on the optical generation of  $\text{S}^-$  small hole polarons.

- A. Shumelyuk, M. Imlau, V. Dieckmann, H. Badorreck, A. Grabar, S. Odoulov.

*Self-diffraction from two-photon absorption gratings in  $\text{Sn}_2\text{P}_2\text{S}_6$*

Opt. Lett. **37**, 4065–4067, (2012). doi: 10.1364/OL.37.004065.

**Abstract:** Self-diffraction with the appearance of higher diffraction orders is discovered when writing a grating with a single sub-100 fs pulse in a nominally

undoped  $\text{Sn}_2\text{P}_2\text{S}_6$  sample. The short time of grating development, dependence of diffraction efficiency on the recording light intensity, correlation of wavelength dependence of efficiency with the spectrum of the two-photon absorption (TPA) constant, and a  $\pi$  phase shift of the diffracted beam allow for attributing the recorded grating to a dynamic amplitude grating of TPA.



# Kapitel 4

## Interferenz verschiedenfarbiger ultrakurzer Lichtpulse

Die Interferenz zwischen zwei Laserstrahlen oder -pulsen setzt eine Kohärenz zwischen diesen voraus [53]. Diese ist gegeben wenn eine feste räumliche oder zeitliche Phasenbeziehung zwischen den beiden Wellenzügen herrscht. Die Interferenz von Licht mit unterschiedlicher Frequenz ist daher schwierig zu beobachten, da durch die kontinuierliche Änderung der Phasenbeziehung ein bewegtes Interferenzmuster entsteht, welches sich mit nahezu Lichtgeschwindigkeit bewegt. Durch die Verwendung von ultrakurzen Laserpulsen lässt sich ein eingefrorenes Muster beobachten, welches durch die Kürze der Pulse kaum verschmiert. Dies ermöglicht die Aufzeichnung von statischen und dynamischen holographischen Gittern. Die Selbstbeugung der Pulse an einem dynamischen Gitter führt dabei zu Frequenzverschiebungen durch den Doppler-Effekt.

### 4.1 Publikationen

Der Autor hat zu dem im Folgenden aufgeführten Artikel im Bereich Interferenz verschiedenfarbiger ultrakurzer Lichtpulse beigetragen. Die Zusammenfassung wird hier mit freundlicher Genehmigung der *Nature Publishing Group* angegeben, die vollständige Publikation findet sich im Anhang unter A.5.

- S. Odoulov, A. Shumelyuk, H. Badorreck, S. Nolte, K.-M. Voit, M. Imlau.  
*Interference and holography with femtosecond laser pulses of different colours*  
Nat. Comm. **6**, 5866, (2015). doi: 10.1038/ncomms6866.

**Abstract:** Interferometry and holography are two domains that are based on observation and recording of interference fringes from two light beams. While the aim of the first technique is to reveal and map the phase difference of two wave fronts, the main task of the second technique is to reconstruct one of the two recording waves via diffraction of the other wave from the recorded fringe pattern (hologram). To create fringes, mutually coherent waves from the same laser are commonly used. It is shown here that fringes can be observed and holograms can be recorded with ultrashort, sub-picosecond pulses even of different colour, generated in our experiment with two parametric amplifiers seeded, both by the same mode-locked Ti-sapphire laser. The appearance of permanent and transient gratings is confirmed by recording of an image-bearing hologram,

by observation of two-beam coupling gain in a pump-probe experiment and by frequency conversion in Raman-Nath self-diffraction from a moving grating.

- H. Badorreck, A. Shumelyuk, S. Nolte, M. Imlau, and S. Odoulov.

*Doppler-shifted Raman-Nath diffraction from gratings recorded in LiNbO<sub>3</sub> with ultra-short laser pulses of different color*

Opt. Mater. Exp. **6**, 517–522, (2016). doi: 10.1364/OME.6.000517.

**Abstract:** Nominally undoped LiNbO<sub>3</sub> crystals feature a pronounced mixed (absorption/refraction) nonlinear response in the blue-green spectrum domain that is sufficient for the excitation of moving dynamic gratings and the observation of selfdiffraction with Doppler shifted higher orders. This type of Raman-Nath selfdiffraction can be successfully used for up- and down- frequency conversion as well as for characterization of the recording pulses.

# Kapitel 5

## Zusammenfassung

In der vorliegenden Arbeit werden die nichtlinearen optischen Eigenschaften der Materialien Lithiumniobat und Di-Zinn-Hexathiohypodiphosphat aufgrund der Suszeptibilität 3. Ordnung und kleiner Polaronen untersucht. Zudem wird gezeigt, dass die Interferenz verschiedenfarbiger Laserpulse die Aufzeichnung von statischen und dynamischen holographischen Gittern ermöglicht. Ein Teil dieser Arbeit ist in den im Anhang angegebenen 5 Publikationen bereits veröffentlicht.

Lithiumniobat wird mit einer Erweiterung des Z-Scan Experiments untersucht, welches die Pulslängenabhängige Messung der nichtlinearen Absorption und der nichtlinearen Brechungsindexänderung ermöglicht. Dabei konnte festgestellt werden, dass bei sehr kurzen Pulslängen von 70 fs ein Effekt der Polaronen auf die nichtlineare Absorption vernachlässigbar ist und die Zwei-Photonen-Absorption die nichtlineare Absorption dominiert. Mit größerer Pulslänge gibt es allerdings Abweichungen zwischen der Theorie der Zwei-Photonen-Absorption und den Messergebnissen. Mit der Entwicklung eines Polaronen-Anregungs-Modells, welches eine polaronische Absorption aufgrund wiederholtem optisch induziertem Hopping annimmt, konnte dieser Effekt konsistent erklärt werden. Die Messungen der nichtlinearen Brechungsindexänderung lassen darauf schließen, dass sowohl freie Ladungsträger als auch kleine Polaronen neben der Suszeptibilität 3. Ordnung einen Einfluss auf die Brechungsindexänderung haben, da eine nichtlineare Abhängigkeit von der Intensität auch bei Pulslängen von 70 fs festgestellt werden konnte.

Analog dazu konnte in Di-Zinn-Hexathiohypodiphosphat ein großer Zwei-Photonen-Absorptionskoeffizient festgestellt werden, welcher für Photonenenergien nahe der Bandkante Werte zeigt, die größer sind als theoretischen Überlegungen zeigen. Eine transiente Absorption nach optischer Anregung, gemessen durch ein Anreg-Abtast-Experiment, sowie Literatur legen nahe, dass in  $\text{Sn}_2\text{P}_2\text{S}_6$  gebundene Lochpolaronen durch optische Anregung entstehen können. Durch den hohen Zwei-Photonen-Absorptionskoeffizienten konnte das Aufzeichnen eines kontrastreichen, dynamischen Amplitudengitters mittels Femtosekundenpulsen gezeigt und nachgewiesen werden.

Die Kürze der Femtosekundenpulse ermöglicht aber nicht nur das Aufzeichnen eines Zwei-Photonen-Absorptionsgitters aufgrund der hohen Intensitäten, sondern erlaubt zudem die Beobachtung von Interferenz zwischen verschiedenfarbigen Pulsen. In der Zeitspanne der Pulslänge beträgt die Bewegung der Interferenzstreifen, welche in der Größenordnung der Lichtgeschwindigkeit liegt, nur ein Bruchteil der Streifenabstand, sodass das Interferenzmuster eingefroren und beobachtbar erscheint. Somit lassen sich statische Hologramme in holographischen Filmen, wie auch dynamische

Hologramme aufzeichnen. Über ein dynamisches holographisches Gitter mittels Zwei-Photonen-Absorption konnte so eine Frequenzkonversion durch Dopplerverschiebung in Lithiumniobat gezeigt werden.

# Literaturverzeichnis

- [1] J. C. Maxwell. *A Dynamical Theory of the Electromagnetic Field*. Philosophical Transactions of the Royal Society of London **155**, pp. 459–512 (1865).
- [2] A. Einstein. *Über einen die Erzeugung und Verwandlung des Lichtes betreffenden heuristischen Gesichtspunkt*. Ann. Phys. **4**, 132–148 (1905).
- [3] A. Einstein. *Zur Quantentheorie der Strahlung*. Phys. Z. **18**, 121–128 (1917).
- [4] T. H. Maiman. *Stimulated Optical Radiation in Ruby*. Nature **187**, 493–494 (1960).
- [5] P. A. Franken, A. E. Hill, C. W. Peters, G. Weinreich. *Generation of Optical Harmonics*. Phys. Rev. Lett. **7**, 118–119 (1961).
- [6] M. Göppert-Mayer. *Über Elementarakte mit zwei Quantensprüngen*. Ann. Phys. **9**, 273 (1931).
- [7] W. Kaiser, C. G. B. Garrett. *Two-Photon Excitation in  $\text{CaF}_2:\text{Eu}^{2+}$* . Phys. Rev. Lett. **7**, 229 (1961).
- [8] D. Gabor. *A new microscopic principle*. Nature **161**, 777–778 (1948).
- [9] E. N. Leith, J. Upatnieks. *Reconstructed Wavefronts and Communication Theory*. J. Opt. Soc. Am. **52**, 1123–1130 (1962).
- [10] Y. N. Denisjuk. *Manifestation of optical properties of an object in wave field of radiation in scatters*. Doklady Akademii NAUK SSSR **144**, 1275 (1962).
- [11] A. J. DeMaria, W. H. Glenn Jr., M. J. Brienza, M. E. Mack. *Picosecond laser pulses*. Proc. IEEE **57**, 2–25 (1969).
- [12] R. L. Fork, B. I. Greene, C. V. Shank. *Generation of optical pulses shorter than 0.1 psec by colliding pulse mode locking*. Appl. Phys. Lett. **38**, 671–672 (1981).
- [13] M. Hentschel, R. Kienberger, Ch. Spielmann, G. A. Reider, N. Milosevic, T. Brabec, P. Corkum, U. Heinzmann, M. Drescher, F. Krausz. *Attosecond metrology*. Nature **414**, 509–513 (2001).
- [14] A. H. Zewail. *Laser Femtochemistry*. Science **242**, 1645–1653 (1988).
- [15] H. J. Caulfield, S. Dolev. *Why future supercomputing requires optics*. Nature Photon. **4**, 261–263 (2010).
- [16] S. Tay, P.-A. Blanche, R. Voorakaranam, A. V. Tunç, W. Lin, S. Rokutanda, T. Gu, D. Flores, P. Wang, G. Li, P. St Hilaire, J. Thomas, R. A. Norwood, M. Yamamoto, N. Peyghambarian. *An updatable holographic three-dimensional display*. Nature **451**, 694–698 (2008).
- [17] P.-A. Blanche, A. Bablumian, R. Voorakaranam, C. Christenson, W. Lin, T. Gu, D. Flores, P. Wang, W.-Y. Hsieh, M. Kathaperumal, B. Rachwal, O. Siddiqui, J. Thomas, R. A. Norwood, M. Yamamoto, N. Peyghambarian. *Holographic three-dimensional telepresence using large-area photorefractive polymer*. Nature **468**, 80–83 (2010).

- [18] R. S. Weis, T. K. Gaylord. *Lithium niobate: Summary of physical properties and crystal structure*. Appl. Phys. A **37**, 191 (1985).
- [19] L. Arizmendi. *Photonic applications of lithium niobate crystals*. Phys. Stat. Sol. A **201**, 253 (2004).
- [20] M. M. Fejer, G. A. Magel, D. H. Jundt, R. L. Byer. *Quasi-phase-matched second harmonic generation: tuning and tolerances*. IEEE J. Quantum Electron. **28**, 2631–2654 (1992).
- [21] F. S. Chen, J. T. LaMacchia, D. B. Fraser. *Holographic Storage in lithium niobate*. Appl. Phys. Lett. **13**, 223–225 (1968).
- [22] K. Buse, A. Adibi, D. Psaltis. *Non-volatile holographic storage in doubly doped lithium niobate crystals*. Nature **393**, 665–668 (1998).
- [23] D. Emin. *Polarons*. Cambridge University Press Cambridge, (2013).
- [24] O F Schirmer.  *$O^-$  bound small polarons in oxide materials*. J. Phys. Condens. Matter **18**, R667 (2006).
- [25] O. F. Schirmer, M. Imlau, C. Merschjann, B. Schoke. *Electron small polarons and bipolarons in  $LiNbO_3$* . J. Phys. Condens. Matter **21**, 123201 (2009).
- [26] Y. Qiu, K. B. Ucer, R. T. Williams. *Formation time of a small electron polaron in  $LiNbO_3$ : measurements and interpretation*. Phys. Stat. Sol. C **2**, 232 (2005).
- [27] S. Sasamoto, J. Hirohashi, S. Ashihara. *Polaron dynamics in lithium niobate upon femtosecond pulse irradiation: Influence of magnesium doping and stoichiometry control*. J. Appl. Phys. **105**, 083102 (2009).
- [28] O. Beyer, D. Maxein, K. Buse, B. Sturman, H. T. Hsieh, D. Psaltis. *Femtosecond time-resolved absorption processes in lithium niobate crystals*. Opt. Lett. **30**, 1366 (2005).
- [29] C. Merschjann. *Optically generated small polarons: Time-resolved pump-multiprobe experiments in lithium niobate vs. random-walk charge-transport simulations in oxide crystals*. University of Osnabrück, 2007.
- [30] B. Schoke. *Optisch erzeugte kleine Polaronen in Lithiumniobat: Einfluss homogener und räumlich periodisch modulierter Konzentrationen von intrinsischen und extrinsischen Defekten auf die transiente polaronische Absorption*. Universität Osnabrück, 2010.
- [31] H. Brüning, V. Dieckmann, B. Schoke, K.-M. Voit, M. Imlau, G. Corradi, C. Merschjann. *Small-polaron based holograms in  $LiNbO_3$  in the visible spectrum*. Opt. Express **20**, 13326–13336 (2012).
- [32] V. Storchak, J. H. Brewer, G. D. Morris. *Quantum transport of electronic polarons in sapphire*. Phys. Rev. B **56**, 55–58 (1997).
- [33] S. Torbrügge, M. Imlau, B. Schoke, C. Merschjann, O. F. Schirmer, S. Vernay, A. Gross, V. Wesemann, D. Rytz. *Optically generated small electron and hole polarons in nominally undoped and Fe-doped  $KNbO_3$  investigated by transient absorption spectroscopy*. Phys. Rev. B **78**, 125112 (2008).
- [34] A. Ruediger, O. Schirmer, S. Odoulov, A. Shumelyuk, A. Grabar. *Studies of light-induced charge transfer in  $Sn_2P_2S_6$  by combined EPR/optical absorption spectroscopy*. Opt. Mater. **18**, 123 (2001).

- [35] O. F. Schirmer, M. Imlau, C. Merschjann. *Bulk photovoltaic effect of  $\text{LiNbO}_3\text{:Fe}$  and its small-polaron-based microscopic interpretation*. Phys. Rev. B **83**, 165106 (2011).
- [36] G. Magyar, L. Mandel. *Interference Fringes Produced by Superposition of Two Independent Maser Light Beams*. Nature **198**, 255–256 (1963).
- [37] P. A. M. Dirac. *Quantum Mechanics*. Oxford University Press, London, 4th ed (1958).
- [38] H. Badorreck. *Aufbau und Charakterisierung eines fs-Spektroskopie-Experiments im UV/VIS/NIR*. Masterarbeit, Universität Osnabrück, (2011).
- [39] J.-C. Diels, W. Rudolph. *Ultrashort Laser Pulse Phenomena*. Academic Press (Elsevier) (2006).
- [40] P. F. Moulton. *Spectroscopic and laser characteristics of  $\text{Ti:Al}_2\text{O}_3$* . J. Opt. Soc. Am. B **3**, 125 (1986).
- [41] Coherent. *Operator's Manual: Libra Ultrafast Amplifier Laser System*.
- [42] H. Sun. *Thin lens equation for a real laser beam with weak lens aperture truncation*. Opt. Eng. **37**, 2906 (1998).
- [43] R. Battesti, C. Rizzo. *Magnetic and electric properties of a quantum vacuum*. Reports on Progress in Physics **76**, 016401 (2013).
- [44] P.W. Milonni, J.H. Eberly. *Laser Physics*. John Wiley & Sons, Inc. (2010).
- [45] B. E. A. Saleh, M. C. Teich. *Grundlagen der Photonik*. Wiley-VCH (2007).
- [46] M. Sheik-Bahae, A. A. Said, T. H. Wei, D. J. Hagan, E. W. Van Stryland. *Sensitive Measurement of Optical Nonlinearities Using A Single Beam*. IEEE J. Quantum Electron. **26**, 760 (1990). 100
- [47] H. Kogelnik. *Coupled wave theory for thick hologram gratings*. Bell Syst. Tech. J. **48**, 2909 (1969).
- [48] R. Mosimann, P. Marty, T. Bach, F. Juvalta, M. Jazbinsek, P. Günter, A. A. Grabar. *High-speed photorefraction at telecommunication wavelength  $1.55 \mu\text{m}$  in  $\text{Sn}_2\text{P}_2\text{S}_6\text{:Te}$* . Opt. Lett. **32**, 3230 (2007).
- [49] R. DeSalvo, A.A. Said, D.J. Hagan, E.W. Van Stryland, M. Sheik-Bahae. *Infrared to ultraviolet measurements of two-photon absorption and  $n_2$  in wide bandgap solids*. IEEE J. Quantum Electron. **32**, 1324 (1996).
- [50] B.R. Bennett, Richard A. Soref, J.A. del Alamo. *Carrier-induced change in refractive index of  $\text{InP}$ ,  $\text{GaAs}$  and  $\text{InGaAsP}$* . IEEE Journal of Quantum Electronics **26**, 113–122 (1990).
- [51] A.A. Bugayev. *Non-linear refractive index of silicon and  $\text{GaAs}$  induced by free-carrier generation*. Optical and Quantum Electronics **22**, 485–489 (1990).
- [52] M. Imlau, H. Brüning, B. Schoke, R.-S. Hardt, D. Conradi, C. Merschjann. *Hologram recording via spatial density modulation of  $\text{NbLi}_{4+}/5+$  antisites in lithium niobate*. Opt. Express **19**, 15322 (2011).
- [53] R. J. Glauber. *The Quantum Theory of Optical Coherence*. Phys. Rev. **130**, 2529–2539 (1963).



# Anhang A

## Publikationen

Im Folgenden sind die Veröffentlichungen aufgeführt, die auf den Websites der Journals unter der jeweiligen angegebenen URL zu finden sind (soweit angegeben).



# Scanning nonlinear absorption in lithium niobate over the time regime of small polaron formation

Holger Badorreck, Stefan Nolte, Felix Freytag, Pia Bäune, Volker Dieckmann, and Mirco Imlau\*

*School of Physics, Osnabrueck University,  
Barbarastr. 7, 49076 Osnabrueck, Germany*

*\*Corresponding author: mimlau@uos.de*

**Abstract:** Nonlinear absorption is studied in presence of small polaron formation in lithium niobate using the  $z$ -scan technique and ultrashort laser pulses with pulse durations of 70 – 1.000 fs. A model for the analysis of the transmission loss as a function of pulse duration is introduced that considers (i) the individual contributions of two-photon and small polaron absorption, (ii) the small polaron formation time and (iii) an offset time between the optical excitation of free carriers by two-photon absorption and the appearance of small polarons. It is shown that the model allows for the analysis of the experimentally determined  $z$ -scan data with high precision over the entire range of pulse durations using a two-photon absorption coefficient of  $\beta = (5.6 \pm 0.8) \text{ mm/GW}$ . A significant contribution by small polaron absorption to the nonlinear absorption is uncovered for pulse durations exceeding the characteristic small polaron formation time of  $\approx 100$  fs. It can be concluded that the small polaron formation time is as short as (70 – 110) fs and the appearance of small polaron formation is delayed with respect to two-photon absorption by an offset of about 80 fs.

©2015 Optical Society of America. This work was published in Optical Materials Express and can be found at the URL <http://dx.doi.org/10.1364/OME.5.002729>. One print or electronic copy may be made for personal use only. Systematic reproduction and distribution, duplication of any material in this paper for a fee or for commercial purposes, or modifications of the content of this paper are prohibited.

## 1 Introduction

Lithium niobate,  $\text{LiNbO}_3$  (LN), acts as a reference material in the field of nonlinear optics and experiences increasing attention as frequency converter due to its sound second-order nonlinearity  $\chi^{(2)}$ , chemical and mechanical stability as well as availability [1]. For efficient conversion, LN is exposed to very intense, short and ultra-short

laser pulses; at high intensities, however, the problem of nonlinear absorption arises due to a predominant contribution of third order nonlinearities  $\chi^{(3)}$ , in particular two-photon absorption (TPA). Besides limiting the conversion efficiency, TPA plays a major role in irreversible bulk laser-induced damage mechanisms of ferroelectric crystals by heating as well as via the generation of free carriers [2]. In LN the subsequent formation of small polarons from optically excited free carriers must be considered [3], as well, i.e. carriers that become trapped with strong coupling within a self-induced distortion of the surrounding unit cell [4]. The contribution of small polarons to the nonlinear absorption is determined by their broad band ( $\approx 1$  eV) and pronounced absorption features [5] and characterized by a transient absorption with lifetimes in the regime from  $\mu\text{s}$  to  $\text{ms}$  at room temperature, thus commonly exceeding the pulse duration. Nonlinear interactions of small polarons with short, intense laser pulses in LN have been already addressed by different research groups [6–9]. However, the dependency of nonlinear absorption on incident laser pulses with different pulse durations has not been studied, so far, which is the topic of this work. The pulse duration dependency is of particular interest for nonlinear optical applications using sub-ps laser pulse durations that fall in the time regime of small polaron formation; the latter has been estimated to values much below 400 fs [6, 7, 9–11]). Without this knowledge, nothing is known about the individual contribution of TPA and small polaron absorption to the transmission loss of a propagating (ultra-)short laser pulse. Furthermore, it remains unclear to what extent pulse durations exist where the contribution of small polaron absorption becomes negligible.

In LN, first efforts have been made to separate optically excited carriers from the Kerr third order nonlinearity by means of grating recording [12] or transient absorption [8], demonstrating the impact of carrier dynamics in the time regime subsequent to the incident ultrashort laser pulse (240 fs). Furthermore, the two-photon absorption coefficient  $\beta$  has been determined using various pulse durations in the range of 80 fs – 55 ps yielding values of  $\beta$  between 1.5 and 5.2 mm/GW in the green spectral range (Refs. [7, 13–17], cf. review [11]).

We here study the dependency of nonlinear absorption on the duration of incident (ultra-)short laser pulses in lithium niobate by systematically scanning the transmission loss over the time regime of  $70 \text{ fs} < \tau < 1.000 \text{ fs}$  by means of  $z$ -scan technique. For analysis, the differential equation for the intensity decrease of a propagating laser pulse along the crystal coordinate is derived. The temporal interplay of non-instantaneous processes with rise/relaxation times in the sub-ps time regime are considered: TPA, free carrier relaxation, small polaron formation and cascaded carrier excitation. The model extensions are motivated by a significant deviation – increasing for longer pulse durations – between experimental data and data analysis based on TPA (cf. original work from Sheik-Bahae [18]), but also TPA with free-carrier absorption [19]. Using our model for analysis, the experimental findings are described over the entire range of pulse durations with high precision. A deconvolution of the individual contributions – particularly of small polaron and two-photon absorption – to nonlinear absorption along the time coordinate becomes possible. We discuss the obtained temporal evolution of the small polaron impact from the viewpoint of a more precise estimate for the small polaron formation time, the existence of an offset of small polaron appearance upon the incident laser pulse as proposed by

Qiu et al. [6] and pulse durations that are insignificantly affected by small polaron formation. It can be concluded, that the pulse duration dependency of nonlinear absorption yields important information for the area of nonlinear applications with intense, (ultra-)short laser pulses of LN, but also of the variety of nonlinear optical materials showing small polaron formation in general.

## 2 Modeling

### 2.1 Temporal evolution of optically excited carriers in lithium niobate

For our study, we refer to the potential scheme depicted in Fig. 1, particularly describing the interplay of two-photon and small polaron absorption. In what follows,

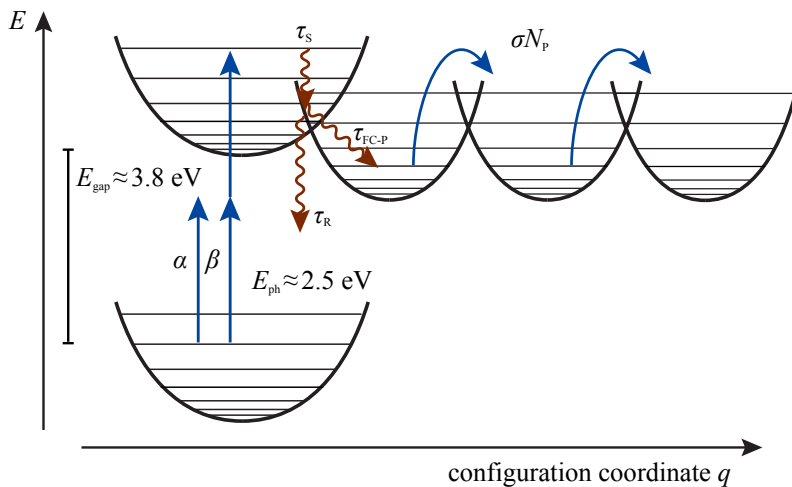


**Figure 1:** Potential diagram of the band-to-band excitation by one-photon ( $\alpha$ ) and two-photon ( $\beta$ ) absorption with photon energies of  $E_{\text{ph}} = 2.5 \text{ eV}$ , electron-phonon cooling process with time constant  $\tau_S$ , relaxation to the ground state ( $\tau_R$ ) and subsequently formation of small polarons ( $\tau_{\text{FC-P}}$ ) in lithium niobate. Absorption cross section  $\sigma$  and number of polarons  $N_P$  determine the absorption triggered by optically induced transport of small polarons [11].

the configuration coordinate  $q$  will be identified as spatial displacements of carriers in the real crystal lattice in the nanoscopic regime as well as the time axis covering the sub-ps regime.

We focus our considerations on the absorption of incident (ultra-)short sub-ps laser pulses with a photon energy of  $E_{\text{ph}} = 2.5 \text{ eV}$  via one-photon and two-photon absorption in a nominally undoped LN crystal. The probability of the former is small because of the large band gap of lithium niobate ( $\alpha = 20 \text{ cm}^{-1}$  at  $\approx 3.8 \text{ eV}$  [20]), i.e. the LN crystal is transparent for this photon energy at low incident laser intensities. At the contrary, two-photon absorption dominates the nonlinear absorption at elevated intensities. For the regime of sub-ps laser pulses, the TPA coefficient  $\beta$  is reported to values of  $\beta = 5.2 \text{ mm/GW}$  (80 fs, 400 nm, Mg-doped LN) [7] and  $\beta = 3.5 \text{ mm/GW}$  (240 fs,  $\approx 480 \text{ nm}$ , nominally undoped LN) [17]. The response time of TPA being related to bound electrons is nearly instantaneous; an estimate of  $\tau_{\text{TPA}} \approx 5 \text{ fs}$  has been

deduced from degenerate recording of TPA gratings for LN crystals [21], such that  $\tau_{\text{TPA}} \ll \tau$  for all pulse durations (70 – 1.000 fs) in our study. The temporal dynamics of TPA will thus be neglected in the differential equations given in the theoretical subsection below.

With TPA, free carriers far from the thermal equilibrium (hot carriers) are generated by means of valence-to-conduction band excitation. Energy relaxation to the lowest levels of the conduction band occurs preliminary via the emission of phonons; for semiconductors, this electron-phonon cooling process is characterized by a relaxation time of  $\tau_{\text{S}} \approx 100$  fs [22]. For LN,  $\tau_{\text{S}} = 80$  fs has been calculated for relaxation from an energetic level 0.5 eV above the conduction band minimum (T=296 K) [6]. By experimental means, ultrafast pump-probe-spectroscopy with LN did not show indications of an energy relaxation of hot carriers, so far [6, 8], whereas the time-resolved measurement of the reflectivity of a lithium niobate surface reveals a delayed signal with  $\tau_{\text{S}} = 600$  fs that has been attributed to free electron generation [23].

In the next step, the carrier may either relax to the ground state by recombination with a hole and a characteristic time constant  $\tau_{\text{R}}$ . Or carrier localization occurs followed by strong vibrational coupling, i.e. a small polaron is formed with characteristic time constant  $\tau_{\text{FC-P}}$  (*small polaron formation time*). In LN,  $\tau_{\text{FC-P}} \approx 100$  fs for small free  $\text{Nb}_{\text{Nb}}^{4+}$  polarons (room temperature) [6, 7] and  $\tau_{\text{FC-P}} < 400$  fs for small bound  $\text{Nb}_{\text{Li}}^{4+}$  polarons [9].

If the pulse duration exceeds the temporal regime until small polaron formation, the optical excitation from a small polaron must be considered, as well, and the carrier relaxes repeatedly into a small polaron. We assume that this process can be repeated several times over the incident pulse duration, i.e. cascaded excitation occurs [11].

In a similar way, the remaining holes in the valence band become localized as  $\text{O}^-$  hole polarons in the vicinity of lithium vacancies [3, 24, 25]. In the following, however, we will not distinguish between the particular types of small electron and hole polarons [24, 26, 27], because of probing at a single photon energy and the overlap of the absorption features of small free and bound electron and small hole polarons [5]. All types of small polarons result from the intrinsic defect structure of  $\text{LiNbO}_3$  that – although complex – has been modeled from first principles in very recent articles by *Li et al.* [28, 29]. We, thus, use LN crystals grown from the congruently melting composition in our experimental study.

## 2.2 Transfer to $z$ -scan technique

The starting point for the determination of the nonlinear absorption composed by TPA and small polaron absorption is the  $z$ -scan technique. It has been developed originally for the analysis of near-instantaneous third order nonlinearities, particularly of the two-photon coefficient  $\beta$  and the nonlinear index of refraction  $n_2$  [18]. A nonlinear optical sample is shifted (*scanned*) along the  $z$ -coordinate through the focus of a laser pulse with spatial and temporal Gaussian profile. The transmission as a function of  $z$  is expressed by

$$T(z) = \frac{1}{q(z)\sqrt{\pi}} \int_{-\infty}^{\infty} \ln(1 + q(z) \exp(-s^2)) ds \quad (1)$$

with  $q(z) = \beta I d_{\text{eff}} / (1 + z^2/z_0^2)$ , the peak intensity  $I$ , the two-photon absorption coefficient  $\beta$ , the effective sample thickness  $d_{\text{eff}}$  and integration constant  $s$ . The additional impact of free-carrier absorption to the transmission was derived in Ref. [19]; Ogusu et al. [30] introduced the appearance of a transient free carrier absorption with silicon as an example. Based on these theoretical concepts, we need to add the characteristic time of electron-phonon relaxation  $\tau_S$ , i.e. a temporal offset prior to small polaron formation, as a particular feature of small polaron dynamics. Then, the change of the pulse intensity through a sample as a function of the propagation depth  $L$  and time  $t$  is given by:

$$\frac{\partial I(L, t)}{\partial L} = -[\alpha + \beta I(L, t) + \sigma N_P(L, t)]I(L, t). \quad (2)$$

Here,  $\alpha$  is the one-photon absorption coefficient, and  $\sigma$  and  $N_P$  are the absorption cross section and number density of small polarons. The temporal evolution of the latter is modeled according to Fig. 1 by considering the number density of free carriers  $N_{\text{FC}}$ , the subsequent electron-phonon cooling ( $\tau_S$ ), carrier recombination ( $\tau_R$ ) and/or small polarons formation ( $\tau_{\text{FC-P}}$ ) during pulse duration ( $\tau$ ) via:

$$\frac{\partial N_P(L, t)}{\partial t} = \frac{N_{\text{FC}}(L, t - \tau_S)}{\tau_{\text{FC-P}}} \quad (3)$$

with the temporal evolution of free carriers:

$$\frac{\partial N_{\text{FC}}(L, t)}{\partial t} = \frac{\alpha I(L, t)}{h\nu} + \frac{\beta I^2(L, t)}{2h\nu} - \frac{N_{\text{FC}}(L, t - \tau_S)}{\tau_R} - \frac{N_{\text{FC}}(L, t - \tau_S)}{\tau_{\text{FC-P}}} \quad (4)$$

Differential equation (2) is solved numerically for data analysis; Figure 2 highlights the impact of pulse duration on the transmission of a  $z$ -scan measurement. For numerical

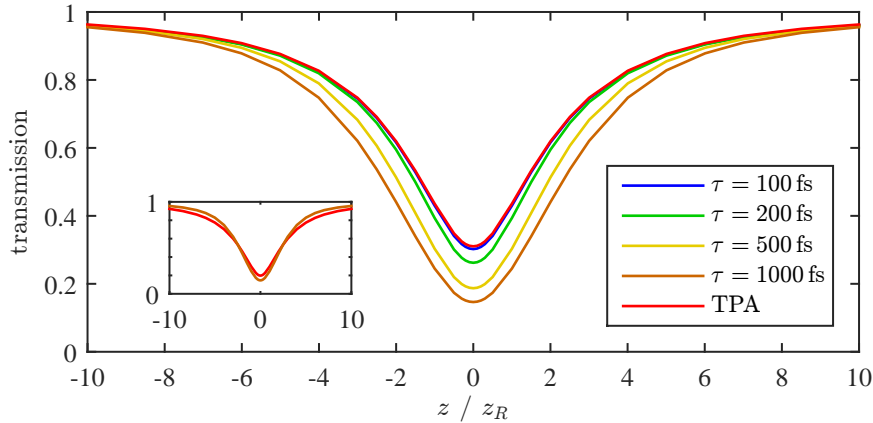


**Figure 2:** Numerical solution of Eq. (2) as a function of pulse duration (100 fs – 1.000 fs) and the following model parameters:  $\alpha = 0 \text{ m}^{-1}$ ,  $\beta = 5 \text{ mm/GW}$ ,  $\tau_S = 100 \text{ fs}$ ,  $\tau_{\text{FC-P}} = 100 \text{ fs}$ ,  $\tau_R = 100 \text{ fs}$ , and  $I = 8.6 \text{ PW/m}^2$ . For comparison the red graph representing Eq. (1) is also shown. The inset highlights the change in the shape of the transmission traces exemplarily for a pulse duration of 1.000 fs and a fitted graph using the original  $z$ -scan theory Eq. (1) with an TPA-coefficient increased by a factor of 2.2 in comparison to the main figure.

solution, the following model parameters are used:  $\alpha = 0 \text{ m}^{-1}$ ,  $\beta = 5 \text{ mm/GW}$ ,  $\tau_S = 100 \text{ fs}$ ,  $\tau_{\text{FC-P}} = 100 \text{ fs}$ ,  $\tau_R = 100 \text{ fs}$  and the pulse duration is varied from 100 fs to 1.000 fs while the peak intensity  $I$  at  $z = 0$  is kept constant at  $8.6 \text{ PW/m}^2$ . The plots show the characteristic drop of the transmission while scanning along the  $z$ -coordinate with a minimum transmission at  $z = 0$ , and are mirror symmetric to  $z = 0$ . The additional contribution of non-instantaneous absorption processes results in a pronounced increase of the transmission loss in the order of several tens of percentage, i.e. the increase of nonlinear absorption by small polaron formation, with increasing pulse duration is obvious. For comparison, the result of Eq. (1) considering the action of TPA, only, is depicted in addition (red curve). The numerical solution Eq. (2) converges to the result of Eq. (1) for pulse durations equal to the electron-phonon cooling rate,  $\tau \simeq \tau_S$ , or below. Thus, it is possible to estimate the characteristic time constants of small polaron formation from  $z$ -scan experiments as a function of pulse duration, if  $\tau$  is in the order of  $\tau_S$ . It is important to note, that the analysis of nonlinear absorption using Eq. (1) and pulse durations exceeding  $\tau_S$  will result in an overestimate of the TPA coefficient  $\beta$ . This is due to the fact, that the numerical solutions not only show an increase in the transmission loss, but also a change in the shape of  $T(z)$  (cf. inset of Fig. 2). A limit of the numerical analysis is that it is not possible to distinguish between several types of small bound polarons; this, however, may be solved by performing a systematic study at different photon energies of the incident pulse.

### 3 Experimental section

#### 3.1 Setup and lithium niobate samples

The systematic scan of the nonlinear absorption over the time regime of 70 fs – 1.000 fs has been performed using the common  $z$ -scan technique described in Ref. [18] with an incident laser pulse of spatial and temporal Gaussian profile that – as an original feature – has been compressed/stretched to the desired pulse duration. The extended setup, as depicted schematically in Fig. 3, is composed by (i) a prism pulse stretcher/compressor, (ii) a spatial frequency filter, and (iii) the common  $z$ -scan configuration. An optical parametric amplifier (Coherent Inc., model: OPerA solo) pumped by a regeneratively amplified  $\text{Ti}^{3+}$ :Sapphire laser (Coherent Inc., model: Libra-F HE) serves as the source for ultrashort laser pulses (pulse energy maximum:  $150 \mu\text{J}$  at  $2.5 \text{ eV}$ , center wavelength:  $488 \text{ nm}$ ). A neutral density filter is used for intensity adjustment. The repetition rate of  $250 \text{ Hz}$  is reduced to  $12.5 \text{ Hz}$  using a Chopper wheel, in order to avoid cumulative absorption from pulse to pulse due to long-lived small polarons (maximum characteristic lifetime  $\approx 3 \text{ ms}$  at room temperature, see e.g. Ref [11]). The pulses first enter a prism pulse stretcher/compressor that allows for tuning the pulse duration by means of adjustment of prism P2 and mirror M using a linear stage (LS). A spectral width of  $\Delta\lambda = 5 \text{ nm}$  is obtained, equal with a bandwidth limited pulse duration of  $\tau \approx 70 \text{ fs}$ . For the purpose of our study, the pulse duration is varied up to 1.000 fs and characterized by means of a scanning autocorrelator (APE, model pulseCheck 15). After the stretcher/compressor, the pulses enter a spatial frequency filter that consists of two concave mirrors (focal length:  $500 \text{ mm}$ ),

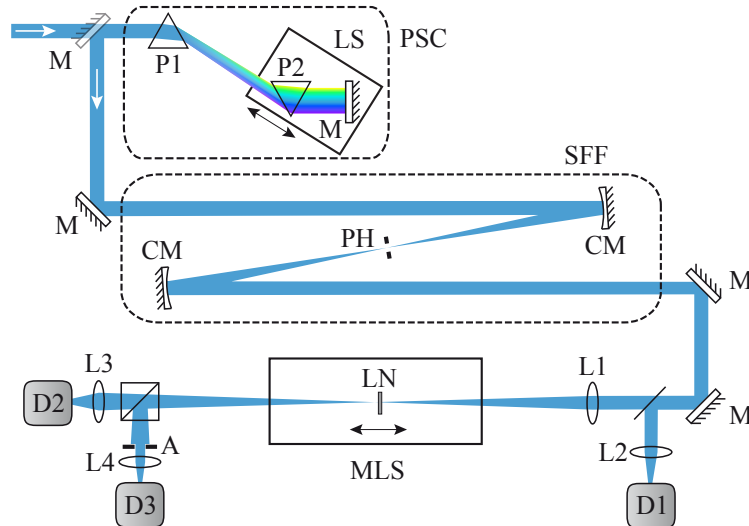


**Figure 3:** Sketch of the optical setup composed by a prism stretcher/compressor (PSC) (P1; P2 on a linear stage LS), a spatial frequency filter (SFF) (CM: concave mirrors with  $f = 500$  mm, PH: pinhole with diameter of  $100 \mu\text{m}$ ) and a common configuration for  $z$ -scan technique: L1: lens ( $f = 150$  mm), LN: lithium niobate crystal, MLS: motorized linear stage, L2-L4: lenses ( $f = 50$  mm), D1-D3: Si-PIN detectors (photosensitive area  $\gg$  beam spot), A: aperture with diameter of  $4$  mm. Incident pulses obey a maximum pulse energy of  $150 \mu\text{J}$  at  $2.5$  eV (center wavelength:  $488$  nm) and are adjusted in intensity by a neutral density filter. The repetition rate of  $250$  Hz is reduced to  $12.5$  Hz using a Chopper wheel. The pulse duration can be varied with PSC from  $70$  fs –  $1.000$  fs.

avoiding chromatic aberration, and a pinhole (diameter  $d = 100 \mu\text{m}$ ). Astigmatism is minimized by a small angle of incidence of approximately  $2$  degree. The pulse spatial radius is determined to  $(r = 2.0 \pm 0.1)$  mm. Both,  $M^2$  and  $r$ , are required for the calculation of beam waist and intensity of each pulse as a function of position  $z$ . A nearly spatial ( $M^2 = 1.1 \pm 0.1$ ) and temporal Gaussian beam profile is verified using beam profile measurements and an autocorrelator, thus, fulfilling the experimental conditions of the  $z$ -scan technique to a great extent [31]. The as-prepared pulses are focused by lens L1 ( $f = 150$  mm) and propagate through the lithium niobate crystal LN. The position of LN can be shifted along the direction of pulse propagation ( $z$ -coordinate) by means of a motorized linear stage (MLS). Incident and transmitted pulse energies are detected using biased Si-PIN detectors D1-D3 (Thorlabs, *DET10a*). The detectors D2 and D3 are equipped with opened and closed apertures, respectively, thus allowing for the determination of both nonlinear absorption and nonlinear index of refraction. Lenses L2-L4 focus the pulses to a spot size less than the photosensitive area of the detector.

All studies were performed with thin  $a$ -cut plates (aperture  $8 \times 6$  mm<sup>2</sup>, thickness  $d = (260 \pm 10)$   $\mu\text{m}$ ) of nominally pure LN grown from a congruently melting composition (CrysTec GmbH). The thickness ensures that the sample is much thinner than the Rayleigh length, avoiding asymmetric  $z$ -scan traces and effects of the group velocity dispersion (GVD). Front and back surfaces are carefully polished to optical grade with nearly plan-parallelism (wedge below  $5$  arcmin). The one-photon absorption coefficient is determined to  $\alpha = (0.16 \pm 0.1) \text{cm}^{-1}$  for extraordinary ( $\mathbf{e} \parallel \mathbf{c}$ ) light polarisation and  $\lambda = 488$  nm.

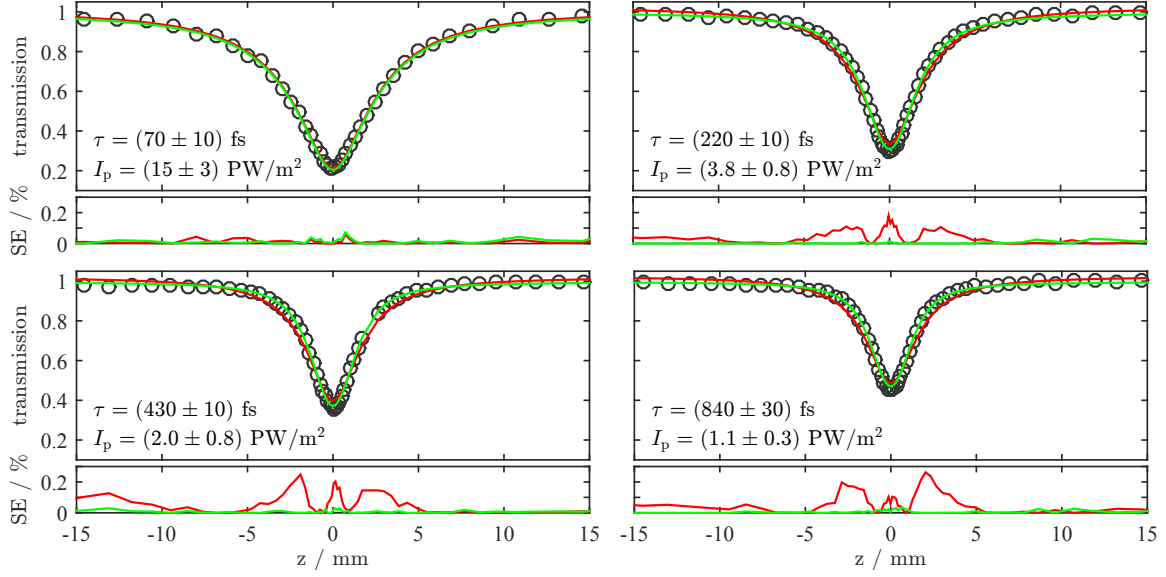


**Figure 4:** (Upper parts): Experimentally determined transmission as a function of scanning coordinate  $z$  for four pulse durations: (a)  $(70 \pm 10)$  fs, (b)  $(220 \pm 10)$  fs, (c)  $(430 \pm 10)$  fs and (d)  $(840 \pm 30)$  fs, all for a constant pulse energy of  $(270 \pm 30)$  nJ and at a center wavelength of  $\lambda = 488$  nm. The results of our numerical fitting procedure according to Eqs. (2) to (4) are shown as green lines with the following model parameters: a two-photon absorption coefficient of  $\beta = (5.6 \pm 0.8)$  mm/GW, a small polaron absorption cross section of  $\sigma = (210 \pm 70) \times 10^{-22}$  m<sup>2</sup>, and characteristic times for electron-phonon relaxation of  $\tau_S = 80$  fs, for interband relaxation of  $\tau_R = 100$  fs and for small polaron formation of  $\tau_{FC-P} = 100$  fs. For comparison, fitting of Eq. (1) to the experimental data is shown as red line. (Lower parts): squared error of the fits with respect to the experimental data as a function of  $z$ .

### 3.2 Experimental results

The experimentally determined  $z$ -scan traces are plotted in Fig. 4, exemplarily, for four pulse durations: (a)  $(70 \pm 10)$  fs, (b)  $(220 \pm 10)$  fs, (c)  $(430 \pm 10)$  fs and (d)  $(840 \pm 30)$  fs, all for a constant pulse energy of  $(270 \pm 30)$  nJ and at a center wavelength of  $\lambda = 488$  nm. The upper parts of the figures show the transmission  $T$  obtained from the signal ratio of diodes D2 and D1 as a function of  $z$ -coordinate from -15 mm to +15 mm. The travel range is chosen such that one-photon absorption dominates the transmission at  $\pm 15$  mm; the transmission is normalized to unity at  $|z| > 15$  mm and shows a pronounced drop by scanning over the focus of the incident pulse. The minimum of transmission is used to define the position  $z = 0$ ; all data sets are almost mirror-symmetric to  $z = 0$ . Qualitatively, the shape of the  $z$ -scan traces are comparable with each other for all pulse durations, and are characterized by a very low noise. A closer inspection reveals that the shape becomes narrower with increasing  $\tau$ , which is a sign of higher order nonlinearities as discussed above (cf. inset of Fig. 2). In addition, and because of the adjustment of a constant pulse energy for all pulse durations, the varying peak intensity yields an increase of the transmission with increasing  $\tau$  from  $T \approx 20\%$  at 70 fs to  $T \approx 45\%$  at 840 fs.

The data plots are analyzed by numerical solution of Eqs. (2) to (4). Fitting was performed iteratively by optimizing the squared error between fit and experimental data and the same model parameters for all data sets; the fitting results are shown

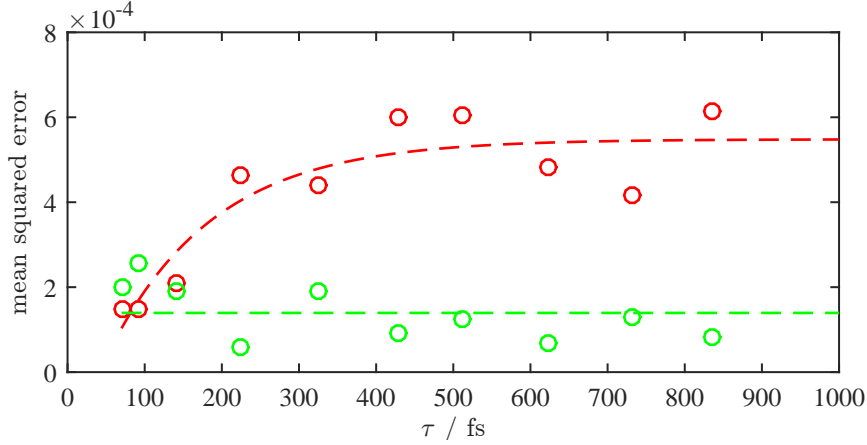


**Figure 5:** Mean squared error between fit and experimental data for both, the numerical solution of our model approach according to Eqs. (2) to (4) (green), and the original  $z$ -scan theory using Eq. (1) (red). The dashed lines represent best fits with constant minimum value of the mean squared error  $\text{MSE}_{\min} = (1.5 \pm 0.1) \times 10^{-4}$  (green) and a fit with Eq. (5) to the data points (red) with saturation amplitude  $\text{MSE}(t = \infty) = (4 \pm 0.1) \times 10^{-4}$ , characteristic time constant  $\tau_{\text{exp}} = (137 \pm 8)$  fs, temporal offset of  $\tau = (86 \pm 5)$  fs, and minimum value of mean squared error  $\text{MSE}_{\min} = (1.5 \pm 0.1) \times 10^{-4}$ .

as green curves in Fig. 4(a)-(d) with the following model parameters: a two-photon absorption coefficient of  $\beta = (5.6 \pm 0.8)$  mm/GW, a small polaron absorption cross section of  $\sigma = (210 \pm 70) \times 10^{-22}$  m<sup>2</sup>, and characteristic times for electron-phonon relaxation of  $\tau_S = 80$  fs, for interband relaxation of  $\tau_R = 100$  fs and for small polaron formation of  $\tau_{\text{FC-P}} = 100$  fs. A high degree of agreement is obvious from the inspection by eye over the entire range of scanning. The lower plots of Fig. 4(a)-(d) highlight the squared error of the fits with respect to the experimental data as a function of  $z$  with values much below 0.1% throughout the data set, typically below 0.03%. For comparison, the data sets have been also analyzed using Eq. (1), i.e. the  $z$ -scan theory considering two-photon absorption, only, yielding the red curves in Fig. 4(a)-(d). For the shortest pulse duration of 70 fs, the data can be modeled by the  $z$ -scan theory with very good coincidence, expressed by a squared error of below 0.1%. From this data set, the fit yields a two-photon absorption coefficient of  $\beta = (5.8 \pm 0.8)$  mm/GW (for the nonlinear refractive index  $n_2$  we obtained a value of about  $5 \times 10^{-20}$  m<sup>2</sup>/W). For longer pulse durations, a deviation of the original TPA theory to the experimentally determined traces becomes obvious and is more pronounced with increasing pulse duration (exceeding a squared error of  $\approx 0.2\%$ ). The evolution of *mean* squared errors (MSE) between fit and data set is plotted for both theoretical approaches in Fig. 5 for all measured pulse durations. Again, the plot highlights the excellent agreement of our model approach with the experimental data over the entire regime of pulse durations; a minimum value of mean squared error  $\text{MSE}_{\min} = (1.5 \pm 0.1) \times 10^{-4}$  is reached throughout the pulse durations. The original  $z$ -scan theory describes the data with high precision in the regime of the shortest pulse durations (below 100 fs), as well. However, a characteristic rise of MSE of Eq. (1) becomes obvious for pulse durations  $\geq 100$  fs with a development that can be best described by a single-exponential growth function. We thus have fitted the

function

$$\text{MSE}(t) = \text{MSE}(t = \infty) \times \left[ 1 - \exp\left(\frac{-(t - t_{\text{offset}})}{\tau_{\text{exp}}}\right) \right] + \text{MSE}_{\text{min}} \quad (5)$$

to the data set yielding the following parameters: saturation amplitude  $\text{MSE}(t = \infty) = (4 \pm 0.1) \times 10^{-4}$ , characteristic time constant  $\tau_{\text{exp}} = (137 \pm 8)$  fs, temporal offset of  $\tau = (86 \pm 5)$  fs, and minimum value of mean squared error  $\text{MSE}_{\text{min}} = (1.5 \pm 0.1) \times 10^{-4}$ .

## 4 Discussion

From the experimental viewpoint, a very high quality of transmission traces are collected using the applied optical setup that represents an extension of the common  $z$ -scan technique. In particular, the important conditions of a Gaussian spatial profile is obtained, using a spatial frequency filter, and a Gaussian temporal profile is verified by autocorrelation measurements. A diode-pumped, regeneratively amplified Ti:Sa-laser system obeys an excellent beam profile and pointing stability and, thus, is ideally suited for generation of harmonic, Gaussian pulses by means of an optical parametric amplifier. The RMS noise of the pulse energy at the OPAs' output ( $\ll 5\%$ ) could be reduced successfully by selection of incident pulses with equal pulse energy using diode D1. The disadvantage of this procedure is the extended measurement time, which is further enlarged by the low pulse repetition rate of 12.5 Hz and the two dimensional parameter range  $(z, \tau)$  of our particular study. However, all these efforts are justified considering the outmost marginal deviations between the model approaches typically of below 0.03% (cf. Fig. 4).

As a superior result, a more detailed insight to the underlying physics of nonlinear absorption in lithium niobate is obtained, and clear evidence for small polaron formation and its contribution to nonlinear absorption is found. From the dependency of the shape of the  $z$ -scan trace as a function of pulse duration and its analysis, it is possible to derive a set of important material parameters that will be discussed in the following. First, the two-photon absorption coefficient  $\beta = (5.6 \pm 0.8)$  mm/GW is obtained from the complex numerical fitting procedure, that uses a single set of parameters for all pulse durations. Thus, the transmission is described throughout the regime of pulse durations from 70 fs – 1.000 fs with the same TPA coefficient – a result that is to be expected as  $\beta$  is a material parameter independent on  $\tau$ . Considering the high quality of the numerical fits, a reliable value of  $\beta$  with an error of  $\approx 15\%$  occurs for the LN crystal under investigation. Nearly the same value ( $\beta = (5.8 \pm 0.8)$  mm/GW) is obtained using the original  $z$ -scan theory at the shortest pulse duration of  $(70 \pm 10)$  fs, that underlines the reliability of the obtained value. Moreover, it is an important (first) anchor for proving the action of our model approach as nonlinear absorption persists solely from TPA for pulse durations much below the small polaron formation time. The TPA value itself is much larger than the state-of-the-art knowledge in literature. For comparable pulse durations and photon energies, values of  $\beta = 5.2$  mm/GW (80 fs, 400 nm, Mg-doped LN) [7] and  $\beta = 3.5$  mm/GW (240 fs,  $\approx 480$  nm, nominally undoped LN) [17] are reported. Besides the possibility, that this difference may be attributed to the impact of small

polaron absorption according to our model approach, we like to emphasize the role of stoichiometry on the TPA coefficient. It is well established, that the position of the band gap energy is strongly dependent on the crystals' stoichiometry. Being an absorption process of higher order, the transition probability for TPA is expected to change in accordance with the linear absorption feature [32]. Therefore, differences in the TPA coefficient may be due to differences in stoichiometry of the studied LN crystals, which seems to be very likely to us.

New insights are revealed to the relaxation dynamics of optically excited free carriers, characterized by  $\tau_S$ . First evidence for this intermediate process was presented by Qiu et al. [6] performing time-resolved fs-absorption spectroscopy in Mg-doped LN crystals. As a remarkable characteristic of the small polaron formation dynamics, a temporal offset was discovered prior to the rise of small polaron absorption. No change of the transmission was observed during this temporal offset. A similar observation is reported in the work of Beyer et al. [8] using 240 fs laser pulses. Here, we also need to take into account a temporal offset prior to small polaron formation. In advance of the results of Qiu et al. [6], the time of the incident pulse does not need to be determined which is a particular feature of the approach of pulse duration scanning; the time constant  $\tau_S$  is equal to the pulse duration where the transmission trace starts to alter its shape. Therefore, the temporal offset  $\tau_S = 80$  fs can be determined with appealing precision. The lack of free-carrier absorption may be attributed either to the fact that the photon energy of the probing pulse is insensitive to the free-carrier absorption cross section or the carrier-phonon relaxation time  $\tau_S$  falls much below the pulse duration ( $\tau_S \ll (70 \pm 10)$  fs in our case). However, as pointed out in Ref. [22],  $\tau_S$  exceeds  $10^{-13}$  s in most semiconductors and for common optical phonon modes. Further studies, particularly with shorter pulse durations need to be performed for clarification.

From the rise of the nonlinear absorption as a function of pulse duration we further obtain the small polaron formation time of  $\tau_{FC-P} = 100$  fs in the numerical modeling procedure. This value is in good coincidence with the formation times obtained by transient absorption measurements [6, 7, 9]. Combining, however, our result on the presence of an offset time of  $\tau_S = 80$  fs and the transient data from Sasamoto et al. using also very short, 80 fs pump and probe laser pulses [7], it is possible to conclude an upper limit of  $\tau_{FC-P} = 100$  fs. It is because the transmission loss due to two-photon absorption and due to small polaron absorption can not be resolved on the temporal axis in pump-probe experiments and overlap with each other.

Another parameter obtained from our study is the small polaron absorption cross section  $\sigma$  that is by more than one order of magnitude higher than the values published by Merschjann et al. [5]. We note that it is not possible to find a converging numerical solution using Merschjann's value as fixed fitting parameter, even by neglecting relaxation of excited carriers to the ground state ( $\tau_R = \infty$ ). One explanation for the striking difference is an oversimplification of our model approach presented in section 2. In particular, the dynamics of holes with the possibility of  $O^-$  small hole polaron formation in LN [25] has been disregarded. Such holes obey nearly the same absorption cross section at a photon energy of 2.5 eV as it is the case for small bound  $Nb_{Li}^{4+}$  and/or small free  $Nb_{Nb}^{4+}$  polarons, although the maxima of the respective absorption features are fairly different (2.5 eV for  $O^-$  and 1.6 eV for  $Nb_{Li}^{4+}$ ). It is thus likely

to assume that half of the contribution to small polaron absorption at 2.5 eV must be attributed to  $O^-$  hole polarons. As a consequence, a value reduced by a factor of two will be obtained for the absorption cross section. Nevertheless, as individual types of small polarons are not resolved by our study, further pulse duration dependencies using different photon energies are required for a more quantitative analysis of this aspect. We like to add, that there is a severe difference in the boundary conditions of small polaron absorption between the study of Merschjann et al. [5] and the present one: Merschjann's cross sections were determined using pump-probe experiments, i.e. under the conditions of no light, whereas small polarons are inspected during the presence of a strong pump in our study, i.e. with light. Considering the presence of specific charge transport phenomena in LN, particularly of bulk photovoltaic currents [33], a difference in the absorption features of small polarons with and without light illumination can not be excluded.

It is noteworthy that all parameters discussed above and obtained from the rather complex numerical solution of Eqs. (2) to (4) show a correlation with each other. Particularly, the ratio between  $\tau_{\text{FC-P}}$  and  $\tau_{\text{R}}$  is not independent from other model parameters and directly impacts the density numbers  $N_{\text{FC}}$  and  $N_{\text{P}}$  as well as the polaron absorption coefficient  $\sigma$ . As a consequence, the characteristic times can be varied in a limited regime, only. The offset time  $\tau_{\text{S}}$  can be varied between 70 fs and 90 fs while the polaron formation time is limited to  $70 \text{ fs} < \tau_{\text{FC-P}} < 110 \text{ fs}$ . At the same time, it is very reasonable that the increase of the number of fitting parameters in general results in the optimization of fitting functions. However, in the present case, the extension of the original  $z$ -scan theory by small polaron absorption is justified by the striking deviation of the transmission traces between theory and experimental data with increasing pulse duration. As this deviation rises after a characteristic offset time, the data plot of Fig. 5 showing the mean squared error as a function of pulse duration, can be applied also for the determination of the offset time  $\tau_{\text{S}}$  yielding  $\tau_{\text{S}} = (86 \pm 5) \text{ fs}$  – in accordance with the numerical results of our model approach.

## 5 Summary and Conclusion

The pulse duration dependency of nonlinear absorption has been studied in lithium niobate by means of  $z$ -scan technique over the time regime of 70 – 1.000 fs and has been analyzed from the viewpoint of small polaron formation using a numerical approach. It is shown, that the transmission loss of (ultra-)short laser pulses propagating through LN crystals can be described with remarkable precision and can be attributed to the complex interplay of near-instantaneous nonlinearities, particularly of two-photon and small-polaron absorption. Surprisingly, very minor alterations in the shape of the well-known transmission traces of the  $z$ -scan technique result in severe changes in the set of nonlinear optical coefficients; for instance, using the original  $z$ -scan theory, the TPA coefficient  $\beta$  may be overestimated by a factor of three in the regime of long pulse durations.

Besides the precise determination of  $\beta$  or the absorption cross section of small polarons under illumination  $\sigma$ , the amount of information on the underlying photo-

physical processes obtained from our study is unexpectedly high: the proposed offset of transient absorption features during the time regime of electron-phonon cooling has been verified by experimental means and could be determined to  $(80 \pm 10)$  fs. Furthermore, a more accurate regime of the small polaron formation time of 70 – 110 fs has been obtained.

These results are of utmost importance for the physics and microscopic modeling of the small polaron approach in LN [25,26] and the further understanding of the small-polaron based bulk photovoltaic effect [33]. But also for the field of applications in nonlinear photonics as frequency converter – particularly in the growing field of ultrafast laser systems. In more general, the presented theoretical model and the experimental approach of pulse duration scanning can be transferred to the wide field of oxide materials showing small polaron formation and can be applied in the area of ultrafast lasers.

## Acknowledgments

The authors gratefully acknowledge discussion from G. Corradi, L. Kovács (SZFKI, Hungary), and from A. Büscher. Financial support by the DFG (IM 37/5-2, INST 190/137-1 FUGG, INST 190/165-1) is gratefully acknowledged.

## References

- [1] M. Fejer, G. Magel, D. H. Jundt, and R. Byer, “Quasi-phase-matched second harmonic generation: tuning and tolerances,” *IEEE J. Quantum Electron.* **28**, 2631–2654 (1992).
- [2] O. A. Louchev, H. H. Hatano, N. Saito, S. Wada, and K. Kitamura, “Laser-induced breakdown and damage generation by nonlinear frequency conversion in ferroelectric crystals: Experiment and theory,” *J. Appl. Phys.* **114**, 203101 (2013).
- [3] O. F. Schirmer and D. von der Linde, “Two-Photon and X-Ray-Induced  $\text{Nb}^{4+}$  and  $\text{O}^-$  Small Polarons in  $\text{LiNbO}_3$ ,” *Appl. Phys. Lett.* **33**, 35 (1978).
- [4] D. Emin, *Polarons* (Cambridge University Press, Cambridge, 2013).
- [5] C. Merschjann, B. Schoke, D. Conradi, M. Imlau, G. Corradi, and K. Polgar, “Absorption cross sections and number densities of electron and hole polarons in congruently melting  $\text{LiNbO}_3$ ,” *J. Phys. Chem. Sol.* **21**, 015906 (2009).
- [6] Y. Qiu, K. B. Ucer, and R. T. Williams, “Formation time of a small electron polaron in  $\text{LiNbO}_3$ : measurements and interpretation,” *Phys. Stat. Sol. C* **2**, 232 (2005).
- [7] S. Sasamoto, J. Hirohashi, and S. Ashihara, “Polaron dynamics in lithium niobate upon femtosecond pulse irradiation: Influence of magnesium doping and stoichiometry control,” *J. Appl. Phys.* **105**, 083102 (2009).
- [8] O. Beyer, D. Maxein, K. Buse, B. Sturman, H. T. Hsieh, and D. Psaltis, “Investigation of nonlinear absorption processes with femtosecond light pulses in lithium niobate crystals,” *Phys. Rev. E* **71**, 056603 (2005).
- [9] O. Beyer, D. Maxein, T. Woike, and K. Buse, “Generation of small bound polarons in lithium niobate crystals on the subpicosecond time scale,” *Appl. Phys. B* **83**, 527–530 (2006).

- 
- [10] H. Yochum, K. Ucer, R. Williams, P. Sheldon, V. Nagirnyi, V. Denks, L. Grigorjeva, D. Millers, and E. Kotomin, “Short-pulse excitation and spectroscopy of  $\text{KNbO}_3$ ,  $\text{LiNbO}_3$  and  $\text{KTiOPO}_4$ ,” *Rad. Eff. Def. Sol.* **150**, 271–276 (1999).
- [11] M. Imlau, H. Badorreck, and C. Merschjann, “Optical nonlinearities of small polarons in lithium niobate,” *Appl. Phys. Rev.* (in press).
- [12] D. Maxein and K. Buse, “Interaction of Femtosecond Laser Pulses with Lithium Niobate Crystals: Transmission Changes and Refractive Index Modulations,” *J. Holography Speckle* **5**, 1–5 (2009).
- [13] A. Seilmeier and W. Kaiser, “Generation of tunable picosecond light pulses covering the frequency range between 2700 and 32,000  $\text{cm}^{-1}$ ,” *Appl. Phys. A* **23**, 113 (1980).
- [14] R. DeSalvo, A. Said, D. Hagan, E. Van Stryland, and M. Sheik-Bahae, “Infrared to ultraviolet measurements of two-photon absorption and  $n_2$  in wide bandgap solids,” *IEEE J. Quantum Electron.* **32**, 1324 (1996).
- [15] H. Li, F. Zhou, X. Zhang, and W. Ji, “Picosecond Z-scan study of bound electronic Kerr effect in  $\text{LiNbO}_3$  crystal associated with two-photon absorption,” *Appl. Phys. B* **64**, 659 (1997).
- [16] R. Ganeev, I. Kulagin, A. Rysanyansky, R. Tugushev, and T. Usmanov, “Characterization of nonlinear optical parameters of KDP,  $\text{LiNbO}_3$  and BBO crystals,” *Opt. Commun.* **229**, 403–412 (2004).
- [17] O. Beyer, D. Maxein, K. Buse, B. Sturman, H. T. Hsieh, and D. Psaltis, “Femtosecond time-resolved absorption process in lithium niobate crystals,” *Opt. Lett.* **30**, 1366 (2005).
- [18] M. Sheik-Bahae, A. A. Said, T. H. Wei, D. J. Hagan, and E. W. Van Stryland, “Sensitive Measurement of Optical Nonlinearities Using A Single Beam,” *IEEE J. Quantum Electron.* **26**, 760 (1990).
- [19] A. A. Said, M. Sheik-Bahae, D. J. Hagan, T. H. Wei, J. Wang, J. Young, and E. W. Van Stryland, “Determination of Bound-electronic and Free-carrier Nonlinearities In  $\text{ZnSe}$ ,  $\text{GaAs}$ ,  $\text{CdTe}$ , and  $\text{ZnTe}$ ,” *J. Opt. Soc. Am. B* **9**, 405 (1992).
- [20] S. Redfield and W. J. Burke, “Optical Absorption Edge of  $\text{LiNbO}_3$ ,” *J. Appl. Phys.* **45** (1974).
- [21] A. Shumelyuk, Institute of Physics, National Academy of Sciences, 46, Prospekt Nauki, 03 650 Kyiv, Ukraine, H. Badorreck, S. Nolte, M. Imlau, and S. Odoulov are preparing a manuscript to be called “Selfdiffraction from moving gratings recorded in  $\text{LiNbO}_3$  with ultra-short laser pulses of different colors.”
- [22] A. Othonos, “Probing ultrafast carrier and phonon dynamics in semiconductors,” *J. Appl. Phys.* **83**, 1789–1830 (1998).
- [23] M. Garcia-Lechuga, J. Siegel, J. Hernandez-Rueda, and J. Solis, “Imaging the ultrafast Kerr effect, free carrier generation, relaxation and ablation dynamics of Lithium Niobate irradiated with femtosecond laser pulses,” *J. Appl. Phys.* **116**, 113502 (2014).
- [24] O. F. Schirmer, O. Thiemann, and M. Wöhlecke, “Defects in  $\text{LiNbO}_3$  — I. Experimental Aspects,” *J. Phys. Chem. Solids* **52**, 185 (1991).
- [25] O. F. Schirmer, “ $\text{O}^-$  bound small polarons in oxide materials,” *J. Phys. Condens. Matter* **18**, R667 (2006).

- [26] O. F. Schirmer, M. Imlau, C. Merschjann, and B. Schoke, “Electron small polarons and bipolarons in  $\text{LiNbO}_3$ ,” *J. Phys. Condens. Matter* **21**, 123201 (2009).
- [27] B. Faust, H. Müller, and O. F. Schirmer, “Free small polarons in  $\text{LiNbO}_3$ ,” *Ferroelectrics* **153**, 297 (1994).
- [28] Y. Li, W. G. Schmidt, and S. Sanna, “Intrinsic  $\text{LiNbO}_3$  point defects from hybrid density functional calculations,” *Phys. Rev. B* **89**, 094111 (2014).
- [29] Y. Li, S. Sanna, and W. G. Schmidt, “Modeling intrinsic defects in  $\text{LiNbO}_3$  within the Slater-Janak transition state model,” *The Journal of Chemical Physics* **140**, 234113 (2014).
- [30] K. Ogusu and K. Shinkawa, “Optical nonlinearities in silicon for pulse durations of the order of nanoseconds at  $1.06\ \mu\text{m}$ ,” *Opt. Express* **16**, 14780–14791 (2008).
- [31] P. B. Chapple, J. Staromlynska, J. A. Hermann, T. J. McKay, and R. G. Mcduff, “Single-Beam Z-Scan: Measurement Techniques and Analysis,” *J. Nonlinear Opt. Phys. Mater.* **06**, 251–293 (1997).
- [32] M. Sheik-Bahae, D. J. Hagan, and E. W. Van Stryland, “Dispersion and band-gap scaling of the electronic Kerr effect in solids associated with two-photon absorption,” *Phys. Rev. Lett.* **65**, 96–99 (1990).
- [33] O. F. Schirmer, M. Imlau, and C. Merschjann, “Bulk photovoltaic effect of  $\text{LiNbO}_3\text{:Fe}$  and its small-polaron-based microscopic interpretation,” *Phys. Rev. B* **83**, 165106 (2011).



# Optical nonlinearities of small polarons in lithium niobate

Mirco Imlau<sup>1,\*</sup>, Holger Badorreck<sup>1</sup>, Christoph Merschjann<sup>2</sup>

<sup>1</sup>*Physics Department, Osnabrueck University, Barbarastr. 7, 49076 Osnabrueck, Germany*

<sup>2</sup>*Fachbereich Physik, Freie Universität Berlin, Arnimallee 14, 14195 Berlin, Germany*

*\*mirco.imlau@uni-osnabrueck.de*

Reprinted with permission from Appl. Phys. Rev. **2**, 040606, (2015).

doi: 10.1063/1.4931396. Copyright 2015, AIP Publishing LLC.

**Abstract:** An overview of optical nonlinearities of small bound polarons is given, which can occur in the congruently melting composition of LiNbO<sub>3</sub>. Such polarons decisively influence the linear and nonlinear optical performance of this material, that is important for the field of optics and photonics. On the basis of an elementary phenomenological approach, the localization of carriers in a periodic lattice with intrinsic defects is introduced. It is applied to describe the binding energies of four electron and hole small polarons in LiNbO<sub>3</sub>: small free Nb<sub>Nb</sub><sup>4+</sup> polarons, small bound Nb<sub>Li</sub><sup>4+</sup> polarons, small bound Nb<sub>Li</sub><sup>4+</sup>:Nb<sub>Nb</sub><sup>4+</sup> bipolarons, and small bound O<sup>-</sup> hole polarons. For the understanding of their linear interaction with light, an optically induced transfer between nearest-neighboring polaronic sites is assumed. It reveals spectrally well separated optical absorption features in the visible and near-infrared spectral range, their small polaron peak energies and lineshapes. Nonlinear interaction of light is assigned to the optical formation of short-lived small polarons as a result of carrier excitation by means of band-to-band transitions. It is accompanied by the appearance of a transient absorption being spectrally constituted by the individual fingerprints of the small polarons involved. The relaxation dynamics of the transients is thermally activated and characterized phenomenologically by a stretched exponential behavior, according to incoherent 3D small polaron hopping between regular and defect sites of the crystal lattice. It is shown that the analysis of the dynamics is a useful tool for revealing the recombination processes between small polarons of different charge. Nonlinear interaction of small polarons with light furthermore results in changes of the index of refraction. Besides its causal relation to the transients via Kramers-Kronig relation, pronounced index changes may occur due to optically generated electric fields modulating the index of refraction via the linear electro-optic effect, also. Based on a microscopic picture and by considering the local structural environment of bound polarons, the appearance of photovoltaic currents is explained straightforwardly as a result of the optically induced carrier transfer. Both transient absorption and index changes are spatially confined to the intensity profile of the interacting light allowing for the recording of efficient mixed absorption and phase volume holograms. By means of holographic spectroscopy, these small-polaron based optical nonlinearities are verified either without or with the action of the linear electro-optic effect; their prominent features are highlighted by appropriate experimental studies wherein the

ultrafast response on the picosecond time scale is the most recognized one. Based on these findings, the consequences for applications of LiNbO<sub>3</sub> in the field of nonlinear optics & photonics are presented. Besides visionary examples like real-time, 3D holographic displays, the impact of optical nonlinearities of small polarons for present applications are discussed with frequency conversion and respective limiting effects, such as green-induced infrared absorption and optical damage, as important example.

## Contents

<b>1</b>	<b>Introduction</b>	<b>53</b>
<b>2</b>	<b>Structure physics of small polarons in lithium niobate</b>	<b>55</b>
2.1	Holsteins' Molecular-Crystal Model (MCM) . . . . .	55
2.2	Small free and bound polarons in LiNbO <sub>3</sub> . . . . .	57
<b>3</b>	<b>Optical absorption features of small polarons</b>	<b>59</b>
3.1	Modelling . . . . .	59
3.2	Experimental fingerprints . . . . .	60
<b>4</b>	<b>Optical generation of small polarons</b>	<b>61</b>
4.1	Light-induced small polaron absorption . . . . .	63
4.1.1	Fundamental description . . . . .	63
4.1.2	Thermally activated decay . . . . .	64
4.2	Experimental examples . . . . .	66
4.2.1	Number densities of optically generated small polarons . . . . .	66
4.2.2	Recombination dynamics of optically generated small polarons . . . . .	68
4.2.3	Optical formation time of small polarons . . . . .	69
<b>5</b>	<b>Optical excitation from polaronic centers</b>	<b>70</b>
5.1	Directed optical transfer of small polarons from Fe <sub>Li</sub> . . . . .	71
5.1.1	Absorption features . . . . .	71
5.1.2	Net currents . . . . .	72
<b>6</b>	<b>Hologram recording by means of small polarons</b>	<b>75</b>
6.1	Population density holograms . . . . .	76
6.1.1	Hologram recording mechanism . . . . .	76
6.1.2	Modeling . . . . .	77
6.1.3	Results & analysis . . . . .	80
6.2	Holograms by means of the electro-optic effect . . . . .	82
6.2.1	Results . . . . .	83
<b>7</b>	<b>Impact on Nonlinear Photonics &amp; Conclusion</b>	<b>86</b>
7.1	Developing fields . . . . .	87
7.2	Present applications . . . . .	89

# 1 Introduction

Various manifestations of small polarons [1, 2] affect strongly the linear and nonlinear optical properties in the oxide crystal lithium niobate,  $\text{LiNbO}_3$  [3]: free electron  $\text{Nb}_{\text{Nb}}^{4+}$  polarons, polarons bound to antisite defects,  $\text{Nb}_{\text{Li}}^{4+}$ , and  $\text{Nb}_{\text{Nb}}^{4+}:\text{Nb}_{\text{Li}}^{4+}$  bipolarons [4]. In addition to these three types of electron polarons, also  $\text{O}^-$  hole small polarons bound to Li-vacancies can occur [5]. Such polarons show strong absorption bands peaked near 1.0 eV ( $\text{Nb}_{\text{Nb}}^{4+}$ ), 1.6 eV ( $\text{Nb}_{\text{Li}}^{4+}$ ), and 2.5 eV (both,  $\text{Nb}_{\text{Nb}}^{4+}:\text{Nb}_{\text{Li}}^{4+}$  and  $\text{O}^-$ ). These peak energies are related to the respective polaron stabilization energies  $E_p$  and, in addition, to the binding defect potentials for the bound species [6, 7]. The absorption bands are rather asymmetric with pronounced high energy tails, having half-widths of typically one electron Volt. Thus, they fall within the large band gap of lithium niobate ( $\alpha = 20 \text{ cm}^{-1}$  at  $\approx 3.8 \text{ eV}$  [8]) over a wide spectral range.

Using laser light, short-lived small polarons are generated in nominally undoped  $\text{LiNbO}_3$  by optical interband excitation of carriers and/or by carrier-release via photoionization of extrinsic impurity centers [9]. Particularly, free polarons,  $\text{Nb}_{\text{Nb}}^{4+}$ , bound polarons,  $\text{Nb}_{\text{Li}}^{4+}$ , and  $\text{O}^-$  hole polarons are formed and yield a pronounced transient small polaron absorption in the visible and near-infrared spectral range. Besides, laser-induced dissociation of bipolarons,  $\text{Nb}_{\text{Nb}}^{4+}:\text{Nb}_{\text{Li}}^{4+}$ , that can be created as stable species at room temperature by raising the Fermi level, e.g., by chemical reduction, leads to the formation of pairs of bound polarons,  $\text{Nb}_{\text{Li}}^{4+}$ , and free polarons,  $\text{Nb}_{\text{Nb}}^{4+}$ . All optically generated small polarons recombine within several micro- and milliseconds at room temperature, either with themselves for charge compensation or with intrinsic  $\text{Nb}_{\text{Li}}$  defect centers. The generation of small polarons without the action of light but by heating is possible, e.g., considerable  $\text{Nb}_{\text{Nb}}^{4+}$  are present in thermal equilibrium at rather elevated temperatures [10].

Number densities of optically generated small polarons reach up to tens of  $10^{22} \text{ m}^{-3}$  and strongly absorb light in the near-infrared and visible spectral range taking into account the typical polaron absorption cross sections exceeding  $4 \cdot 10^{-22} \text{ m}^2$  [11–13]. In recent years, this particular type of transient absorption, assigned to small polaron generation, has been applied for purposes of spectroscopic studies of carrier localization phenomena in lithium niobate related to both electrons and holes [14, 15]. These studies already uncovered the impact of the intrinsic defect structure on the small polaron formation. A time delay between free-carrier excitation and small polaron localization of about hundred femtoseconds at room temperature was found [16, 17] and a detailed model approach to the thermally-activated diffusive hopping of small polarons upon their formation could be deduced [18, 19].

Furthermore, the optical formation of small polarons is accompanied by pronounced changes of the index of refraction, either causally by considering Kramers-Kronig relation [20, 21] or via the small-polaron based photovoltaic effect [22] and the action of the linear electro-optical effect (Pockels effect). Only recently it was shown, that the optical interaction of light with charges localized as small polarons at intrinsic defects and a distorted structural environment may result in the formation of a non-zero net current and the build-up of huge internal electric fields [22]. This bulk photovoltaic effect [23–27] is one of the most important features of *doped*  $\text{LiNbO}_3$ , i.e. crystals with extrinsic defect centers, such as  $\text{Fe}_{\text{Li}}$ . It is because it represents an important step

within the cascade of charge-transport phenomena [28, 29] that result in the photorefractive effect [30–33] allowing for a variety of photorefractive phenomena in various photovoltaic ferroelectrics [34]. Due to the application of continuous-wave laser light, a phenomenological description of the photovoltaic effect served convincingly over the last decades. With the introduction of high-power, (ultra-)short pulse laser systems, and the appearance of novel nonlinear phenomena in nominally undoped LiNbO<sub>3</sub> (e.g. the appearance of transient absorption with stretched exponential decay [15]), a microscopic analysis of light-matter-interaction became inevitably necessary [22]. Its relation to optically induced index changes in nominally undoped LiNbO<sub>3</sub> is studied comprehensively by means of holographic spectroscopy [35, 36] and using short, intense laser pulses. Hologram recording with a single nanosecond laser pulse and efficiencies > 20% define a remarkable small-polaron based photosensitive response of  $S = 8 \text{ J/cm}^2$  [36] over the visible and near-infrared spectral range. According to the metastable nature of optically generated small polarons, respective holograms decay within micro- and milliseconds at room temperature and show stretched-exponential decay dynamics. They thus superimpose with the optical nonlinearities induced by two-photon absorption and Drude-Lorentz nonlinearity in LiNbO<sub>3</sub> observed instantaneously with the laser pulse [37].

Obviously, the optical generation of small polarons and their nonlinear optical features must be considered for the various fields of applications of lithium niobate in nonlinear photonics, mainly based on its acousto-optical, nonlinear optical, electro-optical and photorefractive properties [33, 38–40]. Already it has been shown, that small bound polarons may act as intermediate shallow traps in a multi-step recording scheme for phase holograms featuring non-destructive read-out [41, 42]. Because of its increasing role as frequency converter, laser-induced damage mechanisms in lithium niobate needs to be analyzed in the framework of small polarons and, particularly, of their optical nonlinearities. The striking role of charged point defects is reported in several prominent oxides widely applied for frequency conversion [43–45]. Among the materials showing polaronic effects are KNbO<sub>3</sub> [46], LiTaO<sub>3</sub> [47], KTiOPO<sub>4</sub> [48], LiB<sub>3</sub>O<sub>5</sub> [49], and  $\beta$ -BaB<sub>2</sub>O<sub>4</sub> [45]. Especially the latter three materials are technologically of utmost importance for high-power laser applications. LiNbO<sub>3</sub> itself, particularly periodically poled LiNbO<sub>3</sub> (PPLN), plays an important role for low-power, tunable frequency conversion.

In order to deal adequately with the features of small polarons in the numerous possible optical applications of LiNbO<sub>3</sub>, it is essential to understand their microscopic structures and the related nonlinear optical properties, which is the aim of this review. LiNbO<sub>3</sub> here serves as reference material due to its variety of small polaron features, the possibility of targeted optical formation of small polarons, and pronounced nonlinearities of the crystal itself.

This article is organized as follows: In chapter 2, the four types of electron and hole polarons are presented from the structural viewpoint allowing for the description of binding by *Holsteins' Molecular-Crystal Model* (MCM) [50]. The groundstate optical features, such as the respective small polaron peak energies and the spectral dependencies, are discussed in Chapter 3 based on an optically induced charge transfer between next-neighboring polaronic sites. The generation of small polarons by optical means is in the focus of chapter 4. Here, band-to-band excitation of electron-hole

pairs, the excitation from extrinsic defect centers and the optical dissociation of bipolarons is presented. The relation of number densities to the appearance of transient absorption is derived. Models for the appearance of a stretched exponential decay within the recombination process are summarized. This chapter is supported by experimental results on the typical transients over the visible and near-infrared spectral range and of ultra-fast spectroscopic studies that reveal the small polaron formation time. Chapter 5 summarizes the microscopic approach of the small-polaron based effect. Besides the appearance of a net current due to a local asymmetry of the  $\text{Nb}_{\text{Li}}$  point defect under investigation, the possibility for the excitation of carriers with energies resonant with bandlike states is discussed. Thereby, ballistic transport to distances over the first coordination sphere become possible. The appearance of large photovoltaic fields is explained by the superposition of coherent and incoherent transport mechanisms with different mobilities. These fields are shown to modulate the index of refraction via the linear electro-optic effect in Chapter 6. Besides, population density gratings of small polarons are modeled and verified by experimental results using ns-pulses for the recording of elementary gratings and holographic spectroscopy. These findings are analyzed in the framework of applications of  $\text{LiNbO}_3$  in the final chapter 7. With frequency conversion as an example, the role of small polarons in optical damage scenario as well as the possibilities to reduce appropriate effects by a detailed knowledge of optical nonlinearities of small polarons are demonstrated, thereby, showing their impact.

## 2 Structure physics of small polarons in lithium niobate

Self-trapped charge carriers were introduced by L. D. Landau in 1933 to explain optical properties of alkali halides [51]. According to T. Holstein, self-trapping may occur if the charge carrier (electron or hole) distorts the surrounding lattice via Coulomb and short-range interactions [50, 52]. The displacements of the surrounding ions leads to a potential well in which the otherwise free carrier is localized. The quasiparticle composed of the self-trapped carrier and the accompanying pattern of ionic displacements is called polaron [53]. With increasing coupling strength the polaronic radius shrinks, eventually restricting the potential well to a single lattice site, a so-called *small polaron*. Following the definition of David Emin [1], small polarons thus are characterized by strong coupling as it is the case for large polarons and are distinguished from weakly-coupled polarons.

### 2.1 Holsteins' Molecular-Crystal Model (MCM)

It is possible to describe the main features of this quasiparticle using Holstein's one-dimensional Molecular-Crystal Model (MCM) [50]. This model describes the polaron localized at one cation site in a three-dimensional crystal by an appropriate relaxation of its neighbor ions. Therefore, the most simple conceivable arrangement is the following: Instead of a number of neighbors in a real crystal only two of them are assumed, forming a one-dimensional chain. The polaron, localized at site  $p$ , is then

assumed to be stabilized by a change of the distance of the partners in the molecule,  $q_p$ . This concept is depicted in Fig. 1.

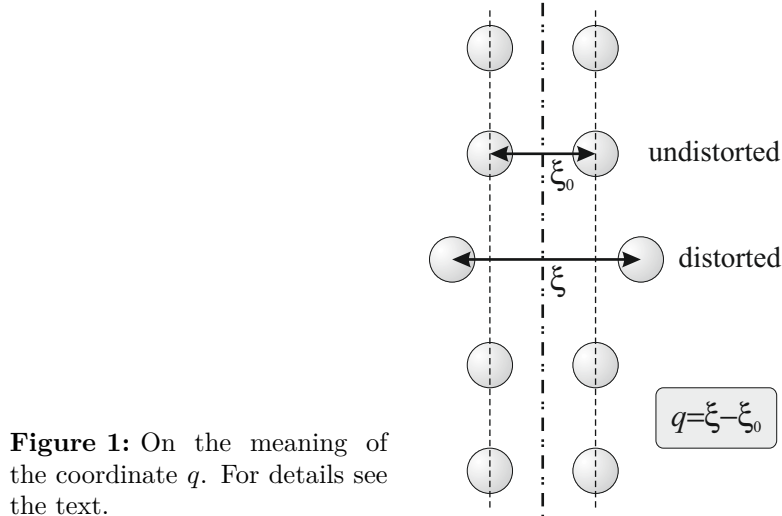


**Figure 1:** On the meaning of the coordinate  $q$ . For details see the text.

The results of the one-dimensional model can be transferred to realistic three-dimensional crystals [54] using slight corrections which will be marked upon occurrence. The following considerations (see Fig. 2) are essentially based on the works of Holstein [50,52], Appel [55], and Austin and Mott [54]. For more detailed studies the reader is referred to those articles.

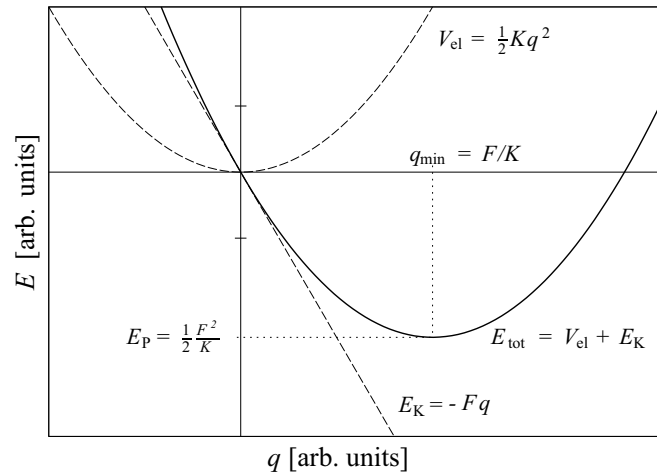


**Figure 2:** Sketch of the energies relevant for the small polaron problem (after [50,52,54])

One may begin with a situation where an excess electron is placed at an originally undistorted site ( $q = 0$ ). The electronic energy at  $q$  is then changed by  $E_K = -Fq$ , where  $F$  denotes the part of the electron-lattice coupling force that consists of short-range interaction [56]. At the same time the elastic energy is enhanced due to the induced lattice distortion:  $V_{\text{el}} = 1/2Kq^2$ . The total energy of the system is given as the sum of electronic and elastic energies  $E_{\text{tot}} = 1/2Kq^2 - Fq$ . By minimizing this energy ( $q_{\text{min}} = F/K$ ) one obtains the *polaron energy*  $E_P$ :

$$E_{\text{min}} = -\frac{1}{2} \frac{F^2}{K} = -E_P. \quad (1)$$

The case of strong electron-phonon coupling is present, i.e. a small polaron, if the energy  $E_P$  becomes large. As derived, the electron can be localized at any site of the crystal lattice.

Real crystals contain intrinsic and/or extrinsic point defects, whose formal charge may differ from that of the regular sites. The energy of a polaron at such a site is additionally decreased by  $-E_C$ . Due to different ionic environments the values of the polaronic force constant may slightly differ from those of the above addressed situation, labeled by  $F'$  instead of  $F$ . In this case, the polaron energy becomes

$$E_{\min,D} = -E'_p - E_C = -E_{GP} \quad (2)$$

The resulting state is often referred to as *bound small polaron* or simply bound polaron, while the former is called *free polaron* with the polaron energy  $E_{FP} = E_P$ . The electrons localized in this way can nevertheless move in the crystal lattice, taking the induced lattice distortion with them. At room temperature, the charge transport proceeds via hopping transitions (*incoherent motion* [1, 7]).

As to the situation of  $\text{LiNbO}_3$ , Faust et al. found that the conductivity can be well described by the hopping model for temperatures down to 150 K [57]. Again, MCM can be applied for a detailed description of the polaronic hopping transport. Consideration of thermally activated transport yields that the thermal activation energy equals half the polaron binding energy

$$E_a = E_{FP}/2. \quad (3)$$

We note that it was shown by Austin and Mott that in real ionic crystals the activation energy may be less than  $E_{FP}/2$  [54].

## 2.2 Small free and bound polarons in $\text{LiNbO}_3$

To date three different types of small electron polarons and one type of small hole polaron have unambiguously been identified in  $\text{LiNbO}_3$  [4, 57, 58].

It has been proposed in earlier works that the features described here and in the following sections may be explained by electrons located at or in oxygen vacancies,  $V_O$  [11, 59]. However, measurements of the mass density [60] and ESR results [61] were highly incommensurate with the oxygen-vacancy model and it was disproved for  $\text{LiNbO}_3$  (see Sec. 6.2 in Ref. [4], see also Refs. [58, 62]). In addition, another electron quad-polaronic center, the so-called  $Q$ -polaron, has been proposed in order to describe the high-frequency absorption in reduced  $\text{LiNbO}_3$  [63], but has been disproved meanwhile (see Sec. 6.1 in Ref. [4]). Therefore, no further comments are given concerning this point.

All types of small polarons result from the intrinsic defect structure of  $\text{LiNbO}_3$  that - although complex - has been modeled from first principles in very recent articles by *Li et al.* [64, 65]. A sketch of the polarons addressed in this work is given in Fig. 3.

The *free small electron polaron* (FP) in  $\text{LiNbO}_3$  consists of an electron that is localized at a regular Nb site [57]. It is represented throughout this work as  $\text{Nb}_{\text{Nb}}^{4+}$  or free polaron and is the most shallow electron trap known in  $\text{LiNbO}_3$ . Faust et al. could identify the free polaron only in samples doped with Mg or Zn above the

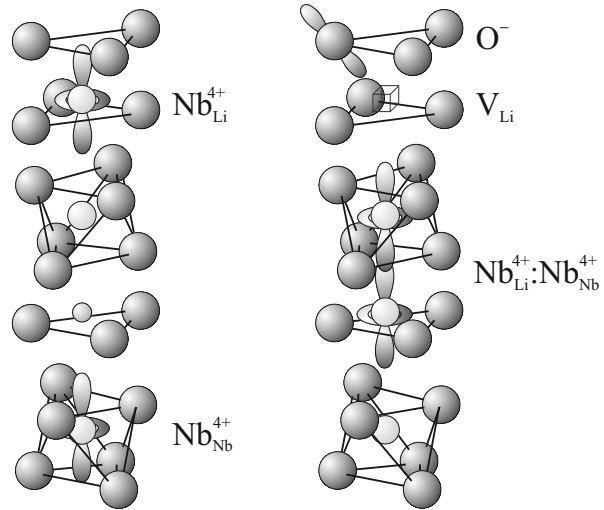


**Figure 3:** Structure of  $\text{LiNbO}_3$  with the intrinsic defects  $\text{Nb}_{\text{Li}}$  and  $\text{V}_{\text{Li}}$ . The related small polarons are depicted using their idealized orbital structure. Lattice distortions are not shown.

optical-damage resistance threshold [57]. This is due to the fact that in samples below the threshold deeper traps,  $\text{Nb}_{\text{Li}}$ , are still present.

*Bound small electron polarons* (GP),  $\text{Nb}_{\text{Li}}^{4+}$  or simply bound polarons, show properties similar to  $\text{Nb}_{\text{Nb}}^{4+}$ , except at higher binding and absorption energies [58]. This type of electron polaron is found in congruently melting  $\text{LiNbO}_3$ , in reduced samples by exposure to visible or ultraviolet light at cryogenic temperatures, or at high temperatures without illumination [58,61,66]. In both cases they are metastably created upon optical or thermal dissociation of bipolarons. Another possibility to obtain bound polarons in unreduced crystals is illumination with intense pulsed light [9, 67, 68]. Bound polarons further play a decisive role for the photorefractive effect in  $\text{LiNbO}_3$  and  $\text{LiNbO}_3:\text{Fe}$ . They substantially affect the photoconductivity and are in fact the shallow photosensitive level in the two-center model [69]. Two-color holography is possible utilizing these shallow traps [70].

The ground state of electrons in reduced congruently melting  $\text{LiNbO}_3$  is the *bound small bipolaron* (BP),  $\text{Nb}_{\text{Li}}^{4+}:\text{Nb}_{\text{Nb}}^{4+}$  [66]. In the presence of bipolarons a largely enhanced dark conductivity and photoconductivity is found [71]. The related activation energies are evaluated and discussed in Ref. [4]. Light illumination or elevated temperatures lead to a reversible dissociation of bipolarons in favor of metastable bound  $\text{Nb}_{\text{Li}}^{4+}$  polarons [58,61,66]. While the former mechanism can be applied for two-color holography in reduced undoped  $\text{LiNbO}_3$  [41], the latter is mainly responsible for the conductivity in reduced samples [71]. Deducing the thermal activation energy and the bipolaron binding energy from experimental data is not as straightforward as for single polarons. This is due to the fact that, in contrast to the above given model, this is a two-site bipolaron (*Heitler-London bipolaron*) [72]. It could, however, be shown that the difference between the binding energy of the bipolaron and that of two bound polarons is about 0.27 eV [66].

*Bound small hole polarons* (HP),  $\text{O}^-$ , are defect electrons located at an oxygen ion in the vicinity of a cation vacancy, most probably  $\text{V}_{\text{Li}}$  [5]. They can be created in  $\text{LiNbO}_3$  by electron- and X-ray irradiation [73,74], as well as by two-photon processes of intense green light [68]. Since the spatial relation of the Li vacancies among themselves and to  $\text{Nb}_{\text{Li}}$  antisite defects is not known, the contribution of hole polarons to

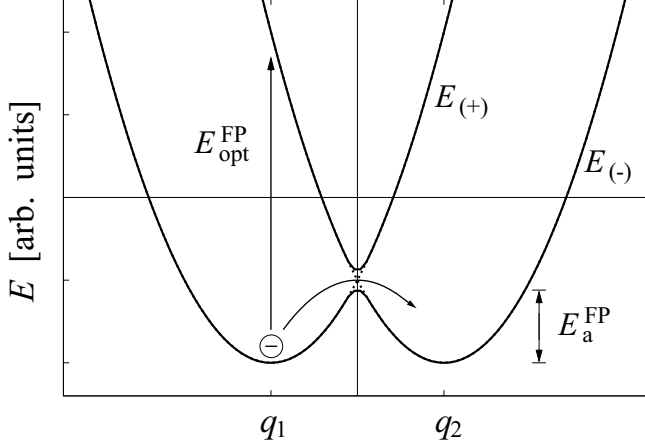


**Figure 4:** Optically induced transport of small free polarons

the thermally and optically activated charge transport in  $\text{LiNbO}_3$  is to date still unclear. Therefore, no definite values can be given for the hole polaron binding energy and thermal activation energy.

### 3 Optical absorption features of small polarons

#### 3.1 Modelling

The optical absorption features of small polarons can be attributed to their optically activated transport. Assuming that the electron is initially at site 1 ( $q_1$ ) (cf. Fig. 4), the minimum energies for free polarons are given by

$$E_1 = \frac{1}{2}Kq^2 - Fq_1 \quad \text{and} \quad E_2 = \frac{1}{2}Kq^2 - Fq_2 = 0, \quad (4)$$

since  $q_2 = q_{\min,2} = 0$  without the excess electron. For frequencies  $\omega$  exceeding the phonon frequencies ( $\omega \gg \omega_{\text{LO}}$ ) the Franck-Condon principle states that the lattice distortion does not change essentially during an electronic transition. Therefore, one has only to consider the electronic energy, with the coordinates of minimum total energy,  $q_{\min,1} = F/K$  and  $q_{\min,2} = 0$ , unchanged. One then finds the energy for a photon-assisted hopping of free polarons:

$$E_{\text{FP}}^{\text{opt}} = E_{\min}(q_2 \rightarrow q_1) \quad (5)$$

$$= E_{\text{C},2}(q_2 = q_{\min,2}) - E_{\text{C},1}(q_1 = q_{\min,1}) \quad (6)$$

$$= \frac{F^2}{K} = 2E_{\text{FP}}. \quad (7)$$

This energy corresponds to the vertical transition depicted in Fig. 4.

For a bound polaron the electronic energy at the initial site has the additional perturbation  $-E_{\text{C}}$ . The energy required for the photon-assisted hopping of bound polarons reads

$$E_{\text{opt}}^{\text{GP}} = \frac{F^2}{K} + E_{\text{C}} = 2E_{\text{FP}} + E_{\text{C}} \quad (8)$$

Again this energy can be ascribed to the vertical transition from initial to final potential, that now differ in their minimum energy. The frequency dependence of the AC transport has initially been derived from the MCM by Reik and Heese [75]. Subsequent authors [3, 6, 7, 76] found that in the classical limit ( $2k_B T > \hbar\omega_{LO}$ ) the conductivity related to polarons can be described by

$$\sigma_{\text{pol}}(\omega, T) = Ne\mu_0^{\text{na}} \frac{k_B T}{\hbar\omega} \exp\left[-\frac{(E_{\text{opt}}^{\text{P}} - \hbar\omega)^2}{8E_{\text{FP}}^* k_B T}\right] \quad (9)$$

$$\mu_0^{\text{na}} = g \frac{ea^2}{k_B T} W_0^{\text{na}}, \quad (10)$$

$$W_0^{\text{na}} = \frac{J^2}{\hbar} \left(\frac{\pi}{4E_a k_B T}\right)^{\frac{1}{2}} \quad (11)$$

Here,  $N$  is the number density of polarons,  $a$  is the hopping distance,  $g$  is a dimensionless number of order 1, and  $\mu_0^{\text{na}}$  and  $W_0^{\text{na}}$  are the nonadiabatic polaron mobility and hopping rate, respectively. The energy  $E_{\text{opt}}^{\text{P}}$  has to be replaced by the respective maximum energy for optical transitions of free and bound polarons,  $E_{\text{opt}}^{\text{FP}}$  or  $E_{\text{opt}}^{\text{GP}}$ , and  $E_{\text{FP}}^*$  is  $E_{\text{FP}}$  or  $E'_{\text{FP}}$ . The optical absorption coefficient  $\alpha$  is

$$\alpha_{\text{pol}}(\omega, T) = \frac{1}{n\epsilon_0 c} \sigma_{\text{pol}}(\omega, T) \quad (12)$$

with  $c$  being the velocity of light,  $n$  the refractive index of the material, and  $\epsilon_0$  the vacuum permittivity. The resulting absorption band resembles a Gaussian curve, with a prefactor  $1/\omega$ , centered at  $\omega_{\text{max}} = E_{\text{opt}}^{\text{P}}/\hbar$ , with a full width at half maximum

$$\omega_{\text{FWHM}} \approx 4\sqrt{2\ln[2]E_{\text{FP}}^* k_B T} \quad (13)$$

that is more pronounced at lower frequencies ( $\omega < \omega_{\text{max}}$ ).

### 3.2 Experimental fingerprints

Comparisons with experimental data, e.g., for free polarons in  $\text{LiNbO}_3$  [57], show that the theory presented above is probably oversimplified. One possible reason may be that here only transitions from the electronic ground state at the initial site to the ground state at the final site are considered [5]. The orbital structure of polarons including their bound excited states as well as excitation to states with ballistic transport is neglected.

The absorption spectra of the individual electron and hole polarons in  $\text{LiNbO}_3$  are modeled by means of the spectral dependence of the respective absorption cross section in Fig. 5 according to Ref. [77].

The *free polaron* is characterized by a broad optical absorption band in the near infrared spectral range, centered at about  $E_{\text{opt}}^{\text{FP}} = 1.0 \text{ eV}$  ( $\cong 1280 \text{ nm}$ ) - besides showing typical ESR spectra [57, 79]. At the same time, measurements of the electrical conductivity yield an activation energy for phonon-assisted hopping transport,  $E_a^{\text{FP}} = 0.2 - 0.3 \text{ eV}$ . These values are in line with the theory for the free small polaron; the corresponding polaron binding energy is  $E_{\text{FP}} = 0.5 \text{ eV}$  [57]. However,

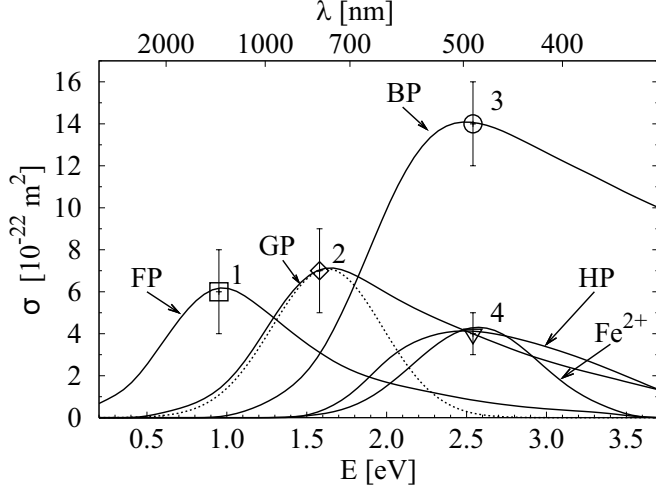


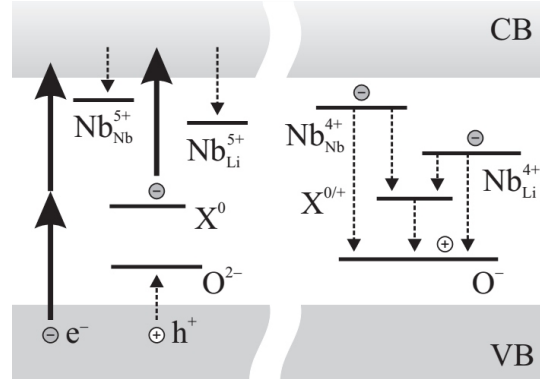
**Figure 5:** Spectral dependence of the absorption cross section of small free (FP) and bound (GP) electron polarons, of bipolarons (BP) and of small hole polarons (HP). The spectral fingerprint of  $\text{Fe}_{\text{Li}}^{2+}$ , that can be described by small polaron theory, as well, is depicted for reasons of comparison. Note, that the absorption cross section of BP is about two times higher than those of the single polarons because the oscillator strength is proportional to the number of electrons in an absorbing system. Reproduced with permission [78] from Ref. [77].

detailed investigations of the absorption spectra indicate a slight additional binding of about 0.1 eV, influencing the optical absorption at low temperature [57]. One possible reason could be a location of  $\text{Nb}_{\text{Nb}}^{4+}$  in the vicinity of a  $\text{Mg}^{2+}$  (or respective impurity) ion on  $\text{Li}^+$  site [62]. The electronic charge transport in  $\text{LiNbO}_3$  proceeds via  $\text{Nb}^{4+}$  [62]. There is strong evidence that these  $\text{Nb}^{4+}$  ions are mainly existing in form of free polarons, and that the transport is essentially of thermally activated hopping type [18, 62]. *Bound polarons* are accompanied by an absorption band centered at  $E_{\text{opt}}^{\text{GP}} = 1.6 \text{ eV}$  ( $\cong 760 \text{ nm}$ ), which implies a polaron binding energy  $E'_{\text{FP}} \approx 0.55 \text{ eV}$  and the additional term  $W_{\text{D}} \approx 0.5 \text{ eV}$  [58, 67]. The thermal activation energy may be estimated to be  $E_{\text{a}}^{\text{GP}} \approx 0.65 \text{ eV}$ . *Bipolarons* feature a broad absorption band, which is centered at  $E_{\text{opt}}^{\text{BP}} = 2.5 \text{ eV}$  ( $\cong 500 \text{ nm}$ ) and covers the whole visible spectral range, giving the samples a grayish color [61]. The BP absorption cross section is about two times higher than those of the single polarons because the oscillator strength is proportional to the number of electrons in an absorbing system. The *hole polaron* exhibits a broad absorption band in the visible range, centered at  $E_{\text{opt}}^{\text{HP}} \approx 2.5 \text{ eV}$  ( $\cong 500 \text{ nm}$ ) [73]. A detailed ESR and optical investigation of the hole-polaron absorption is hindered by the band of  $\text{Nb}_{\text{Li}}^{4+}$ , which always appeared in the cited works. The optical absorption of  $\text{O}^-$  is described by a photon-assisted hopping of the hole between equivalent adjacent  $\text{O}^{2-}$  ions, which are located around the Li vacancy, thus restricting the hole polaron to one single  $\text{V}_{\text{Li}}$  [5].

## 4 Optical generation of small polarons

Generation of small polarons can be performed by optical means using different photon energies in the UV/VIS spectral ranges and flux densities; the most prominent generation paths are summarized in the following and are depicted in Figs. 6, 7. It is noteworthy to state that optically generated small polarons always represent non-equilibrium states - contrary to thermally stable small polarons, such as e.g. by thermal pre-treatment that enhances the presence of carriers in the crystal bulk. Thus, optically generated small polarons vanish after a specific small polaron lifetime

**Figure 6:** Generation and relaxation of small polarons in nominally undoped LiNbO<sub>3</sub>. Left: The driving process of polaron formation is band-to-band excitation, resulting in electron-hole pairs. According to the band gap of 3.8 eV, two-photon absorption dominates this process in the visible and near-infrared spectral range. Carrier localization results in the formation of small free Nb<sub>Nb</sub><sup>4+</sup>, small bound Nb<sub>Li</sub><sup>4+</sup>, and small O<sup>-</sup> hole polarons. At low intensities, the contribution of carriers excited via single-photon absorption from extrinsic defect centers X<sup>0</sup> may be considered until these are depopulated. Right: Recombination paths are imprinted by electron-hole recombination of FP and GP with HP. The recharging of the extrinsic X<sup>0/+</sup> center may represent an intermediate step depending on the transfer probabilities.



defining the loss of the localized carrier, i.e. they are metastable.

For generation, the presence of charge carriers, holes or electrons, is inevitable, which - in principle - can be performed in nominally undoped LiNbO<sub>3</sub> via one-photon absorption from the valence to the conduction band (band-to-band transition). However, due to the large band gap of 3.8 eV, this type of small polaron generation requires ultraviolet light (< 325 nm) available from excimer lasers. In this case, small polaron generation and interband photorefraction may superimpose [80, 81].

More prominent is the mechanism depicted in Fig. 6 first described by *Schirmer et al.* [68] for the generation of small bound polarons. Accordingly, electrons are excited from the valence band to the conduction band by a two-photon absorption (TPA) process. They are then trapped at Nb<sub>Li</sub> antisite defects to form small bound Nb<sub>Li</sub><sup>4+</sup> polarons. The remaining holes in the valence band become localized as O<sup>-</sup> hole polarons in the vicinity of lithium vacancies [5, 58, 68]. Upon their recombination the light-induced absorption changes totally vanish in the dark.

The formation time of small bound polarons has been systematically studied by *Sasamoto et al.* [17] using femtosecond pump-probe spectroscopy and nominally undoped LiNbO<sub>3</sub>. Pulses with durations of 80 fs at a wavelength of 400 nm allowed for the statement that small bound polarons are formed within a timescale of 100 fs, that is consistent with the results of other authors [13, 37, 82–84]. For details see experimental section (Chapter 4.2) below.

A similar model and study related to small free Nb<sub>Nb</sub><sup>4+</sup> polaron formation was introduced by *Qiu et al.* [16]. Accordingly, electrons excited via two-photon absorption are first generated (*hot carriers*); then they relax to the lower edge of the conduction band by energy dissipation to the lattice (thermalization) where small free Nb<sub>Nb</sub><sup>4+</sup> polarons (and/or Nb<sub>Li</sub><sup>4+</sup> bound polarons in crystals grown from the congruently melting composition) are generated. The transfer to Nb<sub>Li</sub><sup>4+</sup> bound polarons may also occur upon thermally activated transport via Nb<sub>Nb</sub> centers. It is noteworthy, that two-photon absorption overlaps the possible transient signals of hot carriers, and thus may not be observed experimentally in LiNbO<sub>3</sub> [83]. Nevertheless, the validity of these models has been studied by femtosecond experiments in several groups in the

last decade yielding several important measures. For instance, the efficiency of the carrier generation by TPA is well determined using laser pulses with duration of 80 fs up to 10 ns (values of  $\beta \approx (1.5 - 4)$  GW/mm at 532 nm are reported and summarized in Chapter 4.2). Further studies are in progress.

The optical generation of small polarons in nominally pure, thermally reduced LiNbO<sub>3</sub> has been addressed by *Jermann et al.* [69]. They found that Nb<sub>Li</sub><sup>4+</sup>:Nb<sub>Nb</sub><sup>4+</sup> bipolarons are dissociated by green light such that Nb<sub>Li</sub><sup>4+</sup> bound polarons are formed (cf. Fig. 7). In the dark, the bound polarons recombine and form bipolarons again [69]. At that time, the role of Nb<sub>Nb</sub><sup>4+</sup> free polarons was not analyzed [69]. In this process, it is very much likely, that the electron localized at the regular Nb<sub>Nb</sub> site is optically transferred to a next-neighboring Nb<sub>Nb</sub> site, i.e. that the small bound GP remains at its position. *Merschjann et al.* were able to deconvolve the appearance

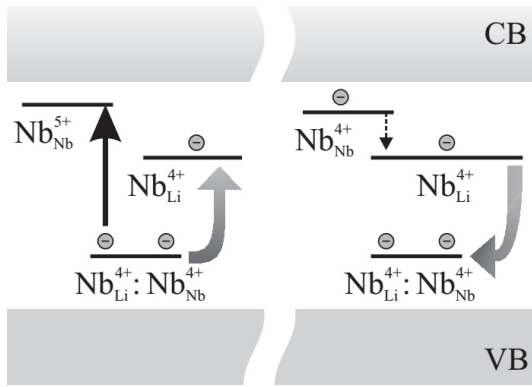


**Figure 7:** Generation and relaxation of small polarons in thermally reduced LiNbO<sub>3</sub>. Left: The Nb<sub>Li</sub><sup>4+</sup>:Nb<sub>Nb</sub><sup>4+</sup> bipolaron is optically dissociated and, thereby, a small free Nb<sub>Nb</sub><sup>4+</sup> and bound Nb<sub>Li</sub><sup>4+</sup> polaron are formed. Right: by incoherent hopping of both, FP and BP, the two small polarons recombine to a bipolaron.

and recombination dynamics of free small Nb<sub>Nb</sub><sup>4+</sup> polarons upon bipolaron gating in thermally reduced LiNbO<sub>3</sub> by means of time-resolved spectroscopy and ns-laser pulses at 2.5 eV [15]. Its formation time was estimated to values below 100 fs using fs-spectroscopy [16, 85].

## 4.1 Light-induced small polaron absorption

### 4.1.1 Fundamental description

The formation of small polarons and their subsequent dynamical behavior upon light exposure is reflected by the build-up of a transient absorption, i.e. a small polaron absorption that is proportional to the product of number density and absorption cross section (cf. Fig. 5). This type of optically induced transient absorption often is called *light-induced absorption*. The total absorption of a nominally undoped LiNbO<sub>3</sub> at a specific optical frequency thus is composed of a fundamental absorption  $\alpha_0(\omega)$ , and the sum of the absorptions of all types of small polarons,  $\alpha_i(\omega)$ . The fundamental absorption stems from electronic transitions between valence band and conduction band. One assumes here that  $\alpha_0(\omega)$  does not depend on the experimental conditions (time, temperature, illumination, etc.), but solely on the light frequency  $\omega$ . On the other hand the absorption of the different polaronic centers involved may well depend on time, temperature and illumination features (photon energy, intensity,

pulse duration, light polarization):

$$\alpha(\omega, t) = \alpha_0(\omega) + \sum_i \alpha_i(\omega, t). \quad (14)$$

Note that the dependencies of  $\alpha_i$  on  $I$  is not explicitly given in this formula. However, experimental results will show that these dependencies are of crucial importance and have been omitted here only for reasons of clarity.

The absorption by photosensitive centers is the product of the respective absorption cross sections  $\sigma_i(\omega)$  and their time-dependent number densities  $N_i(t)$ :

$$\alpha_i(\omega, t) = N_i(t)\sigma_i(\omega) \quad (15)$$

One may split  $N_i(t)$  into a time-independent and a time-dependent part. This leads to

$$\begin{aligned} \alpha_i(\omega, t) &= [N_{0,i} + N_{\text{li},i}(t)]\sigma_i(\omega) \\ &= \alpha_{0,i}(\omega) + \alpha_{\text{li}}(\omega, t) \end{aligned} \quad (16)$$

where  $\alpha_{\text{li}}(\omega, t)$  is the time-dependent light-induced absorption change (or simply light-induced absorption) for the respective center. By combining these equations, one obtains the formula for the time-dependent total absorption, namely

$$\begin{aligned} \alpha(\omega, t) &= \alpha_0(\omega) + \sum_i \alpha_{0,i}(\omega) + \sum_i \alpha_{\text{li},i}(\omega, t) \\ &= \alpha(\omega) + \alpha_{\text{li}}(\omega, t) \end{aligned} \quad (17)$$

Thus the total absorption of the crystal can be described as a sum of the steady-state absorption  $\alpha(\omega)$  and the light-induced absorption  $\alpha_{\text{li}}(\omega, t)$ . The latter is of utmost importance for the study or impact of small polarons in  $\text{LiNbO}_3$ .

#### 4.1.2 Thermally activated decay

According to the two-center model [12] the relaxation of light-induced absorption changes should follow a mono-exponential law, i.e., the decay rate is directly proportional to the number density of metastable centers. However, time-resolved measurements of  $\alpha_{\text{li}}(t)$  in  $\text{LiNbO}_3$  show that this is not the case at all [9, 47, 67, 69]. The observed decay spectra are in general best described by an empirical law of stretched exponential functions, named after Kohlrausch, Williams and Watts [86–88]. This so-called KWW function is given by

$$\alpha_{\text{li}}(t) = \alpha_{\text{li}}^{(0)} \cdot \exp \left[ -(t/\tau)^\beta \right] \quad (18)$$

with the characteristic absorption  $\alpha_{\text{li}}^{(0)}$ , the characteristic lifetime  $\tau$ , and the stretching factor  $0 \leq \beta \leq 1$ , where  $\beta \equiv 1$  denotes the case of a mono-exponential relaxation. Also sums of KWW functions are used to describe the decay of  $\alpha_{\text{li}}(t)$ :

$$\alpha_{\text{li}}(t) = \sum_{i=1}^n \alpha_{\text{li}}^{(i)} \cdot \exp \left[ -(t/\tau)^\beta \right] \quad (19)$$

It should be noted, here, that in most cases the parameter  $\alpha_{\text{li}}^{(0)}$  is not identical with the experimentally determined amplitude of the light-induced absorption  $\alpha_{\text{li}}^{\text{max}} = \alpha_{\text{li}}(\omega, t = 0)$  as a result of limited temporal resolution in ns-pump-probe experiments (see also Ref. [67]). Furthermore, the characteristic lifetime  $\tau$  does not represent one single lifetime of the metastable state. It is rather to be considered as a *mean value* of many different lifetimes, thus Eq. 18 may be seen as a superposition of an infinite number of different mono-exponential decays with a certain distribution of lifetimes.

While a general answer to the underlying physics of stretched relaxation dynamics in LiNbO<sub>3</sub> could not yet be given, some approaches do indeed exist. *Berben et al.* were the first to apply Eq. 18 to the decay of  $\alpha_{\text{li}}(t)$  in LiNbO<sub>3</sub>:Fe [9]. They suggested a distance-dependent charge transport in such a way that charge carriers take the distance between the initial shallow center and the final deep trap in one hopping transition. According to this model the probability for the jump should depend on the distance  $r$  between initial and final site, obeying a power law,  $p \propto r^{-x}$ , where  $x$  is an empirical parameter. Numerical simulations [9] showed that the resulting decay curves may well be described by Eq. 18. However, the parameter  $x$  could not be deduced from first principles [9]. Later, *Wevering et al.* found a mathematical description, based on the aforementioned idea, that lead indeed to a stretched exponential function, namely  $\alpha_{\text{li}}(t) \propto \exp[-(t/\tau)^{k/3}]$ , where  $k$  is an integer [47]. Nevertheless, the values for  $k$  have to be chosen empirically, without knowing their physical meaning. Another approach has been given by *Sturman et al.* [89]. This model is based on a random walk of nearest-neighbor hopping transitions. After several hopping processes the carrier finally recombines with a trap. Thereby a stretched-exponential relaxation is not obtained directly. However, if the distances between nearest neighbors are randomly distributed, like e.g., in an amorphous material, a numerical simulation yields decay curves that are well described by Eq. 18 [89]. It turns out that this feature depends essentially on the distribution of distances, where the longest transition distance mainly determines the lifetime ( $p \propto \exp[-r]$ ). Applied to LiNbO<sub>3</sub>,  $r$  describes the distance between initial and final site of the optically induced transition.

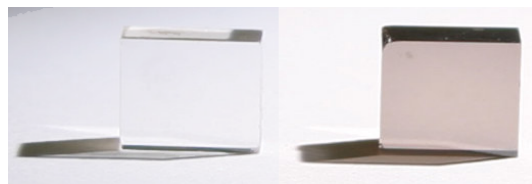
An important step towards a more microscopic understanding of the underlying transport processes was published by *Carnicero et al.* [18] using Monte Carlo simulations. Besides deducing the average, unidirectional transport length in the order of several nanometers (depending on stoichiometry and pump beam intensity, see below), the presence of the *site correlation effect* was introduced. This effect is based on the observation that an optically generated charge carrier, localized as small polaron at a specific lattice site, has a high probability to be captured by its original trap center, i.e. the center where it was excited from. Based on these findings, *Merschjann et al.* continued with systematic studies considering a broad spectrum of experimental studies [90]. In Ref. [19], the effect of *trap saturation* is taken into account additionally, in order to derive an extended microscopic model for the non-exponential relaxation. Thereby it is shown that the relaxation dynamics can be successfully reconstructed without consideration of a structural or energetic disorder. Furthermore, the access to particular microscopic measures such as the lifetime of single hopping events and localized-carrier densities is enabled. A further theoretical approach introduced by *Guilbert et al.* is in preparation [91]; it is the aim to represent a powerful numerical

tool for the modelling of relaxation dynamics for a wide spectrum of experimental parameters, including temperature. Thus, more detailed insight into this complex research field is to be expected.

## 4.2 Experimental examples

Figure 8 shows photographs of two single crystals of  $\text{LiNbO}_3$  grown from a congruent nominally undoped melt via Czochralski growth technique (Crystal Technology, Inc.) as typically prepared for optical studies (e.g. the surface is polished to optical quality). The left sample is as-grown, while the right sample is thermally pre-treated. Thus it features a grayish coloration due to the presence of  $\text{Nb}_{\text{Li}}^{4+}:\text{Nb}_{\text{Nb}}^{4+}$  bipolarons (BP) and small bound  $\text{Nb}_{\text{Li}}^{4+}$  polarons (GP) [19, 20] as a result of chemical reduction.

**Figure 8:** Photographs of nominally undoped (left) and thermally reduced (right)  $\text{LiNbO}_3$ , as used for most of the optical studies in this chapter and chapter 6. The pre-treated sample was kept at elevated temperature of  $(970 \pm 10)$  K at a reduced pressure of  $p < 10^{-4}$  mbar for a duration of 6 h.



### 4.2.1 Number densities of optically generated small polarons

The nonlinear optical properties of optically generated small polarons are proportional to their number density  $N$ , which is strongly dependent on the intensity of the incoming laser pulse. An optical measure for  $N$  is the light-induced absorption  $\alpha_{\text{li}}^{\text{max}}$  being proportional to  $N$  in product with the absorption cross sections. Its dependence as a function of pump beam intensity is depicted in Fig. 9 for nominally undoped (upper) and thermally reduced  $\text{LiNbO}_3$ . The data were collected using a setup for time-resolved pump-multiprobe spectroscopy, described in Refs. [15, 92]. Here, intensities of the pump light  $I_{\text{p}} \leq 760$  GW/m<sup>2</sup> at a wavelength of  $\lambda = 532$  nm were used.

The initial amplitudes are strongly dependent on the pump beam intensity and reflect number densities of small polarons in the order of  $N \approx 10^{23}$  m<sup>-3</sup> considering the absorption cross sections of Fig. 5. The data are given for probe wavelengths of 488, 785 and 1310 nm, thus being close to the maxima of the small polaron absorption features of hole and bi-polarons, of bound bipolarons and of free polarons. Remarkably,  $\alpha_{\text{li}}^{\text{max}}$  grows quadratically as a function of intensity in the nominally undoped sample, that reflects the underlying two-photon absorption process schematically sketched in Fig. 6. In contrast, for thermally reduced  $\text{LiNbO}_3$ ,  $\alpha_{\text{li}}^{\text{max}}(I_{\text{p}})$  saturates at  $\approx 350$  GW/m<sup>2</sup> for all three wavelengths, however, with negative sign for a probe wavelength of 488 nm. This observation can be assigned to the process of bipolaron dissociation: positive values at 785 and 1310 nm refer to the generation of small bound and free polarons, while the negative values at 488 nm are due to the optical dissociation of bipolarons. Furthermore, as the number density of BP is limited, the number density of generated small polarons must saturate. In particular, the number density of generated small polarons must be equivalent to the number density of

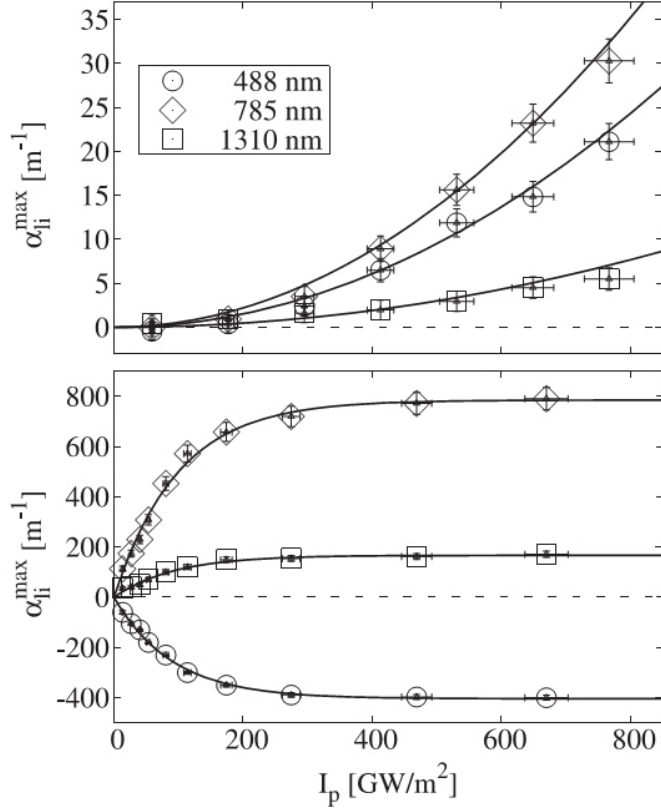


**Figure 9:** Intensity dependency of the maximum optically induced absorption due to small polarons in nominally undoped (upper) and thermally reduced LiNbO<sub>3</sub> (lower) for the three probe wavelengths 488, 785, and 1310 nm at room temperature. Reproduced with permission [93] from Ref. [92].

dissociated bipolarons. Taking the differences in the absorption cross sections into account, but also the spectral overlap of the particular small polaron features at the probing wavelength, it is possible to deduce the number densities of the generated small polarons [77], as depicted in table 1.

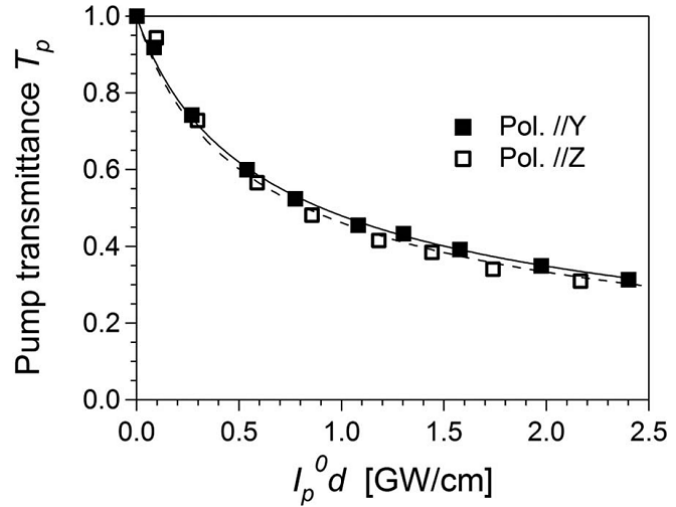
	$N(10^{22} \text{ m}^{-3})$	$N/N_{\text{sites}}$	$\sigma(10^{-22}) \text{ m}^2$	$\lambda(\text{nm})$	Ref.
FP	$30 \pm 5$	$1.5 \times 10^{-5}$	$6 \pm 2$	1310	
GP	$12 \pm 3$	$6.0 \times 10^{-4}$	$7 \pm 2$	785	[14,22,23]
BP	$70 \pm 8$	$3.5 \times 10^{-3}$	$14 \pm 2$	488	
HP	$30 \pm 5$	$3.8 \times 10^{-4}$	$4 \pm 1$	488	
Fe <sub>Li</sub> <sup>2+</sup>	$2 \pm 1$	–	$4.5 \pm 0.8$	488	[20,31]

**Table 1:** Estimated number densities (saturation, ns-pulse experiments) and absorption cross sections for the different kinds of photochromic centers. For bipolarons the number density in the dark is given. Reproduced with permission [94] from Ref. [77].

The efficiency of the two-photon absorption process thus determines the number density of excited carriers, and subsequent formation of small polarons; its measure is the two-photon absorption coefficient  $\beta$  that can be obtained experimentally by means of pump beam transmittance as a function of pump beam intensity or via  $z$ -scan technique [95]. The values of  $\beta$  typically are in the order of a few cm/GW, so that it is reasonable to use fs- or ps-laser pulses enabling sufficient peak intensities for experimental studies. In order to suppress the influence of intrinsic defects, that are accompanied with a shift of the band edge [96] as well as with absorption features

of small bound polarons, Mg-doped, stoichiometric samples are applied by *Sasamoto et al.* [17]. Fig. 10 shows the results for both, ordinary and extra-ordinary light polarization and the use of 80 fs laser pulses at 400 nm. The experimentally determined

**Figure 10:** Pump transmittance  $T_p$  measured for Mg-doped, stoichiometric LiNbO<sub>3</sub> as a function of the product of pump beam intensity  $I_p^0$  and sample thickness  $d$ . Solid and dashed lines indicate theoretical fitting curves for ordinary light polarization ( $\parallel Y$ ) and extraordinary light polarization ( $\parallel Z$ ), respectively. Reproduced with permission [97] from Ref. [17].



values of  $\beta$  from different authors, congruent crystals and pulse durations from femto- to nanoseconds are summarized in table 2. All data refer to extraordinary light polarization; the values for ordinary light polarization are slightly smaller in the order of 10%.

crystal	wavelength (nm)	pulse duration (fs)	$\beta$ [ $10^{-12}$ (m/W)]	Ref.
stoichiometric:				
Mg-doped LiNbO <sub>3</sub>	400	80	(5.2±0.4)	[17]
congruent:				
LiNbO <sub>3</sub>	≈ 480	240	≈ 3.5	[37]
LiNbO <sub>3</sub>	528.8	7.000	1.5	[98]
LiNbO <sub>3</sub>	532	25.000	2.5	[99]
LiNbO <sub>3</sub>	532	30.000	3.8	[100]
LiNbO <sub>3</sub>	532	55.000	2.1	[101]

**Table 2:** Experimentally determined values of  $\beta$  for various crystals and pulse durations.

We note that  $\beta$  is strongly dependent on  $\lambda$  and grows as a function of photon energy as it is shown e.g. in the study of *Beyer et al.* [37] for the visible spectral range (400 – 800 nm).

#### 4.2.2 Recombination dynamics of optically generated small polarons

Fig. 11 shows a typical temporal decay behavior of the small-polaron based light-induced absorption in the dark, i.e. upon a short ns-laser pulse at a wavelength of 532 nm, exemplarily for thermally reduced LiNbO<sub>3</sub> (cf. right sample in Fig. 8). The dominating process is the optical dissociation of Nb<sub>Li</sub><sup>4+</sup>:Nb<sub>Nb</sub><sup>4+</sup>-bipolarons as depicted in Fig. 7(left half), i.e. small free Nb<sub>Nb</sub><sup>4+</sup> and bound Nb<sub>Li</sub><sup>4+</sup> polarons are generated. The plot of Fig. 11 covers a regime of 9 time decades, from nanoseconds to seconds,

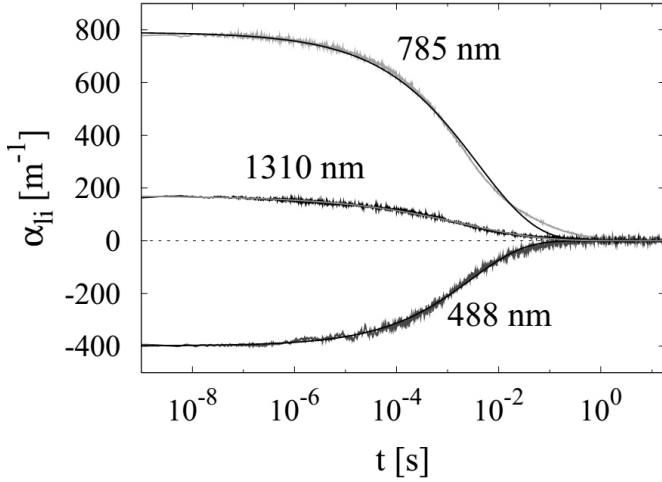


**Figure 11:** Temporal dynamics of the light induced absorption and transparency in a thermally reduced sample of LiNbO<sub>3</sub> upon exposure with a single ns-laser pulse ( $\tau_p = 8$  ns,  $\lambda_p = 532$  nm, intensity  $I_p = 670$  GW/m<sup>2</sup>,  $\mathbf{e} \perp \mathbf{c}$ ). Transient absorption is found at 785 and 1310 nm due to the formation of small bound polarons while transient transparency occurs at 488 nm, that is assigned to the optical dissociation of BP. Besides, the decay dynamics reveal a mean lifetime in the millisecond regime, for all wavelengths. Reproduced with permission [102] from Ref. [92].

whereby for all of the three probe wavelengths close to the maximum absorption features of FP (1310 nm), of GP (785 nm) and of HP as well as BP (488 nm) a similar decay behavior with a characteristic decay time in the order of several milliseconds is found ( $\tau_{\text{FP}} = (2 \pm 1) \times 10^{-3}$  s,  $\tau_{\text{GP}} = (4 \pm 2) \times 10^{-3}$  s, and  $\tau_{\text{BP}} = (3 \pm 1) \times 10^{-3}$  s. As there is no difference between the signal dynamics at 1310 nm and 785 nm, despite a difference in the starting amplitude  $\alpha_{\text{li}}^0$ , it must be concluded that the measurement is not sensitive to the presence of Nb<sub>Nb</sub><sup>4+</sup> polarons, maybe as a result of limited sensitivity in the time regime up to  $\mu$ s and/or the strong signal at 785 nm. According to Fig. 5, there is a distinct amplitude of the GP absorption feature at 1310 nm, such that both signals are due to the time decay of GP. The negative starting amplitude at 488 nm inevitably points to the optical dissociation of BP, that is already terminated in the beginning of the temporal spectrum, i.e. the dissociation time can not be deduced from this measurement and is expected to be in the sub-ps range, as demonstrated in the subsequent chapter. Nevertheless, the recombination time can be determined and coincides within the error bars with the GP decay time. This is reasonable according to Fig. 7. In all these spectra, the appearance of O<sup>-</sup> hole polarons is not found. The shape of all temporal dynamics is well described by stretched exponential functions according to Eq. 18 (solid lines in Fig. 11).

### 4.2.3 Optical formation time of small polarons

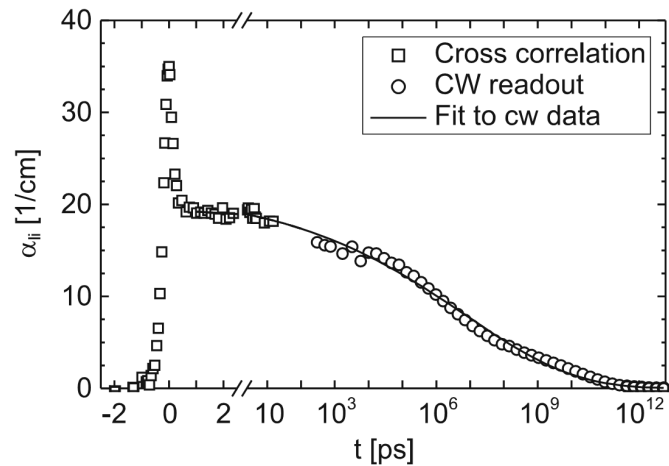
The small polaron formation time has been addressed in literature by a few authors, already [13, 16, 17, 37, 82–84]. As the formation time is expected in the sub-ps-time regime, studies based on ultrafast spectroscopy with sufficiently small pulse durations, i.e.  $\ll 1$  ps, and large pulse energies appropriate for the small absorption features ( $> 1$  mJ) are required inevitably. The first experimental data on the interaction of fs-laser pulses with nominally undoped LiNbO<sub>3</sub> have been published by the research group of *R. T. Williams* [82]. Based on systematic studies, it is meanwhile possible to assign the complex transient signals to specific small polaron species, as summarized in the following.

The formation time of small free Nb<sub>Nb</sub><sup>4+</sup> polarons at room temperature has been determined by *Qiu et al.* in Ref. [16] to 110 fs. Here, Mg-doped LiNbO<sub>3</sub> crystals

were studied in order to suppress the strong absorption feature of small bound  $\text{Nb}_{\text{Li}}^{4+}$  polarons (cf. Fig. 5). Based on these findings, *Sasamoto et al.* performed a systematic study on congruently melting and stoichiometric Mg-doped  $\text{LiNbO}_3$ , both for ordinary and extraordinary light polarization, and compared the results with appropriate nominally undoped samples. The small polaron formation time below 100 fs was verified; additionally, for the case of stoichiometric Mg-doped  $\text{LiNbO}_3$ , an increase of the number density of excited electrons of up to  $N_{\text{el}} \sim 1.2 \times 10^{24} \text{ m}^{-3}$  was found being well below the typical number density of  $\text{Nb}_{\text{Li}}^{5+}$  antisite defects in congruently melting  $\text{LiNbO}_3$  ( $\sim 30 \times 10^{24} \text{ m}^{-3}$ ). Furthermore,  $N_{\text{el}}$  is large in comparison with the small polaron number density of  $N \approx 10^{23} \text{ m}^{-3}$  (s. previous chapter). Thus it is concluded, that only a fraction of optically excited carriers are trapped as small free polarons.

Fig. 12 shows the formation and relaxation dynamics of small bound  $\text{Nb}_{\text{Li}}^{4+}$  polarons in the time regime from 0.24 picoseconds until 1 second after the excitation pulse by *Beyer et al.* according to Ref. [13]. For this study, congruently grown, undoped

**Figure 12:** Light-induced absorption  $\alpha_{\text{li}}$  versus the pump-probe delay  $t$  detected at the wavelengths  $\lambda_r = 776 \text{ nm}$  up to 15 ps and  $\lambda_r = 785 \text{ nm}$  starting 300 ps after excitation with pump light of the wavelength  $\lambda_p = 388 \text{ nm}$  and the peak intensity  $I_p^0 \approx 170 \text{ GW/cm}^2$ . The light polarization is extraordinary for pump and probe light. Around  $t = 0$  the time scale is linear; for the long-term evolution the scale is logarithmic, starting from  $t = 3 \text{ ps}$ . Reproduced with permission [103] from Ref. [13].



$\text{LiNbO}_3$  samples were used and studied in a pump-probe experiment described in Ref. [83] using 240 fs pulses at 388 nm. The data show a pronounced peak around  $t = 0 \text{ ps}$ , that is attributed to two-photon absorption. Within this peak, the build-up of a transient absorption signal develops at a probing wavelength close to the maximum absorption feature of  $\text{Nb}_{\text{Li}}^{4+}$ ; a first plateau is reached below 400 fs. The further decay follows a stretched exponential behavior over ten time decades. The spectra are inevitably assigned to  $\text{Nb}_{\text{Li}}^{4+}$  due to the spectral, intensity and time dependency.

## 5 Optical excitation from polaronic centers

The optical excitation from polaronic centers has already been addressed in chapter 3. These considerations, however, were restricted to the simplified model of an optical transfer between next-neighboring polaronic sites. For the particular case of  $\text{LiNbO}_3$ , this model must be refined as (i) the local structure of an initial polaronic site is surrounded by several final atomic sites, that allow for an optical transfer into different directions and (ii) the optical excitation from a polaronic site may result in coupling to extended bandlike states, depending on the energy of the exciting photon. Both

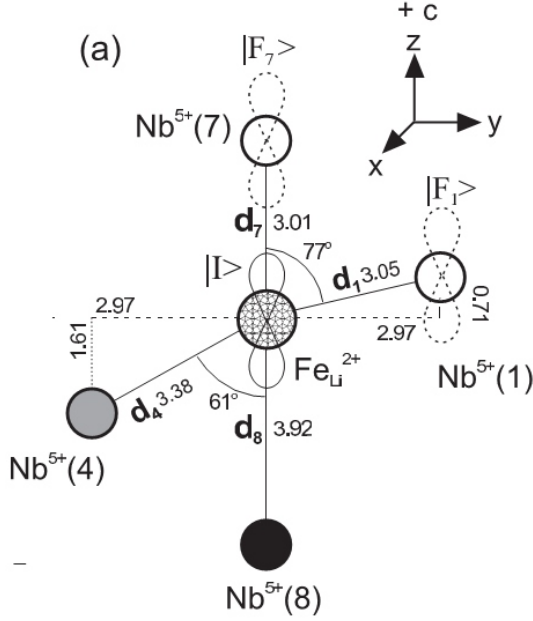


**Figure 13:** Arrangement of  $\text{Fe}_{\text{Li}}^{2+}$  and next-neighboring  $\text{Nb}_{\text{Nb}}^{5+}$ -ions in  $\text{LiNbO}_3$ , assuming atomic positions unchanged with respect to the defect-free crystal ([104]). The lengths of the interionic vectors  $\mathbf{d}_i$  are given in Å. The picture shows a cut along a  $yz$ -glide mirror plane. For three sites, as examples, the axial structure (symmetry  $A_1$  in the  $3m$  group) of the involved orbitals of  $(3z^2-r^2)$  type are indicated. For  $\text{Fe}_{\text{Li}}^{2+}$  ( $3d^6$ ), shown hatched, the orbital of the last electron is labeled  $|I\rangle$ . For the  $\text{Nb}_{\text{Nb}}^{4+}$  neighbors 1 and 7, they are called  $|F_1\rangle$  and  $|F_7\rangle$ . Reproduced with permission [105] from Ref. [22].

features result in a directed transport of carriers, resembling the bulk photovoltaic current density  $\mathbf{j}_{\text{phv}}$ . Together with the compensating, counter-directed incoherent current  $\mathbf{j}_{\text{incoh}}$ , characterized by the underlying hopping transport mechanism and, thus, a low mobility, the build-up of space-charge fields with values up to  $10^5$  V/cm become possible and are reported for  $\text{LiNbO}_3$  [23]. Such fields will be decisive for light-induced changes of the index of refraction that will be shown in the subsequent chapter on small-polaron based hologram recording.

The starting point of this chapter is Ref. [22], where the small-polaron based bulk photovoltaic effect is explained with Fe-doped  $\text{LiNbO}_3$  as an example and  $\text{Fe}^{2+}$  is considered as small polaronic center. Thus, and as Fe is incorporated on a Li site ( $\text{Fe}_{\text{Li}}$ ), the optical excitation from small  $\text{Nb}_{\text{Li}}^{4+}$  or from  $\text{Nb}_{\text{Li}}^{4+}:\text{Nb}_{\text{Nb}}^{4+}$  can be treated in the same manner as given by the following models.

## 5.1 Directed optical transfer of small polarons from $\text{Fe}_{\text{Li}}$

### 5.1.1 Absorption features

We first focus on the impact of local structure on the absorption spectrum  $\alpha(\omega)$ , that allows for understanding the complexity of the absorption shape as well as its dependence on the light polarization.

Fig. 13 indicates the relative atomic positions of  $\text{Fe}_{\text{Li}}^{2+}$  and its eight  $\text{Nb}_{\text{Nb}}^{5+}$  neighbors in the  $yz$  glide mirror plane (for reasons of clarity only two of the eight  $\text{Nb}_{\text{Nb}}^{5+}$  ions (1,4) of the  $xy$ -plane are shown). We assume that Fe exactly replaces a Li site of the defect-free crystal [104] and that the structural positions of Li and Nb remain unchanged with respect to the defect-free crystal. Each of the  $\text{Nb}_{\text{Nb}}$  sites will be a possible final location of an electron transferred optically from  $\text{Fe}_{\text{Li}}^{2+}$ . A single Fe-Nb pair can thus serve as the elementary unit with which the basic facts of the absorption process (see chapter 3) can be elucidated. The orbital of the last electron in  $\text{Fe}_{\text{Li}}^{2+}$  ( $3d^6$ ), also having axial symmetry  $A_1$  [106] will be symbolized by  $|I\rangle$ . There is a finite

probability that  $|I\rangle$  is leaking to each of its eight  $\text{Nb}_{\text{Nb}}^{5+}$  neighbors described by effective transfer integrals  $J_i$  ( $i = 1, \dots, 8$ ). The absorption  $\alpha_i(\omega)$  depends on the distances  $d_i$  between  $\text{Fe}_{\text{Li}}^{2+}$  and  $\text{Nb}_{\text{Nb}}^{5+}$ , and on  $J_i$ :

$$\alpha_i(\omega) \sim \frac{d_i^2 J_i^2}{\omega} \cdot \exp \left[ -\frac{(\hbar\omega - 2E_p - E_C)^2}{4E_p \hbar\omega_0} \right] \quad (20)$$

with the representative phonon energy  $\hbar\omega_0$ . Then, the observed optical absorption band of  $\text{Fe}_{\text{Li}}^{2+}$  at about 2.6 eV is described by  $\sum_i \alpha_i$ .

It is possible to understand the slight dependency of the resulting absorption spectrum for extraordinary and ordinary light, i.e. along and perpendicular to the polar  $c$ -axis. For this purpose, it is noteworthy that the magnitude of  $\alpha_i$  is strongly dependent on the product  $d_i^2 J_i^2$ , whereby  $J_i(d)$  itself decreases in an exponential way as a function of the distance  $d$ . Thereby, transitions with small  $d_i$  dominate the absorption spectrum, which are  $d_{1,2,3}$  for ordinary and  $d_7$  for extraordinary light. The difference in their length, however, is small, so that a weak polarization dependence of about 10% is to be expected and experimentally found [4].

### 5.1.2 Net currents

In the next step we analyze the appearance of a local current density along  $c$  as a result of the optically induced, time-dependent charge transfer between  $\text{Fe}_{\text{Li}}^{2+}$  and  $\text{Nb}_{\text{Nb}}^{5+}$ . Again, we consider the optical transitions along the different directions  $d_i$ , now restricted to their projections onto the  $c$ -direction. We assume the current density to be proportional to  $\alpha_i$ , neglect contributions originating from the displacement of ions, and get the following expression (summation over repeated indices is implied):

$$j_z \propto \left\{ \sum_{1,2,3,7} \langle I' | r_k | F'_i \rangle \langle F'_i | r_l | I' \rangle - \sum_{4,5,6,8} \langle I' | r_k | F'_i \rangle \langle F'_i | r_l | I' \rangle \right\} \\ \times e_k e_l^* = j_{+c} - j_{-c} \quad (21)$$

Here, the matrix elements  $\langle I' | r_k | F'_i \rangle$  and  $\langle F'_i | r_l | I' \rangle$  represent the values expected for the respective transition dipole arms  $r_l$  and  $r_k$  [22]; they are multiplied with the related components  $e_k$  and  $e_l^*$  of the polarization unit vectors of the electromagnetic waves. The sums of Eq. (21) add current densities parallel and anti-parallel to the  $c$ -direction. We further like to point to the analogy of Eq. (21) to the phenomenological expression of the bulk photovoltaic effect in  $\text{LiNbO}_3$ :  $j_i = \beta_{ikl} e_k e_l * I$  with the third rank complex photovoltaic tensor  $\beta_{ikl}$  [107]. According to the local defect structure depicted in Fig. 13, Eq. 21 simplifies assuming extraordinary light as, in this case, essentially transitions along  $d_7$  and  $d_8$  are activated. Since the dipole changes along  $d_7$  are expected to dominate due to its smaller distance (see above), a non-zero current density  $j_z > 0$  results. (Equivalent considerations are made in Ref. [22] to derive the current density  $j_y$ , but are omitted here, as only  $j_z$  will be decisive for the further considerations of optical nonlinearities.) Equation (21) will be modified by additional terms, if current contributions originating from the displacement of the ions are considered. This, however, requires the precise knowledge of structural changes upon optically induced polaron transport. For the case of  $\text{Nb}_{\text{Li}}^{4+} \rightarrow \text{Nb}_{\text{Li}}^{5+}$ ,

*Nahm and Park* [108] reported ionic displacements in the order of 0.04 Å along the  $c$ -axis. A systematic study for  $\text{Fe}_{\text{Li}}$  is on its way [109].

As a consequence of the structural analysis it becomes clear that also intrinsic defects, if located at Li sites in  $\text{LiNbO}_3$ , will lead to comparable photovoltaic current densities. This explains, that the optical absorption by a small bound polaron  $\text{Nb}_{\text{Li}}^{4+}$  causes photovoltaic currents [61]. The orbital topology of this defect is identical to that of  $\text{Fe}_{\text{Li}}^{2+}$  [4, 108]. However, since the defect potential of  $\text{Nb}_{\text{Li}}^{4+}$  is smaller ( $E_C = 0.53$  eV,  $E'_p = 0.58$  eV) than that of  $\text{Fe}_{\text{Li}}^{2+}$  ( $E_C = 1.22$  eV,  $E'_p = 0.70$  eV) [4], the transfer absorption cross section of  $\text{Nb}_{\text{Li}}^{4+}$  is larger than that of  $\text{Fe}_{\text{Li}}^{2+}$  (cf. Table 1). This supports the increase of the photorefractivity in LN, mainly determined by the bulk photovoltaic effect [28, 29] if the  $\text{Nb}_{\text{Li}}^{4+}$  charge state is populated [12]. Moreover, the absorption cross section of the  $\text{Nb}_{\text{Li}}^{4+}:\text{Nb}_{\text{Nb}}^{4+}$  bipolarons is about twice as large than that of  $\text{Nb}_{\text{Li}}^{4+}$  [77], as the two electrons in the bipolaron ground state [4] cause a doubling of the oscillator strength (see Fig. 5), in line with the sum rule for oscillator strengths. Bipolarons in LN are therefore likely to lead to stronger photovoltaic currents, which is the starting point for our small-polaron based holographic studies [35, 36] presented in chapter 6. In contrast, defects on regular  $\text{Nb}_{\text{Nb}}$  sites are not expected to be active in the generation of photovoltaic current densities because the bonds to their twelve next-neighboring  $\text{Nb}_{\text{Nb}}^{5+}$  ions have equal projections along the positive as well as the negative  $c$  axis, i.e.  $j_z = j_{+c} - j_{-c} \approx 0$ .

Upon this first optical transition (usually on the sub-ps-time scale, see experimental section 4.2, above), it is very likely that the displaced electron at  $\text{Nb}_{\text{Nb}}^{5+}$  will recombine with  $\text{Fe}_{\text{Li}}^{3+}$  triggered by the generated, local electric field. Furthermore, as sketched in Fig. 14 a), there is no barrier for this decay in the potential landscape, i.e. recombination will occur via multi-phonon emission without intermediate thermal excitation (see Appendix of Ref. [22]).

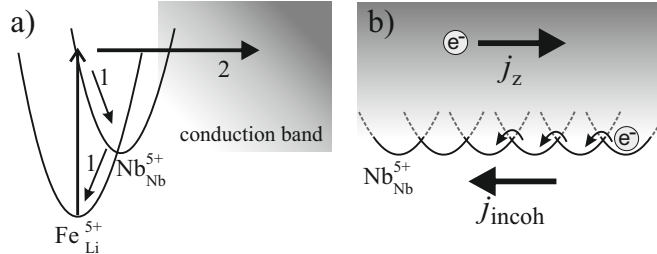


**Figure 14:** a) Scheme of the Fe-Nb potential landscape according to Ref. [22]. Upon small polaron optical excitation from  $\text{Fe}_{\text{Li}}^{2+}$  to  $\text{Nb}_{\text{Nb}}^{5+}$ , the electron is (1) moved forward to a potential centered around  $\text{Nb}_{\text{Nb}}^{5+}$ , followed by a relaxation of the Franck-Condon excited lattice to the new electronic state  $\text{Nb}_{\text{Nb}}^{4+}$ , accompanied by multi-phonon emission. Relaxation back to the potential landscape of  $\text{Fe}_{\text{Li}}^{3+}$  occurs without intermediate thermal excitation. (2) The Franck-Condon excited electron, having energies resonant with the conduction band, tunnels away from the initial  $\text{Nb}_{\text{Nb}}$  site. This transport is terminated by the formation of a small  $\text{Nb}_{\text{Nb}}^{4+}$  polaron. b) Excitations resonant with bandlike states cause the appearance of a high mobility transport (e.g. ballistic) expressed by current  $j_z$ . The mobility of the counter-directed, incoherent current  $j_{\text{incoh}}$  is much smaller due to incoherent 3D hopping via  $\text{Nb}_{\text{Nb}}$  (as shown) or  $\text{Nb}_{\text{Li}}$  (and/or  $\text{Fe}_{\text{Li}}$ ) (not shown).

Considering only path 1 in Fig. 14 a), the current density described above would disappear within a few femtoseconds. However, electric fields up to  $10^5$  V/cm [23] are well established to occur in congruently melting  $\text{LiNbO}_3$ .

As schematically sketched in Fig. 14 a), we need to consider also a certain probability that the Franck-Condon excited electron, having energies resonant with the conduction band, tunnels away from the initial  $\text{Fe}_{\text{Li}}$  site reached after optical transfer (path 2). Such a situation has been proven by experiments with very well-characterized model systems,  $\text{O}^-$  hole small polarons in oxide materials [5]. It should be noted that optical transfers exceeding the first  $\text{Nb}_{\text{Nb}}$  coordination sphere around  $\text{Fe}_{\text{Li}}$  may also contribute to the net current density  $j_z$ .

As a result, the mixture between local and extended states is rather involved and strongly dependent on the energy of the exciting photon. For the case of a small bound polaron  $\text{Nb}_{\text{Li}}^{5+}$ , *Nahm and Park* [108] have calculated the related excited energy levels lying in the conduction band continuum, all projected into a unit cell in  $\mathbf{k}$  space, resulting from the combined influence of bandlike tunneling, the defect potential, and the polaron-type lattice distortions. Although rather complex, it becomes possible to understand the frequency dependence of the photovoltaic current density on the photon energy, represented by the spectral dependence of the Glass factor  $\kappa(\omega)$  [31]: at low photon energies, the influence of the local potential dominates, thus, the polaron absorption features are well described by polaron theory as presented in chapter 3. With increasing photon energy, the influence of band-like-states increases, resulting in a pronounced tail of  $\kappa(\omega)$ . This behavior is terminated as soon as the contribution of the band-to-band transition predominates. Consequently, the Glass factor shows a pronounced maximum, shifted to slightly higher energies (3.1 eV) in comparison with the maximum of the small polaron absorption feature (see Fig. 5).

The transport processes described above are terminated by ionic displacements around the electron, forming a  $\text{Nb}_{\text{Nb}}^{4+}$  free small polaron. The formation time of the  $\text{Nb}_{\text{Nb}}^{4+}$  polarons from optically created non-thermalized electrons has been determined to be about  $10^{-13}$  s at room temperature [16, 17] (see Chapter 4.2). Their formation represents the initial step toward incoherent motion, since small polarons are characterized by hopping-type diffusive site changes (cf. Fig. 14b)). For the  $\text{Nb}_{\text{Nb}}^{4+}$  conduction polarons, the related activation energy is 0.27 eV [17]. During their diffusion, they can also be trapped at defects having lower-lying levels, such as  $\text{Nb}_{\text{Li}}^{5+}$  antisite defects present at 1% of all Li sites in congruently melting  $\text{LiNbO}_3$ , or at one of the further impurities, such as  $\text{Fe}_{\text{Li}}^{3+}$ . These steps form a cascade of events ordered by characteristic time spans in the range from sub- $\mu\text{s}$  to seconds [15, 92] and are visualized experimentally by transient absorption spectroscopy shown in chapter 4.1.2.

Incoherent hopping results by itself in a current density  $\mathbf{j}_{\text{incoh}}$  (cf. Fig. 14b)) but is characterized by a different, lower mobility in comparison to  $j_z$ . Because, however,  $j_z$  is directed along  $+c$ , continuity requires that also the complete diffusive current  $j_{\text{incoh}}$  is directed along  $c$  (which is not *a priori* clear for a diffusive transport mechanism) and compensates for  $j_z$  ( $|j_z| = |j_{\text{incoh}}|$ ). For an extended analytic treatment of these events, we thus refer to the related elaboration by Heyszenau [110]. As a result, the open-circuit photovoltaic electric field is expressed by:

$$E_{\text{phv}} = \Lambda_z(\omega)/\mu\tau \quad (22)$$

with the mean transport length  $\Lambda_z(\omega)$ , the mobility of the incoherently transported electrons  $\mu$  and their lifetime  $\tau$ . This field, that is as well dependent on the optical

excitation from small bound polarons as on the mediation with band-like states, enables and explains efficient small-polaron based hologram recording with single ns-laser pulses, if cascaded excitation is taken into account, as it is demonstrated in the following chapter.

## 6 Hologram recording by means of small polarons

The optical features of small polarons in  $\text{LiNbO}_3$  presented, so far, offer two distinct nonlinearities for the recording and read-out of short-lived, thick volume holograms: either (i) by means of a population density modulation (of different types) of small polarons or (ii) via the small-polaron based photovoltaic effect, i.e. index modulations resulting from photovoltaic fields and the linear electro-optic effect. The features of respective holograms are expected to reflect the individual peculiarities of the underlying recording mechanisms, with the ultrafast nonlinear response over a broad spectral range being the most important one. Thus, small polaron based holograms particularly are of importance for the (developing) field of ultrafast, dynamical holography. Moreover it is noteworthy, that  $\text{LiNbO}_3$  thereby experiences a renaissance as fs-hologram recording material based on the variety of small polarons. Besides the issue of applications, holography is well suited for the study of optical nonlinearities and related transport mechanism. It will be shown that novel small polaron features are uncovered by means of holographic spectroscopy [111].

The role of small polarons in holography has been addressed earlier by *Jermann et al.* within the two-center model [12]. Here, the polaronic centers act as intermediate trap for the recording of holograms; in this case, the spatial modulation of the index of refraction is due to a charge redistribution between *extrinsic* defect centers and the electro-optic effect. Furthermore, it has been shown that small bound polarons may act as intermediate shallow traps in a multi-step recording scheme for phase holograms featuring non-destructive read-out [41, 42]. *L. Hesselink et al.* were the first to deal with a spatial modulation density of  $\text{Nb}_{\text{Li}}^{4+/5+}$  for hologram recording [41]; although not using the language of small polarons at that time, their approach is already quite close to what we call *small polaron based holography*. The variety and complexity of hologram features reflecting the small polaron nature were not discovered until 2011 [35, 36]. In what follows, the principle steps of small polaron based hologram recording based on the build-up of a spatial density modulations as well as on the small polaron-based photovoltaic effect are summarized with thermally reduced  $\text{LiNbO}_3$  as an example. These samples are particularly suited, as single (ultra-)short laser pulses in the blue-green spectral range can be applied to modulate the number densities of small bound polarons  $\text{Nb}_{\text{Li}}^{4+}$ , of hole polarons  $N_{\text{HP}}(x)$  and bipolarons  $N_{\text{BP}}(x)$ . In the first part of experimental studies presented below, the time resolution of the optical setup prevents the observation of small free  $\text{Nb}_{\text{Nb}}^{4+}$  polarons; this, however, is acceptable as hologram recording is predominantly expected for modulated number densities of bound polarons as well as of the contribution of the polaron-based photovoltaic effect.

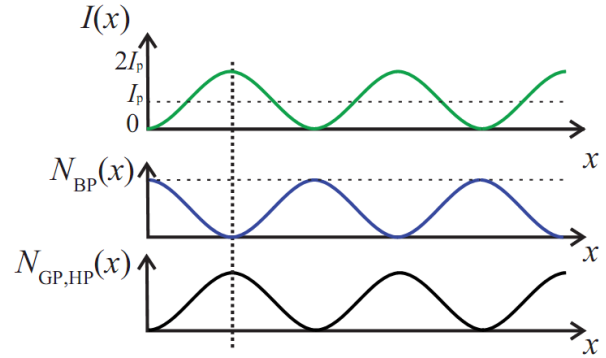
## 6.1 Population density holograms

As a prerequisite for hologram recording by means of small polaron density modulations, the action of the linear electro-optic effect needs to be excluded. This is realized by choosing the direction of the grating vector  $\mathbf{K}$  perpendicularly to the polar  $c$ -axis with light polarizations of pump and probe beams parallel to  $c$  and  $s$ -polarization. Thereby, the recording without an electro-optic contribution, i.e.  $r_{331} = 0$  according to the point symmetry group  $3m$  of  $\text{LiNbO}_3$  was studied [112].

### 6.1.1 Hologram recording mechanism

Taking into account small-polaron generation according to chapter 4 together with an exposure to an inhomogeneous, i.e. sinusoidal intensity pattern  $I(x) = I_p[1 + \cos(|\mathbf{K}|x)]$ , the appearance of spatially periodic density modulations of small bound electron and hole polarons as well as of bipolarons can be expected as sketched in Fig. 15 [35]. For

**Figure 15:** Sinusoidal intensity pattern  $I(x)$  applied for exposure in our experiments with average intensity  $I_p = I_R + I_S$  and modulation depth unity. Spatially periodic density modulations of small bound polarons  $N_{\text{GP}}(x)$ , hole polarons  $N_{\text{HP}}(x)$  and bipolarons  $N_{\text{BP}}(x)$ . Reproduced with permission [113] from Ref. [35].



the recording, we assume equal intensities of reference and signal beams ( $I^R = I^S$ ) yielding a modulation depth of  $m = 2\sqrt{I_R I_S} / (I_R + I_S) \mathbf{e}_p^R \cdot \mathbf{e}_p^S = \mathbf{e}_p^R \cdot \mathbf{e}_p^S$ . Here,  $\mathbf{e}_p^R, \mathbf{e}_p^S$  denote the respective light polarizations. Furthermore, a symmetric angle of incidence  $\Theta_B$  with respect to the sample's normal is assumed (*unslanted grating* [114]). Obviously, the resulting number densities  $N_{\text{GP}}(x)$  and  $N_{\text{HP}}(x)$  appear in phase with  $I(x)$  while  $N_{\text{BP}}(x)$  is phase-shifted by  $\pi$ .

It is possible to probe these spatial density modulations via light diffraction by considering the related spatial modulations of absorption  $\alpha(x)$  and index of refraction  $n(x)$  that are mutually linked via Kramers-Kronig relation [20]. Fig. 16 shows the overall spatial absorption modulation  $\alpha(x)$  that can be expected from the individual contributions of bound  $\alpha_{\text{GP}}(x)$ , hole  $\alpha_{\text{HP}}(x)$  and bipolarons  $\alpha_{\text{BP}}(x)$  at a probing wavelength  $\lambda = 785$  nm and for extraordinary light polarization.

Here, we note that the pronounced band width of  $\approx 1$  eV of small polaron absorption features enters the modeling, i.e. the tails of the absorption features of bipolarons and hole polarons at 785 nm are considered. Accordingly, a spatial modulation of the index of refraction  $n_1(x)$  is generated, as it results causally from Kramers-Kronig relation. It is in phase with  $\alpha(x)$  and composed from individual index changes  $n_{\text{GP}}(x), n_{\text{HP}}(x), n_{\text{BP}}(x)$  related to the particular small polaron number densities.

For Bragg-incidence and the assumption of an un-slanted, mixed (absorption and index) elementary holographic volume grating, with a mutual phase shift between

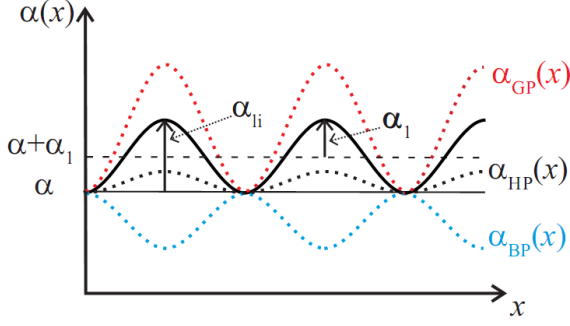


**Figure 16:** Spatial modulation of the absorption coefficient  $\alpha(x)$  with amplitude  $\alpha_1$  and average value of  $\alpha + \alpha_1$ . The overall absorption change in the maximum of the fringe pattern  $\alpha_{li} = 2\alpha_1$  is composed by absorption changes of the individual polaron type:  $\alpha_{li,GP}$ ,  $\alpha_{li,HP}$  and  $\alpha_{li,BP}$ . All absorption contributions are related to  $\lambda = 785$  nm and extraordinary light polarization. Reproduced with permission [115] from Ref. [35].

light and absorption/index modulation of 0 or  $\pi$ , the diffraction efficiency can be expressed via Kogelnik's formula [114]:

$$\begin{aligned} \frac{I^{(1st)}}{I_0} &= \exp\left(\frac{-2(\alpha + \alpha_1) \cdot d_h}{\cos \Theta_B}\right) \\ &\times \left[ \sin^2\left(\frac{\pi \cdot n_1 \cdot d_h}{\lambda \cos \Theta_B}\right) + \sinh^2\left(\frac{\alpha_1 \cdot d_h}{2 \cos \Theta_B}\right) \right] \end{aligned} \quad (23)$$

with the effective thickness of the recorded hologram  $d_h \leq d$  and the Bragg angle in the medium  $\Theta_B$ .

### 6.1.2 Modeling

Eq. (23) can be used to estimate the diffraction efficiency for the given experimental conditions of Fig. 18 (probe light at  $\lambda = 785$  nm, pump beam intensity  $I_p = 380$  GW/m<sup>2</sup> and Bragg angle  $\Theta_B = 11.5^\circ$ ,  $\mathbf{K} \perp c$ -axis, extraordinary light polarization and  $s$ -polarization) and the groundstate absorption  $\alpha(785) = (270 \pm 10)$  m<sup>-1</sup> (cf. Table 4). For this purpose, we need to determine the maximum amplitudes of absorption and index modulations,  $\alpha_1(785)$  and  $n_1(785)$ , as well as the hologram thickness  $d_h$ .

The amplitude  $\alpha_1(785)$  can be deduced from transient absorption spectra, as depicted in Fig. 11. Particularly the initial value of the light-induced absorption  $\alpha_{li}(785)$  is to be identified with the value obtained within the intensity maximum of the fringe pattern  $2 \cdot I_p = 760$  GW/m<sup>2</sup> and yields  $\alpha_1(785) = \alpha_{li}(785)/2 = (130 \pm 15)$  m<sup>-1</sup>.

The amplitude  $n_1(785)$  can be deduced from the application of the Kramers-Kronig relation to the spectral dependence  $\alpha_1(\lambda)$ . We model  $\alpha_1(\lambda)$  as follows: The light-induced absorption is related to the changes of the number densities of light-induced bound polarons  $N_{li,GP}$ , bipolarons  $N_{li,BP}$ , and hole polarons  $N_{li,HP}$  via:

$$\begin{aligned} \alpha_{li}(\lambda) &= \alpha_{li,GP}(\lambda) + \alpha_{li,HP}(\lambda) + \alpha_{li,BP}(\lambda) \\ &= N_{li,GP} \cdot \sigma_{GP}(\lambda) + N_{li,HP} \cdot \sigma_{HP}(\lambda) \\ &\quad + N_{li,BP} \cdot \sigma_{BP}(\lambda) \end{aligned} \quad (24)$$

with

$$N_{li,GP} = -(2 \cdot N_{li,BP} + N_{li,HP}) \quad (25)$$

Eq. (24) can be evaluated by considering the values of the light-induced absorption at the maximum of the individual polaron absorption bands, i. e.  $\alpha_{li}(785)$  and

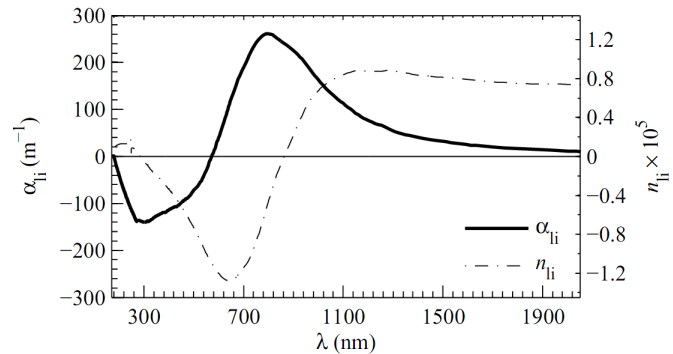
$\alpha_{\text{li}}(488)$ , that have been experimentally determined for the case of homogeneous exposure ([92], cf. Fig. 11). Further, the values of the individual absorption cross sections are required which can be deduced from Fig. 5. As a result, the light-induced number densities listed in Table 3 have been obtained.

number densities	
$N_{\text{li,GP}}$	$(+60.0 \pm 15.0) \cdot 10^{22} \text{ m}^{-3}$
$N_{\text{li,BP}}$	$(-26.0 \pm 10.0) \cdot 10^{22} \text{ m}^{-3}$
$N_{\text{li,HP}}$	$(+7.6 \pm 3.0) \cdot 10^{22} \text{ m}^{-3}$

**Table 3:** Estimated changes of the number densities of light-induced bound polarons  $N_{\text{li,GP}}$ , bipolarons  $N_{\text{li,BP}}$ , and hole polarons  $N_{\text{li,HP}}$ . Values are evaluated based on the experimental data shown in Fig. 11 and corresponding experimental conditions. Reproduced with permission [116] from Ref. [35].

Now, the individual polaron line shapes of the optically induced absorption features can be determined using the band shapes of small polarons (cf. Chapter 3). This allows to model the dispersion of the light-induced absorption  $\alpha_{\text{li}}(\lambda)$  over the visible and near-infrared spectral range as depicted in Fig. 17.

**Figure 17:** Spectral dependence of  $\alpha_{\text{li}}(\lambda)$  determined from the analysis of the experimentally determined light-induced absorption at 785 nm and 488 nm, the literature data on polaron absorption cross sections and the previously published experimental band shapes of small polarons [5, 57, 66, 117]. The dispersion  $n_{\text{li}}(\lambda)$  is calculated from  $\alpha_{\text{li}}(\lambda)$  applying the Kramers-Kronig relation, Eq. (26). For details see text. Reproduced with permission [118] from Ref. [35].



With the help of  $\alpha_{\text{li}}(\lambda)$ , and neglecting uncertainties due to confined integral limits, the dispersion of the index change  $n_{\text{li}}(\lambda)$  is calculated via the Kramers-Kronig relation [21]:

$$n_{\text{li}}(\omega) = \frac{2}{\pi} P \int_0^{\infty} \frac{\omega' \Delta \kappa_{\text{li}}(\omega')}{\omega'^2 - \omega^2} d\omega', \quad (26)$$

where  $P$  denotes the Cauchy principal value,  $\Delta \kappa_{\text{li}} = \alpha_{\text{li}}(\omega) \cdot c / (2 \cdot \omega)$ ,  $\omega = 2 \cdot \pi \cdot c / \lambda$ , and  $c$  is the vacuum speed of light. The resulting spectrum is plotted as dashed line in Fig. 17. From this dependence, we find an amplitude of the light-induced refractive index modulation at our probe wavelength of  $n_1(785) = n_{\text{li}}(785)/2 = (-3.0 \pm 1.0) \cdot 10^{-6}$ .

Finally, Eq. (23) requires an estimate for the hologram thickness  $d_{\text{h}} \leq d$ . This value is taken from the analysis of the rocking curve in the configuration  $\mathbf{K} \parallel c$ -axis (cf. Fig. 22) to  $d_{\text{h}} = (0.62 \pm 0.07) \text{ mm}$ . As it is smaller than the crystal thickness due to

absorption losses of the diffracted beam within the crystal volume, it becomes necessary to modify the estimate of the diffraction efficiency via Eq. (23) by an additional term  $\exp\{-2(\alpha + \alpha_1)(d - d_h)/\cos\theta_B\}$ . All values necessary for the calculation and the determined value for  $I^{(1st)}/I_0$  are summarized in Table 4.

Parameters entering Eq. (23)	
$\alpha(785)$	$(270 \pm 10) \text{ m}^{-1}$
$\alpha_{\text{li}}(785)$	$(260 \pm 15) \text{ m}^{-1}$
$\alpha_1(785) = \alpha_{\text{li}}(785)/2$	$(130 \pm 15) \text{ m}^{-1}$
$n(785)$	$(2.1776 \pm 0.0005)$
$n_1(785) = n_{\text{li}}(785)/2$	$(-3.0 \pm 1.0) \cdot 10^{-6}$
$d_h$	$(0.62 \pm 0.07) \text{ mm}$
$I^{(1st)}/I_0$	$(6.0 \pm 2.0) \cdot 10^{-4}$

**Table 4:** Modelling output for  $I^{(1st)}/I_0$  via Eq. (23) and a small-polaron based hologram with  $\mathbf{K} \perp c$ -axis, light polarization parallel  $c$ -axis and  $s$ -polarization. The index of refraction  $n(785)$  is taken from Ref. [119]., see text for details. Reproduced with permission [120] from Ref. [35].

According to our model, the bipolaron density is reduced via optical gating processes in the bright regions of the fringe pattern and yields an increase of the number density of small bound polarons by  $N_{\text{li,GP}}$  with

$$N_{\text{li,GP}} = 2N_{\text{li,BP}} \quad . \quad (27)$$

Here,  $N_{\text{li,BP}}$  denotes the number density of optically gated bipolarons. Because of the limited number density of bipolarons  $N_{\text{BP}}$  in the groundstate, a saturation behavior according to

$$N_{\text{li,BP}} = N_{\text{BP}} \left[ 1 - \exp\left(\frac{-I_p}{I_c}\right) \right] \quad (28)$$

is to be expected and has been experimentally verified [92]. Here,  $I_{p,c}$  denote pump and characteristic intensities, see also Fig. 9. Because of the relation given by Eq. (27), the intensity dependence of small bound polarons shows saturation with the same characteristic intensity  $I_c$ , but an amplitude by a factor of two larger compared with Eq. (28). Furthermore, the absorption amplitude and the increase of polaron number density are directly linked via the absorption cross section. Hence, saturation as a function of pump beam intensity also appears for the amplitudes  $\alpha_{1,\text{BP,GP,HP}}$  and, taking into account Kramers-Kronig relation, for  $n_{1,\text{GP,BP,HP}}$ . Note, that small polaron formation via two-photon absorption is neglected, thus, for large intensities, the diffraction efficiency inevitably saturates. For small amplitudes  $\alpha_1, n_1$  and  $\alpha_1 \ll \alpha_0$ , its intensity dependence can be approximated by

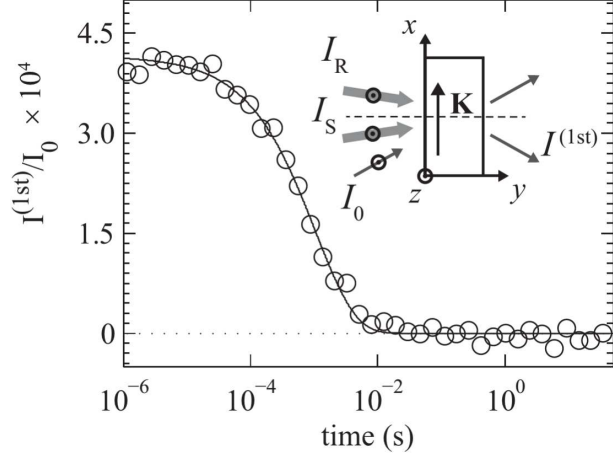
$$\eta(I_p) \approx (c_1 n_1(I_p))^2 + (c_2 \alpha_1(I_p))^2 = \eta^{\text{sat.}} \left[ 1 - \exp\left(\frac{I_p}{I_c}\right) \right]^2 \quad . \quad (29)$$

determined solely by two fitting parameters: the saturation value  $\eta^{\text{sat.}}$ , and the characteristic intensity  $I_c$ .

### 6.1.3 Results & analysis

Fig. 18 highlights the temporal dynamics of the first order diffracted probe beam obtained after hologram recording within a classical two-beam interferometer at a probing wavelength of 785 nm. For efficient generation of small polaron number den-

**Figure 18:** Temporal dynamics of the intensity of the first order diffracted beam  $I^{(1st)}$  for  $\mathbf{K} \perp c$ -axis,  $\mathbf{e}_p \parallel c$ -axis,  $s$ -polarization. Recording conditions:  $\lambda_p = 532$  nm,  $\Theta_B = 11.5^\circ$ , spatial frequency  $\Lambda = 1.4 \mu\text{m}$ ,  $I_p = I_R + I_S = 380$  GW/m<sup>2</sup> and 230 GW/m<sup>2</sup>, respectively. Bragg-matched probing conditions:  $\lambda = 785$  nm,  $\mathbf{e} \parallel c$ -axis with  $s$ -polarization. The data are normalized to the intensity of the incoming probe beam  $I_0$  and a logarithmic time scale is applied. The straight lines correspond to a fit of a stretched-exponential function Eq. (18) to the data set. The insets sketch the respective recording and probing configurations. Reproduced with permission [121] from Ref. [35].



sities, a single pulse of a frequency-doubled YAG:Nd-laser (Innolas *Spitlight 600*,  $|\mathbf{k}_p| = 2\pi/\lambda_p$ ,  $\lambda_p = 532$  nm, maximum applied intensity  $I_p^{\max} = 760$  GW/m<sup>2</sup>, 10 Hz repetition rate, and average pulse duration  $\tau_{\text{FWHM}} \approx 8$  ns, Gaussian spatial beam profiles  $2\omega_0 \approx 4$  mm) was used. The pulse was split by a 50:50-beam splitter, i.e., equal intensities were adjusted along the two optical paths ( $I^R = I^S$ ) yielding a modulation depth of  $m = 2\sqrt{I^R I^S}/(I^R + I^S) \mathbf{e}_p^R \cdot \mathbf{e}_p^S = \mathbf{e}_p^R \cdot \mathbf{e}_p^S$ . Here,  $\mathbf{e}_p^R, \mathbf{e}_p^S$  denote the respective light polarizations. A symmetric angle of incidence  $\Theta_B$  was chosen with respect to the sample's normal. A fiber-coupled GaAlAs-diode laser (Coherent *Cube*,  $|\mathbf{k}| = 2\pi/\lambda$ ,  $\lambda = 785$  nm) served for Bragg-matched as well as off-Bragg continuous wave (cw) probing. Its intensity was limited to  $I_0 = 10$  kW/m<sup>2</sup>, thus not affecting the polaron-density dynamics.

In Fig. 18, the intensity  $I^{(1st)}(t)$  is normalized to the intensity of the incoming probe beam  $I_0$  and is to be identified with the diffraction efficiency  $\eta$ . It is plotted on a logarithmic time scale and characteristically shows a non-exponential decay to zero. Fitting a stretched exponential function according to the empirical dielectric decay function by Kohlrausch, Williams and Watts (KWW) [87]

$$\frac{I^{(1st)}(t)}{I_0} = \frac{I^{(1st)}(t=0)}{I_0} \exp\left[-(t/\tau)^\beta\right] \quad (30)$$

to the experimental data (solid line in Fig. 18) yields the starting amplitude  $I^{(1st)}(t=0)/I_0$ , the decay time  $\tau$  and the stretching coefficient  $\beta$  given in Table 5.

By comparison, a striking coincidence between the estimate  $\eta \approx 6 \cdot 10^{-4}$  with the experimentally determined value of  $\eta = (4.2 \pm 1.0) \cdot 10^{-4}$  is obvious. Furthermore, from temperature dependent measurements  $\tau(T)$  in the temperature regime 300 – 410 K, and by using an Arrhenius plot, an activation energy  $E_a$  (see Table 5) of  $\bar{E}_a = (0.57 \pm$

	$\mathbf{K} \perp c$ -axis
$I^{(1st)}(t = 1\mu s)/I_0$	$(4.2 \pm 1.0) \cdot 10^{-4}$
$\tau$	$(1.1 \pm 0.3)$ ms
$\beta$	$(0.69 \pm 0.20)$
$E_a$	$(0.55 \pm 0.07)$ eV

**Table 5:** Parameters obtained by fit of Eq. (30) to the data of Fig. 18. The activation energies  $E_a$  were determined via an Arrhenius plot from temperature dependent spectra. Reproduced with permission [122] from Ref. [35].

0.07) eV has been determined. This activation energy also is in good agreement with the model approach as it reflects the barrier height of thermally activated hopping of small bound polarons.

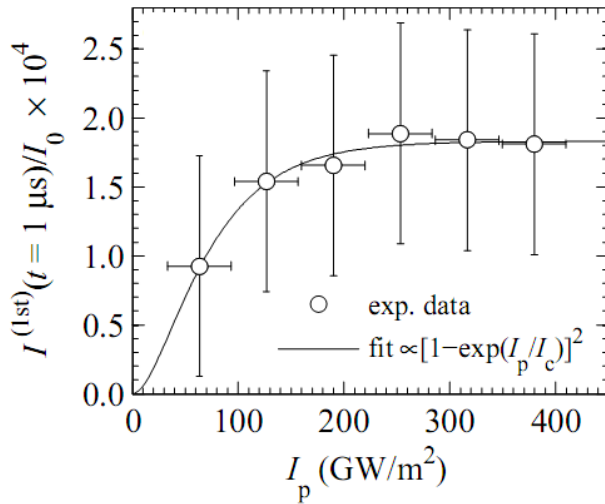


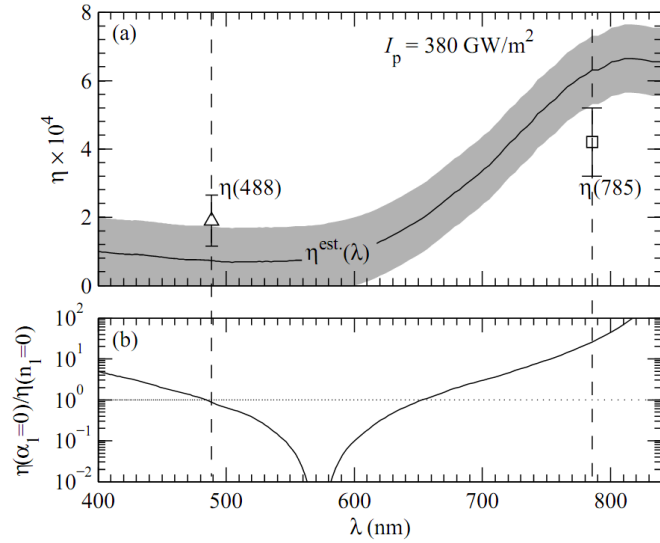
**Figure 19:** Normalized intensity of the first order diffracted beam  $I^{(1st)}/I_0$  at  $t = 1\mu s$  as a function of pump intensity  $I_p$  for  $\mathbf{K} \perp c$ -axis ( $s$ -polarization). The solid line corresponds to a fit of a saturation function Eq. (29) with  $\eta^{\text{sat.}} = (1.8 \pm 0.8) \cdot 10^{-4}$  and  $I_c = (52 \pm 10)$  GW/m<sup>2</sup>. For details see text. Reproduced with permission [123] from Ref. [36].

In the next step, the dependence of the starting amplitude on the intensity of the recording beams is verified, see Fig. 19 [36]. The diffraction efficiency saturates at a value of about  $1.8 \cdot 10^{-4}$  and pump beam intensities larger than  $200 \text{ GW/m}^2$  and can be described well by equation (29) (solid line in figure).

Appropriate experimental studies have been performed with probing light in the blue-green spectral range at  $488 \text{ nm}$  [36] while keeping all other conditions. In this case, the contributions of the optical features of particular polarons differ according to their absorption fingerprints in Fig. 5. As the dispersive features of the latter are known, it is possible to model the dispersive behavior of the diffraction efficiency over the entire blue-green spectral range. Fig. 20 shows the results of modeling together with the experimentally determined values. Coincidence is found within the experimental error. Moreover, as a specific feature of the underlying small polaron based hologram recording mechanism, anormal dispersion behavior of  $\eta$  is found. This is mainly due to the pronounced small polaron absorption bands in the visible spectral range. As a result, the mutual contribution of light-induced index and absorption changes vary from  $400$  to  $900 \text{ nm}$ ; within the spectral window of  $480 - 655 \text{ nm}$ , the presence of a pure index grating can be assumed. This is of importance particularly

for applications, as efficient holograms can be recorded in this spectral range or the impact of optical lensing by small polarons becomes apparent, here (See Chapter 7).

**Figure 20:** (a) Dispersion of the diffraction efficiency  $\eta_{\text{est}}$ . (solid line) that has been estimated according to Eq. (3) and the parameters published in Ref. [35]. The grey area denotes the error for  $\eta_{\text{est}}$ . The experimentally determined efficiencies at a probing wavelength of 488 nm and 785 nm have been added for comparison. (b) Dispersion of the ratio of the diffraction efficiency for a pure absorption grating and a pure index grating. A predominant contribution of the absorption grating is found at 785 nm while amplitude and index grating likewise contribute to the overall efficiency at 488 nm. Reproduced with permission [124] from Ref. [36]



## 6.2 Holograms by means of the electro-optic effect

The key difference for hologram recording with  $\mathbf{K} \parallel c$ -axis is that the action of the linear electro-optic coefficient with non-vanishing tensor elements  $r_{113} \neq 0$  and  $r_{333} \neq 0$  needs to be considered. In this case, index modulations may arise in presence of an electrical field  $E$  via

$$n_1(\lambda) = -\frac{1}{2}n_{\text{eff}}^3(\lambda)r_{\text{eff}}(\lambda)E \quad (31)$$

which is valid for index changes in crystals of the point symmetry 3m. Here,  $n_{\text{eff}}(\lambda)$  and  $r_{\text{eff}}(\lambda)$  denote the effective index of refraction and the effective electro-optic tensor element at wavelength  $\lambda$ .

How can the appearance of an internal electric field be explained using the small-polaron approach? This question has been addressed in its detail in chapter 5 based on microscopic considerations of optically induced charge transfer from a polaronic to its next-neighboring site. The structural environment within the first coordination sphere of the  $\text{Nb}_{\text{Li}}^{4+}$  site is responsible for the appearance of a net current (see chapter 5.1.2). In addition, there is a probability that the Franck-Condon excited electrons may tunnel away from its initial polaronic site, if its energy becomes resonant with the conduction band. In such a case, the unidirectional carrier transport length  $\Lambda_{\text{ballistic}}^{\text{uni}}$  exceeds by far the first coordination sphere. By means of Monte-Carlo Simulations to describe the dynamics of the counter-directed incoherent hopping transport, *Carnicero et al.* succeeded in modeling of the experimental data with the assumption of  $\Lambda_{\text{ballistic}}^{\text{uni}} \approx 1 - 3$  nm for Fe-doped  $\text{LiNbO}_3$ , being strongly dependent on the pump intensity and stoichiometry [18]. This transport length should not be mixed up with the mean transport length  $\Lambda_z$  determined by *Glass et al.* ( $\approx 1\text{\AA}$ ) [23] and applied for

the estimate of the photovoltaic field strength. The latter takes charge displacements in both  $+c$ - and  $-c$ -directions into account, thus expressing the net charge displacement and determining the net current density  $j_z$ . In contrast, for holography, the uni-directional carrier displacement  $\Lambda_{\text{ballistic}}^{\text{uni}}$  is decisive: Considering the recording of a transmission phase hologram in the visible spectral range, we are dealing with grating constants of the fringe pattern in the regime from  $\Lambda_{\text{grating}} \approx 500 - 5000 \text{ nm}$ . For the build-up of an electric field that modulates the index of refraction via the Pockel's effect, it is necessary to redistribute carriers from bright to dark regions, i.e. over distances of up to  $\Lambda_{\text{grating}}/2$ . Within a single event of optical excitation and  $\Lambda_{\text{ballistic}}^{\text{uni}}$ , that is in the order of a few nm as stated above, it is thus not possible to record an (efficient) hologram. For this purpose, cascaded excitation from polaronic centers needs to be considered, i.e. the repeated optical excitation and transfer of a carrier from one polaronic site to the other during the light pulse. In such a way, by means of hundred-fold re-excitation, carriers may get over distances of several hundreds of nanometers. Another origin for long-range transport may be impact-ionization as proposed by *Garcia-Lechuga et al.* [125].

It is possible to roughly estimate the pulse duration necessary for the recording of a phase hologram with maximum efficiency, i.e. described by a photovoltaic field according to Eq. (22). The total duration of a laser pulse  $\tau_{\text{pulse}}$  is determined by the single transfer time between two polaronic sites under illumination  $\tau_{\text{transfer}}$  in product with the number of re-excitation processes  $N_{\text{casc}}$ :  $\tau_{\text{pulse}} = \tau_{\text{transfer}} \times N_{\text{casc}}$ . The single transfer time  $\tau_{\text{transfer}}$  can be identified with the polaron formation time as experimentally determined using fs-spectroscopy [13, 17, 82] and summarized in the previous Chapter 4.2. Although not determined for the optical excitation from polaronic sites itself, so far, we do not expect different orders of magnitudes for the formation times and, here, assume  $\tau_{\text{transfer}} \approx 100 \text{ fs}$ . With  $N_{\text{casc}} \approx 100$ , we get  $\tau_{\text{pulse}} = 10 \text{ ps}$ . It is thus likely, that efficient holograms based on small-polarons can be recorded using ps- and ns-laser pulses, while recording with pulse durations from  $0.1 - 10 \text{ ps}$  will be less efficient, although possible. The latter has been demonstrated by *Reckenthaeler et al.* using  $200 \text{ fs}$  laser pulses and it is shown, that the gratings recorded with such small pulse durations are mainly due to free carriers [126]. In Ref. [127], *Gamaly et al.* recorded gratings in stoichiometric  $\text{LiNbO}_3$  with a characteristic lifetime of  $0.1 - 1 \text{ seconds}$  that points to a contribution of small polarons.

We like to note that the aspect of temporal recording dynamics marks the most striking difference to the classical photorefractive effect [34]. Conductivity and dielectric permittivity determine the photorefractive recording time. The crossing point then is the carrier mobility of small polarons. Keeping this in mind, the principle mechanism for hologram recording using the polaron-based photovoltaic effect is:

$$I(z) \rightarrow j_z(z) \rightarrow \rho_{\text{polaron}}(z) \rightarrow E_{\text{phv}}(z) \rightarrow n(z)$$

with the polaron density  $\rho_{\text{polaron}}(z)$ .

### 6.2.1 Results

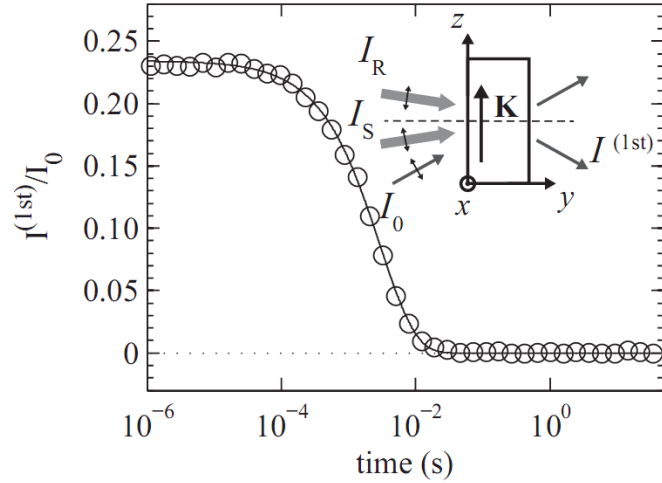
A striking feature of hologram recording by means of the small-polaron based photovoltaic effect is the possibility to record efficient phase gratings within a single

picosecond or nanosecond laser pulse in nominally undoped  $\text{LiNbO}_3$ . Experimental studies [35, 36] verify further features, as it is demonstrated in the following for ns-laser pulse experiments.

In order to get a dominant contribution of the small-polaron based photovoltaic effect, thermally reduced samples of  $\text{LiNbO}_3$  are applied for the studies. Then, a pronounced number density of small bound  $\text{Nb}_{\text{Li}}^{4+}:\text{Nb}_{\text{Nb}}^{4+}$  bipolarons are present that act as a source for carrier excitation. The photon energy of the laser pulse is chosen such that both, optically induced transfer to the next-neighboring polaron site (that is a regular  $\text{Nb}_{\text{Nb}}^{5+}$  site) and tunneling via an energetic state resonant with the conduction band become possible. According to the dispersion behavior of the Glass constant, and the bipolaron absorption feature, this is verified by  $E_{\text{pump}} = 2.5 \text{ eV}$  (532 nm), for which a frequency-doubled YAG:Nd-laser ( $\tau_{\text{pulse}} \approx 8 \text{ ns}$ ) is used. It should be added, that the net current  $j_z$  may be larger in comparison with  $\text{Fe}_{\text{Li}}$  or  $\text{Nb}_{\text{Li}}$  due to the capture of two electrons that induce a stronger lattice distortion.

Fig. 21 exemplarily shows the result of a dynamic measurement of the diffraction efficiency in thermally reduced, nominally undoped  $\text{LiNbO}_3$  upon recording an elementary grating in transmission geometry, for  $\mathbf{K} \parallel c$ -axis, and with a single ns-laser pulse at 532 nm. The probing light was chosen to a wavelength of 785 nm, i.e. at the

**Figure 21:** Temporal dynamics of the intensity of the first order diffracted beam  $I^{(1\text{st})}$  for  $\mathbf{K} \parallel c$ -axis,  $\mathbf{e}_p \parallel c$ -axis and  $p$ -polarization. Recording conditions:  $\lambda_p = 532 \text{ nm}$ ,  $\Theta_B = 11.5^\circ$ , spatial frequency  $\Lambda = 1.4 \mu\text{m}$ ,  $I_p = I_R + I_S = 380 \text{ GW/m}^2$  and  $230 \text{ GW/m}^2$ , respectively. Bragg-matched probing conditions:  $\lambda = 785 \text{ nm}$ ,  $\mathbf{e} \parallel c$ -axis with  $p$ -polarization. The data are normalized to the intensity of the incoming probe beam  $I_0$  and a logarithmic time scale is applied. The straight lines correspond to a fit of a stretched-exponential function Eq. (18) to the data set. The insets sketch the respective recording and probing configurations. Reproduced with permission [128] from Ref. [35].



maximum of the small bound polaron absorption feature (see Fig. 5).

A remarkable diffraction efficiency of up to  $\eta = (0.23 \pm 0.05)$  ( $0 \leq \eta \leq 1$ ) was obtained; it decayed to zero in a non-exponential way on the ms-time scale. These values are not in accord with  $\eta = (2.5 \pm 1.0) \cdot 10^{-4}$  and  $n_1(785) = (-1.8 \pm 1.0) \cdot 10^{-6}$  that can be estimated from the light-induced absorption features and Kramers-Kronig relation (Eq. 26) analogously to the considerations of the previous sections. Hence, an effect that contributes to a light-induced index change in excess of Kramers-Kronig relation must be considered.

Because of the pronounced efficiency and the complete self-erasure of the lifetime-limited recorded grating, it became possible to record a rocking curve, i.e. the diffraction efficiency as a function of angular detuning at a given time delay of  $1 \mu\text{s}$  after

the ns-laser pulse. The detuning results in dephasing of waves that constitute the diffracted beam, such that the integral amplitude decreases [129]. For this purpose, the recording was repeated using the same experimental configuration except the angle of the probing beam, that was detuned by  $\delta\theta_B$  in a range of  $\pm 0.5^\circ$  with respect to the Bragg angle  $\theta_B$ . Then, the values of  $\eta$  at a delay time of  $1\ \mu\text{s}$  with respect to the pulse were deduced from each singular measurement and plotted as a function of  $\delta\theta_B$ . The result is depicted in Fig. 22. A rather pronounced dependence  $\eta(\delta\theta_B)$  is obvious

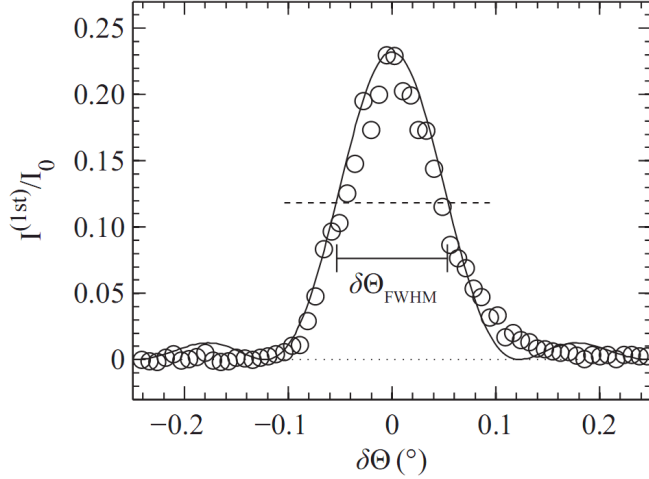


**Figure 22:** Angular dependence of the intensity of the normalized first order diffracted beam  $I^{(1st)}/I_0$  at  $t = 1\ \mu\text{s}$  after the pump pulse as a function of the deviation  $\delta\Theta$  of the Bragg-angle  $\Theta_B$ . The solid line represents the result of fitting Eq. (32) to the experimental data. Reproduced with permission [130] from Ref. [35].

with a characteristic full width at half maximum of  $\approx 0.5^\circ$ . Due to the pronounced value of  $\eta$  exceeding the maximum value of a lossy grating, the rocking curve is fitted by coupled-wave theory for a pure phase grating [111, 114]

$$\frac{I^{(1st)}(\delta\Theta)}{I_0} = \exp\left(\frac{-2(\alpha + \alpha_1)d_h}{\cos \Theta_B}\right) \sin^2\left(\frac{\sqrt{\nu^2 + \zeta^2}}{1 + \zeta^2/\nu^2}\right) \quad (32)$$

with

$$\nu = \pi n_1 d_h \cos(2\Theta_B)/(\lambda \cos \Theta_B),$$

and

$$\zeta = 2\delta\Theta \pi n d_h \sin \Theta_B/\lambda.$$

Here,  $n$  is the index of refraction of the unexposed sample and  $n_1$  is the index modulation amplitude and the factor  $\cos(2\Theta_B)$  accounts for  $p$ -polarization. The solid line in Fig. 22 represents the fit of function Eq. (32) to the experimental data and yields an amplitude of the index modulation up to  $n_1(785) = (-2.7 \pm 0.6) \cdot 10^{-4}$  and a hologram thickness of  $d_h = (0.62 \pm 0.07)$  mm.

Assuming that the electro-optic effect is the reason for the pronounced diffraction efficiency, an electric field must be present in addition to the spatial density modulation of small polarons. We now take into account that the light wave vectors propagate at a small angle with respect to the normal of the crystal and that the

relation  $r_{333} \approx 3 \cdot r_{113}$  (see e.g. Ref. [131]) holds. Thereby we approximate  $n_{\text{eff}}$  with the index of refraction for extraordinary light polarization  $n_e$  and  $r_{\text{eff}} \approx r_{333}$ . At wavelength of  $\lambda = 785$  nm, we find  $n_e(785 \text{ nm}) = (2.1776 \pm 0.0005)$  [119]. The electro-optic coefficient has been precisely determined to  $r_{333}(632.8 \text{ nm}) = 31.4 \text{ pm/V}$  in Ref. [132]. Together with the dispersive behavior published in Ref. [133] we extrapolate  $r_{333}(785 \text{ nm}) = 30.8 \text{ pm/V}$ . All values hold for lithium niobate grown from the congruent melt and at room temperature. Then, the estimate for the electric field strength is  $E = -2 \cdot n_1 / (n_3^3 \cdot r_{333}) \approx 17 \text{ kV/cm}$ .

Such a high electric field strength can not be explained with the diffusion mechanism with a saturation field of  $E_{\text{diff}} = (k_{\text{B}}T/e)(2\pi/\Lambda) \approx 1.25 \text{ kV/cm}$ . Here,  $k_{\text{B}}$  is the Boltzmann constant and  $e$  the electron charge. We can also exclude drift mechanisms in the absence of an externally applied electric field. Instead, electric fields with a strength up to  $100 \text{ kV/cm}$  are common for Fe-doped lithium niobate induced via the bulk photovoltaic effect [23]. Because of the absence of Fe-doping with significant concentration and a predominant valency  $2+$  upon thermal reduction, a photovoltaic current may be assigned to the optical generation of small polarons in the samples under study.

A second remarkable feature of the recorded gratings is the shape of the temporal decay, which is non-exponential and best described by the phenomenological stretched exponential function (Eq. 18, solid line in Fig. 21). This observation can not be assigned to holograms recorded *conventionally* via the *photorefractive effect* in doped lithium niobate, that inevitably obey a single-exponential decay behavior. Furthermore, the corresponding lifetimes are determined by the dielectric relaxation time [134].

In contrast, taking an electric field related to optically generated small bound polarons into account, a field decay according to the relaxation behavior of bound polaron densities must be expected. The latter is well-known to exhibit a non-exponential decay behavior upon exposure to single ns-laser pulses due to incoherent 3D hopping transport (see e.g. Refs. [15,67,92]) as it is the case for the samples under study. The decay lifetime of small bound  $\text{Nb}_{\text{Li}}^{4+}$  polaron densities is thermally activated with an activation energy of  $E_{\text{a}} = (0.53 \pm 0.07) \text{ eV}$ , and decays in the ms-range ( $\tau = (2.8 \pm 0.4) \text{ ms}$ ). The coincidence with the corresponding data of the hologram relaxation dynamics in the same sample ( $\tau = (3.0 \pm 0.3) \text{ ms}$  and  $\bar{E}_{\text{a}} = (0.57 \pm 0.07) \text{ eV}$ ) is striking.

All these results thus strongly support the validity of bound-polaron-based bulk photovoltaic currents; thus, a relation between the optically generated small bound polaron density and the appearance of an electric field, that alters the index of refraction via the linear electro-optic effect, seems likely. The underlying currents that result in the build-up of the electric field may be assigned to carriers from  $\text{Nb}_{\text{Li}}^{4+}:\text{Nb}_{\text{Nb}}^{4+}$  bipolarons.

## 7 Impact on Nonlinear Photonics & Conclusion

This chapter addresses the question: What is the overall impact of the reviewed considerations and experimental findings ?. At a first glance, there is an obvious

fundamental interest in defect physics, charge localization, non-equilibrium transport mechanism as well as light-matter-interaction on the nano- and ultrafast time scale beyond many other topics of solid state physics and optics from theory, experiment and modeling. This is due to the fact that the small polaron problem contains a variety of modern physical questions and problems, some of them still to be solved, allowing for synergetic effects in research of different disciplines.

However, more striking is the impact of optical nonlinearities of small polarons in the field of nonlinear photonics. Nonlinear photonics strongly develops in the 21st century and is accompanied by an increasing demand of nonlinear optical nano-materials with instantaneous and/or (ultra-)fast optical response. Here,  $\text{LiNbO}_3$  represents a promising candidate, and small polarons are at the origin of the interaction of (ultra-)short laser pulses with nanoscaled *quasiparticles*.

## 7.1 Developing fields

Optical nonlinearities of small polarons in particular allow for the realization of some widely discussed, visionary applications, including three-dimensional, real-time holographic displays. The state-of-the-art systems use re-recordable photosensitive *soft* media, e.g. photo-addressable polymers, and allow for a proof-of-principle and the further improvement of these techniques. So far, however, the hologram recording time, the maximum efficiency, more precisely the *sensitivity* and *dynamic range*, as well as the possibilities for self-erasure of recorded holograms limit the transfer to commercial systems. Small-polaron based holography here may represent an important step towards real-time applications, as it is demonstrated by holographic image recording using a single ns-laser pulse and thermally reduced, nominally undoped  $\text{LiNbO}_3$  in Ref. [135]. Figure 23 shows a photograph of the reconstructed image, that appears for a moment, i.e. a duration of a few milliseconds, upon the ns-recording process. Since large pulse intensities are required for recording, the image is posi-

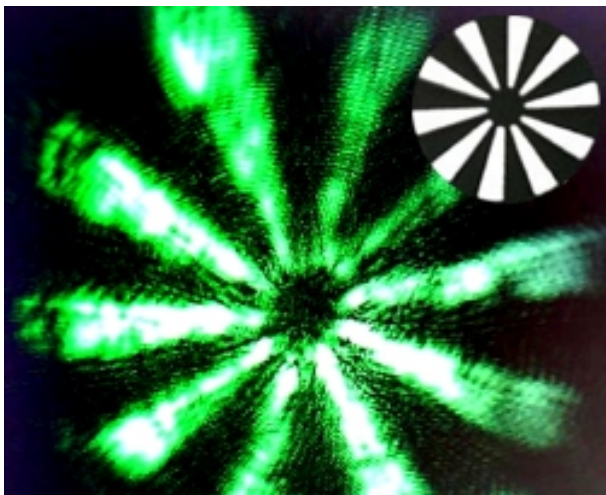


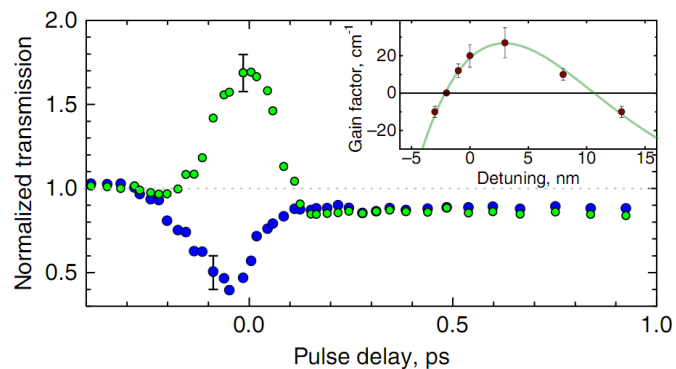
**Figure 23:** Photograph of a reconstructed image recorded using a holographic setup with a ns-laser pulse (532 nm) and thermally reduced, nominally pure  $\text{LiNbO}_3$  crystals as hologram recording material. The image (a metal gobo, see inset) was placed within the signal beam and cleaned-up using a 4f-optic. Recording was performed with a single 8 ns laser pulse (total pulse energy  $\approx 22$  mJ). The image was photographed using a charge-coupled device (CCD) and an electromechanical shutter, that opened the diffracted laser beam one millisecond after the laser pulse for a duration of 5 ms.

tioned within a 4f-optical setup of the signal beam, which also serves as a beam-clean up by Fourier filtering. According to the small polaron dynamics, the efficiency of the reconstructed image showed a temporal decay, that can be modeled by a stretched-

exponential function with characteristic decay time of  $\approx 3$  ms. The recording mechanism follows the model approach presented in Chapter 6 and is based on a spatial modulation of the optical dissociation of  $\text{Nb}_{\text{Li}}^{4+}:\text{Nb}_{\text{Li}}^{4+}$  bipolarons. It is noteworthy that the millisecond decay represents self-erasure of the hologram, thus, further hologram recording becomes possible at a repetition rate of up to 100 Hz, quite reasonable for display technologies. Even higher repetition rates become possible either by heating the crystal, i.e. acceleration of the incoherent hopping mechanism, or by using small free  $\text{Nb}_{\text{Nb}}^{4+}$  polarons instead. A further advantage of this type of hologram recording is the possibility to record holograms with different colors in the blue, green (by means of  $\text{O}^-$  or  $\text{Nb}_{\text{Li}}^{4+}:\text{Nb}_{\text{Li}}^{4+}$ ) and red (by means of  $\text{Nb}_{\text{Li}}^{4+}$ ) spectral range. At the same time, holograms can be reconstructed over a broad spectral range; both spectral dependencies of recording and reconstruction are important pre-requisites for color holography. Despite these promising features,  $\text{LiNbO}_3$  remains an expensive crystalline material, which may be applied in small-frame 3D-displays, such as for head-mounted displays, or for applications in real-time interferometry, e.g. optical correlators for scanning fingerprints in the framework of security issues. *Gamaly et al.* used nominally undoped, stoichiometric  $\text{LiNbO}_3$  for the demonstration of 3D write-read-erase memory bits using 150 femtosecond laser pulses [127].

A very recent holographic application based on the ultrafast, small polaron response time, is described in Ref. [136], where light-amplification of a weak signal beam is realized by means of wave-mixing with a strong pump. The underlying mechanism is the possibility to generate a light interference pattern even with beams of different color, i.e. frequency detuned beams, if pulses with a pulse duration in the sub-ps-time regime are chosen. As depicted in Fig. 24, amplification is observed in nominally undoped  $\text{LiNbO}_3$ . A prerequisite of light amplification is either the possibility to record

**Figure 24:** Probe beam transmission versus time delay of the probe pulse with respect to the pump pulse in nominally undoped  $\text{LiNbO}_3$ . The wavelengths of the probe pulse are 485 nm and 493 nm for blue and green dots, respectively, the pump wavelength is  $\approx 490$  nm. The inset shows the detuning dependence of the net gain factor (amplification minus absorption) for probe and pump pulses matched in time. Reproduced with permission [137] from Ref. [136].



the fringe pattern, that is demonstrated in Chapter 6 as well as in Ref. [136], and a significant nonlinearity in the recording/read-out process. Although the underlying mechanism of the amplification process itself is not fully understood, so far, the role of small polarons can not be excluded.

## 7.2 Present applications

Optical nonlinearities of small polarons need to be discussed in the framework of present applications of LiNbO<sub>3</sub> in nonlinear photonics, as well. Very prominent is to use lithium niobate as a nonlinear optical crystal for frequency conversion. Here, small polarons limit the crystal's conversion efficiency, its operation lifetime, as well as the tolerable energy of the pump beam and the repetition rate of the pulse laser system itself, as it will be discussed in the following. It will be shown that, from a fundamental viewpoint, understanding of optical nonlinearities of small polarons has a large impact on optimizing converter features of LiNbO<sub>3</sub>. Examples include pre-treatment and/or doping with appropriate external dopants or tuning of the laser system parameters according to small polaron features.

Let us assume the generation of harmonic light pulses at  $\lambda_{\text{SHG}} = 532 \text{ nm}$  by pumping a nominally undoped LiNbO<sub>3</sub> crystals with short, intense Gaussian laser pulses of a  $Q$ -switched YAG:Nd-laser operated at  $\lambda_{\text{pump}} = 1064 \text{ nm}$  with intensity  $I_{\text{pump}}$ , repetition rate  $f_{\text{rep}}$  and pulse durations in the nanosecond regime. Intensities of the generated harmonic pulses  $I_{\text{SHG}}$  exceeding  $1 \text{ GW/cm}^2$  at the output of the crystal are assumed. The aspect of quasi phase-matching, necessary for efficient frequency conversion in LiNbO<sub>3</sub> will be discussed separately below, as it is responsible for further peculiarities of small polaron dynamics.

Regarding a first infrared laser pulse, free carrier excitation will occur in LiNbO<sub>3</sub> by interband two-photon absorption due to the (self-)generated harmonic laser pulse at 532 nm (chapter 4). The carrier density will be spatially limited to the beam path of the pulse and will increase towards the output surface of the crystal in accordance with the rise of the harmonic intensity. At the end of the ns-pulse a fraction of such carriers is trapped at Nb<sub>Nb</sub> and/or Nb<sub>Li</sub>, giving rise to the appearance of a transient absorption. Here, we remind of their spectrally broad absorption features of the order of  $\approx 1 \text{ eV}$  (cf. 5). In particular, the absorption related to small free Nb<sub>Nb</sub><sup>4+</sup> as well as to small bound Nb<sub>Li</sub><sup>4+</sup> polarons cover the wavelength of the laser pump beam at 1064 nm (1.165 eV). Phenomenologically, this effect is called *green light-induced infrared absorption* (GRIRA) [138], a terminology that is common in laser physics to describe equivalent phenomena in the nonlinear optical crystal KTiOPO<sub>4</sub> (KTP) [139]. It must be added, that also O<sup>-</sup> polarons are formed in this process, and that the absorption at 532 nm (2.33 eV) is constituted by contributions of FP, GP and HP. This transient absorption (or GRIRA), decays in a stretched exponential way with characteristic lifetimes in the microsecond (Nb<sub>Nb</sub><sup>4+</sup>) and millisecond (Nb<sub>Li</sub><sup>4+</sup>) regime as another small polaron feature in LiNbO<sub>3</sub>.

For a laser system in single pulse operation mode, there are no further consequences of GRIRA. However, in repetition mode, the appearance of GRIRA means, that subsequent laser pulses will be strongly attenuated at both fundamental and harmonic wavelengths, if the time delay to the initial pulse falls within the small polaron lifetime  $\tau_{\text{lifetime}}$ . In this case, absorption (i) suppresses the intensity of the harmonic wave, thus affecting the conversion efficiency, (ii) heats the crystal mainly by the interaction with the intense fundamental wave [140], that (iii) results in the effect of thermal lensing via the thermo-optic effect. In case of very high intensities, even (iv) an irreversible thermo-mechanical damage of the crystal must be expected. From the viewpoint of a

laser system with intra-cavity frequency conversion, GRIRA furthermore represents an increase of laser-cavity losses, and, depending on the magnitude of the absorption change, may result in the complete break-down of laser operation.

Besides, the generation of small polarons in the beam path of the laser pulses is accompanied with changes in the index of refraction (chapter 6) that are a second source for laser break-down in intra-cavity setups. The index changes exhibit a spatial profile transversal to the beam path, that is determined by the spatial (Gaussian) intensity profile of the laser pulses, and act as a focusing or de-focusing index lens depending on the sign of the index change. This effect results in pronounced fanning e.g. of femtosecond laser pulses in LiNbO<sub>3</sub> [141] and has a similar effect on the laser systems operation as the so-called *optical damage*, that has been studied intensively in the framework of the photorefractive effect in LiNbO<sub>3</sub> particularly with the aim to reduce its action by stoichiometry [142–146]. In contrast, index changes based on optical nonlinearities of small-polarons are short-lived and recover on a millisecond time scale.

In order to overcome such manifold problems related with GRIRA, the repetition rate  $f_{\text{rep}}$  of the laser system must be chosen such that small polarons completely relax between two subsequent laser pulses, i.e.  $f_{\text{rep}} \leq 1/\tau_{\text{lifetime}}$ . If higher repetition rates are required, one may take advantage of the hopping process, mainly responsible for the magnitude of the decay time of the transient absorption and being thermally activated. For this purpose, a LiNbO<sub>3</sub> crystal simply needs to be operated at elevated temperatures. Here, care must be taken not to activate further unwanted phenomena such as proton transport.

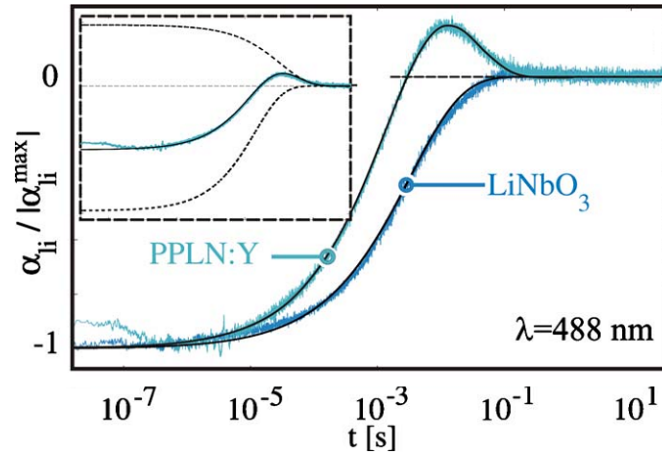
The general tendency in laser physics, however, is to completely suppress the appearance of transient optical nonlinearities, i.e. to suppress the formation of small polarons at all. This can be realized for small bound polarons by removing the related intrinsic (or extrinsic) defect centers. For LiNbO<sub>3</sub>, appropriate techniques have been well developed over the last decades. One possibility is to use stoichiometric (or near-stoichiometric) LiNbO<sub>3</sub> crystals (reviewed, e.g. in Ref. [39]). Or, Nb<sub>Li</sub> antisites can be removed by doping of LiNbO<sub>3</sub> with optically not active extrinsic defects, that are incorporated in the crystal lattice on a Li site such as Mg<sub>Li</sub> or Y<sub>Li</sub> (reviewed, e.g. in Ref. [146]). Such additional dopants can be found in most of the commercial LiNbO<sub>3</sub> frequency converters. In both cases, however, small free polarons are not removed due to their structural relation with the undisturbed Nb<sub>Nb</sub> crystal sub-lattice, so that GRIRA and causally related index changes remain (contrary to photovoltaic driven effects). Nevertheless, the spectral features of GRIRA as well as its dynamics changes significantly, as it is demonstrated in the transient absorption study of *Conradi et al.* [147] for LiNbO<sub>3</sub> with different Mg<sub>Li</sub> dopant concentrations in the VIS and by *Kitaeva et al* up to the infrared [148]. For the case of frequency conversion using ultrafast laser systems, the formation of small polarons was studied in MgO-doped crystals in Ref. [149]. As the pulse duration may fall below the small polaron formation time of  $\approx 100$  fs, however, the interaction with free-carrier absorption (FCA) much larger than small polaron absorption needs to be considered [150]. The FCA magnitude is higher due to a comparable large number density of free carriers (below 1% of free carriers are trapped as small polarons, see also table 1) as well as larger absorption cross section [85].

We note, that the interaction of fundamental and harmonic pulses with  $\text{Nb}_{\text{Nb}}^{4+}:\text{Nb}_{\text{Li}}^{4+}$  bipolarons can be discussed in the same manner by considering optical dissociation of BP, and formation of FP and HP. Although, it seems that thermally reduced  $\text{LiNbO}_3$  may not be considered for frequency conversion, the appearance of a transient transparency due to BP dissociation and particularly at the wavelength of the harmonic, may be of interest. *Merschjann et al.* were able to demonstrate that, for a so-called *moderate* thermal pre-treatment of  $\text{LiNbO}_3$ , it becomes possible to completely suppress the appearance of a transient, i.e., of GRIRA. In this case, however, the BP groundstate absorption is to be considered for the initial pulse, which is comparably weak at 1064 nm and may be less critical if the nonlinear optical crystal is placed externally to the laser cavity.

So far, the appearance of GRIRA is discussed without consideration of the ferroelectric domain structure in  $\text{LiNbO}_3$ . For efficient frequency conversion, i.e. in order to make use of the larger nonlinear optical coefficients of  $\text{LiNbO}_3$ , *quasi phase matching* is applied [151,152]. For this purpose, a periodic inversion of the direction of spontaneous polarization is required, that is realized by periodic electric-field poling of the crystal bulk [153]. Even at elevated temperature, however, this remains challenging taking into account the huge coercitive field of several kV/mm of  $\text{LiNbO}_3$  from the congruently melt. As a result, thin slabs of periodically poled  $\text{LiNbO}_3$  (PPLN) are commercially available that are well suitable as frequency converters in small-sized, low-power laser systems. An interesting approach for the synthesis of bulk PPLN, based on temperature fluctuations during Czochralski growth, is presented by *Feng et al.* [154]. Periodic temperature fluctuations may be induced by displacing the rotation axis from the symmetry axis of the temperature field. In order to accentuate the growth striations produced, the melt is doped with yttrium,  $\text{Y}_{\text{Li}}$ . From the boule, PPLN crystals with thicknesses of several millimeter can be successfully prepared, and it is shown by *Naumova et al.* that further dopants can be applied [155].

As a specific feature of this crystal growth technique, stoichiometry and concentration of  $\text{Y}_{\text{Li}}$  are spatially modulated in direction of the propagating laser pulses [156], thus, the type of pulse-induced small polarons and respective number densities are expected to vary significantly. It becomes rather difficult to estimate the interplay of optical effects of the different regimes, and to predict overall pulse propagation. Nevertheless, the comprehensive knowledge of optical nonlinearities of small polarons obtained for  $\text{LiNbO}_3$ , so far (cf. Chapter 3), allows for the modeling, e.g., of the dynamics of the transient absorption/ GRIRA, in PPLN:Y. A respective comprehensive study is presented by *Schoke et al.* in Ref. [157]. Figure 25 highlights the temporal evolution of the light-induced absorption in a PPLN:Y crystal in direct comparison to single-domain, nominally pure  $\text{LiNbO}_3$ . The crystals have been thermally pre-treated to probe the stoichiometry alteration by means of a  $\text{Nb}_{\text{Li}}^{4+}:\text{Nb}_{\text{Nb}}^{4+}$  bipolaron modulation. For the PPLN:Y sample a transient transparency at 488 nm initially induced by the pump pulse changes to a transient absorption at 1 ms prior to its decay ( $\tau > 0.1$  s). Obviously, this behavior is a result of two super-imposed decay components with different time constants and opposite sign in their amplitudes. The key in understanding this behavior are the different contributions from different layers of the PPLN crystal to the overall signal: congruent layers contribute mainly by  $\text{Nb}_{\text{Li}}$  defects, particularly by the bipolaron behavior, which is responsible for a light-induced

**Figure 25:** Transient absorption in periodically poled  $\text{LiNbO}_3$  and reduced single-domain nominally pure lithium niobate probed at  $\lambda = 488 \text{ nm}$ ,  $I_P = 800 \text{ GW/m}^2$ . Insets: complete plots for PPLN:Y according to a superposition of two stretched exponentials given by Eq. 18 (solid line), with its single components (lines). Reproduced with permission [158] from Ref. [159].



transparency in the blue spectral range and a short recombination time due to a high antisite concentration in such layers. (Near-)stoichiometric layers account for hole polaron properties, i.e., a light-induced absorption in the blue spectral range and a comparably long lifetime. Hence, the deconvolution of the signal in two components according to the inset of Fig. 25 essentially indicates the respective contributions of bipolaron recombination and hole polaron relaxation to the overall signal.

We like to note that all these considerations are not only valid for the nonlinear optical crystal  $\text{LiNbO}_3$ . Polaronic effects are found in nearly any nonlinear optical crystal and are discussed at the origin of the so-called *blue light-induced infrared absorption*, (*BLIIRA*) in  $\text{KNbO}_3$  [46, 160], (*GRIRA*) [139] or *gray tracking* in  $\text{KTiOPO}_4$  [48, 161, 162] and in  $\text{LiTaO}_3$  [47]. Furthermore, polarons limit the performance of  $\text{LiB}_3\text{O}_5$  (LBO) [49], and  $\beta\text{-BaB}_2\text{O}_4$  (BBO) [45], which are technologically of utmost importance for high-power laser applications. Even the surface growth of amorphous Si on LBO crystals is discussed to originate from small polarons that are charging the exposed surface area [163]. Studies of optical nonlinearities of small polarons are supported in any of these materials by means of electron-spin resonance at low temperatures [43, 44].

In conclusion, the exciting interplay between optical nonlinearities commonly assigned to continuum systems on the one side and small polarons that represent localities on the other side is surveyed. The key in closing the gap between continuum and locality is either the appearance of optical excitation from small polarons to energy levels that are resonant with bandlike states as well as the observation of ensembles of small polarons with large number density. It is well demonstrated - and without any doubt - that the small polaron approach is very powerful to describe the linear and nonlinear optical properties of  $\text{LiNbO}_3$ . It particularly satisfies the demands for the understanding of processes on the atomic length and ultrafast time scale in the age of nanoscience and femtonics with appropriate techniques widely available for investigations. An outstanding strength is the all-over modeling, e.g. the broadband, asymmetric absorption bands, and of transport issues, e.g. the low-mobility incoherent current density, and of the possibility to assign tensorial properties of the photo-galvanic effect with the atomic structure of  $\text{LiNbO}_3$  and of carrier dynamics over several magnitudes of time, i.e. from femtoseconds to seconds. Moreover, any of

the (phenomenologically) well-known effects, e.g. the bulk photovoltaic effect, green-induced infrared absorption (GRIRA), light-induced index changes, and many more, can be explained comprehensively. It is the basis for predictions and material tuning and/or material engineering in the framework of existing - as well as visionary - applications in the field of nonlinear photonics. Although a small polaron theory is developed in a convincing way, a variety of experimental studies particularly on the nanoscale and in the ultrafast time domain are expected. This will further raise the impact of optical nonlinearities of small polarons in  $\text{LiNbO}_3$ .

**Acknowledgment** The authors thank Ortwin Schirmer for fruitful discussions, Gabor Corradi for fruitful discussions and  $\text{LiNbO}_3$  samples for holographic measurements, Bettina Schoke, Stefan Torbrügge, Sarah Masch for fruitful discussion and experimental support, Gerda Cornelsen and Werner Geisler for sample preparation and the Deutsche Forschungsgemeinschaft (projects IM37/5, INST 190/137-1 FUGG, INST 160/165-1 FUGG) and the Deutscher Akademischer Austausch Dienst in cooperation with the Hungarian Scholarship Board Office (projects 50445542, 54377942, 57139940) for financial support.

## References

- [1] D. Emin. *Polarons*. Cambridge University Press Cambridge, (2013).
- [2] D. Emin. *Polarons*. McGraw Hill Encyclopedia of Science and Technology, 10th edn (2007).
- [3] P. Calvani. *Optical properties of polarons*. Riv. Nuovo Cimento **24**, 1–71 (2001).
- [4] O. F. Schirmer, M. Imlau, C. Merschjann, B. Schoke. *Electron small polarons and bipolarons in  $\text{LiNbO}_3$* . J. Phys.: Condens. Matter. **21**, 123201 (2009).
- [5] O. F. Schirmer.  *$O^-$  Bound Small Polarons in Oxide Materials*. J. Phys.: Condens. Matter **18**, R667 (2006).
- [6] D. Emin. *Phonon-assisted transition rates I. Optical-phonon-assisted hopping in solids*. Adv. Phys. **24**, 305 (1975).
- [7] D. Emin. *Optical Properties of Large and Small Polarons and Bipolarons*. Phys. Rev. B **48**, 13691 (1993).
- [8] S. Redfield, W. J. Burke. *Optical Absorption Edge of  $\text{LiNbO}_3$* . J. Appl. Phys. **45** (1974).
- [9] D. Berben, K. Buse, S. Wevering, P. Herth, M. Imlau, Th. Woike. *Lifetime of Small Polarons in Iron-Doped Lithium-Niobate Crystals*. J. Appl. Phys. **87**, 1034 (2000).
- [10] Jianmin Shi, Holger Fritze, Gunter Borchardt, Klaus-Dieter Becker. *Defect chemistry, redox kinetics, and chemical diffusion of lithium deficient lithium niobate*. Phys. Chem. Chem. Phys. **13**, 6925–6930 (2011).
- [11] K. L. Sweeney, L. E. Halliburton. *Oxygen Vacancies in Lithium Niobate*. Appl. Phys. Lett **43**, 336 (1983).
- [12] F. Jermann, J. Otten. *Light-Induced Charge Transport in  $\text{LiNbO}_3:\text{Fe}$  at High Light Intensities*. J. Opt. Soc. Am. B **10**, 2085 (1993).

- [13] O. Beyer, D. Maxein, Th. Woike, K. Buse. *Generation of small bound polarons in lithium niobate crystals on the subpicosecond time scale*. Appl. Phys. B **527** (2006).
- [14] P. Herth, T. Granzow, D. Schaniel, T. Woike, M. Imlau, E. Krätzig. *Evidence for Light-Induced Hole Polarons in LiNbO<sub>3</sub>*. Phys. Rev. Lett. **95**, 067404 (2005).
- [15] C. Merschjann, D. Berben, M. Imlau, M. Wöhlecke. *Evidence for Two-Path Recombination of Photoinduced Small Polarons in Reduced LiNbO<sub>3</sub>*. Phys. Rev. Lett. **96**, 186404 (2006).
- [16] Yong Qiu, K. B. Ucer, R. T. Williams. *Formation time of a small electron polaron in LiNbO<sub>3</sub>: measurements and interpretation*. phys. stat. sol. (c) **2**, 232 (2005).
- [17] S. Sasamoto, J. Hirohashi, S. Ashihara. *Polaron dynamics in lithium niobate upon femtosecond pulse irradiation: Influence of magnesium doping and stoichiometry control*. J. Appl. Phys. **105**, 083102 (2009).
- [18] J. Carnicero, M. Carrascosa, G. García, F. Agulló-López. *Site Correlation Effects in the Dynamics of Iron Impurities Fe<sup>2+</sup>/Fe<sup>3+</sup> and Antisite Defects Nb<sub>Li</sub><sup>4+</sup>/Nb<sub>Li</sub><sup>5+</sup> after a Short-Pulse Excitation in LiNbO<sub>3</sub>*. Phys. Rev. B **72**, 245108 (2005).
- [19] C. Merschjann, M. Imlau, H. Brüning, B. Schoke, S. Torbrügge. *Nonexponential relaxation dynamics of localized carrier densities in oxide crystals without structural or energetic disorder*. Phys. Rev. B **84**, 052302 (2011).
- [20] D. C. Hutchings, M. Sheik-Bahae, D. J. Hagan, E. W. Van Stryland. *Kramers-Krönig relations in nonlinear optics*. Optical and Quantum Electronics **24**, 1 (1992).
- [21] Hrsg. V. Lucarini, J. J. Saarinen, K.-E. Peiponen, E. M. Vartiainen. *Kramers-Kronig Relations in Optical Materials Research*. Springer Verlag (2005).
- [22] O. F. Schirmer, M. Imlau, C. Merschjann. *Bulk photovoltaic effect of LiNbO<sub>3</sub>:Fe and its small-polaron-based microscopic interpretation*. Phys. Rev. B **83**, 165106 (2011).
- [23] A. M. Glass, D. von der Linde, T. J. Negran. *High-Voltage Bulk Photovoltaic Effect and the Photorefractive Process in LiNbO<sub>3</sub>*. Appl. Phys. Lett. **25**, 233 (1974).
- [24] G. Chanussot, A. M. Glass. *A Bulk Photovoltaic Effect due to Electron-Phonon Coupling in Polar Crystals*. Phys. Lett. **59A**, 405 (1976).
- [25] W. Jösch, R. Munser, W. Ruppel, P. Würfel. *The Photovoltaic Effect and the Charge Transport in LiNbO<sub>3</sub>*. Ferroelectricity **21**, 623 (1978).
- [26] V. M. Fridkin. *Review of Recent Work on the Bulk Photovoltaic Effect in Ferro- and Piezoelectrics*. Ferroelectrics **53**, 169 (1984).
- [27] F. el Guibaly. *Models for the Bulk Photovoltaic Effect in Ferroelectric Crystals*. Can. J. Phys. **66**, 649 (1988).
- [28] K. Buse. *Light-Induced Charge Transport Processes in Photorefractive Crystals I: Models and Experimental Methods*. Appl. Phys. B **64**, 273–291 (1997).
- [29] K. Buse. *Light-Induced Charge Transport Processes in Photorefractive Crystals II: Materials*. Appl. Phys. B **64**, 391 – 407 (1997).
- [30] A. M. Glass. *The Photorefractive Effect*. Opt. Eng. **17**, 470 (1978).
- [31] E. Krätzig, H. Kurz. *Photorefractive and Photovoltaic Effects in Doped LiNbO<sub>3</sub>*. Opt. Acta **24**, 475 (1977).
- [32] B. I. Sturman, V. M. Fridkin. *The photovoltaic and photorefractive effects in noncentrosymmetric materials*. Clarendon, Oxford (1996).

- [33] K. Buse, J. Imbrock, E. Krätzig, K. Peithmann. *Photorefractive effects in LiNbO<sub>3</sub> and LiTaO<sub>3</sub>*. In *Photorefractive Materials and Their Applications II*, Hrsg. P. Günter, J.-P. Huignard, Springer–Verlag, 1989.
- [34] P. Günter, J.-P. Huignard (eds.). *Photorefractive Materials and Their Applications I, II and III*. Springer–Verlag (Heidelberg 1988, 1989).
- [35] M. Imlau, H. Brüning, B. Schoke, R.-S. Hardt, D. Conradi, C. Merschjann. *Hologram recording via spatial density modulation of Nb<sub>Li</sub><sup>4+/5+</sup> antisites in lithium niobate*. *Opt. Express* **19**, 15322–15338 (2011).
- [36] H. Bruening, V. Dieckmann, B. Schoke, K-M Voit, M. Imlau, G. Corradi, C. Merschjann. *Small-polaron based holograms in LiNbO<sub>3</sub> in the visible spectrum*. *Opt. Express* **20**, 13326–13336 (2012).
- [37] O Beyer, D Maxein, K Buse, B Sturman, HT Hsieh, D Psaltis. *Femtosecond time-resolved absorption processes in lithium niobate crystals*. *Opt. Lett.* **30**, 1366–1368 (2005).
- [38] L. Arizmendi. *Photonic applications of lithium niobate crystals*. *phys. stat. sol. (a)* **201**, 253 (2004).
- [39] K. Kitamura H. Hatano, Y. Liu. *Growth and photorefractive properties of stoichiometric LiNbO<sub>3</sub> and LiTaO<sub>3</sub>*. In *Photorefractive Materials and Their Applications II*, Hrsg. P. Günter, J.-P. Huignard, Springer–Verlag, 1989.
- [40] T. Volk, M. Wöhlecke. *Lithium Niobate - Defects, Photorefraction and Ferroelectric Switching*. Berlin: Springer (2008).
- [41] L. Hesselink, S. S. Orlov, A. Lie, A. Akella, D. Lande, R. R. Neurgaonkar. *Photorefractive Materials for Nonvolatile Volume Holographic Data Storage*. *Science* **282**, 1089 (1998).
- [42] K. Buse, A. Adibi, D. Psaltis. *Non-Volatile Holographic Storage in Doubly Doped Lithium Niobate Crystals*. *Nature* **393**, 665 (1998).
- [43] L. E. Halliburton, N. C. Giles, T. H. Myers. *Development of nonlinear optical materials for optical parametric oscillator and frequency conversion applications in the near- and mid-infrared*. Final technical report A342373 (2003).
- [44] M. M. Chirila, N. Y. Garces, L. E. Halliburton, S. G. Demos, T. A. Land, H. B. Radousky. *Production and thermal decay of radiation-induced point defects in KD<sub>2</sub>PO<sub>4</sub> crystals*. *J. Appl. Phys.* **94**, 6456 (2003).
- [45] W. Hong, L. E. Halliburton, K. T. Stevens, D. Perlov, G. C. Catella, R. K. Route, R. S. Feigelson. *Electron paramagnetic resonance study of electron and hole traps in β-BaB<sub>2</sub>O<sub>4</sub> crystals*. *J. Appl. Phys.* **94**, 2510–2515 (2003).
- [46] M. Zgonik, M. Ewart, C. Medrano, P. Günter. *Photorefractive effects in KNbO<sub>3</sub>*. Springer, New York (2007).
- [47] S. Wevering, J. Imbrock, E. Krätzig. *Relaxation of Light-Induced Absorption Changes in Photorefractive Lithium Tantalate Crystals*. *J. Opt. Soc. Am. B* **18**, 472 (2001).
- [48] G. J. Edwards, M. P. Sripsick, L. E. Halliburton, R. F. Belt. *Identification of radiation-induced hole center in KTiOPO<sub>4</sub>*. *Phys. Rev. B* **48**, 6884–6891 (1993).
- [49] W. Hong, M. M. Chirila, N. Y. Garces, L. E. Halliburton, D. Lupinski, P. Villeval. *Electron paramagnetic resonance and electron-nuclear double resonance study of trapped-hole centers in LiB<sub>3</sub>O<sub>5</sub> crystals*. *Phys. Rev. B* **68**, 094111 (1993).

- [50] T. Holstein. *Studies of Polaron Motion: 1. The Molecular Crystal Model*. Ann. Phys. **8**, 325 (1959).
- [51] L. D. Landau. *Über die Bewegung der Elektronen im Kristallgitter*. Phys. Z. Sowjetunion **3**, 664–665 (1933).
- [52] T. Holstein. *Studies of Polaron Motion: 2. The Small Polaron*. Ann. Phys. **8**, 343 (1959).
- [53] S. I. Pekar. Sov. Phys. JETP **16**, 335 (1946).
- [54] I. G. Austin, N. F. Mott. *Polarons in Crystalline and Non-Crystalline Materials*. Adv. Phys. **18**, 41 (1969).
- [55] J. Appel. *Polarons*. In *Solid State Physics*, Hrsg. F. Seitz, D. Turnbull, H. Ehrenreich, Academic Press – New York and London, 1968.
- [56] D. Emin. *Pair breaking in semiclassical singlet small-bipolaron hopping*. Phys. Rev. B **53**, 1260–1268 (1996).
- [57] B. Faust, H. Müller, O. F. Schirmer. *Free Small Polarons in LiNbO<sub>3</sub>*. Ferroelectrics **153**, 297 (1994).
- [58] O. F. Schirmer, O. Thiemann, M. Wöhlecke. *Defects in LiNbO<sub>3</sub> — I. Experimental Aspects*. J. Phys. Chem. Solids **52**, 185 (1991).
- [59] J. L. Ketchum, K. L. Sweeney, L. E. Halliburton, A. F. Armington. *Vacuum Annealing Effects in Lithium Niobate*. Phys. Lett. **94A**, 450 (1983).
- [60] D. M. Smyth. *Defects and Transport in LiNbO<sub>3</sub>*. Ferroelectrics **50**, 419 (1983).
- [61] O. F. Schirmer, S. Juppe, J. Koppitz. *ESR-, Optical and Photovoltaic Studies of Reduced Undoped LiNbO<sub>3</sub>*. Cryst. Latt. Def. and Amorph. Mat. **16**, 353 (1987).
- [62] O. F. Schirmer, H.-J. Reyher, M. Wöhlecke. *Characterization of Point Defects in Photorefractive Oxide Crystals by Paramagnetic Resonance Methods*. In *Insulating Materials for Optoelectronics – New Developments*, Hrsg. F. Agulló-López, World Scientific Publishing, 1995.
- [63] I. Sh. Akhmadullin, V. A. Golenishchev-Kutuzov, S. A. Migachev. *Electronic structure of deep centers in LiNbO<sub>3</sub>*. Phys. Solid State **40**, 1012–1018 (1998).
- [64] Yanlu Li, W. G. Schmidt, S. Sanna. *Intrinsic LiNbO<sub>3</sub> point defects from hybrid density functional calculations*. Physical Review B **89** (2014).
- [65] Yanlu Li, Simone Sanna, Wolf Gero Schmidt. *Modeling intrinsic defects in LiNbO<sub>3</sub> within the Slater-Janak transition state model*. Journal of Chemical Physics **140** (2014).
- [66] J. Koppitz, O. F. Schirmer, A. I. Kuznetsov. *Thermal Dissociation of Bipolarons in Reduced Undoped LiNbO<sub>3</sub>*. Europhys. Lett. **4**, 1055 (1987).
- [67] P. Herth, D. Schaniel, Th. Woike, T. Granzow, M. Imlau, E. Krätzig. *Polarons generated by laser pulses in doped LiNbO<sub>3</sub>*. Phys. Rev. B **71**, 125128 (2005).
- [68] O. F. Schirmer, D. von der Linde. *Two-Photon and X-Ray-Induced Nb<sup>4+</sup> and O<sup>-</sup> Small Polarons in LiNbO<sub>3</sub>*. Appl. Phys. Lett. **33**, 35 (1978).
- [69] F. Jermann, M. Simon, R. Böwer, E. Krätzig, O. F. Schirmer. *Light-Induced Absorption Changes in Reduced Lithium Niobate*. Ferroelectrics **165**, 319 (1995).
- [70] K. Buse, F. Jermann, E. Krätzig. *Two-Step Photorefractive Hologram Recording in LiNbO<sub>3</sub>:Fe*. Ferroelectrics **141**, 197 (1993).

- [71] P. Nagels. *Experimental Hall Effect Data for a Small-Polaron Semiconductor*. In *The Hall Effect and its Applications*, Hrsg. C. L. Chien, C. R. Westlake, Plenum Press, New York, 1980.
- [72] A Alexandrov, J Ranninger. *Theory of bipolarons and bipolaronic bands*. Phys. Rev. B **23**, 1796–1801 (1981).
- [73] L. E. Halliburton, K. L. Sweeney, C. Y. Chen. *Electron Spin Resonance and Optical Studies of Point Defects in Lithium Niobate*. Nucl. Instrum. Meth. Phys. Res. **B1**, 344 (1984).
- [74] L. Arizmendi, J. M. Cabrera, F. Agullo-Lopez. *Defects Induced in Pure and Doped LiNbO<sub>3</sub> by Irradiation and Thermal Reduction*. J. Phys. C: Solid State Physics **C17**, 515 (1984).
- [75] H. G. Reik, D. Heese. *Frequency Dependence of the Electrical Conductivity of Small Polarons for High and Low Temperatures*. J. Phys. Chem. Solids **28**, 581–596 (1967).
- [76] M. Klinger. *Quantum Theory of Non-Steady-State Conductivity in Low Mobility Solids*. Phys. Lett. **7**, 102–104 (1963).
- [77] C. Merschjann, B. Schoke, D. Conradi, M. Imlau, G. Corradi, K. Polgar. *Absorption cross sections and number densities of electron and hole polarons in congruently melting LiNbO<sub>3</sub>*. J. Phys.: Condens. Matter **21**, 015906 (2009).
- [78] *Reproduced with permission from J. Phys. Cond. Matt. 21, 015906 (2009). DOI: 10.1088/0953-8984/21/1/015906. © IOP Publishing. Reproduced by permission of IOP Publishing. All rights reserved.*
- [79] J. Koppitz, O. F. Schirmer, M. Wöhlecke, A. I. Kuznetsov, B. C. Grabmaier. *Threshold Effects in LiNbO<sub>3</sub>:Mg Caused by Change of Electron-Lattice Coupling*. Ferroelectrics **92**, 233–241 (1989).
- [80] G Montemezzani, P Rogin, M Zgonik, P Günter. *Interband photorefractive effects in KNbO<sub>3</sub> induced by ultraviolet illumination*. Opt. Lett. **18**, 1144–1146 (1993).
- [81] G Montemezzani, P Rogin, M Zgonik, P Günter. *Interband photorefractive effects - theory and experiments in KNbO<sub>3</sub>*. Phys. Rev. B **49**, 2484–2502 (1994).
- [82] HM Yochum, KB Ucer, RT Williams, PA Sheldon, V Nagirnyi, V Denks, L Grigorjeva, D Millers, EA Kotomin. *Short-pulse excitation and spectroscopy of KNbO<sub>3</sub>, LiNbO<sub>3</sub> and KTiOPO<sub>4</sub>*. Rad. Eff. Def. Sol. **150**, 271–276 (1999). 8th Europhysical Conference on Defects in Insulating Materials (EURODIM98), Univ. Keele, Keele, England, Jul. 06-11, 1998.
- [83] O Beyer, D Maxein, K Buse, B Sturman, HT Hsieh, D Psaltis. *Investigation of nonlinear absorption processes with femtosecond light pulses in lithium niobate crystals*. Phys. Rev. E **71** (2005).
- [84] H. Badorreck. *Aufbau und Charakterisierung eines fs-Spektroskopie-Experiments im UV/VIS/NIR*. Masterarbeit, Osnabrueck University, (2011).
- [85] H. Badorreck, S. Nolte, F. Freytag, M. Imlau. *Two-photon absorption in presence of small polaron formation in lithium niobate*. Proceedings, Photorefractive Photonics (PR'15), Villars, Switzerland (2015).
- [86] R. Kohlrausch. *Über das Dellmann'sche Elektrometer*. Ann. Phys. Chem. **72**, 353–405 (1847).

- [87] G. Williams, D. C. Watts. *Non-symmetrical Dielectric Relaxation Behaviour Arising from a Simple Empirical Decay Function*. Trans. Faraday Soc. **66**, 80 (1970).
- [88] F. Alvarez, A. Alegría, J. Colmenero. *Relationship between the Time-Domain Kohlrausch-Williams-Watts and Frequency-Domain Havriliak-Negami Functions*. Phys. Rev. B **44**, 7306–7312 (1991).
- [89] B. Sturman, E. Podivilov, M. Gorkunov. *Origin of Stretched Exponential Relaxation for Hopping-Transport Models*. Phys. Rev. Lett. **91**, 176602 (2003).
- [90] C. Merschjann. *Optically generated small polarons: Time-resolved pump-multiprobe experiments in lithium niobate vs. random walk charge transport simulations in oxide crystals*. Universität Osnabrück, 2007.
- [91] L. Guilbert. 'Swiss cheese model'. private communication (2014).
- [92] C. Merschjann, B. Schoke, M. Imlau. *Influence of Chemical Reduction on the Particular Number Densities of Light-Induced Small Electron and Hole Polarons in Nominally Pure LiNbO<sub>3</sub>*. Phys. Rev. B **76**, 085114 (2007).
- [93] *Reproduced with permission from Phys. Rev. B 76, 085114 (2007). DOI: 10.1103/PhysRevB.76.085114. © APS Publishing. Reproduced by permission of American Physical Society (APS) Publishing. All rights reserved.*
- [94] *Reproduced with permission from J. Phys. Cond. Matt. 21, 015906 (2009). DOI: 10.1088/0953-8984/21/1/015906. © IOP Publishing. Reproduced by permission of IOP Publishing. All rights reserved.*
- [95] M. Sheik-Bahae, A. A. Said, T. H. Wei, D. J. Hagan, E. W. Van Stryland. *Sensitive Measurement of Optical Nonlinearities Using A Single Beam*. IEEE J. Quant. El. **26**, 760 (1990). 100
- [96] M. Woehlecke, G. Corradi, K. Betzler. *Optical Methods to Characterise the Composition and Homogeneity of Lithium Niobate Single Crystals*. Appl. Phys. B **63**, 323 (1996).
- [97] *Reproduced with permission from J. Appl. Phys. 105, 083102 (2009). DOI: 10.1063/1.3095763. © AIP Publishing. Reproduced by permission of American Institute of Physics (AIP) Publishing. All rights reserved.*
- [98] A. Seilmeyer, W. Kaiser. *Generation of tunable picosecond light pulses covering the frequency range between 2700 and 32,000 cm<sup>-1</sup>*. Appl. Phys. A **23**, 113 (1980).
- [99] HP Li, F Zhou, XJ Zhang, W Ji. *Picosecond Z-scan study of bound electronic Kerr effect in LiNbO<sub>3</sub> crystal associated with two-photon absorption*. Applied Physics B **64**, 659 (1997).
- [100] R. DeSalvo, A.A. Said, D.J. Hagan, E.W. Van Stryland, M. Sheik-Bahae. *Infrared to ultraviolet measurements of two-photon absorption and n<sub>2</sub> in wide bandgap solids*. IEEE J. Quant. El. **32**, 1324 (1996).
- [101] RA Ganeev, IA Kulagin, AI Ryasnyansky, RI Tugushev, T Usmanov. *Characterization of nonlinear optical parameters of KDP, LiNbO<sub>3</sub> and BBO crystals*. Optics Communications **229**, 403–412 (2004).
- [102] *Reproduced with permission from Phys. Rev. B 76, 085114 (2007). DOI: 10.1103/PhysRevB.76.085114. © APS Publishing. Reproduced by permission of American Physical Society (APS) Publishing. All rights reserved.*
- [103] *Reproduced with permission from Appl. Phys. B 83, 085114 (2006). DOI: 10.1007/s00340-006-2227-9 © Springer Publishing. Reproduced by permission of Springer Publishing. All rights reserved.*

- [104] S. C. Abrahams, J. M. Reddy, J. L. Bernstein. *Ferroelectric Lithium Niobate. 3. Single Crystal X-Ray Diffraction Study at 24°C*. J. Phys. Chem. Solids **27**, 997 (1966).
- [105] *Reproduced with permission from Phys. Rev. B* **83**, 165106 (2011). DOI: 10.1103/PhysRevB.83.165106. © APS Publishing. *Reproduced by permission of American Physical Society (APS) Publishing. All rights reserved.*
- [106] S. Juppe, O. F. Schirmer. *Thermally detected electron spin resonance of Fe<sup>2+</sup> in LiNbO<sub>3</sub>*. Solid State Commun. **76**, 299 (1990).
- [107] V. I. Belinicher, B. I. Sturman. *The Photogalvanic Effect in Media Lacking a Center of Symmetry*. Sov. Phys. Usp. **23**, 199 (1980).
- [108] H. H. Nahm, C. H. Park. *First-principles study of microscopic properties of the Nb antisite in LiNbO<sub>3</sub>: Comparison to phenomenological polaron theory*. Phys. Rev. B **78**, 184108 (2008).
- [109] A. Sanson, A. Zaltron, N. Argiolas, C. Sada, M. Bazzan, W. G. Schmidt, S. Sanna. *Polaronic deformation at the Fe<sup>2+/3+</sup> impurity site in Fe:LiNbO<sub>3</sub> crystals*. Phys. Rev. B **91** (2015).
- [110] H. Heyszenau. *Electron Transport in the Bulk Photovoltaic Effect*. Phys. Rev. B **18**, 1586 (1978).
- [111] Kay-Michael Voit, Mirco Imlau. *Holographic Spectroscopy: Wavelength-Dependent Analysis of Photosensitive Materials by Means of Holographic Techniques*. Materials **6**, 334–358 (2013).
- [112] R. S. Weis, T. K. Gaylord. *Lithium Niobate: Summary of Physical Properties and Crystal Structure*. Appl. Phys. A **37**, 191–203 (1985).
- [113] *Reproduced with permission from Opt. Express* **19**, 15322 (2011). © OSA Publishing. *Reproduced by permission of Optical Society of America (OSA) Publishing. All rights reserved.*
- [114] H. Kogelnik. *Coupled Wave Theory for Thick Hologram Gratings*. Bell Syst. Tech. J. **48**, 2909 (1969).
- [115] *Reproduced with permission from Opt. Express* **19**, 15322 (2011). © OSA Publishing. *Reproduced by permission of Optical Society of America (OSA) Publishing. All rights reserved.*
- [116] *Reproduced with permission from Opt. Express* **19**, 15322 (2011). © OSA Publishing. *Reproduced by permission of Optical Society of America (OSA) Publishing. All rights reserved.*
- [117] H. Kurz, E. Krätzig, W. Keune, H. Engelmann, U. Gonser, B. Dischler, A. Räuber. *Photorefractive Centers in LiNbO<sub>3</sub>, Studied by Optical-, Mössbauer- and EPR-Methods*. Appl. Phys. **12**, 355 (1977).
- [118] *Reproduced with permission from Opt. Express* **19**, 15322 (2011). © OSA Publishing. *Reproduced by permission of Optical Society of America (OSA) Publishing. All rights reserved.*
- [119] D. S. Smith, H. D. Riccius, R. P. Edwin. *Refractive Indices of Lithium Niobate*. Opt. Commun. **17**, 332 (1976).
- [120] *Reproduced with permission from Opt. Express* **19**, 15322 (2011). © OSA Publishing. *Reproduced by permission of Optical Society of America (OSA) Publishing. All rights reserved.*

- [121] *Reproduced with permission from Opt. Express* **19**, 15322 (2011). © OSA Publishing. *Reproduced by permission of Optical Society of America (OSA) Publishing. All rights reserved.*
- [122] *Reproduced with permission from Opt. Express* **19**, 15322 (2011). © OSA Publishing. *Reproduced by permission of Optical Society of America (OSA) Publishing. All rights reserved.*
- [123] *Reproduced with permission from Opt. Express* **20**, 13326 (2012). © OSA Publishing. *Reproduced by permission of Optical Society of America (OSA) Publishing. All rights reserved.*
- [124] *Reproduced with permission from Opt. Express* **20**, 13326 (2012). © OSA Publishing. *Reproduced by permission of Optical Society of America (OSA) Publishing. All rights reserved.*
- [125] Mario Garcia-Lechuga, Jan Siegel, Javier Hernandez-Rueda, Javier Solis. *Imaging the ultrafast Kerr effect, free carrier generation, relaxation and ablation dynamics of Lithium Niobate irradiated with femtosecond laser pulses.* J. Appl. Phys. **116** (2014).
- [126] P. Reckenthaeler, D. Maxein, Th. Woike, K. Buse, B. Sturman. *Separation of optical Kerr and free-carrier nonlinear responses with femtosecond light pulses in LiNbO<sub>3</sub> crystals.* Phys. Rev. B **76** (2007).
- [127] Eugene G. Gamaly, Saulius Juodkazis, Vygantas Mizeikis, Hiroaki Misawa, Andrei V. Rode, Wieslaw Z. Krolikowski, Kenji Kitamura. *Three-dimensional write-read-erase memory bits by femtosecond laser pulses in photorefractive LiNbO<sub>3</sub> crystals.* Curr. Appl. Phys. **8**, 416–419 (2008). 3rd International Conference on Advanced Materials and Nanotechnology, Wellington, New Zealand, Feb 11-16, 2007.
- [128] *Reproduced with permission from Opt. Express* **19**, 15322 (2011). © OSA Publishing. *Reproduced by permission of Optical Society of America (OSA) Publishing. All rights reserved.*
- [129] K.-M. Voit, M. Imlau. *Holographic spectroscopy: analysis of convergent phase development.* Eur. J. Phys. **36** (2015).
- [130] *Reproduced with permission from Opt. Express* **19**, 15322 (2011). © OSA Publishing. *Reproduced by permission of Optical Society of America (OSA) Publishing. All rights reserved.*
- [131] M. Jazbinsek, M. Zgonik. *Material Tensor Parameters of LiNbO<sub>3</sub> Relevant for Electro- and Elasto-optics.* Appl. Phys. B **74**, 407 (2002).
- [132] T. Fujiwara, M. Takahasi, M. Ohama, A. J. Ikushima, Y. Furukawa, K. Kitamura. *Comparison of electro-optic effect between stoichiometric and congruent LiNbO<sub>3</sub>.* Electron. Lett. **35**, 499 (1999).
- [133] S. Fries, S. Bauschulte. *Wavelength Dependence of the Electrooptic Coefficients in LiNbO<sub>3</sub>:Fe.* phys. stat. sol. (a) **125**, 369 (1991).
- [134] N. V. Kukhtarev. *Kinetics of Hologram Recording and Erasure in Electrooptic Crystals.* Sov. Tech. Phys. Lett. **2**, 438 (1976).
- [135] S. Masch. *Aufzeichnung und Rekonstruktion von Bildhologrammen mit kurzen Laserpulsen in LiNbO<sub>3</sub>.* Bachelor Thesis, Universität Osnabrück, (2012).
- [136] S. Odoulov, A. Shumelyuk, H. Badorreck, S. Nolte, K. M. Voit, M. Imlau. *Interference and holography with femtosecond laser pulses of different colors.* Nat. Commun. **6**, 5866 (2015).

- [137] *Reproduced with permission from Nature Communications* **6**, 5866 (2015). DOI: 10.1038/ncomms6866. © Nature Publishing Group. Reproduced by permission of Nature Publishing Group. All rights reserved.
- [138] Y. Furukawa, K. Kitamura, A. Alexandrowski, R. K. Route, M. M. Fejer, G. Foulon. *Green-induced Infrared Absorption in MgO Doped LiNbO<sub>3</sub>*. Appl. Phys. Lett. **78**, 1970–1972 (2001).
- [139] S Wang, V Pasiskevicius, F Laurell. *Dynamics of green light-induced infrared absorption in KTiOPO<sub>4</sub> and periodically poled KTiOPO<sub>4</sub>*. J. Appl. Phys. **96**, 2023–2028 (2004).
- [140] Susumu Kato, Sunao Kurimura, Hwan Hong Lim, Norikatsu Mio. *Induced heating by nonlinear absorption in LiNbO<sub>3</sub>-type crystals under continuous-wave laser irradiation*. Opt. Mat. **40**, 10–13 (2015).
- [141] Q Wu, JJ Xu, GQ Zhang, LJ Zhao, XZ Zhang, HJ Qiao, Q Sun, WQ Lu, GY Zhang, TR Volk. *Fanning scattering in LiNbO<sub>3</sub> at 750-850 nm induced by femtosecond laser pulses*. Opt. Mat. **23**, 277–280 (2003). 8th IUMRS International Conference on Electronic Materials (IUMRS/ICEM), Xian, Peoples R Chiba, Jun 10-14, 2002.
- [142] M. G. Clark, F. J. DiSalvo, A. M. Glass, G. E. Peterson. *Electronic structure and optical index damage of iron-doped lithium niobate*. J. Chem. Phys. **59**, 6209–6219 (1973).
- [143] D. A. Bryan, R. Gerson, H. E. Tomaschke. *Increased Optical Damage Resistance in Lithium Niobate*. Appl. Phys. Lett. **44**, 847–849 (1984).
- [144] Y. Furukawa, M. Sato, K. Kitamura, Y. Yajima. *Optical Damage Resistance and Crystal Quality of LiNbO<sub>3</sub> Single Crystals with Various [Li]/[Nb] Ratios*. J. Appl. Phys. **72**, 3250 (1992).
- [145] E. Krätzig, R. Orlowski. *Reduction of Optical Damage Effects in LiNbO<sub>3</sub> and LiTaO<sub>3</sub>*. Opt. Quantum Electron. **12**, 495 (1980).
- [146] T. R. Volk, M. Wöhlecke, N. Rubinina. *Optical Damage Resistance in Lithium Niobate*. In *Photorefractive Materials and Their Applications II*, Hrsg. P. Günther, J.-P. Huignard, Springer-Verlag, 2007.
- [147] D. Conradi, C. Merschjann, B. Schoke, M. Imlau, G. Corradi, K. Polgar. *Influence of Mg doping on the behaviour of polaronic light-induced absorption in LiNbO<sub>3</sub>*. Physica Status Solidi - Rapid Research Letters **2**, 284 (2008).
- [148] G. K. Kitaeva, K. A. Kuznetsov, A. N. Penin, A. V. Shepelev. *Influence of small polarons on the optical properties of Mg:LiNbO<sub>3</sub> crystals*. Phys. Rev. B **65**, 054304 (2002).
- [149] Satoshi Enomoto, Satoshi Ashihara. *Comparative study on light-induced absorption between MgO:LiNbO<sub>3</sub> and MgO:LiTaO<sub>3</sub>*. J. Appl. Phys. **110** (2011).
- [150] Xiaojun Wu, Sergio Carbajo, Koustuban Ravi, Frederike Ahr, Giovanni Cirimi, Yue Zhou, Oliver D. Muecke, Franz X. Kaertner. *Terahertz generation in lithium niobate driven by Ti:sapphire laser pulses and its limitations*. Opt. Lett. **39**, 5403–5406 (2014).
- [151] JA Armstrong, N Bloembergen, J Ducuing, PS Pershan. *Interactions between light waves in a nonlinear dielectric*. Phys. Rev. **127**, 1918–& (1962).
- [152] MM Fejer, GA Magel, DH Jundt, RL Byer. *Quasi-phase-matched 2nd harmonic-generation - tuning and tolerances*. IEEE J. Quant. El. **28**, 2631–2654 (1992).
- [153] M. Houé, P. D. Townsend. *An Introduction to Methods of Periodic Poling for Second-Harmonic Generation*. Appl. Phys **28**, 1747–1763. (1995).

- [154] D Feng, NB Ming, JF Hong, YS Yang, JS Zhu, Z Yang, YN Wang. *Enhancement of 2nd-harmonic generation in LiNbO<sub>3</sub> crystals with periodic laminar ferroelectric domains*. Appl. Phys. Lett. **37**, 607–609 (1980).
- [155] II Naumova, NF Evlanova, OA Gliko, SV Lavrichev. *Czochralski-grown lithium niobate with regular domain structure*. Ferroelectrics **190**, 107–112 (1997). 4th International Symposium on Ferroic Domains and Mesoscopic Structures (ISFD-4), Vienna, Austria, Mar 25-30, 1996.
- [156] NF Evlanova, II Naumova, TO Chaplina, SA Blokhin, SV Lavrishchev. *Periodically poled Y : LiNbO<sub>3</sub> single crystal: impurity distribution and domain wall location*. J. Cryst. Growth **223**, 156–160 (2001).
- [157] B. Schoke. *Untersuchungen zum Ladungstransport kleiner Polaronen in reduziertem und unreduziertem LiNbO<sub>3</sub> und PPLN:Y*. Diplomarbeit, Universität Osnabrück (2006).
- [158] *Reproduced with permission from Phys. Rev. B* **81**, 132301 (2010). DOI: 10.1103/PhysRevB.81.132301. © APS Publishing. Reproduced by permission of American Physical Society (APS) Publishing. All rights reserved.
- [159] B. Schoke, M. Imlau, H. Brüning, C. Merschjann, G. Corradi, K. Polgár, I. I. Naumova. *Transient light-induced absorption in periodically poled lithium niobate: Small polaron hopping in the presence of a spatially modulated defect concentration*. Phys. Rev. B **81**, 132301 (2010).
- [160] H. Mabuchi, E. S. Polzik, H. J. Kimble. *Blue-light-induced Infrared-absorption in KNbO<sub>3</sub>*. J. Opt. Soc. Am. B. **11**, 2023–2029 (1994).
- [161] V Murk, V Denks, A Dudelzak, PP Proulx, V Vassiltsenko. *Gray tracks in KTiOPO<sub>4</sub>: Mechanism of creation and bleaching*. Nucl. Inst. Meth. Phys. Res. Sec. B - Beam Interact. Mat. Atoms **141**, 472–476 (1998). 9th International Conference on Radiation Effects in Insulators (REI-9), Knoxville, Tennessee, Sep 14-19, 1997.
- [162] B Boulanger, I Rousseau, JP Feve, M Maglione, B Menaert, G Marnier. *Optical studies of laser-induced gray-tracking in KTP*. IEEE J. Quant. El. **35**, 281–286 (1999).
- [163] S. Moeller, A. Andresen, C. Merschjann, B. Zimmermann, M. Prinz, M. Imlau. *Insight to UV-induced formation of laser damage on LiB<sub>3</sub>O<sub>5</sub> optical surfaces during long-term sum-frequency generation*. Opt. Express **15**, 7351–7356 (2007).

# Tin hypthiodiphosphate: nonlinear response in the sub-100 fs time domain

M. Imlau<sup>1,\*</sup>, V. Dieckmann<sup>1</sup>, H. Badorreck<sup>1</sup>, A. Shumelyuk<sup>2</sup>

<sup>1</sup> *Department of Physics, University of Osnabrück, Barbarastr. 7, 49069 Osnabrück, Germany*

<sup>2</sup> *Institute of Physics, National Academy of Sciences, 46, Science Avenue, 03 650 Kyiv, Ukraine*

[mimlau@uni-osnabrueck.de](mailto:mimlau@uni-osnabrueck.de)

**Abstract:** The interaction of sub-100 fs light pulses ( $\tau_p \lesssim 75$  fs) with single crystals of nominally undoped tin hypthiodiphosphate,  $\text{Sn}_2\text{P}_2\text{S}_6$ , is studied in the near-infrared spectral range (590 – 1630 nm). A predominant contribution of the two-photon absorption (TPA) is verified in the measurements of the sample transmission as a function of pulse intensity and of the time delay between pump and probe pulses. Scans over the photon energy show that the two-photon absorption coefficient  $\beta$  increases in a superlinear way for photon energies  $\hbar\omega$  exceeding  $E_g/2$ ; for any quantum energy it is nearly independent of propagation direction and polarization of the incident beam. Such a behavior is qualitatively similar to that predicted by perturbation theory within models with allowed-forbidden transitions. The TPA coefficient saturates at a maximum value of  $\beta \approx 8 \text{ cm GW}^{-1}$  at  $\hbar\omega \approx 1.80 \text{ eV}$ . It drops when reaching the bandgap  $E_g$ . Using pump-probe measurements at 626 nm, a transient absorption is verified that persists for probe pulse delays much longer than the pump pulse duration, up to 2.5 ns. We discuss our results in the framework of the microscopic structure of  $\text{Sn}_2\text{P}_2\text{S}_6$  with emphasis on the optical generation of  $\text{S}^-$  small hole polarons.

©2011 Optical Society of America. This work was published in Optical Materials Express and can be found at the URL <http://dx.doi.org/10.1364/OME.1.000953>. One print or electronic copy may be made for personal use only. Systematic reproduction and distribution, duplication of any material in this paper for a fee or for commercial purposes, or modifications of the content of this paper are prohibited.

## 1 Introduction

Tin hypthiodiphosphate ( $\text{Sn}_2\text{P}_2\text{S}_6$ , SPS) is a low symmetry (monoclinic) ferroelectric-semiconductor crystal ( $Pn$  at room temperature [1]) with a bandgap of 2.35 eV ( $\alpha = 35 \text{ cm}^{-1}$ ) [2]. Its microscopic structure is built from  $\text{Sn}^{2+}$  ions and  $(\text{P}_2\text{S}_6)^{4-}$  clus-

ters with a largely covalent binding character of the P-P and P-S bonds [3]. The energy band structure and charge density distribution has been reported for non-stoichiometric crystals by first-principles in the LDA approach, only recently [4].

SPS provides a remarkable photorefractive nonlinearity at ambient temperatures: The two-beam coupling gain factor exceeds  $20 \text{ cm}^{-1}$  due to its large Pockels coefficient ( $r_{111} \simeq 170 \text{ pm V}^{-1}$ ) and an astonishingly short response time in the order of milliseconds is reported in the red-spectral range (632 nm) [5, 6]. For Te-doped SPS, a photorefractive response was verified even at the communication wavelength of  $1.55 \mu\text{m}$  [7]. Commonly, two types of movable charge carriers of different sign take part in the build-up of space-charge gratings [8] with holes being the dominating carriers [9]. As a result the spectrum of the two-beam coupling gain has a narrow dip at zero frequency detuning. There are several positive consequences of such a behavior. For instance, it is possible to switch from light slowing down to superluminal propagation (or vice versa) by simply changing the input pulse duration [10]. It affects also the temporal dynamics of four-wave mixing coherent oscillators, which may switch to periodic pulses with rapidly changing phase between two discrete values (zero and  $\pi$ ) [11].

So far, the nonlinear response of SPS was widely studied using exposure to continuous wave (cw) laser light. Also, the aspect of exposure to laser pulses with nanosecond [12] or picosecond [13] pulse durations was treated in the framework of near-infrared holographic recording and optical phase conjugation. This revealed a nonlinear response similar to the cw-experiments if referenced to the mean intensity. Taking a further increase of the peak pulse power in the context of wave-mixing phenomena in SPS into account, one might expect to enable nonlinearities that are different from photorefraction and that decay with much shorter relaxation times (below  $\mu\text{s}$ ). The purpose of this work is to study the nonlinear response of nominally undoped SPS exposed to ultra-short laser pulses with pulse duration of 75 fs, pulse intensities up to  $1.5 \text{ PW m}^{-2}$  and over a wide spectral range in the red and near-infrared spectral range from 690 nm till 1600 nm, i.e., for photon energies below the bandgap energy.

## 2 Experimental procedure

Two sets of experiments are described in this paper. The first one aims to measure the transmission changes of the sample as a function of the incident pulse intensity. The second one allows for probing the light-induced transients during and after the pulse in the time domain up to 2.5 ns using a pump-probe technique.

For the transmission studies, the pulse intensity was varied by using neutral density (ND) filters (Fig. 1a) with  $f(\text{L1}) = 350 \text{ mm}$ . The transmission was obtained from the energy ratio of transmitted and incoming beams detected using Si-PIN photodiodes D1 and D3 (Thorlabs DET10A). For this purpose, thin lenses with focal lengths of 35 mm were used to adjust the spatial beam profile to the narrow aperture of the photodiodes (sensitive area of  $A = 0.8 \text{ mm}^2$ ).

The set-up for the pump-probe experiment is sketched schematically in Fig. 1b). Pump and probe beams are slightly focused by concave mirrors KM1 and KM2 ( $r =$

1 m) to the SPS sample with an intersection angle of  $\approx 4.6^\circ$  measured in air. The incident pulse energies are detected by the diodes D3 and D4 via a glass plate placed in front of the SPS sample. The temporal delay between pump and probe pulses is adjusted from  $-0.8$  ns to  $2.5$  ns by an optical delay line (DL) in steps of  $8.3$  fs. Both beams, attenuated if necessary by neutral density filters ND1 and ND2 are chopped by a phase-synchronized chopper wheel to less than  $3$  Hz. Thus, any effect of the previous pump pulse on the actual measurement is suppressed and the thermal load of the sample is reduced.

The ratio of the probe beam signals collected from D1 and D3, proportional to the samples' transmission, is taken to be unity for zero intensity of the pump pulse. In such a way all intensity independent losses (for relatively small linear absorption and for Fresnel reflection from the sample faces) are eliminated from the measured transmittance to ensure the easy extraction of the nonlinear absorption coefficient. (The linear absorption coefficient will be taken into account in what follows, however, when estimating the effective interaction length inside the sample.)

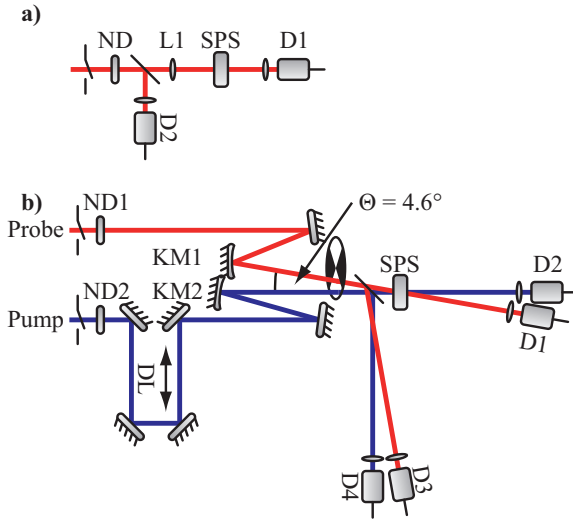


**Figure 1:** Schematic representation of the experimental set-ups. a) Single beam set-up for determination of the nonlinear absorption. The beam is attenuated by ND-filters and slightly focused by lens L1 to the sample. b) Pump-probe setup: both beams, attenuated by ND-filters, are focused to the sample by concave mirrors KM1, KM2. The pump beam is delayed in the time domain by the delay line DL.

Femtosecond pulses in the spectral range of  $600$  nm to  $1600$  nm are generated in two optical parametric amplifiers (Coherent Inc., *OPerA solo*) pumped by a regenerative amplified  $\text{Ti}^{3+}:\text{Al}_2\text{O}_3$  oscillator (Coherent Inc., *Libra-F HE*) at  $\lambda = 802$  nm with a repetition rate of  $1$  kHz. At the sample, pulse energies in the order of  $100 \mu\text{J}$  are available with pulse durations of  $\lesssim 75$  fs (Gaussian shape approximation, determined using interferometric auto correlation, APE Angewandte Physik und Elektronik GmbH, *Pulse Check PD 15ps*). The spatial intensity distribution of the light beam is close to a Gaussian profile and nearly axially symmetric. Thus, it can be expressed via:

$$I_p(x=0) = I_p^0 \exp[-(t/t_p)^2 - (r/r_p)^2] \quad . \quad (1)$$

Here,  $I_p^0$  is the input pulse peak intensity,  $t_p$  and  $r_p$  represent pulse duration and beam radius, respectively.

Our study was performed with nominally undoped SPS samples grown in the Institute of Solid State Physics and Chemistry of Uzhgorod State University by chemical vapor transport. Iodine was used as transport gas. The samples are of good optical

quality and were classified to type I by measurements of the kinetics of the beam-coupling gain [6, 14]. The rectangular sample of nominally undoped SPS (sample identifier: *N159*) used for determination of the two-photon absorption (TPA) coefficient measures  $5.6 \times 6.2 \times 3.5 \text{ mm}^3$  along the crystallographic axes  $x$ ,  $y$ , and  $z$ , respectively, and its  $z$  faces are optically finished. The measurements of the TPA anisotropy were performed with a sample where all faces have been optically finished *K4* ( $8.0 \times 8.0 \times 8.0 \text{ mm}^3$ ). Pump-probe experiments were performed in a thick sample *K16* ( $10.0 \times 8.5 \times 6.5 \text{ mm}^3$ ) that allows for a better signal-to-noise ratio.

### 3 Experimental results and discussion

#### 3.1 Single beam two-photon absorption

The left frame of Fig. 2 represents the reciprocal transmission  $T^{-1}$  as a function of intensity. The data are depicted for the case of beam propagation along the  $z$ -direction for several selected wavelengths in the range from  $E_g/2$  to  $E_g$ .

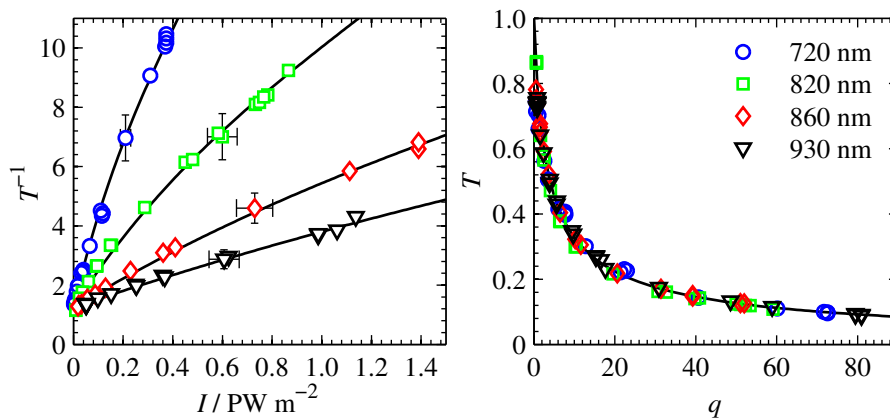


**Figure 2:** Reciprocal transmittance of the 3.5 mm thick SPS sample versus maximum peak on-axis intensity  $I_p^0$  of the 73 fs pulse on the input face (left frame), and sample transmission versus dimensionless parameter  $q = \beta I_p^0 \ell$  (right frame). The light beam propagates along the  $z$ -axis and is polarized along the  $x$ -axis. Circles, squares, diamonds, and triangles mark the wavelengths of the incident pulse as indicated in the legend. The solid lines in the left frame serve to guide the eye, while in the right frame it represents the dependence calculated for solely two-photon absorption (see Eq. (2)).

A noticeable beam attenuation of more than one order of magnitude is clearly observed. It can obviously be assigned to nonlinear absorption, because no pronounced photoinduced scattering or new light beams are detected during the measurements. We'd like to note, that supplementary investigations using the  $z$ -scan technique in principle allow the simultaneous detection of possible nonlinear refractive-index changes induced by the fs pulse. This aspect will be dealt with in the frame of another experimental study.

It is reasonable to assume that the observed beam attenuation is due to two-photon absorption (TPA). This is very likely, because of the photon energies being in a range

below the bandgap energy, and particularly covering  $E_g/2$ . Further, TPA of sub-ps-pulses has already been reported for other wide bandgap ferroelectric photorefractive crystals like  $\text{LiNbO}_3$  [15], as well. For proving this hypothesis, we model the transmission  $T$  as a function of the dimensionless parameter  $q = \beta I_p^0 \ell$  according to Ref. [16]. Here,  $\ell$  is the *effective* sample thickness that takes into account beam extinction due to linear absorption,  $I_p^0$  is the intensity of the incident beam and  $\beta$  is the two-photon absorption coefficient. For the particular case of two-photon absorption, and with the assumption of a laser pulse with spatial and temporal Gaussian shapes,  $T(q)$  can be expressed by:

$$T(q) = \frac{2}{q\sqrt{\pi}} \int_0^\infty \ln [1 + q \exp(-s^2)] ds. \quad (2)$$

Provided  $\ell$  and the peak power of the incident beam  $I_p^0$  are determined,  $\beta$  remains as single free parameter for plotting  $T_{\text{exp}}(q)$  using the experimentally determined transmission values. Optimizing the accordance of  $T_{\text{exp}}(q)$  and  $T(q)$ , we obtain the material parameter  $\beta$ . The fitting procedure is performed by minimizing

$$\chi_T^2(\beta) = \sum_i \frac{[T_{\text{exp}}(q_i) - T(q_i)]^2}{T(q_i)}, \quad (3)$$

i.e., the normalized quadratic deviation of the measured data from the fitting curve at a specific value of  $q$ . The outcome of the fitting procedure is depicted in Fig. 2 (right frame). Here, we have determined the effective sample thickness from the coefficients of the linear absorption and the sample dimension in  $z$ -direction. The incident beam intensity was calculated from Eq. (1) with the energy of the pulse entering the crystal, the beam waist and the pulse duration  $2t_p = \tau_p/\sqrt{\ln 2}$ , with  $\tau_p = 73$  fs being the FWHM of the pulse. Losses for Fresnel reflection from the input face are taken into account. Obviously, an excellent agreement between  $T_{\text{exp}}(q)$  and  $T(q)$  can be obtained, thus supporting the validity of TPA-model approach.

This procedure has been performed over the spectral range of 590 nm to 1630 nm so that we obtained the dispersion of  $\beta(\hbar\omega)$  depicted in Fig. 3.

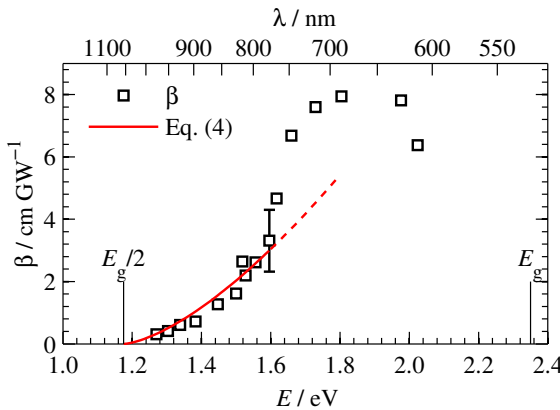


**Figure 3:** Photon energy  $E = \hbar\omega$  dependence of the TPA coefficient  $\beta$  of nominally undoped SPS. The light beam propagates along the  $z$ -axis and is polarized along the  $x$ -axis. The red solid line shows the result of the fit of Eq. (4) to the experimental data in the range of  $E_g/2$  to 1.6 eV. The dashed part (from 1.6 to 1.8 eV) is a continuation of the function using the parameters obtained from the fitting procedure.

The TPA nearly vanishes below  $\hbar\omega = 1.2$  eV, i.e., when the energy of two photons is near to or lower than the bandgap of SPS (at ambient temperature  $E_g \simeq 2.35$  eV

according to Ref. [2]). For photon energies ranging from  $E_g/2$  to 1.6 eV the TPA coefficient follows the functional dependence:

$$\beta \propto \left[ \left( \frac{2\hbar\omega}{E_g} \right) - 1 \right]^{3/2}. \quad (4)$$

In the range of  $1.6 \text{ eV} < \hbar\omega < 1.7 \text{ eV}$ , a pronounced increase of  $\beta$  is found, while it saturates at  $\approx 1.8 \text{ eV}$ . This increase can not be modeled by Eq. (4) that is plotted for comparison in the range from 1.6 to 1.8 eV using the parameters obtained from the fitting procedure (dotted part of the red line in Fig. 3). For photon energies  $\hbar\omega \geq 2.0 \text{ eV}$ , the TPA coefficient decreases. Similar behavior on the photon energy is found for different light polarizations and directions of beam propagation with respect to the crystallographic axes. Slightly smaller values (within 10 %) of  $\beta$  were measured solely for a beam propagating along the  $z$ -axis as compared to the two other directions.

In perturbation theories of two-photon absorption the characteristic superlinear photon energy dependence of  $\beta$  according to Eq. (4) is usually an issue of models with allowed-forbidden transitions [17–19]. As it is shown in Ref. [19] the TPA coefficient follows the dependence of Eq. (4) starting from  $\hbar\omega$  very close to  $E_g/2$ , but then tends to saturation for higher quantum energies. Thus, at least in the range of  $\hbar\omega$  from 1.2 to 1.6 eV the TPA coefficient features one of the two known standard behaviors. However, more careful theoretical analysis is necessary.

For the analysis of the characteristic behavior of  $\beta(\hbar\omega)$  for quantum energies exceeding 1.6 eV, we consider the results obtained with combined EPR/absorption spectroscopy [9]. Very strong light-induced changes of the absorption were found in nominally undoped samples. Predominant is the appearance of a broad absorption feature with a maximum at 2.0 eV and a band width of  $\approx 0.8 \text{ eV}$  [9, 20]. As will be described below, this photochromism can be related to the formation of  $S^-$  small hole polarons [4]. It is reasonable to suggest the possibility that the populated energy levels give rise to single-photon absorption in this spectral region as well, which will affect the two-photon absorption. However, a compelling precondition is that the formation time of the light-induced absorption falls within the duration of the pump pulse, i.e. below 75 fs.

It should be mentioned that nonlinear absorption was also observed for photon energies below  $E_g/2$ . However, the beam attenuation was comparatively weak in this spectral range. Furthermore, its intensity dependence strongly deviated from the behavior shown in Fig. 2 (left frame), i.e., the transmission decreased more rapidly as a function of intensity. It is reasonable to attribute this effect to three-photon absorption.

### 3.2 Pump-probe experiments

Fig. 4 shows the dependence of the probe beam transmission on the temporal delay  $\Delta t$  between pump and probe pulses up to  $\Delta t = 25 \text{ ps}$ . The results are depicted for a probe beam propagation along the  $z$ -axis of the sample, a light polarization parallel to the  $y$ -axis, and identical wavelengths of  $\lambda = 626 \text{ nm}$  (1.98 eV) for pump and probe pulse.

Their respective intensities are set to  $(860 \pm 50) \text{ TW m}^{-2}$  and  $(4.6 \pm 0.3) \text{ TW m}^{-2}$ , i.e., an intensity ratio of  $\approx 190 : 1$ . At 626 nm, the linear absorption was determined to  $\alpha = (0.49 \pm 0.05) \text{ cm}^{-1}$ .

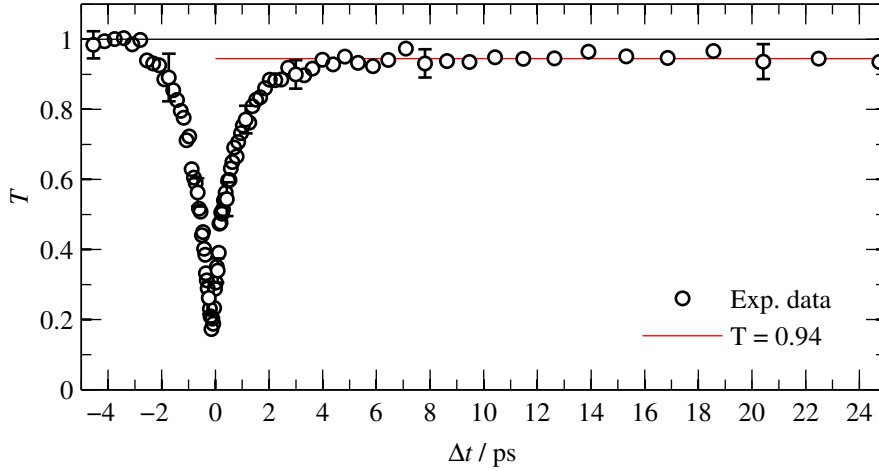


**Figure 4:** Beam attenuation of the SPS sample *K16* as a function of the time delay between pump and probe pulses. Wavelength:  $\lambda = 626 \text{ nm}$ , light polarization parallel  $y$ -axis, and beam propagation along  $z$ -direction. The red line marks the saturation value of the transmission of  $T \approx (94 \pm 2)\%$  for  $\Delta t \gg 5 \text{ ps}$ .

The normalized transmission shows a strong decrease to a value below 20% as compared to the transmission of the unexposed sample, i.e., to the transmission for  $\Delta t \rightarrow -\infty$ . The value of the transmission in the minimum depends on the pulse intensity in accordance with our findings in the previous section (Fig.2, left frame), so that we can attribute this dip to the presence of two-photon absorption. Therefore, the delay time, at which the minimum value of  $T(\Delta t)$  is observed, corresponds to the superposition of pump and probe pulses in the time domain ( $\Delta t = 0$ ).

For probe pulse delays  $\Delta t \gg \tau_p$  (shown up to 25 ps after the pump pulse in the figure), the transmission value remains constant at  $T = (94 \pm 2)\%$  (red line). Hence, the initial value related to the presence of linear absorption is not recovered. This transmission value was still observed for the maximum time delay of  $\Delta t = 2.5 \text{ ns}$  that can be adjusted with our experimental setup. Probing the sample transmission with one of the subsequent probe pulses at  $\Delta t = 1 \text{ s}$ , the initial transmission  $T(\Delta t \rightarrow -\infty)$  was measured. According to this signal recovery we conclude the presence of a transient absorption induced by the pump pulse. This signal can not be assigned to pump-pulse induced damages to the sample's surface or bulk. Influences of the transient absorption induced by the previous pump pulse are eliminated by reducing the repetition rate of our measurement to less than 3 Hz.

Such transients are reported for a variety of ferroelectric semiconductors upon exposure to ns- and fs-laser pulses. The effect can be either attributed to free-carrier absorption or to absorption that is due to formation of small polarons. Respective optically generated carrier densities decay with relaxation times in the range from several tens of picoseconds up to milliseconds (free carriers) and seconds (small bound polarons). For instance, the transients in ferroelectric  $\text{LiNbO}_3$ , where small polaron

formation is confirmed (e.g.  $\text{Nb}_{\text{Li}}^{4+}$  in Ref. [21]), show relaxation times in the range of a few milliseconds (see Ref. [15]).

For non-stoichiometric nominally undoped SPS, the optical formation of  $\text{S}^-$  small hole polarons seems likely in accordance with the recent results of Vysochanskii et al. [4]: Light exposure removes electrons from the valence band, that is formed by 3p orbitals from sulfur and phosphorous. Thus, the remaining hole recharges  $\text{S}^{2-}$  yielding  $\text{S}^-$  that is related with a structural deformation, i.e. small hole polarons [22] appear. The optical features of  $\text{S}^-$  were shown to coincide with the light-induced broad absorption feature at 2.0 eV [4] that were experimentally reported by Ruediger et al. [9].

Taking these aspects into account, we can suggest the following mechanism for the appearance of the transients at 626 nm: The pump pulse (1.98 eV) generates a significant density of  $\text{S}^-$  small hole polarons by removing electrons from the valence band via two-photon absorption. The probe pulse (1.98 eV) is attenuated due to the broad absorption feature of the  $\text{S}^-$  absorption band that is centered at 2.0 eV. The subsequent relaxation of the induced polaron density may occur via hopping of thermally activated polarons between different  $\text{S}^{2-}$  sites with the ultimate electron-hole recombination in the time domain less than one second. It should be noted that similar processes initiated by two-photon absorption were reported upon ns-laser pulse exposure in various nominally undoped ferroelectrics such as  $\text{LiNbO}_3$  and  $\text{KNbO}_3$  [23, 24]. It is likely, that hole polaron formation appears in the temporal range below 200 fs, as it was experimentally studied in the original work of Qiu et al. for small polarons in  $\text{LiNbO}_3$  [25]. Thus, the formation is overlaid by the strong beam attenuation related to two-photon-absorption and can not be resolved in our experiment. Measurements of the temperature dependence of the relaxation time and with different photon energies of pump- and probe pulses are necessary to verify this model approach for SPS.

## 4 Conclusion

Femtosecond pulses with photon energies within the range from 0.76 eV to 2.1 eV are strongly attenuated when propagating through the SPS sample because of instantaneous nonlinear absorption via two-photon or three-photon absorption. The measured TPA coefficients  $\beta$  up to  $8 \text{ cm GW}^{-1}$  are by a factor of two higher than the values reported for other wide bandgap ferroelectrics, such as  $\text{LiNbO}_3$  [15], while being lower in comparison to semiconductor crystals [18]. A second feature of fs-pulse interaction with SPS is the appearance of a metastable transient absorption that is typical for a variety of wide bandgap ferroelectrics. It might be attributed to the optical generation of  $\text{S}^-$  small hole polarons.

### Acknowledgements

The financial support of the Deutsche Forschungsgemeinschaft via projects IM 37/5-1, IM 37/7-1, and INST 190/137-1FUGG is gratefully acknowledged. We are thankful to A. Grabar and I. Stoyka for SPS samples and to S. Odoulov for helpful discussions. A. Shumelyuk is grateful to the German colleagues for their hospitality during his

stay in Osnabrück as DFG guest scientist.

## References

- [1] G. Dittmar, H. Schäfer, “Crystal structure of  $\text{Sn}_2\text{P}_2\text{S}_6$ ,” *Z. Naturforsch. B* **29B**, 312–317 (1974).
- [2] R. V. Gamernyk, Yu P. Gnatenko, P. M. Bukivsiy, P. A. Skubenko, V. Yu Slivka, “Optical and photoelectric spectroscopy of photorefractive  $\text{Sn}_2\text{P}_2\text{S}_6$  crystals,” *J. Phys.: Condens. Matter* **18**, 5323–5331 (2006).
- [3] K. Kuepper, B. Schneider, V. Caciuc, M. Neumann, A. V. Postnikov, A. Ruediger, A. A. Grabar, Yu. M. Vysochanskii, “Electronic structure of  $\text{Sn}_2\text{P}_2\text{S}_6$ ,” *Phys. Rev. B* **67**, 115101 (2003).
- [4] Yu. M. Vysochanskii, K. Glukhov, K. Fedyo, and R. Yevych, “Charge transfer and anharmonicity in  $\text{Sn}_2\text{P}_2\text{S}_6$  ferroelectrics,” *Ferroelectrics*, **414**, 30–40 (2011).
- [5] S. G. Odoulov, A. N. Shumelyuk, U. Hellwig, R. A. Rupp, A. A. Grabar, and I. M. Stoyka, “Photorefraction in tin hypthiodiphosphate in the near infrared,” *J. Opt. Soc. Am. B* **13**, 2352–2360 (1996).
- [6] A. A. Grabar, M. Jazbinsek, A. N. Shumelyuk, Yu. M. Vysochanskii, G. Montemezzani, and P. Günter, “Photorefractive effects in  $\text{Sn}_2\text{P}_2\text{S}_6$ ,” in *Photorefractive materials and their applications II*, P. Günter and J.-P. Huignard, eds. (Springer Verlag, New-York, 2007), pp. 327–362.
- [7] R. Mosimann, P. Marty, T. Bach, F. Juvalta, M. Jazbinsek, P. Günter, A. A. Grabar, I. M. Stoyka, and M. Vysochanskii, “High-speed photorefraction at telecommunication wavelength  $1.55\ \mu\text{m}$  in  $\text{Sn}_2\text{P}_2\text{S}_6:\text{Te}$ ,” *Opt. Lett.* **32**, 2330–2332 (2007).
- [8] A. Shumelyuk, A. Hryhorashchuk, S. Odoulov, “Coherent optical oscillator with periodic zero- $\pi$  phase modulation,” *Phys. Rev. A* **72**, 023819 (2005).
- [9] A. Ruediger, O. Schirmer, S. Odoulov, A. Shumelyuk, A. Grabar, “Studies of light-induced charge transport in  $\text{Sn}_2\text{P}_2\text{S}_6$  by combined EPR/optical absorption spectroscopy,” *Opt. Mat.* **18**, 123–125 (2001).
- [10] A. Shumelyuk, M. Wesner, M. Imlau, and S. Odoulov, “Double-phase conjugate mirror in nominally undoped  $\text{Sn}_2\text{P}_2\text{S}_6$ ,” *Opt. Lett.* **34**, 734–736 (2009).
- [11] A. Shumelyuk and S. Odoulov, “Light pulse manipulation in  $\text{Sn}_2\text{P}_2\text{S}_6$ ,” *J. Opt.* **12**, 104015 (2010).
- [12] G. von Bally, F. Rickermann, S. Odoulov, and A. Shumelyuk, “Near-infrared holographic recording in  $\text{Sn}_2\text{P}_2\text{S}_6$  with nanosecond pulses,” *phys. stat. sol. (a)*, **157**, 199–204 (1996).
- [13] T. Bach, K. Nawata, M. Jazbinsek, T. Omatsu, P. Günter, “Optical phase conjugation of picosecond pulses at  $1.06\ \mu\text{m}$  in  $\text{Sn}_2\text{P}_2\text{S}_6:\text{Te}$  for wavefront correction in high-power Nd-doped amplifier systems,” *Opt. Express* **18**, 87–95 (2010).
- [14] A. A. Grabar, I. V. Kedyk, M. I. Gurzan, I. M. Stoika, A. A. Molnar, Y. M. Vysochanskii, “Enhanced photorefractive properties of modified  $\text{Sn}_2\text{P}_2\text{S}_6$ ,” *Opt. Commun.* **188**, 187–194 (2001).

- 
- [15] O. Beyer, D. Maxien, K. Buse, B. Sturman, T. H. Hsieh, and D. Psaltis, "Investigation of nonlinear absorption processes with femtosecond light pulses in lithium niobate crystals," *Phys. Rev. E*, **71**, 056603 (2005).
- [16] M. Sheik-Bahae, A.A. Said, T.-H. Wei, D. J. Hagan, E. W. Van Stryland, "Sensitive measurement of optical nonlinearities using a single beam," *IEEE J. Quant. Electron.* **26**, 760–769 (1990).
- [17] V. Nathan, A. H. Guenter, S. S. Mitra, "Review of multiphoton absorption in crystalline solids," *J. Opt. Soc. Am. B* **2**, 294–316 (1985).
- [18] E. W. Van Stryland, M. A. Woodall, H. Vanherzeele, and M. J. Soileau, "Energy band-gap dependence of two-photon absorption," *Opt. Lett.* **10**, 490–492 (1985).
- [19] D. C. Hutchings, B. S. Wherrett, "Theory of anisotropy of two-photon absorption in zinc-blende semiconductors," *Phys. Rev. B* **49**, 2418–2426 (1994).
- [20] A. Ruediger, "Light induced charge transfer processes and pyroelectric luminescence in  $\text{Sn}_2\text{P}_2\text{S}_6$ ," PhD-thesis, University of Osnabrück (2001).
- [21] D. Berben, K. Buse, S. Wevering, P. Herth, M. Imlau, T. Woike, "Lifetime of small polarons in iron-doped lithium-niobate crystals," *J. Appl. Phys.* **87**, 1034–1041 (2000).
- [22] O. F. Schirmer, " $\text{O}^-$  Bound Small Polarons in Oxide Materials," *J. Phys.: Condens. Matter* **18**, R667 (2006).
- [23] P. Herth, T. Granzow, D. Schaniel, Th. Woike, M. Imlau, E. Krätzig, "Evidence for light-induced hole polarons in  $\text{LiNbO}_3$ ," *Phys. Rev. Lett.* **95**, 067404 (2005)
- [24] S. Torbrügge, M. Imlau, B. Schoke, C. Merschjann, O. F. Schirmer, S. Vernay, A. Gross, V. Wesemann, D. Rytz, "Optically generated small electron and hole polarons in nominally undoped and Fe-doped  $\text{KNbO}_3$  investigated by transient absorption spectroscopy," *Phys. Rev. B* **78**, 125112 (2008).
- [25] Y. Qiu, K. B. Ucer, R. T. Williams, "Formation time of a small electron polaron in  $\text{LiNbO}_3$ : measurements and interpretation," *phys. stat. sol. (c)* **2**, 232–235 (2005).

# Self-diffraction from two-photon absorption gratings in Sn<sub>2</sub>P<sub>2</sub>S<sub>6</sub>

A. Shumelyuk<sup>1,\*</sup>, M. Imlau<sup>2</sup>, V. Dieckmann<sup>2</sup>, H. Badorreck<sup>2</sup>,  
A. Grabar<sup>3</sup> and S. Odoulov<sup>1</sup>

<sup>1</sup> *Institute of Physics, National Academy of Sciences, 03 650, Kyiv, Ukraine*

<sup>2</sup> *Fachbereich Physik, University of Osnabrück, D-49076, Osnabrück, Germany*

<sup>3</sup> *Uzhgorod National University, 88 000, Uzhgorod, Ukraine*

\* *Corresponding author: shumeluk@iop.kiev.ua*

**Abstract:** Self-diffraction with the appearance of higher diffraction orders is discovered when writing a grating with a single sub 100 fs pulse in a nominally undoped Sn<sub>2</sub>P<sub>2</sub>S<sub>6</sub> sample. The short time of grating development, dependence of diffraction efficiency on the recording light intensity, correlation of wavelength dependence of efficiency with the spectrum of the two-photon absorption constant and a  $\pi$  phase shift of the diffracted beam allow for attributing the recorded grating to a dynamic amplitude grating of two-photon absorption.

©2012 Optical Society of America. This work was published in Optics Letters and can be found at the URL <http://dx.doi.org/10.1364/OL.37.004065>. One print or electronic copy may be made for personal use only. Systematic reproduction and distribution, duplication of any material in this paper for a fee or for commercial purposes, or modifications of the content of this paper are prohibited.

Tin hypthiodiphosphate (Sn<sub>2</sub>P<sub>2</sub>S<sub>6</sub>, SPS) is a promising nonlinear material for dynamic holographic recording with CW light [1] as also with repetition rate pulsed radiation up to the picosecond range [2]. It has been shown recently that femtosecond light pulses with photon energies within the range from 1.5 to 2.1 eV are strongly attenuated in nominally undoped SPS crystals via two-photon absorption (TPA), with a TPA coefficient  $\beta$  that reaches a maximum value up to 8 cm/GW [3]. Thus for the peak pulse intensities  $I \approx 1$  GW/cm<sup>2</sup> the product  $\beta I = 8$  cm<sup>-1</sup> is roughly one order of magnitude larger than the linear absorption of SPS  $\alpha \leq 1$  cm<sup>-1</sup> [1] and the recording of high contrast amplitude gratings could be expected.

Apart from instantaneous amplitude gratings of nonlinear absorption the interfering fs pulses may also record phase gratings in wide bandgap photorefractive crystals as SPS: an instantaneous index grating via optical Kerr effect and inertial index grating via excitation of free carriers or polarons [4, 5] as also space charge grating [5, 6]. Gratings related to other nonlinear effects can be expected, too. In this paper we report on dynamic grating recording with single femtosecond pulses and describe the

studies that allow for identifying the process that contributes the most to the grating appearance.

The SPS crystals are grown in the Institute of Solid State Physics and Chemistry of Uzhgorod State University by chemical vapor transport. The most part of the measurements presented below are performed with a  $z$ -cut nominally undoped sample (sample identifier K16, with thickness  $\ell = 6.5$  mm along  $z$ -axis). A 1 kHz repetition rate tunable laser with sub-100 fs pulses (see Ref. 3) is used as a light source (600-760 nm,  $\bar{P} \leq 20$   $\mu$ J). The pulse energy at the sample input face is controlled with a set of calibrated neutral density filters. The attenuation with relatively small temporal pulse broadening (roughly within 5 per cent) is ensured.

To record a grating, a 20 lines/mm Ronchi ruling is imaged into the SPS sample with a symmetric telescope formed by two lenses  $L_1$  and  $L_2$  with the focal length  $F_1 = 150$  mm (Fig.1). The amplitude mask  $AM_1$  is placed in the Fourier plane of the first lens  $L_1$  that selects only +1. and -1. diffraction orders from the multitude of the diffraction spots. In such a way a high contrast fringe pattern with cosine intensity distribution is projected inside the sample, with the fringe spacing  $\Lambda = 25$   $\mu$ m. This technique has been successfully used in the past for photorefractive grating recording with spatially incoherent light [7]. It appears to be especially attractive when writing gratings with femtosecond pulses [8] because of the best possible temporal and spatial overlap of short pulses.

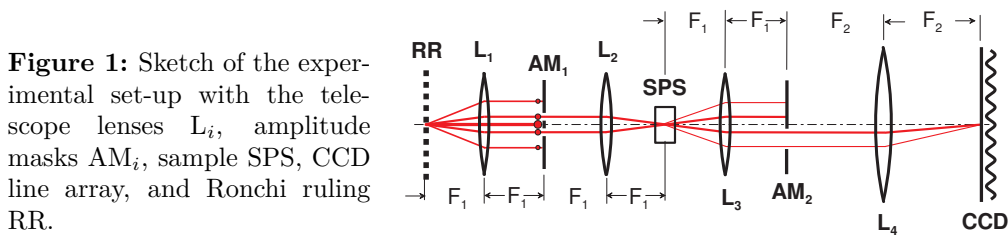


**Figure 1:** Sketch of the experimental set-up with the telescope lenses  $L_i$ , amplitude masks  $AM_i$ , sample SPS, CCD line array, and Ronchi ruling RR.

Apparently, the selfdiffraction from a homogeneous in depth dynamic grating with 25  $\mu$ m spacing in a 6.5-mm-thick sample should be well beyond Raman-Nath type as the relevant Klein-Cook factor  $Q = (2\pi\lambda\ell/\Lambda^2n) \approx 14$  is larger than 10 [9] and Moharam-Gaylord criterion [10],  $\rho = (\lambda^2/n\Delta n\Lambda^2) \approx 22 \gg 10$  is also met with justified assumption that  $\Delta n \leq 10^{-5}$ . Several different phenomena can lead, however, to the appearance of the higher diffraction orders. The most plausible is in strong reduction of the effective depth  $\ell_{eff}$  of the dynamic grating (up to  $\approx 100$   $\mu$ m at  $I \approx 10$  GW/cm<sup>2</sup>) and consequent violation of the Klein-Cook criterion. Whatever the real reason is, higher diffraction orders, apart from the transmitted two recording beams, are clearly observed in the Fourier plane of the lens  $L_3$  placed behind the SPS sample.

By selecting the first non-Bragg order [11] with the mask  $AM_2$  the energy of the diffracted pulse can be measured with a Si-PIN detector (not shown in Fig. 1). Being normalized to the recording pulse energy it gives the measure of the integral diffraction efficiency  $\eta$ .

The lens  $L_3$  is also a part of the second telescope which is imaging the output surface of the SPS sample to the CCD line array (with magnification, as the focal length of the lens  $L_4$  is  $F_1 = 2250$  mm.) The intensity distribution along the wavevector of the fringe pattern is measured with the CCD line array and stored in a data acquisition

system. The spatial filtering in the Fourier plane of the lens  $L_3$  allows for passing the fringe patterns formed either by the two transmitted recording beams or by one recording and one diffracted beams to the CCD line array. By determining the phase shift between these two fringe patterns one can distinguish, as it is explained below, the type of the recorded grating (amplitude or phase grating).

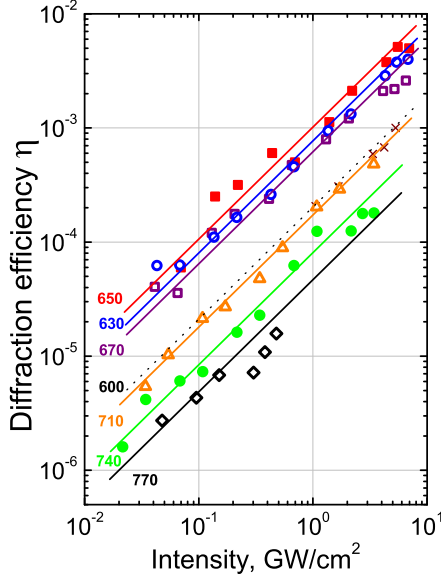


**Figure 2:** Intensity dependence of the diffraction efficiency for the recording wavelengths 600 nm (crosses), 630 nm (open dots), 650 nm (filled squares), 670 nm (open squares), 710 nm (triangles), 740 nm (filled dots), and 770 nm (diamonds). Solid lines are drawn to guide the eye.

In the first set of experiments we measure the diffraction efficiency  $\eta$  in individual pulses for an established repetition rate regime with 1 Hz frequency. No cumulative effects are detected within the power and energy range of pulses used for recording. After several minutes of continuous periodic excitation the amplitude of the diffracted signal remains the same as in the few initial pulses, fluctuating within  $\pm 5\%$ . This allows for averaging the measured data over the train of consecutive 20 pulses, to reduce their natural scatter.

Then, the intensity dependences of the diffraction efficiency for different recording wavelengths are measured (Fig. 2). The intensity was calculated under approximation of a Gaussian temporal profile; all data refer to the peak intensity values. Within the error bars all dependences of Fig. 2 show roughly a linear increase of the efficiency versus intensity,  $\eta \propto I$ .

Taking into account that  $\eta$  is an average in time and in space (but not local and instantaneous) value of the diffraction efficiency the linear  $\eta \propto I$  dependence in Fig. 2 has no special meaning here and is most probably accidental, typical only for limited intensity range in which our measurements are done. It allows nevertheless to claim that we are dealing with the nonlinear recording and extract from the data of Fig. 2 the normalized spectral sensitivity of SPS to grating recording,

Figure 3 shows the wavelength dependence of the diffraction efficiency  $\eta$  measured at  $I = 1 \text{ GW/cm}^2$ . This dependence fits qualitatively well to the spectrum of the TPA coefficient  $\beta$  for nominally undoped SPS (see Fig. 3 of Ref. 3), with its maximum in the vicinity of  $\lambda = 650 \text{ nm}$ . It might suggest that our dynamic grating is somewhat related to nonlinear absorption in the sample and rule out its attribution to the optical Kerr effect. It does not prove however that selfdiffraction originates just from

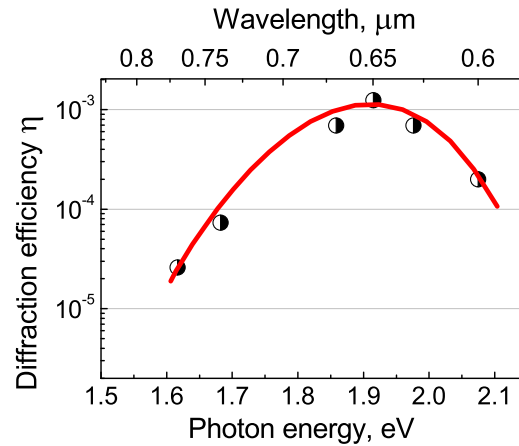


**Figure 3:** Diffraction efficiency of the dynamic grating in the 6.5-mm-thick SPS sample versus recording wavelength for a fixed recording intensity of  $1 \text{ GW/cm}^2$ . Solid line is drawn to guide the eye.

the absorption grating itself: being excited via TPA the gratings of free carriers or polarons can demonstrate similar spectra, too.

While the TPA grating is a pure amplitude grating the free carrier and polaron gratings may feature both amplitude and phase components, with relative weights that depend on the excitation wavelength (see, e.g. the data of Ref. 12). As it was shown in [3] the contribution of free carriers or polarons to the nonlinear absorption in SPS is detectable but very small, less than 7 per cent of TPA at 630 nm. At the same time, even relatively small index variation can result in noticeable diffraction. Thus for identifying the dominant process responsible for selfdiffraction one needs to establish the type of the appearing grating: amplitude, phase, or mixed grating.

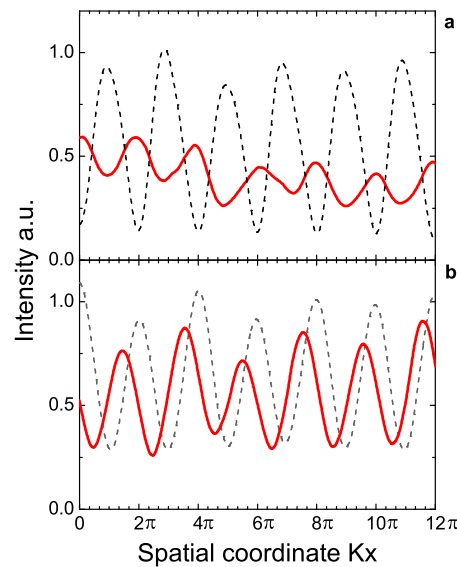


**Figure 4:** Intensity scan of the fringe pattern from the two recording light beams (dashed line) and from the recording and non-Bragg diffracted beams (solid line). (a) Grating recording and simultaneous readout with 75 ps light pulses at  $\lambda = 650 \text{ nm}$  in the 6.5-mm-thick SPS sample. (b) Grating recording and readout with cw He-Ne laser light ( $\lambda = 630 \text{ nm}$ ) in a 0.5-mm-thick SPS sample

It is known [10] that for the phase grating the phase difference between the adjacent orders is  $\pi/2$  while for the amplitude grating this difference is either zero or  $\pi$ . With this in mind, we compare the relative positions of two fringe patterns, one generated by two transmitted recording beams and the other from one recording beam and the adjacent diffracted beam (as it is shown in Fig. 1). The selection of relevant diffraction orders is made in the focal plane of the lens  $L_3$  with aperture  $AM_2$ . The

recorded intensity distributions are shown in Fig. 4a by dashed black and solid color lines. The sample optical imperfections affect the fringe quality, especially for low contrast fringes produced by the recording and diffracted beams. This does not prevent however from concluding that in both cases the fringes with the same spacing are observed and that *they are nearly out-of-phase, i.e., fringes are  $\pi$ -shifted*.

To check the validity of such a technique of phase shift evaluation a similar test is done with cw He-Ne laser radiation. It is expected that the dominant dynamic grating in case of cw recording is the phase grating which is due to space charge redistribution [1].

The whole recording arrangement is kept the same except the laser source and SPS sample. The observation of non-Bragg diffraction orders appeared to be impossible with the 6.5-mm-thick sample. Therefore, a thin  $z$ -cut sample of nominally undoped SPS with  $\ell = 0.5$  mm is used, its  $x$ -axis being aligned perpendicularly to the light fringes. The Klein-Cook factor is small enough,  $Q \approx 1.3$ , to observe Raman-Nath self-diffraction from the thin photorefractive grating.

Figure 4b shows the results of the measurements, with the same color coding, dashed black line for recording fringes and solid color line for fringes from the recording beam and the adjacent non-Bragg diffracted beams. The difference to the result presented in Fig. 4a is evident: now two fringe patterns are dephased roughly to one quarter of fringe spacing, thus indicating a  $\pi/2$ -shift between the adjacent Bragg and first non-Bragg orders.

All results mentioned above lead to the conclusion that the most significant part of the described selfdiffraction of fs-pulse radiation in SPS comes from the dynamic amplitude grating related to two photon absorption.

**Acknowledgements** The financial support of the Deutsche Forschungsgemeinschaft via projects IM 37/5, IM 37/9-1, and INST 190/137-1 FUGG is gratefully acknowledged. A. S. and S. O. are grateful to German colleagues for their hospitality during research stay in Osnabrück.

## References

- [1] A. Grabar, M. Jazbinsek, A. Shumelyuk, Yu. Vysochanskii, G. Momtemezzani and P. Günter, 2007 "Photorefractive effects in Sn<sub>2</sub>P<sub>2</sub>S<sub>6</sub>," in *Photorefractive materials and their applications 2*, P. Günter and J.-P. Huignard, eds. (New York, NY: Springer-Verlag), pp. 327-362.
- [2] T. Bach, K. Nawata, M. Jazbinsek, T. Omatsu, and P. Günter, *Opt. Express*, **18**, 87-95 (2010).
- [3] M. Imlau, V. Dieckmann, H. Badorreck, and A. Shumelyuk, *Opt. Mat. Express*, **1**, 954-960 (2011).
- [4] Z. Wang, X. Zhang, J. Xu, Q. Wu, H. Qiao, B. Tang, R. Rupp, Y. Kong, S. Chen, Z. Huang, B. Li, S. Liu, and L. Zhang, *Chin. Phys. Lett.* **22**, 2831-2833 (2005).
- [5] B. Sturman, O. Beyer, D. Maxein, and K. Buse, *J. Opt. Soc. Am. B*, **24**, 419-429 (2007).

- [6] Md. Masudul Kabir, Daiki Ito, Yu Oichi, Fumihiko Kannari, Jap. J. Applied Physics, **50**, 102702-(1-8) (2010).
- [7] R. Grousseau, S. G. Odoulov, Opt. Commun. **39**, 219-224 (1981).
- [8] A. A. Maznev, T. F. Crimmins, and K. A. Nelson, Opt. Lett. . **23**, 1378-1380 (1998).
- [9] R. J. Collier, C. B. Burckhardt, and L. H. Lin, "Optical holography", Academic Press, NY, 1971, 605 p..
- [10] M. G. Moharam and L. Young, Appl. Opt. , **17**, 1757-1759 (1978).
- [11] We use these notations to distinguish between "Bragg" orders (two recording beams being Bragg-matched to the fundamental grating with the grating vector  $\mathbf{K} = \mathbf{k}_1 - \mathbf{k}_2$ ) and two adjacent, "non-Bragg", orders (i.e., violating Bragg condition for fundamental grating  $\mathbf{K}$ ). Note, that the recording beams are not Bragg-matched for the grating with the doubled spatial frequency  $2K$ , which also occurs under two-photon excitation.
- [12] M. Imlau, Brüning, B. Schoke, R-S Hardt, D. Conradi, C Merschjann, Opt. Express, **19**, 15322-15338 (2011).

# Interference and holography with femtosecond laser pulses of different colors

Serguey Odoulov<sup>1,\*</sup>, Alexandr Shumelyuk<sup>1</sup>, Holger Badorreck<sup>2</sup>,  
Stefan Nolte<sup>2</sup>,  
Kay-Michael Voit<sup>2</sup> and Mirco Imlau<sup>2</sup>

<sup>1</sup>*Institute of Physics, National Academy of Sciences, 03 650 Kyiv, Ukraine,*

<sup>2</sup>*Department of Physics, Osnabrueck University, D-49076 Osnabrueck, Germany,*

\* *Corresponding authors: odoulov@iop.kiev.ua and/or mirco.implau@uni-osnabrueck.de*

**Abstract:** Interferometry and holography are two domains that are based on observation and recording of interference fringes from two light beams. While the aim of the first technique is to reveal and map the phase difference of two wave fronts, the main task of the second technique is to reconstruct one of the two recording waves via diffraction of the other wave from the recorded fringe pattern (hologram). To create fringes, mutually coherent waves from the same laser are commonly used. It is shown here that fringes can be observed and holograms be recorded with ultrashort, sub-picosecond pulses even of different color, generated in our experiment with two parametric amplifiers seeded, both, by the same mode-locked Ti-sapphire laser. The appearance of permanent and transient gratings is confirmed by recording of an image-bearing hologram, by observation of two-beam coupling gain in a pump-probe experiment and by frequency conversion in Raman-Nath selfdiffraction from a moving grating.

This work is reproduced with kind permission of the Nature Publishing Group. The original work can be found on the Nature Communication website at the URL <http://dx.doi.org/10.1038/ncomms6866>.

## 1 Introduction

The idea of wave front recording and reconstruction, known today as holography<sup>1</sup> was formulated by Denis Gabor in 1947. His proof of principle experiment was done with the light of high pressure mercury lamp; it was necessary, however, to wait more than a decade for invention of lasers to ensure holographic recording with really high quality of image reconstruction. The source of coherent radiation is necessary to form the interference pattern of the object wave and reference wave, that could be replicated in the recording material as a hologram. The important requirement to the light source is also its sufficiently large coherence length to ensure high enough contrast of fringes formed by different components of the object wave with the reference wave. Thus, it is universally accepted now that to record a hologram, both waves, object and

reference, should be generated from the same laser which emit, preferably, a single longitudinal TEM<sub>00</sub> mode.

In this letter we report on experiments aiming the holographic grating recording with two laser sources that generate, in addition, light with considerably different optical frequencies, more precisely blue and green light. The success of this counter-intuitive experiment is ensured by using ultrashort,  $\approx 100$  fs pulses from two different optical parametric amplifiers. In our particular experiment the fringes formed by a blue beam with a green one are moving with a speed only 3 times smaller than light velocity. With 100 fs pulses, however, the displacement of the fringe pattern as a whole is less or comparable with one fringe spacing and the fringe contrast averaged over the pulse duration is still quite high.

The field of femtosecond holography is already well established today by the successful demonstration of static holograms recording (see, e.g., Refs. 2-5). So far, the recording was performed in a traditional way by beams from the same femtosecond laser, the spectral content of the two recording beams being identical. Also, starting from papers of Claude Froehly et al.<sup>6</sup> the so called "spectral holography"<sup>6-8</sup> (and later "spectral nonlinear optics"<sup>9</sup>) were used for recording, reconstruction and processing of temporal envelopes of the short pulses. In a series of papers initiated by a publication of Karsten Buse et al.<sup>10</sup> the light with the wavelength other than that necessary for grating recording was used to improve the holographic sensitivity of the medium (some researchers called it "two-color holography".) In all above papers, as also in similarly oriented other papers, the recording of permanent holographic gratings by beams with considerably different frequencies was never considered.

Our interest in grating recording with beams of different color is motivated by its possible impact on the field of ultrafast optics, where the interaction of two or more ultrashort laser pulses within an optical medium is a common situation. The researchers face it in fundamental studies and in different applications, from frequency conversion to sensitive measurements of nonlinear constants of optical materials used in this domain.

At present, the absolute majority of papers that treat nonlinear interaction of two short pulses with different photon energies focus on coupling that depends on the integral intensities,  $I_{pu}$  and  $I_{pr}$  (subscripts  $pu$  and  $pr$  mark pump and probe pulses, respectively). These intensities are different for different frequencies  $\omega$ , depend on time  $t$  and propagation coordinate  $z$  but the interference of the pulse fields, i.e., the small scale variations of total intensity in transverse direction  $x$  is disregarded in the case of different pulse frequencies. This can result in unexpected experimental observations or lead to misinterpretation of the obtained data sets, because the self diffraction from the grating which might be recorded by these fringes brings by itself an additional direct beam coupling. The unusual result of our pump-probe experiments with LiNbO<sub>3</sub> crystal described below, in the beginning of the next Section, serves as a representative example. An example of possible application of the considered phenomenon, the frequency (up- and down-) conversion is demonstrated, which is because of the Raman-Nath diffraction from the the moving grating recorded by pulses of different colors.

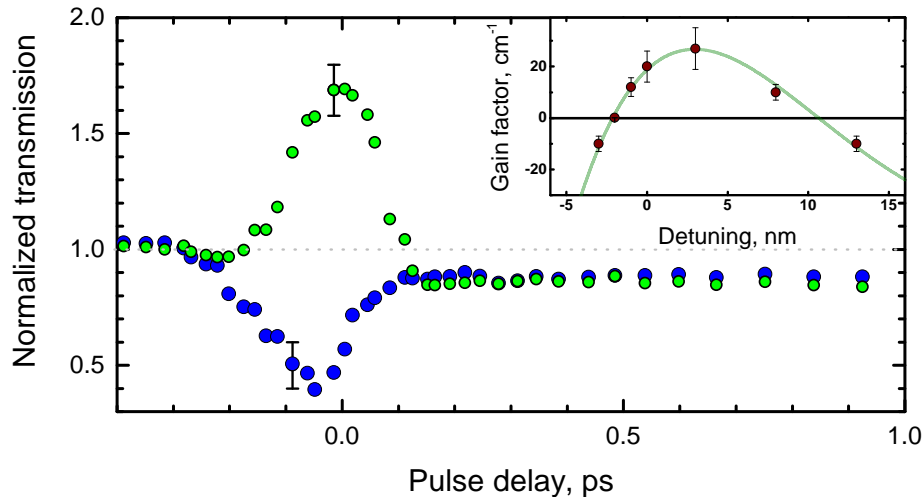


**Figure 1: Pump-probe experiment with  $\text{LiNbO}_3$ .** The probe beam transmission versus time delay of the probe pulse with respect to the pump pulse. The wavelengths of the probe pulse are 485 nm and 493 nm for blue and green dots, respectively, the pump wavelength  $\simeq 490$  nm. The inset shows the detuning dependence of the net gain factor (amplification minus absorption) for probe and pump pulses matched in time.

## 2 Results

**Manifestation of self-diffraction in pump-probe experiments.** When trying to clarify the formation dynamics of small electron (or hole) polarons<sup>11</sup> in  $\text{LiNbO}_3$  the normalized probe pulse transmission  $\Delta T/T$  was measured in a range  $-500 \text{ fs} \leq \Delta t \leq 1000 \text{ fs}$  of the probe pulse delay times. These measurements have been performed within a broad spectral range of the probe wavelength variation,  $400 \text{ nm} \leq \lambda \leq 900 \text{ nm}$ , with the intention to cover spectral manifestations of the small polarons, the pump wavelength being fixed at 490 nm.

Figure 1 shows the normalized probe pulse transmission  $\Delta T/T$  as a function of the probe pulse delay time  $\Delta t$  with respect to the pump pulse. For large wavelength detunings (much larger than FWHM of pulse spectral content  $\approx 5 \text{ nm}$ ) the measured dependence shows a well known dip at  $\Delta t = 0$ , which is due to the two photon absorption (blue data dots, see, e.g., Ref. 12). The unusual and intuitively unexpected feature is the observation of a probe pulse enhancement, instead of depletion, within a considerably large wavelengths interval in the vicinity of total degeneracy. The amplification of the probe pulse with the wavelength 493 nm is shown in Fig. 1 by green dots.

The inset to the Fig. 1 gives the wavelength detuning dependence of a formally introduced exponential gain factor  $\gamma = (1/\ell)\ln T$  ( $\ell$  is the sample thickness). It suggests that the gain becomes large enough to overcome the two-photon absorption within the detunings range of  $-3 \text{ nm} \leq \Delta\lambda \leq +8 \text{ nm}$ . The processes of optical parametric amplification can be excluded in explanation of these findings; instead, the probe amplification by means of self-diffraction from a grating recorded by the pump and probe beams<sup>13,14</sup> seems to be very probable. Several facts support this hypothesis, among them, the absence of gain in the case of cross-polarized pump and

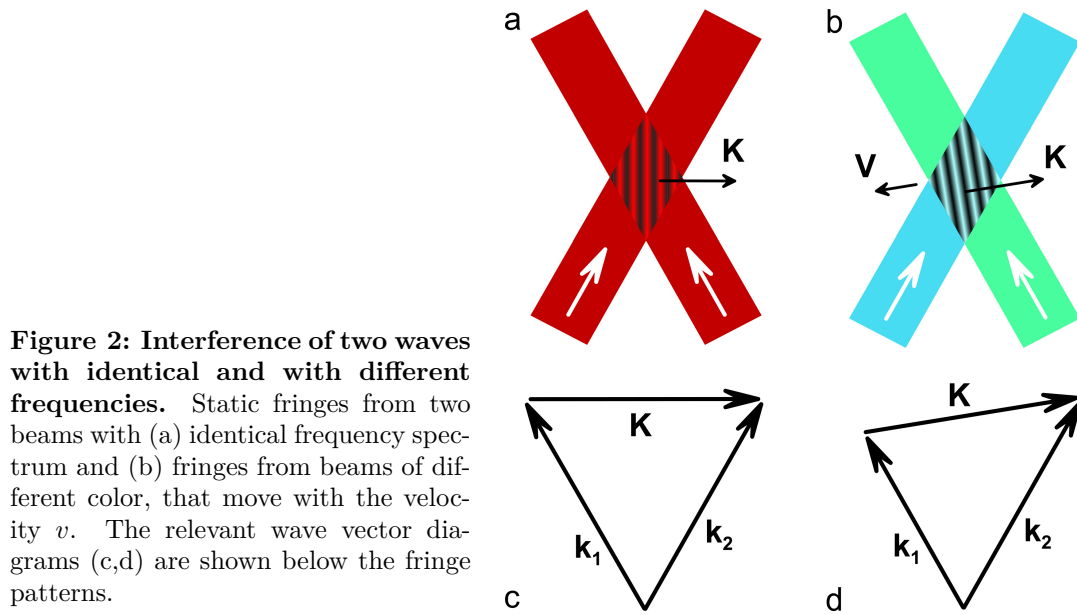


**Figure 2: Interference of two waves with identical and with different frequencies.** Static fringes from two beams with (a) identical frequency spectrum and (b) fringes from beams of different color, that move with the velocity  $v$ . The relevant wave vector diagrams (c,d) are shown below the fringe patterns.

probe pulses and characteristic changes in spectra of amplified probe, with a signature of the pump pulse spectrum. Thus, the inertial grating recording with pulses that differ in wavelengths about 5 nm or more must be considered. The question arises, furthermore, is such a recording possible at all and, if yes, how large the allowed frequency detuning can be. These fundamental questions are addressed qualitatively and analytically below.

**Qualitative considerations and estimates.** After seminal publication<sup>1</sup> it became clear that to record a hologram the two light beams should be mutually coherent. One definition of mutual coherence relates it to the observable visibility of interference fringes formed by two beams that overlap in space<sup>15,16</sup>. For continuous wave (cw) radiation the observation of a high contrast fringe pattern is possible if both beams are nearly monochromatic and have identical frequencies. If two coherent light waves (1 and 2) have different frequencies, the fringe pattern that they form moves with the velocity  $v = \Omega/K$  that depends on frequency detuning of the waves,  $\Omega = \omega_2 - \omega_1$ , and spatial frequency  $K$  ( $\mathbf{K} = \mathbf{k}_2 - \mathbf{k}_1$ ,  $\mathbf{k}_{1,2}$  being the recording beams wave vectors). Taking, for example, blue and green light waves with wavelengths 489 nm and 500 nm which intersect at an angle of  $4^\circ$  we get the fringe velocity  $v \approx 10^8$  m s<sup>-1</sup>. Figure 2 shows the structure of static fringes for the conventional case of hologram recording (for example, two red beams from cw He-Ne laser) and moving fringes in case of interference of beams of two different colors.

Only the nonlinear processes with instantaneous response can follow the fringes that move with a velocity that is comparable with the velocity of light. Forty years ago the possibility to record a dynamic hologram in a medium with ultrafast response was suggested by Yuri Denisjuk<sup>17</sup>. He called this effect "holography with intensity waves". Nowadays it can be implemented, for example, with two-photon absorption gratings<sup>18</sup>, what will be discussed in the last Section of this paper. The main objective of the present paper is, however, to prove that different color recording of a

holographic grating is possible in any medium, regardless how long is its response time, including media for permanent grating recording. To perform such a recording we propose to take a snapshot of the moving fringes with a very short exposure time. A simple calculation allows for estimating the distance of fringe displacement  $\Delta\ell = v\tau$  within the pulse duration  $\tau$ . If this displacement is smaller or comparable with the fringe spacing  $\Lambda = 2\pi/K$  the recorded fringe pattern will not be smeared out completely. This gives a hope that femtosecond lasers can be used for holographic grating recording by beams of different colors. The quantitative criteria for getting sufficiently high contrast of the pattern integrated over the pulse duration are derived in the next section.

**Evaluation of the modulation depth.** In order to calculate the modulation depth for a time integrated fringe pattern as a function of the detuning frequency, we consider the interference of two pulses within the plane waves approximation. The electric field of two waves is

$$\begin{aligned} E_1(\mathbf{r}, t) &= a_1 f(t) \exp(-i\omega_1 t) \exp(-i\mathbf{k}_1 \mathbf{r}), \\ E_2(\mathbf{r}, t) &= a_2 f(t) \exp(-i\omega_2 t) \exp(-i\mathbf{k}_2 \mathbf{r}), \end{aligned} \quad (1)$$

with the amplitudes  $a_{1,2}$ , temporal shape  $f(t)$ , angular frequencies  $\omega_{1,2}$  and wavevectors  $\mathbf{k}_{1,2}$ . The pulse duration  $\tau = \tau_1 = \tau_2$  is defined by the full width at half maximum (FWHM) of the intensity profiles  $I_{1,2}(\mathbf{r}, t) = |E_{1,2}(\mathbf{r}, t)|^2$ . The intensity distribution of the total field in time and space gives then a moving fringe pattern that is represented by

$$\begin{aligned} I(\mathbf{r}, t) &= |E_1 + E_2|^2 \\ &= (a_1^2 + a_2^2) f^2(t) + a_1 a_2 f^2(t) \exp(-i\Omega t + i\mathbf{K}\mathbf{r}) + \text{c.c.} \\ &= f^2(t) [a_1^2 + a_2^2 + 2a_1 a_2 \cos(\Omega t + \mathbf{K}\mathbf{r})]. \end{aligned} \quad (2)$$

Here,  $\Omega = \omega_2 - \omega_1$  denotes the frequency detuning and  $\mathbf{K} = \mathbf{k}_2 - \mathbf{k}_1$  the wavevector of the sinusoidal pattern. The pattern moves with the velocity  $v = \Omega/K$  ( $K = |\mathbf{K}|$ ) along  $\mathbf{K}$ , and its fringe contrast is given by  $m = 2a_1 a_2 / (a_1^2 + a_2^2)$ .

In our experiments, this fringe pattern is generated with ultrashort laser pulses ( $\tau \approx 100$  fs), and the pulse duration is most often much shorter than the temporal response of the detectors used (digital camera, holographic emulsion, human eye). For single-pulse interference, this yields a time-integrated pattern of energy density per unit area:

$$\mathcal{E}(\mathbf{r}) = \int_{-\infty}^{+\infty} I(t, \mathbf{r}) dt. \quad (3)$$

Note, that  $\mathcal{E}(\mathbf{r})$  depends on the temporal shape  $f(t)^2$ , thus on  $\tau$ , as well as on the detuning frequency  $\Omega$ . The modulation depth of the energy distribution  $\mathcal{E}(\mathbf{r})$  is analyzed below by assuming three common  $f(t)$  shapes: rectangular, Gaussian and Hyperbolic Secant. A rectangular pulse can be expressed by  $f^2(t) = \text{rect}[\tau/2, -\tau/2]$  with an intensity that does not change within the total pulse duration  $\tau$ . This particular shape

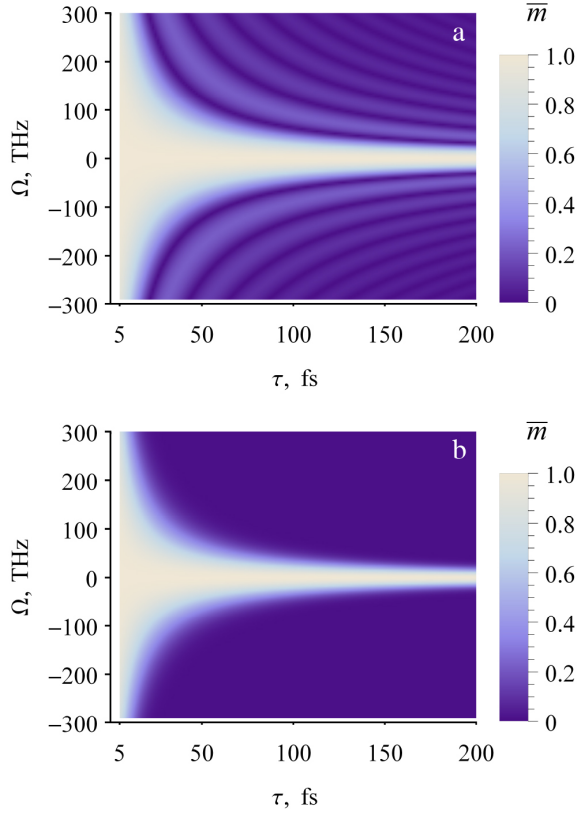


**Figure 3: Calculated modulation depth averaged over the pulse duration.** Modulation depth as a function of frequency detuning  $\Omega$  and pulse duration  $\tau$  for (a) rectangular and (b) Gaussian pulse profiles. The interaction of pulses with identical amplitudes is assumed.

of  $I(t)$  simplifies the integration of equation (3)

$$\begin{aligned} \mathcal{E}(\mathbf{r}) &= \int_{-\tau/2}^{+\tau/2} I(t, \mathbf{r}) dt \\ &\propto a_1^2 + a_2^2 + 2a_1a_2 \frac{\sin(\Omega\tau/2)}{\Omega\tau/2} \cos(\mathbf{K}\mathbf{r}), \end{aligned} \quad (4)$$

and allows to determine the modulation depth of the energy density pattern  $\bar{m}$  as a function of  $\Omega$  and  $\tau$ :

$$\bar{m}(\Omega, \tau) = \frac{2a_1a_2}{a_1^2 + a_2^2} \frac{\sin(\Omega\tau/2)}{\Omega\tau/2} = m \frac{\sin(\Omega\tau/2)}{\Omega\tau/2}. \quad (5)$$

The 2D-plot of  $\bar{m}(\Omega, \tau)$  is illustrated in Fig. 3 a. The largest  $\bar{m} = 1$  is reached, naturally, for  $\Omega = 0$ , whatever is the pulse length  $\tau$ . The detuning range within which the modulation depth is still high (the width of the central white stripe in Fig. 3 a) depends, however, on pulse length and increases quite strongly with decreasing  $\tau$ . (It should be noted that for extremely short pulses (below 5 fs) the  $\bar{m}$  estimate according equation (5) is senseless because the fringe pattern width in  $\mathbf{K}$ -direction becomes comparable or smaller than the fringe spacing  $2\pi/K$ ).

For any arbitrary  $\tau$  (or arbitrary nonzero  $\Omega$ ) the frequency detuning dependence (or pulse length dependence) of  $\bar{m}$  shows additional maxima typical to sinc function. The  $\bar{m}$ -values of these maxima, as it follows from equation (5), are inversely proportional to the product  $\Omega\tau$ .

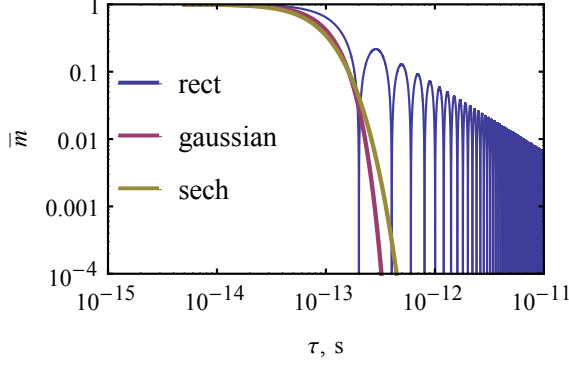


**Figure 4: Effect of the pulse temporal profile on modulation depth.** Comparison of the modulation depth as a function of pulse duration  $\tau$  for rectangular, Gaussian and Hyperbolic Secant pulses. A fixed frequency detuning of  $\Omega = 3 \cdot 10^{13}$  Hz and equal intensities of two pulses are assumed.

The sinc-like behavior vanishes, however, completely under the assumption of a pulse temporal profile with a bell-shaped function, particularly, for a Gaussian profile:

$$f^2(t) = \exp \left[ -4 \ln(2) \cdot (t/\tau)^2 \right] \quad (6)$$

or Hyperbolic Secant profile:

$$f^2(t) = \operatorname{sech}^2 \left[ 2 \cosh^{-1} \left( \sqrt{2} \right) \cdot t/\tau \right], \quad (7)$$

$\tau$  being the FWHM in both cases. Integration of equation (3) then yields:

$$\begin{aligned} \bar{m}(\Omega, \tau) &= \frac{2a_1 a_2}{a_1^2 + a_2^2} \exp \left( -\frac{\tau^2 \Omega^2}{16 \ln(2)} \right) \\ &= m \exp \left( -\frac{\tau^2 \Omega^2}{16 \ln(2)} \right). \end{aligned} \quad (8)$$

and

$$\bar{m}(\Omega, \tau) = m \frac{\pi \tau \Omega}{4 \sinh^{-1}(1)} \operatorname{csch} \left( \frac{\pi \tau \Omega}{4 \sinh^{-1}(1)} \right). \quad (9)$$

Figure 3 b shows the  $\bar{m}(\Omega, \tau)$  plot for Gaussian profile, the plot for Hyperbolic Secant profile is qualitatively similar. The characteristic difference between the modulation depth of rectangular, Gaussian and sech pulses is highlighted in Fig. 4 for a fixed detuning of  $\Omega = 3 \cdot 10^{13}$  Hz as a double-logarithmic plot. The modulation depth for Gaussian and sech pulses drops as a function of pulse duration in a similar way, while the decay for rectangular pulses is not so strong and is characterized by an oscillatory behavior.

From the viewpoint of our pump-probe experiment described above ( $\Omega \approx 3 \cdot 10^{13}$  Hz and  $\tau \approx 100$  fs), it becomes clear that the modulation depth is  $\bar{m}(\Omega, \tau) \approx 0.4$  for a Gaussian pulse ( $\approx 0.6$  for a rectangular pulse), i.e., a fringe pattern with sufficiently high modulation depth is present and is able to cause the recording of a grating.

Note, that the generalization to the case of repetitive rate excitation is natural, provided the phase difference of waves in equation (1) does not change from one pulse to the other. The modulation depth is not affected by the number of pulses  $N$  because all terms in equation (3) are multiplied to the same number of pulses  $N$ .

**Visualization of interference fringes.** The visual observation of two-color beam interference becomes possible by adjusting the small angle between the beams. We note, that the fringe velocity  $v$  depends on the fringe spacing  $\Lambda$ , but the condition  $v\tau/\Lambda \leq 1$  does not impose any restriction to  $\Lambda$ . Thus, the observable fringe contrast should be independent of the angle between the recording beams and a fringe spacing can be adjusted to be large enough for detection with naked eye.

The schematic representation of the experiment on fringe observation and grating recording is shown in the upper left corner of Fig. 5. The temporal overlap of pulses from two optical parametric amplifiers (OPAs) on a diffusing white screen is ensured with an optical delay line. With this arrangement it is possible to observe a fringe pattern on the screen and to register its image.

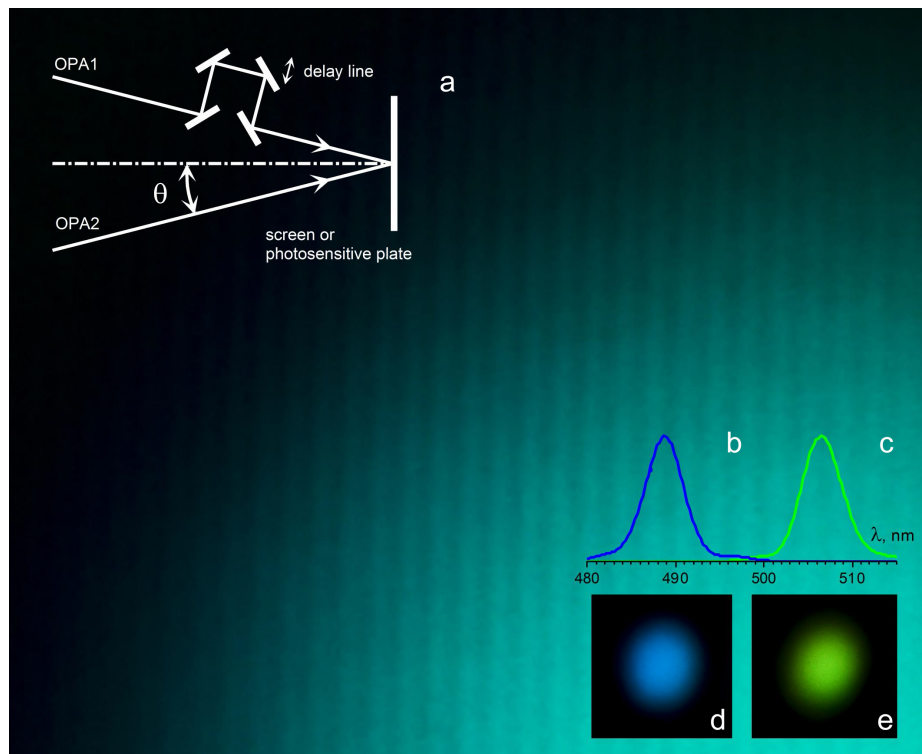


**Figure 5: Observation of fringe pattern from light beams of different colors.** The background image shows a fragment of a fringe pattern from single pulse light beams with  $\lambda = 489$  nm and 506 nm. The geometry of fringe observation (a) is shown in upper left corner. The net difference in colors of two beams is clearly seen from measured spectra, (b) and (c), and from near-field distributions, (d) and (e).

The very first attempt revealed distinct fringes for quite different wavelengths, that were visible both, with single shot and in repetition rate operation mode. An example is shown in Fig. 5 that represents fringes from the beams with 17 nm wavelength detuning. Care is taken to get a uniform transverse intensity distribution in both beams and a good superposition of the spots with nearly equal diameter. The two beams were identically linearly polarized, perpendicularly to the drawing of Fig. 5. The full angle between the beams was deliberately chosen here to be nearly  $0.5^\circ$  to increase the fringe spacing.

The described observation is a purely "linear optic" effect, any kind of nonlinearity

is not involved here. The beams interfere only when they are superposed in space and in time. If the observation screen is moved so that the light spots are completely separated, the fringes are no more visible.

The fact that a fringe pattern could be observed with naked eye at 1 kHz repetition rate proves that spatial position of fringes remains the same from one pulse to the other at least during the physiological limit of human eye response (about 0.04 s). Later this was confirmed when recording the grating with several consecutive pulses: the contrast of the recorded pattern did not deteriorate as compared to single pulse recording. Such a feature could be expected as one and the same mode-locked Ti:Sapphire laser is initially feeding the two channels in which the recording beams are formed. For both recording beams the phase of every new pulse in train is not arbitrary and the effective phase difference is preserved from pulse to pulse.

It should be underlined, however, that for the case of single-pulse experiment no restrictions are imposed for the light sources that provide two interfering beams: they can be the two completely independent lasers with the outputs of different color, that in common sense would be considered completely mutually incoherent. The only necessary condition for fringe observation is the spatial and temporal overlap of output ultrashort pulses and their polarization adjustment. In case of repetition rate experiment there are a few additional requirements, the repetition rates of the two beams should be exactly the same and the coherence time of each beam should be longer than the total time of fringe recording (or fringe observation). As it was mentioned above these conditions were met in full with the fs laser system used in our experiment.

**Modulation depth versus wavelength detuning.** The digitized image like that shown in Fig. 5 allows for evaluating the recorded fringe modulation depth  $\bar{m} = (I_{\max} - I_{\min}) / (I_{\max} + I_{\min})$ . These measurements were done for a series of fringe patterns that have been taken with the fixed wavelength of one OPA  $\lambda_1 = 489$  nm and variable wavelength of the other OPA. The processing of digitized images and extraction of  $\bar{m}$  from the raw data are described in Section Methods. Measurement of fringe contrast. Figure 6 shows the detuning dependence of the fringe contrast (dots). The accuracy of  $\bar{m}$  estimate is high for small frequency detunings, the uncertainty increases up to  $\approx 30\%$  for largest measured detunings, where modulation depth becomes small.

The attempts to fit the measured data with functions calculated in previous section for different intensity profiles of the recording pulses are given by the solid lines: black line represents a  $\text{sinc}(\Omega\tau/2)$  dependence for rectangular pulses; the fit yields  $\tau \approx 110$  fs for the pulse duration. The fitting of functions calculated for Gaussian and Hyperbolic Secant profiles give a somewhat smaller pulse duration, about 80 fs. In all cases, however, the estimated values are in reasonable agreement with the directly measured pulse duration of about 100 fs.

**Grating recording and hologram recording.** The fringe pattern that can be seen with the eye can also be recorded with a photosensitive medium. Such an imprint of fringes represents a plane wave hologram. They were recorded using conventional

**Figure 6: Wavelength detuning dependence of the modulation depth.**

Dots represent the data measured with a fixed wavelength 488 nm of one beam and the wavelength variation within the range 475 - 510 nm for the other beam. Solid lines represent the dependences calculated within the assumption of the rectangular (black), Gaussian (deep red) and Hyperbolic Secant (blue) temporal envelopes of the interfering pulses.

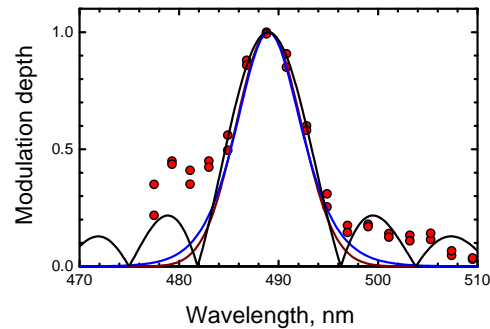
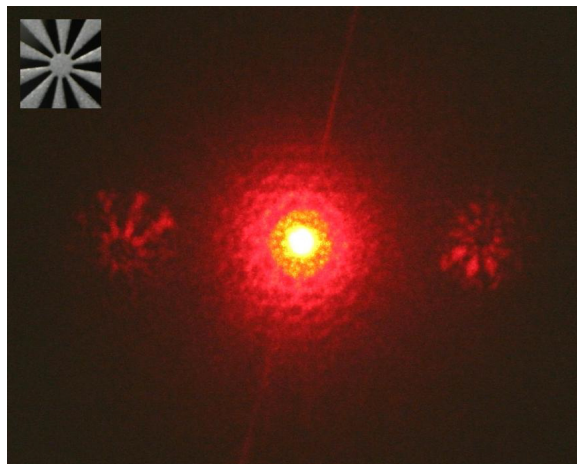


**Figure 7: Image reconstruction from a hologram recorded with pulses of different color.** Readout with a He-Ne laser of the hologram written by femtosecond pulses with 489 nm and 501 nm wavelengths. The inset in the upper left corner shows the amplitude mask installed in one of the two beams during recording, gray color marks the areas with zero transmission.



silver halid photo emulsions with standard chemical development and subsequent bleaching procedure. For close wavelengths of the two recording beams the  $\pm 2$  diffraction orders are clearly seen and the diffraction efficiency in the first order is a few percent.

In the limit of small phase modulations the diffraction efficiency  $\eta$  depends quadratically on fringe contrast  $\bar{m}^{20}$ . Thus the decrease of  $\bar{m}$  with the increasing detuning (see Fig. 6) should inhibit diffraction. Just this behavior was observed experimentally.

We also registered a hologram in a photoemulsion with an image bearing beam. The amplitude mask shown in the upper left corner of Fig. 7 was installed in one of the two recording beams (green beam), which is loosely focused. The angle between the recording beams was increased to  $4^\circ$  to ensure the carrier spatial frequency  $K$  of a hologram to be larger than spatial frequency content of the image. Figure 7 shows the reconstructed images, the pseudoscopic on the left side and orthoscopic on the right side from the central spot which represents the transmitted readout beam from the He-Ne laser. The reconstructed images are quite noisy, however one can recognize unambiguously the original pattern.

### 3 Discussion

It is shown in this paper that the contrast of time average interference pattern of two short light pulses of different color can be remarkably high at least for frequency detuning  $|\Omega| \leq 2\pi/\tau$ . As it follows from data of Fig. 6, the experimental detuning dependence of the modulation depth has rather extended, slightly waving wings. When comparing this result with calculations one can see that the measured values of  $\bar{m}$  for  $|\Omega| \geq 2\pi/\tau$  are obviously larger than that expected for Gaussian and Hyperbolic Secant temporal profiles. This may point to a pulse shape that is certainly not rectangular but doesn't also have smoothly decaying wings typical for Gaussian and Hyperbolic Secant functions. The evident asymmetry of  $\bar{m} = \bar{m}(\Delta\lambda)$  dependence can be attributed to the changes of pulse shape and width with the detuning.

It should be noted that the problem of effective fringe visibility can be considered not only in time domain, what we did above, but also in the frequency domain. Obviously, a considerable reduction of the pulse duration leads to the broadening of its spectrum. Even a slight spectral overlap of the two pulses may lead to the appearance of a fringe pattern with finite modulation depth.

For the case of transform limited pulses, the pulse-bandwidth product is  $\Delta\nu \cdot \tau = \kappa$ . The factor  $\kappa$  is close to unity and depends on the particular pulse shape, for Gaussian pulses  $\kappa = 2\ln(2)/\pi$  holds<sup>21</sup>. Therefore, the modulation depth for Gaussian pulses (see Eq. (8)) can be rewritten in terms of the detuning frequency  $\Omega$  and the spectral width  $\Delta\omega$  of the pulses (with  $\nu = \omega/2\pi$ ):

$$\bar{m}(\Omega, \Delta\omega) = m 2^{-(\Omega/\Delta\omega)^2}. \quad (10)$$

Taking the experimental conditions  $\lambda_1 = 489$  nm,  $\lambda_2 = 506$  nm and  $\tau = 100$  fs, we get  $\Omega/\Delta\omega \approx 4.7$  for an assumed gaussian shape, which indicates a small overlap which is due to the extended wings of gaussian pulses as it is shown in right hand side of Fig. 5.

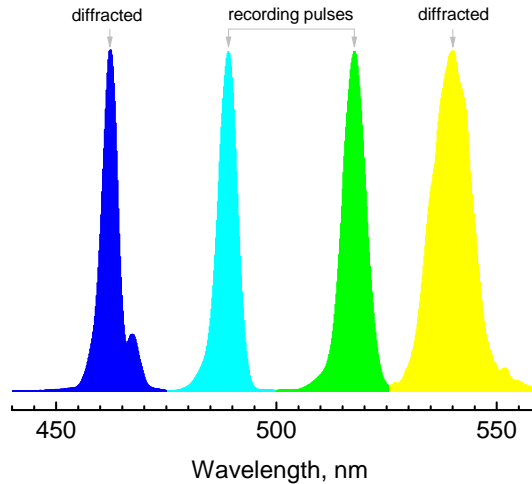
Summarizing, we claim that with 100 fs pulses a recording of holographic grating is possible if the frequencies of two pulses differ up to 4 percent of the mean optical frequency (larger detunings are allowed for shorter pulses). Of course, when read out with one of the two recording beams, a recorded static hologram can not reproduce the wavelength of the other beam. With some distortions it can reproduce, however, the recorded wavefront.

For classical holography the described phenomenon is rather unexpected and obviously new. It can bring new technical solutions for static hologram recording of ultrafast processes, including new variations of Nils Abramson's light-in-flight holography<sup>2,22</sup>.

We believe however that our result will have a major impact in nonlinear wave mixing and nonlinear spectroscopy. The appearance of transient or permanent grating recorded by two interacting waves may strongly influence the interpretation of pump-probe experiments. Our results described above prove that a direct coupling from such a grating because of selfdiffraction affects both the intensity and the spectrum of the probe beam. We limited ourselves in the present paper by consideration of permanent gratings only, as an ultimate case of recording in a material with the

infinite storage time. In fact, a vast variety of  $\chi^3$  nonlinearities with response times ranging from practically zero to infinity can respond to the described moving fringe pattern, thus bringing particular types of coupling.

**Figure 8: Frequency conversion via selfdiffraction from a moving dynamic grating.** Spectra of the transmitted recording pulses and  $\pm 1$  diffraction orders. The thin two photon absorption dynamic grating is recorded in 200- $\mu\text{m}$ -thick sample of  $\text{LiNbO}_3$  by beams that differ to 25 nm in wavelengths and impinge upon the sample at full angle  $\approx 4^\circ$ .



Apart from the coupling because of selfdiffraction, the transient gratings can be revealed through the appearance of higher (non Bragg) orders in case of Raman-Nath diffraction. In media with instantaneous response (other ultimate case compared to described above) the higher orders of diffraction should be up-shifted and down-shifted in frequency exactly by the frequency difference of the recording waves  $\Omega$ . Our preliminary experiments with different color recording of two photon absorption gratings, that are currently in progress and will be published separately, confirmed the possibility of building such a tunable frequency converter. Figure 8 shows an example of up- and downconversion to  $\Delta\lambda \simeq 25$  nm with selfdiffraction from the moving two photon absorption grating in a thin sample of  $\text{LiNbO}_3$ . The severe fundamental restriction on the diffraction efficiency for amplitude gratings<sup>20</sup> resulted in only 0.01 conversion efficiency in this demonstration experiment. A considerable improvement of efficiency is expected with the purely phase moving gratings, profiting from the dominant real part of  $\chi^3$  nonlinearities.

A hologram recording in Leith-Upatnieks geometry, with an oblique reference wave is demonstrated in this article. Taking into account that even in dense medium the spatial width of 100 fs pulse is not less than 10  $\mu\text{m}$  the reflection gratings and Lippman-type (reflection) holograms can be recorded by counterpropagating light pulses, too. This allows also for considering different applications based on nonlinear backward wave four wave mixing with ultrashort pulses.

The dynamic grating techniques have been used successfully in the past for development of autocorrelation type measurements of femtosecond pulse duration<sup>3</sup>. With pulses of different color this technique can be extended for cross correlation experiments. The studies of gratings with instantaneous response recorded by pulses of different colors will be profitable for evaluation of a frequency chirp in ultrashort pulses, i.e., the the short pulse characterization will be another domain to apply the described phenomenon.

And finally this work will trigger new attempts to reconsider the definition of

coherence for pulsed radiation. In particular, the question will be discussed, can the blue pulse and green pulse from two different lasers be considered mutually coherent.

## 4 Methods

**Laser system & optical setup.** The femtosecond laser system used in the experiment consists of several separate devices in chain; Fig. 9 shows it schematically. A mode-locked  $\text{Ti}^{3+}:\text{Al}_2\text{O}_3$  oscillator generates the initial train of femtosecond pulses with a spectrum centered at wavelength  $\lambda = 802\text{ nm}$ . Chirped-pulse amplification (CPA) is used to reach a maximum pulse energy of  $(4 \pm 0.1)\text{ mJ}$  at a repetition rate of  $1\text{ kHz}$ . By tuning the compressor grating (C) the pulse duration is adjusted to  $(100 \pm 10)\text{ fs}$  as determined by interferometric auto correlation (Gaussian shape approximation, A.P.E., model: *Pulse Check PD 15 ps*). The pulses then enter two optical parametric amplifiers (OPA (1) and OPA (2)) with input pulse energies of  $\approx 2.5$  and  $\approx 1.5\text{ mJ}$ , respectively, after passing a telescope and a 65:35 beam splitter.

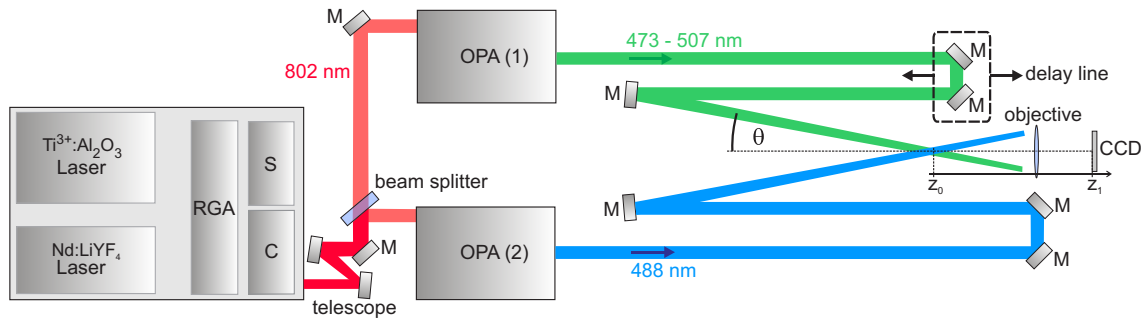


**Figure 9: Experimental setup:** Femtosecond pulses from a  $\text{Ti}^{3+}:\text{Al}_2\text{O}_3$  laser are stretched (S) to the picosecond length, regeneratively amplified (RGA) using a  $\text{Ti}^{3+}:\text{Al}_2\text{O}_3$  that is pumped by a Q-switched  $\text{Nd}:\text{LiYF}_4$  laser ( $\lambda = 527\text{ nm}$ ) and compressed (C) to pulses with  $100 \pm 10\text{ fs}$  duration and  $4\text{ mJ}$  energy (Coherent Inc., *LIBRA-HE*). The amplified fs-pulses serve as a pump for two optical parametric amplifiers (OPA, Coherent Inc., *OPerA Solo*) to generate fs-laser pulses in the blue-green spectral range via sum-frequency conversion. The optical paths lengths of the frequency detuned pulses is adjusted by a delay line. The pulses are superimposed at a small angle in air, so that the fringe pattern could be imaged onto a screen with lens L.

Both OPAs use a supercontinuum source of  $\text{Al}_2\text{O}_3$  for the signal generation and a double-stage parametric amplifier scheme (non-collinear and collinear optical amplifier) for signal amplification. Pulses in the blue-green spectral range ( $470 - 520\text{ nm}$ ) are obtained within a sum-frequency mixing scheme. At the OPA-output, pulse energies up to  $150\text{ }\mu\text{J}$  are available with pulse durations below  $100\text{ fs}$ . The optical paths of the frequency-detuned pulses are matched by using an optical delay line in one of the beams.

For the generation of a fringe pattern, the pulses are superimposed at an angle of a few degrees in air at position  $z_0$ . The pattern is imaged by a lens (magnification factor:  $\times 50$ ) onto a screen and grabbed by a digital camera. A metallic mask was placed in one of the two beam paths to demonstrate holographic image-recording with a holographic emulsion (Slavich, *PPG-03M*) at  $z_0$ . The exposed films were chemically processed and reconstructed by a HeNe-laser.

**Pump-probe experiment.** The transmittance of 200  $\mu\text{m}$ -thick  $y$ -cut sample of a nominally undoped  $\text{LiNbO}_3$  crystal was tested with the  $\approx 100$  fs probe pulse in presence of pump pulse with the same duration. The average intensities of the pump and probe pulses were  $5.6 \text{ PW cm}^{-2}$  and  $0.7 \text{ TW cm}^{-2}$ , respectively. Both pulses, probe and pump, are identically linearly polarized along the crystal  $c$ -axis, they impinge upon the sample in a plane normal to this axis, to avoid a photorefractive grating formation. The spectrum of the pump pulse is fixed at 490 nm while the wavelength of the probe pulse is tunable. The 100  $\mu\text{m}$  beam waist of the probe pulse is roughly 1.5 times smaller than that of the pump pulse. For the wavelength range used in the experiment even with relatively small full angle between the beams ( $\simeq 2.5^\circ$ ) at least 10 interference fringes are expected within the area where two beams overlap.

No cumulation effects have been observed; the measurements are done either within a single short pulse or averaging the data of consecutive 10 pulses.

**Measurements of fringe contrast.** To extract the data on fringe contrast from the digitized image of interference pattern two problems must be solved. First, one needs to be sure that the recording device (digital camera in our case) works within the intensity range where its response to the intensity is linear. Second, for any particular pattern to be processed it is necessary to know the intensity ratio of two interfering beams.

Initially the intensity ratio of two waves with identical frequencies was adjusted to be 1:1, it was however changing when frequency of one wave was tuned. Thus, there are two reasons for decreasing of the measured modulation depth with the detuning frequency, one related to variation of the intensity ratio and the other related to the fringe pattern motion.

Whole measurement procedure was as follows. At first, the two beams were superposed in a best way on a white screen. Then, the digital camera with the removed lens was installed so that its sensitive matrix appeared in a plane of white screen, just in the maximum of the intensity spatial distribution. The matrix dimensions,  $17 \times 22 \text{ mm}^2$  was roughly ten times smaller than FWHM of the interfering beams. The linearity of camera response was ensured by appropriate choice of neutral density filters. To find the intensity ratio of the recording waves, the three measurements were done for every new frequency detuning: the measurements of each interfering beam separately and measurement of fringes from two superposed beams. Figure 6 shows the recalculated detuning dependence of the fringe contrast (dots) which is due to the fringe motion only.

## References

1. Gabor, D. A New Microscopic Principle. *Nature* **161**, 777-778 (1948).
2. Abramson, N. Femtosecond imaging: Motion picture of short pulses. *Nature Photonics* **5**, 389-390 (2011).
3. Brubaker, R. M., Wang, Q. N., Nolte, D. D., Harmon, E. S. & Melloch, M. R. Steady-state four-wave mixing in photorefractive quantum wells with femtosecond pulses. *J.*

- Opt. Soc. Am. B* **11**, 1038-1044 (1994).
4. Horowitz, M., Fischer, B., Barad, Y. & Silberberg, Y. Photorefractive effect in a BaTiO<sub>3</sub> crystal at the 1.5  $\mu\text{m}$  wavelength regime by two-photon absorption. *Opt. Lett.* **21**, 1120-1122 (1996).
  5. Hsieh, H.-T., Psaltis, D., Beyer, O., Maxein, D., von Korff Schmising, C., Buse, K. & Sturman, B. Femtosecond holography in lithium niobate crystals. *Opt. Lett.* **30**, 2233-2235 (2005).
  6. Froehly, C., Colombeau, B. & Vampouille, M. Shaping and analysis of picosecond light pulses. *Progress in Optics* **20**, 63-153 (1983).
  7. Weiner, A. M., Leaird, D. E., Reitze, D. H. & Paek, E. G. Femtosecond spectral holography. *IEEE J. Quant. Electron.* **28**, 2251-2261 (1992).
  8. Oba, K., Sun, P.-C. & Fainman, Y. Nonvolatile photorefractive spectral holography. *Opt. Lett.* **23**, 915-917 (1998).
  9. Mazurenko, Y. T., Putilin, S. E., Spiro, A. G., Beliaev, A. G., Yashin, V. E., & Chizhov, S. A. Ultrafast time-to-space conversion of phase by the method of spectral nonlinear optics. *Opt. Lett.* **21**, 1753-1755 (1996).
  10. Buse, K., Adibi, A. & Psaltis, D., Non-volatile holographic storage in doubly doped lithium niobate crystals. *Nature* **393**, 665-668 (1998).
  11. Imlau, M., Brüning, H., Schoke, B., Hardt, R.-S., Conradi, D. & Merschjann, C. Hologram recording via spatial density modulation of Nb<sub>Li</sub><sup>4+/5+</sup> antisites in lithium niobate. *Opt. Exp.* **19**, 15322-15338 (2011).
  12. Kang, I., Krauss, T. & Wiese, F. Sensitive measurement of nonlinear refraction and two-photon absorption by spectrally resolved two-beam coupling. *Opt. Lett.* **22**, 1077-1079 (1997).
  13. Eichler, H. J., Günter, P. & Pohl, D. W.: *Laser Induced Dynamic Gratings* (Springer-Verlag, Berlin, 1986).
  14. Vinetsky, V. L., Kukhtarev, N. V., Odoulov, S. G. & Soskin, M. S. Dynamic self-diffraction of coherent light beams. *Sov. Phys. Usp.* **22**, 742-756 (1979).
  15. Mandel, L. & Wolf, E.: *Optical coherence and quantum optics* (Cambridge University Press, Cambridge, New-York, 1995).
  16. Glauber, R.: *Optical coherence and statistics of photons, in Quantum Optics and Electronics* (Gordon and Breach, New-York, 1965).
  17. Denisjuk, Yu. On reconstructive abilities of the running intensity waves when recording the dynamic 3D holograms. *Sov. Physics: Techn. Phys.* **44**, 131-133 (1974).
  18. Shumelyuk, A., Imlau, M., Dieckmann, V., Badorreck, H., Grabar, A. & Odoulov, S. Self-diffraction from two-photon absorption gratings in Sn<sub>2</sub>P<sub>2</sub>S<sub>6</sub>. *Opt. Lett.* **37**, 4065-4067 (2012).
  19. Imlau, M., Dieckmann, V., Badorreck, H. & Shumelyuk, A. Tin hypthiodiphosphate: nonlinear response in the sub-100 fs time domain. *Opt. Mat. Exp.* **1**, 953-961 (2011).
  20. Collier, R. J., Burckhardt, C. B. & Lin, L. H.: *Optical Holography* (Academic Press, New York, 1971).
  21. Menzel, R.: *Photonics: Linear and Nonlinear Interactions of Laser Light and Matter* (2nd Edition Springer Science & Business Media, Berlin, Heidelberg, New York, 2007).
  22. Abramson, N. Light-in-flight recording by holography. *Opt. Lett.* **3**, 121-123 (1978).

**Acknowledgements** We thank Prof. Dr. Eckhard Krätzig and Dr. Javid Shirdel for fruitful discussions. Financial support of Deutsche Forschungsgemeinschaft via projects IM37/5-2, INST 190/137-1 FUGG and INST 190/165-1 and of the Alexander von Humboldt Stiftung via Research Award to S. Odoulov is gratefully acknowledged.

**Author contributions** S. O. and M. I. formulated the idea and initiated the project, A. S. conceived the experiment, A. S., H. B, S. N. and M. I. carried out the experiment, S. O., A. S., H. B and K.-M. V made calculations, S. O. and M. I wrote the paper. All authors discussed the results and contributed to the final manuscript.

**Additional information** No Supplementary information is added to this paper. Correspondence should be sent to S. O and/or M. I.

**Competing financial interests** The authors declare no competing financial interests.

# Doppler-shifted Raman-Nath diffraction from gratings recorded in LiNbO<sub>3</sub> with ultra-short laser pulses of different color

Holger Badorreck,<sup>1</sup> Alexandr Shumelyuk,<sup>2</sup> Stefan Nolte,<sup>1</sup>  
Mirco Imlau<sup>1</sup> and Serguey Odoulov<sup>2,\*</sup>

<sup>1</sup>*School of Physics, Osnabrück University, D-49076 Osnabrück, Germany*

<sup>2</sup>*Institute of Physics, National Academy of Sciences, 03 650 Kyiv, Ukraine*

*\*odoulov@iop.kiev.ua*

**Abstract:** Nominally undoped LiNbO<sub>3</sub> crystals feature a pronounced mixed (absorption/refraction) nonlinear response in the blue-green spectrum domain that is sufficient for the excitation of moving dynamic gratings and the observation of selfdiffraction with Doppler shifted higher orders. This type of Raman-Nath selfdiffraction can be successfully used for up- and down-frequency conversion as well as for characterization of the recording pulses.

©2016 Optical Society of America. This work was published in Optical Materials Express and can be found at the URL <http://dx.doi.org/10.1364/OME.6.000517>. One print or electronic copy may be made for personal use only. Systematic reproduction and distribution, duplication of any material in this paper for a fee or for commercial purposes, or modifications of the content of this paper are prohibited.

## 1 Introduction

The experimental observation of Doppler-shifted selfdiffraction from a moving dynamic grating recorded in nominally undoped LiNbO<sub>3</sub> by beams with considerably different optical frequencies is described in this paper. The recording of holographic gratings, both permanent [1] and dynamic [2,3] with ultrashort laser pulses in crystals like LiNbO<sub>3</sub> is not a new phenomenon. In majority of previous works the recording beams featured, however, identical spectra, i.e., the wave mixing was degenerate in frequency. The main difference of our approach is in the use of pulses with large frequency detuning  $\Omega$ . As distinct from recently published results on permanent hologram recording with femtosecond pulses of different colors [4], a pronounced third-order nonlinearity of LiNbO<sub>3</sub> allows for creating of a grating that moves together with light fringes even if their velocity is comparable to the velocity of light.

A similar self-diffraction has been reported earlier for some glasses and crystals [5–7], where it was treated in terms of nonlinear optics as Cascaded Four Wave Mixing (CFWM) and nonlinear refraction responsible for wave coupling. Surprisingly, this effect was never reported, to our best knowledge, for well studied classical nonlinear crystal LiNbO<sub>3</sub>, an important material in nonlinear photonics and widely used in ultrafast optical parametric oscillators/amplifiers. Our first aim is therefore to clarify what can be expected from LiNbO<sub>3</sub> in this respect. Here, pronounced two photon absorption (TPA) is involved in addition to nonlinear refraction. By choosing the recording photons with energy 2.5 eV, i.e., in the vicinity of 0.7 of band gap energy  $E_g \approx 3.63$  eV [8] we come close to the wavelength range in which, according to the data of [9] the nonlinear refraction  $n_2$  is expected to be considerably reduced (with the following change of its sign for larger frequencies). As a result, we do not observe the cascades of diffraction orders even in case of nearly ideal estimated phase matching conditions. At most, six additional beams become visible at ultimate intensities of the recording pulses, three with upshifted and three with downshifted frequencies. This can be explained by a mixed, absorption/refraction nonlinear response of LiNbO<sub>3</sub> in the green-blue spectral range, with relatively high contribution of two-photon absorption. Such explanation is confirmed by estimates of the diffraction efficiencies that can be expected with the known data on real and imaginary parts of  $\chi^{(3)}$  susceptibility of our LiNbO<sub>3</sub> samples [10], obtained in  $z$ -scan measurements.

Our second aim is to show that the reported Raman-Nath selfdiffraction from a moving grating in LiNbO<sub>3</sub> provides a powerful tool of frequency conversion and can be used efficiently for the characterization of the recording pulses themselves (pulse duration, frequency chirp).

## 2 Experiment and discussion

A standard two-beam geometry of transmission grating recording is shown in Fig. 1. Two unexpanded recording beams with  $\simeq 2.5$  mm spots are generated in two OPAs pumped by the same mode locked Ti:Sapphire laser; they consist of trains of  $\simeq 120$  fs pulses with 1 kHz (or 1 Hz) repetition rate, the single pulse energy being in the range from 40 to 80  $\mu$ J. The major part of experimental results presented below are obtained with a fixed wavelength of one of the two pulses  $\lambda_1 = 489$  nm (frequency  $\omega_1 = 3.85 \times 10^{15}$  rad/s) and tunable wavelength of the other pulse. The description of the femtosecond laser system is given in [4, 11].

The plane parallel  $y$ -cut samples of nominally undoped LiNbO<sub>3</sub> (see for details [12]) have the polar axis  $z$  normal to the propagation plane of all beams, sample thickness being 200  $\mu$ m. The electric field vectors of both recording beams are parallel to the crystal  $z$ -axis. The beams impinge upon the sample symmetrically, making in air  $\pm 2^\circ$  with respect to the normal of the input face. Most often the measurements are done with single fs pulses. For long term exposure of the sample in 1 Hz repetition rate operation mode no cumulative effects are observed. This allows for averaging over numerous consecutive pulses what is important in case of weak signals. With the described arrangement we observe quite pronounced self-diffraction into  $\pm 1$  diffraction orders (much weaker  $\pm 2$  and  $\pm 3$  orders can be seen for highest intensities of

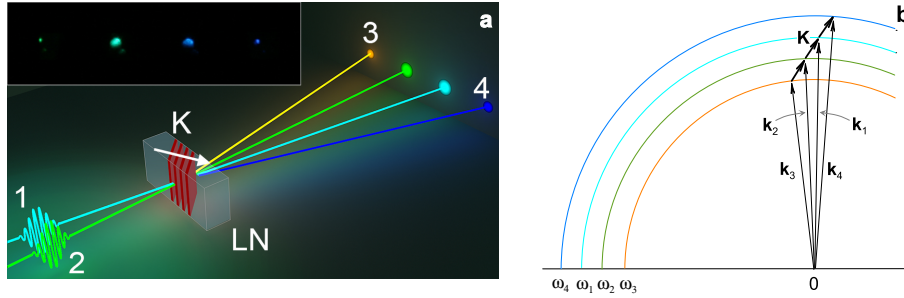


**Figure 1:** (a) Experimental geometry: the incident beams 1 and 2 create a moving grating in the LiNbO<sub>3</sub> sample (LN), two diffracted beams 3 and 4 appear at the output in addition to transmitted beams 1 and 2. These beams form four colored spots in the far-field pattern shown in the upper left inset to this picture. (b) Schematic presentation of the wavevector diagram. The fragments of circles show the  $xy$ -crosssections of Ewald surfaces for the uniaxial crystal LiNbO<sub>3</sub>, with radii equal to  $k_i = \omega_i n_i / c$  for waves of different colors.

the recording beams). The far-field pattern (inset to Fig. 1) gives a representative example, with clearly visible diffraction spots; their spectra measured with Ocean Optics USB4000 spectrometer show obvious Doppler shifts.

The observed phenomenon can be interpreted as follows. Two waves with wavevectors  $\mathbf{k}_1, \mathbf{k}_2$  and frequencies  $\omega_1, \omega_2$  create a periodic dynamic fringe pattern with vector

$$\mathbf{K} = \mathbf{k}_1 - \mathbf{k}_2, \quad (1)$$

which is moving with velocity  $v = \Omega / K$  (see, e.g., [4]). Here  $\Omega$  is the frequency difference  $\Omega = \omega_1 - \omega_2$  and  $K$  is the spatial frequency  $K = |\mathbf{K}|$ . In a medium with third order nonlinearity  $\chi^3(\omega_1, \omega_1, \omega_2, -\omega_2) \neq 0$ , moving fringes lead to the appearance of a moving grating of refractive index or two-photon absorption, or both. This grating can be revealed by the emerging additional waves with wavevectors  $\mathbf{k}_3, \mathbf{k}_4$ , which meet the phase matching conditions that are equivalent to the conditions of diffraction from a grating with grating vector  $\mathbf{K}$  (Eq. (1)):

$$\mathbf{k}_3 = \mathbf{k}_2 - \mathbf{K}, \quad \mathbf{k}_4 = \mathbf{k}_1 + \mathbf{K}, \quad (2)$$

what is shown in the wavevector diagram of Fig. 1(b). It should be underlined that both, the nonlinear index change and nonlinear absorption result from processes which are nondegenerate in frequency. They can, however, be comparably strong as degenerate process. It has been demonstrated convincingly in studies of extremely nondegenerate two-photon absorption in semiconductor crystals [13,14].

As distinct from diffraction from a static grating, the diffraction from the moving grating brings also changes in frequencies of diffracted waves,

$$\omega_3 = \omega_2 - \Omega, \quad \omega_4 = \omega_1 + \Omega, \quad (3)$$

what can be regarded as a consequence of the Doppler shift because of grating motion.

Figure 2(a) represents the experimentally measured frequencies of the twodiffracted waves as functions of frequency variation  $\omega_2$  for the fixed frequency  $\omega_1 = 3.85 \times 10^{15}$  rad/s. Within the experimental error bars these dependences are linear and the

measured data are close to straight lines, as plotted using Eq. (3). The dotted lines show a fixed frequency  $\omega_1$  of the recording beam 1, and adjustable frequency  $\omega_2$  of the recording beam 2.

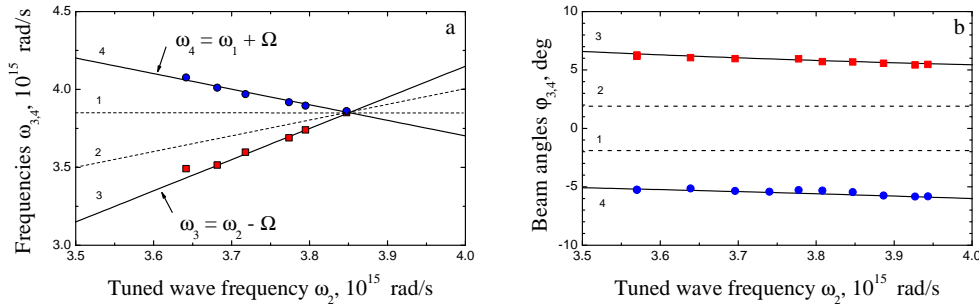


**Figure 2:** Frequencies (a) and propagation angles (b) of four beams behind the sample versus frequency detuning of beam 2. Vertically polarized light beams impinge upon the 200  $\mu\text{m}$ -thick  $y$ -cut  $\text{LiNbO}_3$  plate in a plane parallel to the polar axis.

The propagation angles for the diffracted beams 3 and 4 can be found from Eq. (2). The calculated frequency detuning dependence of these angles are shown in Fig. 2(b) together with the experimental data. Once more, a satisfactory agreement of measured and calculated values can be stated. The dashed lines show fixed angles of the recording beams propagation.

For monochromatic cw waves that record a 3D grating the higher orders of diffraction are usually not phase matched and would not appear. For the recording with 120 fs pulses the restrictions imposed by phase matching are less rigid. Because of the relatively small effective thickness  $d$  the angular selectivity of the grating is rather poor and the tolerance  $|\Delta\mathbf{K}| = 2\pi/d$  in meeting phase matching conditions of Eq. (2) is high. On the other hand, for transmission gratings with small spatial frequency (small angles between the recording beams) the spectral selectivity  $\Delta\omega/\omega$  is quite soft, too, and covers transform limited temporal spectra of the recording pulses.

With the crystal dispersion taken into account, the calculations (see, e.g., Eq. (1) in [5]) show that nearly exact phase matching can be achieved for four consecutive diffraction orders with increasing temporal frequencies if the full crossing angle between the recording waves is reduced to  $1^\circ$ . This should result in the development of Cascaded FWM which was not observed, however, neither for  $1^\circ$  nor for other crossing angles. We believe it is a consequence of the large contribution of two-photon absorption to the recorded dynamic grating responsible for self-diffraction. A TPA grating with moderate contrast can produce by definition only  $\pm 1$  and  $\pm 2$  diffraction orders. On the other hand, the presence of TPA inhibits the grating which is due to the optical Kerr effect because it decreases the light intensity within the  $\text{LiNbO}_3$  sample.

By using  $z$ -scan technique the nonlinear refraction constant  $n_2$  and TPA coefficient  $\beta$  in samples cut from the same  $\text{LiNbO}_3$  crystal have been estimated [11]. The measured values are  $n_2 \approx 5 \times 10^{-20} \text{ m}^2/\text{W}$  and  $\beta \approx 5.8 \text{ mm/GW}$ . The rough estimates of additive contributions to overall diffraction efficiency  $\eta_{Kerr} \approx (\pi n_2 I_0 d / \lambda)^2$  and  $\eta_{TPA} \approx (\beta I_0 d / 2)^2$  show that the contribution from the optical Kerr effect is much smaller than that from the nonlinear absorption  $\eta_{Kerr} / \eta_{TPA} \approx 0.01$ . We want to note,

that possible effects of free carriers and/or small polarons are not considered for the value of  $n_2$  [15], which however does not change the presence of a mixed grating here.

We experimentally estimate also the conversion efficiency  $\eta$  of wave 2 into wave 3 (and 1 into 4). The values fall below  $10^{-2}$  but they remain practically independent of the recording waves detuning within the range of  $\Omega \approx 2 \cdot 10^{14}$  rad/s. It is known that any finite relaxation time of the nonlinear grating results in a diffracted intensity spectrum of Lorentzian type  $\eta \propto [1/(1 + \Omega^2 \tau^2)]^2$  (see, e.g., [16]). Thus, a hypothetical inherent characteristic lifetime of the two-photon absorption grating at least much smaller than the reciprocal detuning range  $1/\Omega$ , i.e.,  $\tau_{TPA} \ll 5$  fs can be theoretically estimated.

### 3 Potential for pulse characterization

The dynamic gratings recording can be useful for the characterization of the recording pulses [17–19]. The four-wave mixing in photorefractive crystal has been successfully used to build a correlator that allows for estimating the femtosecond pulse duration [18]. We show that dynamic gratings in LiNbO<sub>3</sub> can be used for such measurements; they can provide in addition an information about the frequency chirp within the pulse, in a similar way as it is done in Rick Trebino' FROG technique [19].

To perform such measurements the response of self-diffraction to a deliberately introduced time delay  $\Delta t = t_1^0 - t_2^0$  between the recording pulses is studied (subscripts "0" mark the pulse maxima). The time delay is controlled with an optical delay line in the recording beam 1 with larger frequency. Thus taking pulse 2 as a reference with  $t_2^0 = 0$  we have positive  $\Delta t$  for delayed pulse 1. Figure 3 shows time delay dependences of diffracted orders intensities and frequencies.

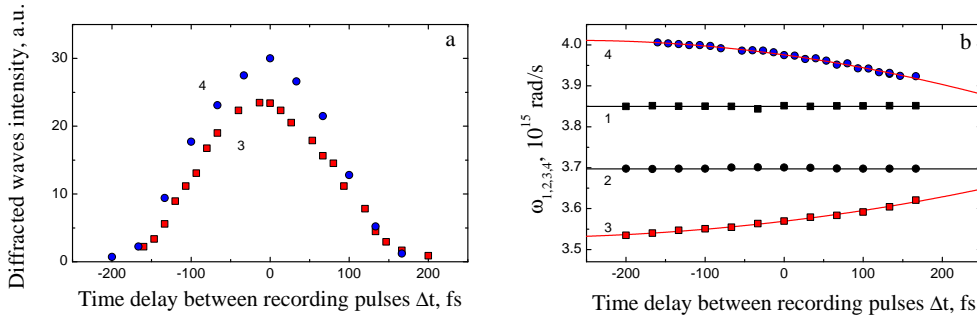


**Figure 3:** Intensities (a) and spectral positions (b) of the diffracted pulses 3, 4 versus time delay between the recording pulses with the wavelengths  $\lambda_1 = 489$  nm and  $\lambda_2 = 509$  nm.

The characteristic bell shaped dependence of the intensity (Fig. 3(a)) reveals information about the pulse duration (see, e.g., [17–19]). For Gaussian shape of the recording pulses the FWHM of the diffraction efficiency should be  $\sqrt{2}$  larger than the FWHM of the pulse itself [18].

The dependence of the diffracted beams frequencies on the mutual pulse delay proves that the instantaneous frequencies within the recording pulses change in time, i.e., pulses are chirped. Let's consider that the central frequencies of the diffracted

pulses 3,4 in Fig. 3(b) can be described by a Taylor series expansion up to second order:

$$\omega_{3,4}(\Delta t) = \omega_{3,4}(0) + \frac{d\omega_{3,4}}{d(\Delta t)} \cdot \Delta t + \frac{d^2\omega_{3,4}}{d(\Delta t)^2} \cdot (\Delta t)^2 + \dots \quad (4)$$

Here  $d\omega/d(\Delta t)$  and  $d^2\omega_{3,4}/d(\Delta t)^2$  are the linear and the second order pulse chirp components.

We assume, in first approximation, only a dominating linear chirp for the frequencies  $\omega_1(t - \Delta t)$  and  $\omega_2(t)$ , the chirp being identical for both pulses because of their common origin. Then the frequency difference  $\omega_1 - \omega_2$  is independent of the running time  $t$  for any arbitrary time delay  $\Delta t$  and remains constant during pulse propagation inside the sample. The higher orders of diffraction 4 and 3 will be upshifted and downshifted in frequency just for  $\omega_1 - \omega_2$  which is a function of pulse delay  $\Delta t$ . This allows to deduce the relationship between the frequency difference of higher diffraction orders  $\Omega_{4-3} = \omega_4 - \omega_3$  and the chirp parameter  $d\omega/dt$  of the incident pulses 1,2

$$\frac{d\omega}{dt} = -\frac{1}{3} \frac{d\Omega_{4-3}}{d(\Delta t)} = -\frac{1}{3} \left( \frac{d\omega_4}{d(\Delta t)} - \frac{d\omega_3}{d(\Delta t)} \right). \quad (5)$$

The comparison of experimental data of Fig. 3(b) with the above considerations brings us to the conclusion that we are dealing with positively chirped pulses,  $d\omega/dt > 0$ . By extracting a linear term of a polynomial fit in Fig. 3(b) the absolute value of the linear chirp is estimated to be  $d\omega/dt \simeq (0.16 \pm 0.02) \cdot 10^{27}$  rad/s<sup>2</sup>. Taking the second order term in Eq. (4) into account, information on higher order chirp coefficients can be obtained, too. The chirp measured in this experiment is the inherent feature of the recording pulses themselves, it could be increased or partially compensated for by using two-grating pulse compressor.

In the limiting case of frequency degenerate recording beams,  $\omega_1 = \omega_2$ , the described technique is identical to the self-diffraction based implementation of FROG [19]. Working with recording pulses that are non-degenerate in frequency ensures an obvious advantage: the signal-to-noise ratio of the diffracted pulses can be largely improved by profiting from spectral filtering in addition to spatial (angular) filtering typical to all self-diffraction techniques. A single-shot variation of this technique is possible if traditional spectrometers with an input slit are used instead of the Ocean Optics spectrometer with small circular input aperture.

## 4 Summary and conclusions

The superposition of two pulses of different color in LiNbO<sub>3</sub> sample results in the appearance of Doppler-shifted diffracted beams, even in the spectral range of pronounced two-photon absorption. As a remarkable feature, the diffracted beams, upshifted and downshifted in frequency, are observed up to  $\pm 3$  order, however with no cascading to the higher diffraction orders. Using the language of transient gratings the phenomenon can be explained by the recording of a mixed nonlinear absorption and nonlinear refraction grating, that moves at a velocity close to the velocity of light.

It becomes possible to explain the appearance of symmetric diffraction orders in  $+/-$  directions, to evaluate the diffraction efficiency and estimate, for the first time for LiNbO<sub>3</sub> the upper limit of the grating relaxation time to be less than 5 fs. Straightforwardly, the findings are applied for simple measurements of the chirp of incident recording beam.

Our results highlight the importance of two-photon absorption nonlinearity and explain the inhibition, in the used frequency range, of Cascaded FWM. It is not excluded, that the latter will emerge in the frequency range with negligible two-photon absorption, in the near infrared.

The described phenomenon is treated in terms of recording and self-diffraction from the dynamic grating which is moving with high velocity and brings therefore Doppler shift for diffracted waves. The purpose is not simply to introduce other language to the field; we are convinced that being extended to strongly nondegenerate interactions it will provide new important results in future, especially related to nonlinear coupling of beams with different colors.

## Acknowledgments

Financial support of Deutsche Forschungsgemeinschaft, DFG (IM37/5-2, INST 190/137-1 FUGG, INST 190/165-1 FUGG) and Alexander von Humboldt Stiftung (S. Odoulov Research Award) is gratefully acknowledged. We thank Prof. Dr. Eckhard Krätzig and Dr. Javid Shirdel for fruitful discussions.

## References

- [1] M. Horowitz, B. Fischer, Y. Barad, and Y. Silberberg, “Photorefractive effect in a BaTiO<sub>3</sub> crystal at the 1.5- $\mu$ m wavelength regime by two-photon absorption,” *Opt. Lett.* **21**, 1120–1122 (1996).
- [2] Hung-Te Hsieh, D. Psaltis, O. Beyer, D. Maxein, C. von Korff Schmising, K. Buse, and B. Sturman, “Femtosecond holography in lithium niobate crystals,” *Opt. Lett.* **30**, 2233–2235 (2005).
- [3] A. Shumelyuk, M. Imlau, V. Dieckmann, H. Badorreck, A. Grabar, and S. Odoulov, “Self-diffraction from two-photon absorption gratings in Sn<sub>2</sub>P<sub>2</sub>S<sub>6</sub>,” *Opt. Lett.* **37**, 4065–4067 (2012).
- [4] S. Odoulov, A. Shumelyuk, H. Badorreck, S. Nolte, K.-M. Voit and M. Imlau, “Interference and holography with femtosecond laser pulses of different colours,” *Nat. Commun.* **6**:5866 doi: 10.1038/ncomms6866 (2015).
- [5] H. Crespo, J. T. Mendonca, and A. Dos Santos, “Cascaded highly nondegenerate four-wave-mixing phenomenon in transparent isotropic condensed media,” *Opt. Lett.* **25**, 829–831 (2000).
- [6] J. L. Silva, R. Weigand, and H. M. Crespo, “Octave spanning spectra and pulse synthesis by nondegenerate cascaded four-wave mixing,” *Opt. Lett.* **34**, 2489–2491 (2009).
- [7] Jinping He, Jun Liu, and Takayoshi Kobayashi, “Tunable multicolored femtosecond pulse generation using Cascaded Four-Wave Mixing in bulk materials,” *Appl. Sci.* **4**, 444–467 (2014).

- 
- [8] S. Cabuk and A. Mamedov, "A study of the LiNbO<sub>3</sub> and LiTaO<sub>3</sub> absorption edge," *Tr. J. of Physics*, **22**, 41-45 (1986).
- [9] M. Sheik-Bahae, D. J. Hagan, and E. W. Van Stryland, "Dispersion and band-gap scaling of the electronic Kerr effect in solids associated with two-Photon Absorption," *Phys Rev. Lett.* **65**, 97-99 (1990).
- [10] H. Badorreck, S. Nolte, F. Freytag, P. Bäune, V. Dieckmann, and M. Imlau, "Scanning nonlinear absorption in lithium niobate over the time regime of small polaron formation," *Opt. Mat. Express* **5**, 2729-2741 (2015).
- [11] M. Imlau, V. Dieckmann, H. Badorreck, and A. Shumelyuk, "Tin hypthiodophosphate: Nonlinear response in the sub-100 fs time domain," *Opt. Mater. Express* **1**, 953-951 (2011).
- [12] M. Imlau, H. Brüning, B. Schoke, R.-S. Hardt, D. Conradi, and C. Merschjann, "Hologram recording via spatial density modulation of Nb<sub>Li</sub><sup>4+/5+</sup> antisites in lithium niobate," *Opt. Express* **19**, 15322-15238 (2011).
- [13] C. M. Cirloganu, L. A. Padilha, D. A. Fishman, S. Webster, D. J. Hagan, and E. W. Van Stryland, "Extremely nondegenerate two-photon absorption in direct-gap semiconductors," *Opt. Express* **19**, 22951-22960 (2011).
- [14] A. Fishman, C. M. Cirloganu, S. Webster, L. A. Padilha, M. Monroe, D. J. Hagan, and E. W. Van Stryland, "Sensitive mid-infrared detection in wide-gap semiconductors using extreme nondegenerate two-photon absorption," *Nat. Photonics* **5**, 561-565 (2011).
- [15] M. Imlau, H. Badorreck, and C. Merschjann, "Optical nonlinearities of small polarons in lithium niobate," *Appl. Phys. Rev.* **2**, 040606 (2015).
- [16] Pochi Yeh, "Two-Wave Mixing in Nonlinear Media," *IEEE J. Quant. Electron.*, **25**, 484-519 (1989).
- [17] H.J. Eichler, P. Günter, and D. Pohl, *Laser-induced dynamic gratings*, Springer Series in Optical Sciences, vol. **50**, Springer Verlag, Berlin, Heidelberg, 1986.
- [18] R. Brubaker, Q. Wang, D. Nolte, E. Harmon, and M. Melloch, "Steady-state four-wave mixing in photorefractive quantum wells with femtosecond pulses," *J. Opt. Soc. Am. B* **11**, 1038-1044 (1994).
- [19] R. Trebino, *Frequency-Resolved Optical Gating: The Measurement of Ultrashort Laser Pulses* (Kluwer Academic Publishers, 2000).

---

## Danksagung

Mein besonderer Dank gilt Herrn Prof. Dr. Mirco Imlau für die freundliche Aufnahme in die Arbeitsgruppe *Ultrakurzzeitphysik*, die spannende Themenstellung und seine stete Unterstützung und Diskussionsbereitschaft im Rahmen meiner Promotion. Mein Dank geht außerdem an Herrn Prof. Dr. Joachim Wollschläger für die Begutachtung dieser Arbeit.

Für die gute Zusammenarbeit im Rahmen seiner Bachelorarbeit und weit darüber hinaus möchte ich Herrn B.Sc. Stefan Nolte danken. Für die Durchführung von Z-Scan Messungen danke ich Herrn M.Sc. Felix Freytag während seiner Promotion und Frau M.Sc. Pia Bäune im Rahmen ihrer Bachelorarbeit.

Herrn M.Sc. Andreas Büscher möchte ich für sehr anregende Diskussionen über Themen der nichtlinearen Optik danken. Desweiteren danke ich der gesamten Arbeitsgruppe für die ständige Hilfsbereitschaft und das angenehme Arbeitsklima.

Bei Herrn Prof. Dr. Serguey Odoulov und Herrn Dr. Alexandr Shumelyuk möchte ich mich für die ausgezeichnete Zusammenarbeit und Diskussionen bedanken. Herrn Dr. Gabor Corradi und Herrn Dr. Krisztián Lengyel danke ich für die gute Zusammenarbeit im Rahmen zweier Forschungsaufenthalte und die Bereitstellung einiger Proben sowie dem Deutschen Akademischen Austauschdienst (DAAD) für die finanzielle Unterstützung.

Den Mitarbeitern der elektronischen und feinmechanischen Werkstätten danke ich für das Anfertigen und die Reparatur verschiedenster Bauteile. Herrn Dr. Rainer Pankrath, Frau Gerda Cornelsen und Herrn Werner Geisler möchte ich für die Probenpräparation danken.

Der Deutschen Forschungsgemeinschaft (DFG) danke ich für die finanzielle Unterstützung im Rahmen des Drittmittelprojektes Holographische Kurzzeitspektroskopie (IM37/5-2).

Meiner Familie gilt ein besonderer Dank, deren Unterstützung mir das Studium und die Promotion ermöglicht hat. Zuletzt geht ein ganz besonderer Dank an meine Freundin Franziska, die mich in all der Zeit unterstützt und motiviert hat.

## Eidesstattliche Erklärung

Ich erkläre hiermit, die vorliegende Arbeit selbstständig und ohne unerlaubte Hilfe verfasst und keine anderen als die angegebenen Hilfsmittel und Quellen verwendet zu haben.

Osnabrück, im Oktober 2015.